Mathematical Modelling of Novel Ultrasonic Transducers with Fractal-Like Geometries

University of South Wales
Prifysgol De Cymru

Sara Canning

School of Computing and Mathematics

University of South Wales

A submission presented in partial fulfilment of the requirements of the University of South Wales/Prifysgol De Cymru for the degree of

Doctor of Philosophy

August 2017

Acknowledgements

I wish to express my sincere appreciation for all the advice my supervisors Professor Paul Roach and Dr Alan Walker have given me throughout my PhD. You have both been tremendously encouraging, and have helped me build confidence and grow as a researcher. Your genuine interest in my research has helped me progress and our meetings have been an enjoyable experience.

I also would like to thank my viva examiners, Professor Anthony Mulholland and Dr Graeme Boswell for easing me through my defence and for their valuable suggestions in improving this thesis. I also gratefully acknowledge the support I have received from a Centenary Doctoral Scholarship from the University of South Wales.

In addition, I would like to thank my family for all the love and support they have given me throughout the years. Lastly, to my husband Lee, I wish to express my gratitude for his encouragement, support and patience, all of which has helped in the completion of this PhD.

Abstract

Piezoelectric ultrasonic transducers have the potential to operate as both a sensor and as an actuator of ultrasonic waves. Standard designed transducers have a regular structure and therefore operate effectively over narrow bandwidths due to their single length scale. Biological transducers of ultrasound benefit from a wide range of length scales giving rise to increased bandwidths. In this thesis, one-dimensional mathematical models are employed to predict the performance of novel ultrasonic transducers whose designs cover a range of length scales. In particular, pre-fractal designs are utilised. A variety of fractal structures have been considered in this thesis. The effect of an infinitely ramified Sierpinski carpet device necessitates an adaptation on the renormalization approach so that a Green function renormalization method can be utilised. The important operating characteristics for the device are derived, and comparison of metrics between the new device alongside the standard design (Euclidean) and a previously investigated Sierpinski gasket device are performed. A model of a three-dimensional pre-fractal transducer is explored using a similar methodology to previous pre-fractal devices. The design considered is inspired by the Sierpinski tetrix fractal. The effectiveness of the design is considered through comparison with standard designs and an earlier pre-fractal device. An extension to the Green function renormalization method is applied to study the behaviour of an ultrasonic wave travelling through intricate structures that are more connected than the fractal-inspired designs. The structures considered are the Cartesian product of two

Sierpinski gasket lattices and the Cartesian product of two Sierpinski carpet lattices. These structures are utilised to obtain the theoretical operating characteristics for novel devices.

Contents

List of Figures

v

List of Tables

xxiii

Nomenclature

D_f	Fractional dimension	ϵ, ϵ_{ij}	Permittivity in 1-D and tensor notation, respectively
$\mathcal{G}$	Fractal graph	x, z, x_L	Spatial variables
$\hat{G}^{(n)}, \hat{G}^{(\pi)}$	Bare Green function matrix	ρ, ρ_T, ρ_L	Density
$G^{(n)}, G^{(\pi)}$	Green function matrix	u, u_L	Particle displacement
$H^{(n)}, H^{(\pi)}$	Adjacency matrix	t	Time
I_n	Identity matrix	C_0	Capacitance
T, T_i	Stress variables in 1-D and tensor notation, respectively	A_r	Cross-sectional area of the transducer/ each fractal lattice edge
Y, Y_T	Young's modulus	l	Transducer thickness
S, S_j	Strain variables in 1-D and tensor notation, respectively	p	Laplace variable
h	Piezoelectric coefficient	v, v_T, v_l	Wave velocity
D, D_i	Displacement variables in 1-D and tensor notation, respectively	α	Forward displacement amplitude
E, E_j	Electric field in 1-D and tensor notation, respectively	β	Backward displacement amplitude

α_L	Forward displacement amplitude of the load	K_F	Front-face reverberation factor
β_L	Backward displacement amplitude of the load	K_B	Back-face reverberation factor
α_B	Forward displacement amplitude of the backing material	f_e	Electrical resonant frequency
β_B	Backward displacement amplitude of the backing material	f_m	Mechanical resonant frequency
V	Voltage	T_F	Front-face transmission coefficient
τ	Transit time	T_B	Back-face transmission coefficient
Q	Electrical charge	Z	Electrical impedance
I	Current	F_F	Force at front-face
Z_a	Impedance	A_F	Front-face stress attenuation factor
Z_0	Series electrical load	ψ	Transmission sensitivity
Z_P	Parallel electrical load	ϕ	Reception sensitivity
U	Voltage attenuation factor	G	Amplitude
Z_T	Mechanical impedance of the transducer	BW	Bandwidth
F	Force	f	Frequency
Z_L	Mechanical impedance of the load	f_u	Upper frequency
Z_B	Mechanical impedance of the backing layer	f_l	Lower frequency
R_F	Front reflection coefficient	GBP	Gain bandwidth product
R_B	Back reflection coefficient	c_{ij}	Elastic modulus tensor

e_{ij}	Piezoelectric stress coefficient	$B^{(n)}$	Boundary condition matrix
v_f	Volume fraction of the ceramic phase	$\underline{c}^{(n)}$	Boundary condition vector
$\check{v}_f$	Volume fraction of the polymer phase	q	Vertex degree
ρ^p	Density of polymer	θ	Dimensionless variable
ρ^c	Density of ceramic	$\bar{G}^{(n)}$	Block diagonal matrix whose v blocks equal $\hat{G}^{(n)}$
n	Generation level	ξ	Ratio of the cross-sectional area of each edge to its length
$N_n,$ N_π	Complete number of vertices for lattice structure	Z_s	Specific acoustic impedance
L_s	Lattice side length	F_T	Force in piezoelectric material
$A, B,$ C, D	Fictitious vertices to accommodate boundary conditions	F_B	Force in backing material
$\bar{H}^{(n)}$	Block diagonal matrix representing connectivity properties of sub-graphs	F_L	Force in the load
$V^{(n)}$	Sparse matrix assigning one to connection of sub-graphs	Φ	Electric potential
Δx	Distance between neighbouring vertices	$\mathcal{G}^{(\pi)}$	Cartesian product graph
$A^{(n)}$	Discretized Laplacian matrix		

Chapter 1

Introduction

1.1 Design and Applications of Ultrasonic Transducers

Transducers are devices which enable the conversion of one form of energy into another. Ultrasonic transducers are employed for the generation and detection of ultrasonic waves [86]. Ultrasound refers to sound waves having frequencies greater or equal to $20\,\mathrm{kHz}$. A transducer is considered to be ultrasonic if it operates within this frequency range. These devices are used extensively in fields such as communication, medicine and non-destructive evaluation [101, 135]. For instance, ultrasonic transducers are used in SONAR (SOund Navigation And Ranging) to help with navigation and communication. Moreover, these devices are utilised to detect subaquatic objects through the emission of ultrasonic sound waves and the distance is determined by measuring the reverted reflected waves. Submarines require the use of these devices to determine and gauge the location of enemy vessels. Additionally, ultrasonic transducers are important instruments that are used within the medical field. In particular, they safely provide a way to image internal organs in the abdomen. Although ultrasonic transducers are used for a vast amount of applications, there are further forms of non-ultrasonic transducers that can be utilised; pressure transducers, for example, are often used in leak detection. However, the work undertaken within this thesis concentrates solely on

ultrasonic devices.

There are two main types of ultrasonic transducers that are used in generating and detecting ultrasonic waves; these are electrostatic and piezoelectric transducers. Electrostatic devices employ an oscillating membrane connected to a back-plate which can incorporate resonating conduits and/or cavities [91, 108, 131, 132, 133, 134]. Electrostatic devices generally have higher sensitivities and bandwidths, however, they suffer from requiring a larger operating voltage than piezoelectric devices [118]. Furthermore, these devices are much more vulnerable to the external surroundings, making their use restricted [70]. Consequently, electrostatic devices will not be explored in this thesis.

In this thesis, mathematical models of novel piezoelectric ultrasonic transducers are investigated. The piezoelectric crystal is the fundamental component of piezoelectric ultrasonic transducers as it is the active material that enables the conversion of mechanical energy into electrical energy, and vice-versa.

The phenomenon which causes the conversion of energies is known as the piezoelectric effect, where the name is derived from the Greek *piezein*, meaning pressure [128]. Discovered in 1880 by Pierre and Jacques Curie, it was found that the application of a mechanical strain on certain crystalline materials resulted in the direct generation of electrical signals [50, 96, 124]. This discovery subsequently led to the production of piezoelectric ultrasonic transducers. In piezoelectric transducers, a piezoelectric material is sandwiched between a backing material and front matching layer [10, 53, 114, 128, 130]. During reception mode, the ceramic expands and contracts through the application of a mechanical stress causing the creation of an electrical current; see Figure 1.1 (a). In transmission mode, the continuous expansion and contraction of the material when an electric current is applied results in the production of mechanical vibrations; see Figure 1.1 (b). Traditional piezoelectric ultrasonic transducers are commonly manufactured using the procedure of cutting piezoelectric ceramic and filling the voids with a non-piezoelectric passive polymer. Preferred design choices are the 1-3 and 2-2 composites. Here,

(a) The piezoelectric element produces a voltage when subject to pressure at its plates.

(b) The piezoelectric element generates vibrations when applied with a voltage.
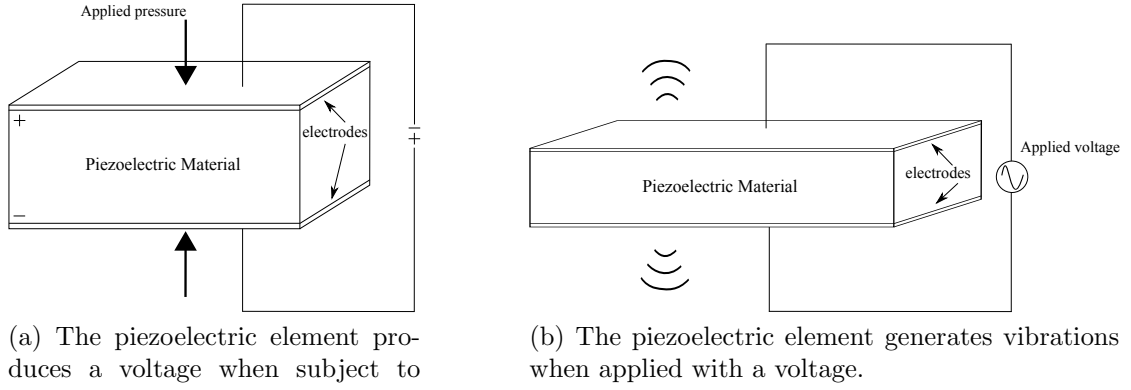
Figure 1.1: Schematic of piezoelectric effect (a) and the reverse piezoelectric effect (b).

the first digit refers to the connectivity of the active material and the second digit denotes the connectivity of the passive element. Hence, for the 1-3 structure, the ceramic phase is continuous in one dimension and the polymer is continuous in all three [96]. The 1-3 design consists of cutting a ceramic block into a series of cross strips, with the polymer filling the voids, and 2-2 designs cut the ceramic in vertical strips so that the ceramic and polymer phases are parallel. The illustrations in Figure 1.2 are of a 1-3 and 2-2 composite transducer, in which the ceramic is represented in yellow and the polymer in black. Due to their one dominant length

(a) 1-3 Connectivity.

(b) 2-2 Connectivity.
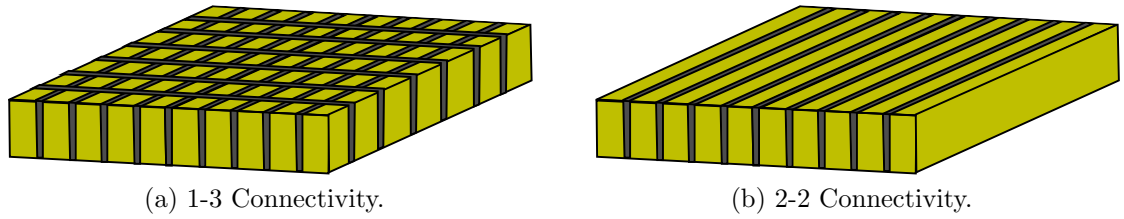
Figure 1.2: Schematic of ceramic-polymer composite transducers.

scale, the regular geometry of these designs restricts their effective performance to a small range of frequencies. The range of length scales is an important aspect to consider when designing new transducers, since the greater the range of length scales the wider the operational bandwidth. That is, the range of frequencies in

which the transducer can operate effectively. Applications of ultrasonic transducers may require high frequency echoes to be received from the production of low frequency sound waves. Thus, wide bandwidth devices are essential [126]. In later chapters, comparisons between current and novel designed transducers will be discussed in terms of the operating characteristics of the devices. Furthermore, the effect of increasing the range of length scales can be determined. In contrast to man-made devices, biological transducers have greater complexity in their structure, including a range of length scales [35, 86, 105]. These result in more effective transmission and reception of ultrasonic waves over a wider range of frequencies. Construction of devices which benefit from a range of length scales, similar to those found in nature, is therefore of great interest [7, 8, 12, 19, 20, 83, 86]. Certain types of bats, moths and dolphins, amongst others animals, have naturally occurring transducers within their biological makeup and use ultrasound to fit their specific purposes. In particular, bats use echolocation to judge their surroundings in instances of poor vision [1]. In such occurrences, bats are able to locate their prey by emitting ultrasonic sound waves and listening out for the returning echoes. The time it takes for the echoes to return allows the bat to determine the distance between the prey and itself, as well as determine the direction of the object. The difference in intensity of the sound received to the bat's two ears allows for a horizontal angle of targets to be formed [59]. Figure 1.3 (a) demonstrates the process of echolocation, allowing the bat to create mental images of its surroundings and Figure 1.3 (b) displays the brown long-eared bat. The visible ridges in the bat ears may help to focus the ultrasonic sounds waves down onto the tragus [119]. The tragus is a soft cartilaginous structure and it is assumed to aid sound down onto the ear canal.

Transducers have several useful metrics for comparison. In particular, the electrical impedance, reception and transmission sensitivities often are used to compare different transducer models [7, 8, 11, 12, 19, 20, 32, 48, 82, 86, 132]. The electrical impedance, defined as the complex ratio of the voltage to the current, is
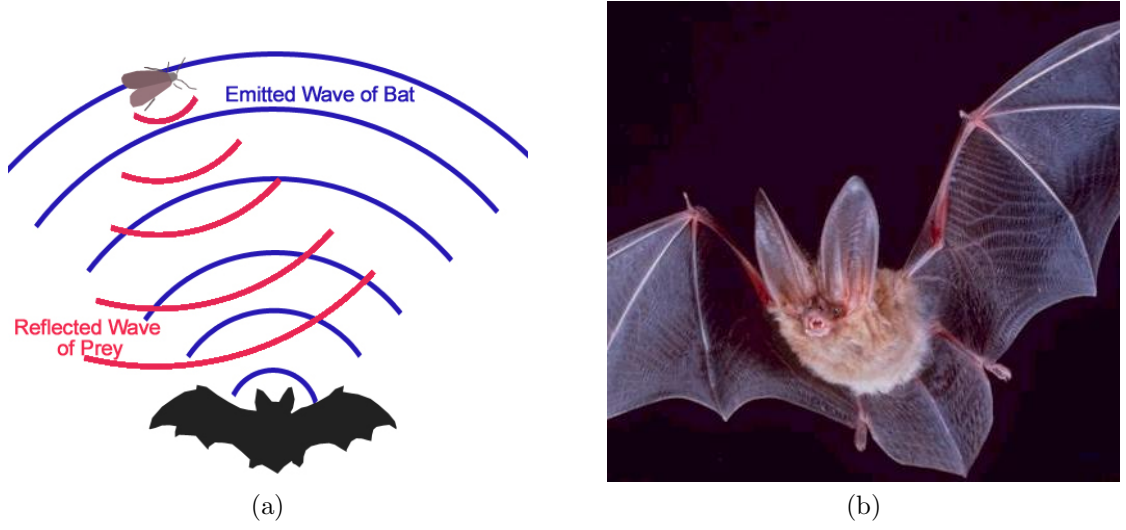
Figure 1.3: Illustrations of (a) returning echoes from the production of sound waves [116] and (b) the brown long-eared bat [9].

important as it gives information regarding the transducer's operating characteristics [96]. The sensitivity of the transducer is given as the ratio of the electrical output to the mechanical input, in reception mode, and as the ratio of an acoustic output to the applied voltage, in transmission mode. The sensitivity of the device is important to consider as it describes the efficiency of energy conversion [31, 54]. Thus, these measures are key indicators into the performance of the ultrasonic transducers. As such, high sensitivity is a desirable characteristic [2, 15].

The research presented in this thesis is concerned with the effects of embedding pre-fractal structures into the design of new ultrasonic devices. Pre-fractal designs are of interest since their structures closely resemble those found in nature. These structures tend to have more sophisticated geometries than current man-made devices and encompass a range of length scales. Implementing fractal-like structures into new designs therefore, ought to improve current transducer performance.

The concept of fractal-inspired ultrasonic transducers has previously been described and the performance of these designs has shown some improvements over current piezoelectric ultrasonic transducers. Therefore, there is further scope to

investigate novel designs incorporating different pre-fractal geometries. Comparison between the standard Euclidean, the novel and a previous fractal-inspired designs will be implemented as means of determining the most suitable design. In the following section, an introduction to fractal geometry and their features is discussed.

1.2   Introduction to Fractals

The term fractal is derived from the Latin *fractus*, meaning broken [27]. Fractal structures are complex geometrical objects which exhibit structural similarity across magnification levels. As a result, these structures cannot be described in Euclidean terms [18, 27, 29, 74, 78]. The formal study of mathematical fractals sets
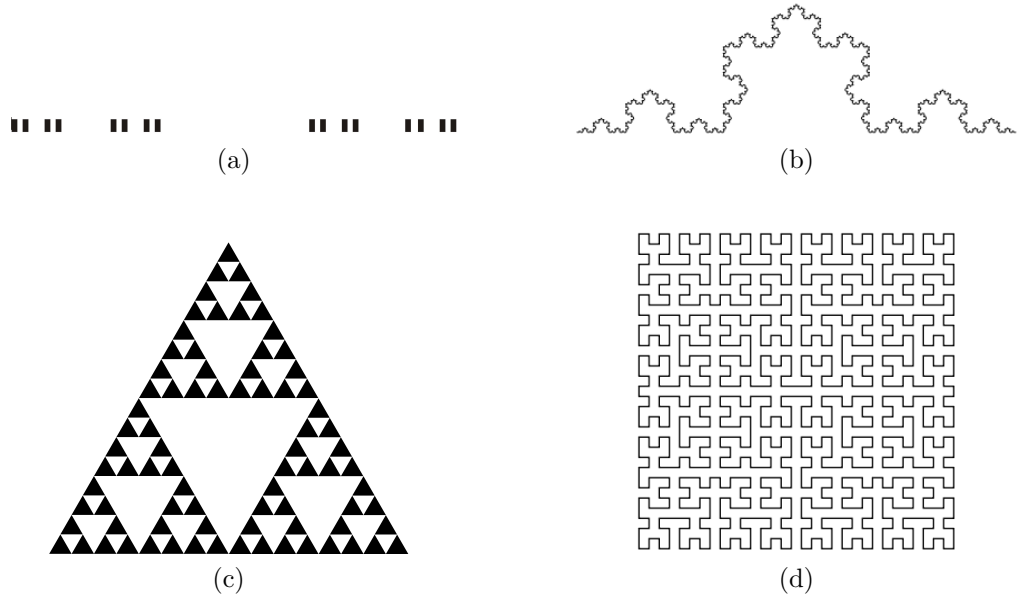
Figure 1.4: Mathematical fractal sets at generation level five for the (a) Cantor set, (b) von Koch curve, (c) Sierpinski gasket and (d) Hilbert curve.

appears to have started in the 19th century, with the introduction of fractals known as the Hilbert curve, Cantor set, von Koch curve and Sierpinski gasket [28, 34]. Figure 1.4 illustrates these structures. Fractal structures can vary extensively in

complexity, where some fractal sets are constructed using a simple iterative process. The middle third Cantor set, for example, is formed from the continual removal of a middle line segment from the previous iteration. Specifically, the initial structure is of a line segment of unit length, and the following generation consists of two line segments obtained by the removal of the middle third segment. Subsequent generations are then found by iteratively applying the same procedure to each of the line segments. Figure 1.4 (a) presents the fourth generation level of the middle third Cantor set. Other fractal sets can form into very detailed structures. One such fractal is the Julia set, for which the constructions begins with the quadratic function $f(z) = z^2 + c$, where c is a complex number [29]. The iterative process is then given by $z_{n+1} = z_n^2 + c$ [5, 79]. These fractal sets are generated by initially indicating the complex numbers, initial value z_0 and fixed c and then continually evaluating the equation given above. Furthermore, the iterations must remain bounded for the associated point to lie in the set. Thus, coloured pixels represent the iterations of the complex number, z_n, that belong to the Julia set. Figure 1.5 illustrates the Julia set fractal, using the example $c = -1.25$. Referring to Figure 1.5, a blue pixel is drawn as it iterates for points of z_n that do not tend to infinity.
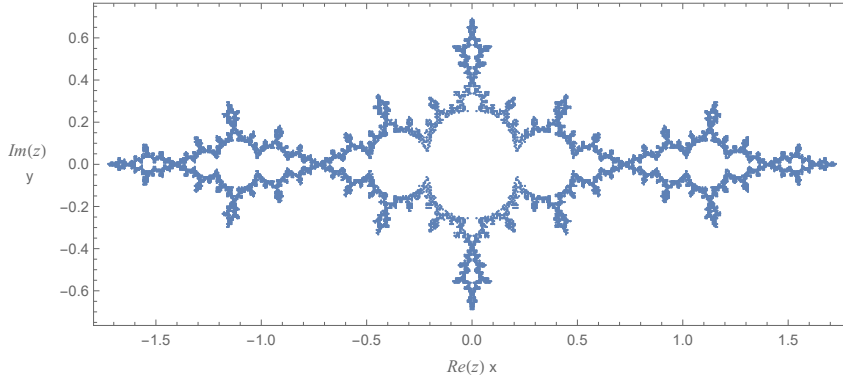
Figure 1.5: The Julia set of $z^2 - 1.25$.

The definition of fractals was introduced by Benoit Mandelbrot in 1975 to define the set of irregular structures. In his essay [74], he highlights the importance of

irregular structures and explains that there are geometric structures that contain an infinite number of distinct length scales. In addition to self-similarity, another important feature of fractals is their dimension. Unlike Euclidean geometry, fractals have non-integer dimensions. It is this property which gives an indication into the complexity of the fractal shape [29] and can provide information for the space filling properties of the set [28]. Due to the nature of fractal geometries, several different descriptions on the dimension of the set, such as the Hausdorff and Box-counting dimensions, have been defined [28]. The reason for this is that some definitions are not appropriate for certain fractals. There is no one definition that can be applied to every set. References made to the fractional dimension, refers usually to Hausdorff Besicovitch dimension [74]. For many fractals, the formation of the self-similar structure is obtained by scaling a segment n by a factor of s. Using the Hausdorff Besicovitch definition, the fractional dimension D_f can be found from $s^{D_f} = n$. Or, to express this in terms of the dimension,

$$D_f = \frac{\log (n)}{\log (s)}. \tag{1.1}$$

To illustrate the dimension of some fractal structures, the dimensions of the geometric patterns shown in Figure 1.4 are obtained. In regards to the Hilbert curve (Figure 1.4 (d)), this pattern is obtained from the process of mapping a one-dimensional interval into a two-dimensional plane, and so it has dimension $D_f = 2$. For the middle third Cantor set the dimension is $D_f = \log (2)/\log (3)$, since it is obtained by replacing iterations by two copies that are scaled by a factor of three. For the von Koch curve, a single line segment is replaced with four line segments obtained by removing the middle third segment, and replacing it by the other two sides of the equilateral triangle. Therefore its dimension can be given by $D_f = \log (4)/\log (3)$. The Sierpinski gaskets are formed by replacing a two-dimensional triangle with three copies of itself, that are scaled by a factor of two. Thus, $D_f = \log (3)/\log (2)$.

Progressing from mathematical fractal sets, there are natural phenomena that can be described in terms of fractal features. Natural objects have been shown

8

to exhibit self-similarity over a wide range of length scales. In particular, self-similar geometry can been seen when examining a formation of ice crystals or the branching of a tree; see Figure 1.6. That is to say, these natural occurrences appear

<div align="center">(a)   (b)</div>

Figure 1.6: Images displaying (a) the formation of ice crystals [109] and (b) the spanning of tree branches [44].

to look the same at any magnification and so they are characterised as fractals.

Mathematical modelling can assist with the construction of new devices that operate effectively over a larger range of frequencies. Particularly, it is possible to consider the implementation of fractal-like structures into the design of new ultrasonic transducers. These novel designs have a greater range of length scales than traditional designs, and so ought to result in improved transmission and reception responses.

In previous research [86], a fractal-inspired device had been investigated utilising a Green function renormalization technique. Within this thesis, novel pre-fractal designs will be modelled similarly. Consequently, the subsequent section discusses the renormalization approach.

1.3   Green Functions Renormalization

Throughout this thesis, each fractal-inspired transducer has been modelled utilising the Green function renormalization method (or an adaptation of this). In

a collection of papers [38, 39, 40, 41, 110], a renormalization approach was employed to study transport phenomena in complex structures; in particular fractal geometries were studied. Green function renormalization is a useful method for providing physical quantities from the derivation of a small amount of pivotal Green functions [39]. In these papers, use is made of known Green functions for a given matrix to derive the exact Green functions of a related matrix [111]. This involved treating a fractal structure as a graph, $\mathcal{G}$. Then, any structure from the fractal set was likewise regarded as a graph from the sequence of graphs $\{\mathcal{G}^{(n)}\}$, where n is in reference to the iteration. A Green function $G_{ij}^{(n)}$, for any fractal lattice is defined to be the $(i, j)^{\text{th}}$ element of the resolvent matrix $G^{(n)}(p)$ [111]. That is,

$$G^{(n)}(p) = (pI_n - H^{(n)})^{-1}, \tag{1.2}$$

where p is a complex variable and $H^{(n)}$ and I_n represent the adjacency and identity matrices respectively.

The Green function renormalization approach was applied to transport phenomena in complex structures by initially considering a discretized representation of the transport equation [41]. The discretized form is then non-dimensionalized. The dimensionless equation can then be expressed in two forms; one accounting for boundary conditions and the other neglecting boundary conditions. The boundary conditions relate to transport entities that enter and exit the system through the input and output vertices of the graph. The input/output vertices correspond to external vertices of the graph $\mathcal{G}$, or more specifically, the lattice representation of the graph; see Figure 1.7. The process of obtaining pivotal Green functions was

Figure 1.7: Connection process to obtain the second generation from the first generation for the one-dimensional line. Solid circles represent the input/output vertices and the empty circles correspond to internal vertices.

achieved by firstly ignoring boundary conditions. These were later re-introduced through a suitable algebraic equation. The dimensionless equation was then more conveniently expressed in the frequency domain rather than in the time domain. Consequently, taking Laplace transforms of the non-dimensionalized equation resulted in a linear algebraic equation, which encompassed the Green function matrix.

In the following chapters, a similar methodology is taken to derive expressions for the important operational characteristics of novel transducers designs.

1.4   Thesis Objectives and Organisation

The purpose of this thesis is to investigate the behaviour of ultrasonic transducers which possess a range of length scales, with the aim of improving on transmission and reception sensitivities. Designs that implement a fractal-like geometry are analysed and the important operating characteristics derived. The propagation of an ultrasonic wave within a pre-fractal structure is analysed using the Green function renormalization method and the pivotal elements are obtained from the fractal lattice counterparts. To determine the most appropriate design that can be used in the manufacture of new devices, comparisons are made between novel fractal-inspired designs with regular designed transducers.

In Chapter 2, a one-dimensional model for a standard piezoelectric plate transducer is reviewed. The effect of introducing a polymer phase into the regular design is then discussed. The design considered is the widely used 1-3 composite transducer. The performances of the two devices are modelled using the linear systems model. The constitutive piezoelectric equations are described in this chapter and are utilised in subsequent chapters. A model for a previously investigated Sierpinski gasket inspired transducer is also presented in this chapter. For each device, expressions for the non-dimensionalized electrical impedance and the transmission and reception sensitivities as a function of the operating frequency are presented, and comparisons of figures of merit are made. Consequently, this chapter presents

a review of previous related research and provides some new comparisons of transducer output.

In Chapter 3, models for three devices inspired by the Sierpinski carpet are introduced and an adapted Green function renormalization method is used to attain the important relations for each model. For each model, the operating characteristics are determined for the first three fractal generation levels. To establish whether there is an improvement in device transmission and/or reception responses, the results are compared with the Sierpinski gasket inspired device and the standard Euclidean transducer.

In Chapter 4, a model of a transducer design based on a three-dimensional fractal, the Sierpinski tetrix, is considered. The Green function renormalization method is employed to investigate the performance of a Sierpinski tetrix inspired transducer. Comparisons of the operating responses are performed between the three-dimensional pre-fractal design along with the Sierpinski gasket inspired device and standard Euclidean design.

Chapter 5 introduces two new transducer designs inspired by the Cartesian product of two pre-fractal lattices. For these structures, the behaviour of the device is analysed at the first fractal generation level. The derivation of the electrical impedance, transmission and reception sensitivities require an extension to the Green function renormalization method. The extension to the model is outlined in this chapter. The efficiency of these devices is considered by comparing the operating characteristics to the Euclidean transducer, as well as to two pre-fractal devices. The thesis findings are summarised and potential future research is discussed in Chapter 6.

In short, this thesis reviews previous piezoelectric ultrasonic transducer designs, models a range of possible new designs and illustrates the potential benefits of their construction. A summary of the original contributions is now given. In Chapter 2 all models have been further analysed to obtain the useful figures of merit for each of the transducers' operating characteristics. That is, the maximum amplitude,

3-dB bandwidth and gain bandwidth product. These metrics have also been calculated in subsequent chapters. In addition, Chapter 2 highlights an inaccuracy made previously on the fractal-inspired device. The correction has been made to this model within this chapter. The Green function renormalization method is adapted in Chapter 3 to illustrate the transmission and reception profiles of three new designs inspired by the Sierpinski carpet fractal. The Green function renormalization method is then utilised in Chapter 4 to investigate the transmission and reception responses of a new Sierpinski tetrix inspired transducer. In Chapter 5, the Green function renormalization method is extended to determine the likely behaviour of two new theoretical designs, whose lattice counterparts are obtained from the Cartesian product of two graphs.

Chapter 2

Analysis and Extension of Previous Ultrasonic Research

2.1   Introduction

This chapter reviews published results on the mathematical modelling of piezo-electric ultrasonic transducers. First, a monolithic piezoelectric plate transducer is presented in Section 2.2. In Section 2.3, a 1-3 composite transducer, which is made of piezoelectric ceramic diced and filled with a polymer, is then considered. Lastly in Section 2.4, the analysis of a transducer benefiting from a pre-fractal structure is explored. The pre-fractal structure considered in this section is the Sierpinski gasket.

The derivations of equations reproduced in this chapter were verified, and the analysis, results and images have been newly produced by the current author to aid understanding of the work. This has also aided the development of new work presented in subsequent chapters that has employed a similar methodology. As such, this is a demonstration of the soundness of the approach adopted throughout this study. Additionally, these models have been extended to determine the maximum amplitude (gain), 3-dB bandwidth and the gain bandwidth product for the important operating characteristics.

2.2 Monolithic Piezoelectric Plate Transducers

Monolithic piezoelectric plate transducers consist of plane parallel plates that are formed from a piezoelectric material, such as piezoelectric crystals or ferroelectric ceramics [99]. These devices are constructed with a backing layer and a front matching layer to help control vibrations when pulses of electricity are applied to the piezoelectric element [33, 37, 99, 129, 130]. The passive backing material, which is positioned to the rear of the piezoelectric element, prevents unwanted vibrations emanating from the back face of the transducer. The material of this layer is most commonly constructed out of an epoxy resin [26, 37, 88, 90] due to its good acoustic impedance matching and high ultrasound absorbency [88]. However, the incorporation of this backing material generally results in reduced sensitivity [37, 96]. Thus, single or multiple matching layers are included to the transducer's front face to help minimise the reduction in sensitivity. These elements are then encased in a housing to protect them; see Figure 2.1.
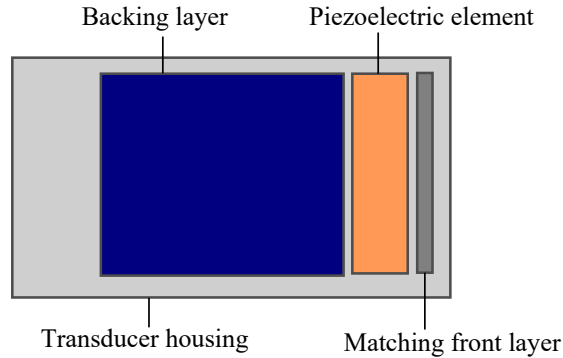
Figure 2.1: Typical arrangement of a simple piezoelectric ultrasonic transducer.

It has previously been established that the dynamics of thickness mode transducers can be approximately described by a one-dimensional model. One approach that has been successful in describing the behaviour of such transducers is the linear systems model [46]. Previous authors [47, 48, 56, 82, 84, 96, 98, 102] have utilised or adapted this model to derive an expression for the transducer model by coupling the piezoelectric equations with the one-dimensional wave equation.

The linear systems model is used in this section; other approaches include Mason's model and the KLM model [64, 67, 76].

The one-dimensional constitutive piezoelectric equations are particularly useful as they relate elastic variables, stress T and strain S, to the electric variables, field E and displacement D [57]. These are given as

$$T = YS - hD, \tag{2.1}$$

$$E = -hS + \frac{D}{\epsilon}, \tag{2.2}$$

where Y represents the Young's modulus, h is the piezoelectric constant and ϵ is the permittivity. The piezoelectric material is the active element of the transducer as it is the primary component allowing for the conversion between energies. Electric charges do not flow easily within the piezoelectric material as a result of it being a good insulator. Thus, according to Gauss' Law, the displacement component is constant inside the transducer [96, 130],

$$\frac{\partial D}{\partial x} = 0, \tag{2.3}$$

where x is the spatial variable. The stress equation of motion is

$$\frac{\partial T}{\partial x} = \rho \frac{\partial^2 u}{\partial t^2}, \tag{2.4}$$

where ρ is the density, u is the particle displacement and t is time. Using equations (2.1)-(2.4) the one-dimensional wave equation for the mechanical displacement $u(x,t)$ can be obtained

$$\rho \frac{\partial^2 u}{\partial t^2} = Y \frac{\partial^2 u}{\partial x^2}. \tag{2.5}$$

The piezoelectric equations (2.1), (2.2) and wave equation (2.5) are linked since the strain is defined as

$$S = \frac{\partial u}{\partial x}. \tag{2.6}$$

The capacitance of the device is the way in which the transducer is able to store an electrical charge. Since the piezoelectric material is clamped, (that is movement is

16

restricted in response to an applied electric field [26, 117]) the clamped capacitance is required. This clamped capacitance, C_0, is given by the following relationship

$$C_0 = \frac{A_r \epsilon}{l}, \tag{2.7}$$

where A_r is the cross-sectional area and l is the transducer thickness. It is possible to solve the one-dimensional wave equation by firstly taking Laplace transforms with respect to t to give

$$p^2 \bar{u} = v^2 \frac{\partial^2 \bar{u}}{\partial x^2}, \tag{2.8}$$

where p is the complex Laplace variable and v is the wave velocity given by $v^2 = Y/\rho$. Furthermore, it is assumed that initial displacement and velocity are both zero [96]. As shown in equation (2.8) and throughout the remainder of this section, an overhead bar will indicate terms in the Laplace domain.

A solution for the particle displacement is then found by solving equation (2.8), to find

$$\bar{u}(x, p) = \alpha e^{-\frac{p}{v}x} + \beta e^{\frac{p}{v}x}, \tag{2.9}$$

where α and β are the displacement amplitudes which relate to the forward and backwards travelling waves within the transducer material [71].

The voltage V is obtained by integrating the electrical field over the limits $x = 0$ and $x = l$, where these correspond to the front and rear faces respectively. Thus, by first expressing the electric field, given in equation (2.2), as

$$\bar{E} = -h\frac{\partial \bar{u}}{\partial x} + \frac{\bar{Q}}{A_r \epsilon}, \tag{2.10}$$

where Q is the electrical charge and $\bar{D} = \bar{Q}/A_r$, the voltage across the transducer may be expressed as

$$\bar{V} = -h[\alpha(e^{-p\tau} - 1) + \beta(e^{p\tau} - 1)] + \frac{\bar{Q}}{A_r \epsilon}l, \tag{2.11}$$

where $\tau = l/v$ is the transit time of the plane wave through the transducer [96]. To obtain an expression for the electrical charge Q, the current I is integrated over

the time domain t. Then by taking Laplace transforms, the following expression is defined,

$$\bar{Q} = \frac{\bar{I}}{p} = -\frac{\bar{V}}{p\bar{Z}_a}, \tag{2.12}$$

where the current is given by $I = V/Z_a$, and Z_a is the impedance of an arbitrary electrical load. Thus, a solution for the voltage can be expressed as

$$\bar{V} = -h[\alpha(e^{-p\tau} - 1) + \beta(e^{p\tau} - 1)]\bar{U}, \tag{2.13}$$

where U is the voltage attenuation factor that is given by

$$\bar{U} = \frac{pC_0\bar{Z}_a}{(1 + pC_0\bar{Z}_a)}. \tag{2.14}$$

The performance of the transducer depends on certain factors, including the backing material and front matching layer [37, 88, 129, 130]. Vibrations in the transducer are caused when short pulses of electricity are applied to the piezo-electric material. It is of interest to only allow vibrations to emanate from the front face of the transducer. In order to prevent vibrations at the back, a damping material is attached to the rear face. Without this damping material these vibrations will continue to ring, prohibiting the transducer from listening for returning echoes [37]. The impedance matching layer of the device is positioned between the piezoelectric material and the front face of the transducer, with the purpose of keeping reflected waves within the matching layer in phase when they exit [2]. For the backing material it is desirable that the attenuation parameter is high so that vibrations at the back are prevented. For that reason it may be assumed that there is only a wave travelling away from the piezoelectric material. Thus, the amplitude of the backward propagating wave within the backing material is zero, that is $\beta_B = 0$. The application of boundary conditions at the transducer's surfaces results in

$$\bar{u}(0) = \alpha + \beta \qquad \text{and} \qquad \bar{u}(l) = \alpha e^{-p\tau} + \beta e^{p\tau}. \tag{2.15}$$

18

Thus, continuity of displacement results in

$$\alpha_L + \beta_L = \alpha + \beta, \tag{2.16}$$

$$\alpha e^{-p\tau} + \beta e^{p\tau} = \alpha_B e^{-p\frac{l}{v_B}}, \tag{2.17}$$

where the subscripts L and B refer to the mechanical load and backing layer, respectively. The load is simply the generic term referring to the point in the circuit where power is drawn. The force, F, at the front face of the transducer is related to the cross-sectional area A_r through

$$\bar{F} = A_r \bar{T}. \tag{2.18}$$

As such equation (2.1) may be expressed as $\bar{F} = Y\bar{S}A_r - h\bar{Q}$. Using the definition for the strain, shown in (2.6), as well as the solution for the particle displacement found in (2.9), it can be shown that

$$Y\bar{S}A_r = pZ_T(-\alpha e^{-p\frac{x}{v}} + \beta e^{p\frac{x}{v}}), \tag{2.19}$$

where Z_T is the mechanical impedance of the device given by

$$Z_T = \sqrt{Y\rho}A_r. \tag{2.20}$$

Using equation (2.19) along with the relationship for stress, strain and electrical displacement shown in equation (2.1), the following expression relating force and particle displacement may be obtained

$$\bar{F} + h\bar{Q} = pZ_T(-\alpha e^{-p\frac{x}{v}} + \beta e^{p\frac{x}{v}}). \tag{2.21}$$

Rearranging then gives an expression for the force

$$\bar{F} = pZ_T(-\alpha e^{-p\frac{x}{v}} + \beta e^{p\frac{x}{v}}) - h\bar{Q}. \tag{2.22}$$

Hence, continuity of force gives

$$pZ_L(-\alpha_L + \beta_L) = pZ_T(-\alpha + \beta) - h\bar{Q}, \tag{2.23}$$

19

$$pZ_T(-\alpha e^{-p\tau} + \beta e^{p\tau}) - h\bar{Q} = pZ_B(-\alpha_B e^{-p\frac{l}{v_B}}), \qquad (2.24)$$

where Z_L and Z_B are the mechanical impedances of the load and the backing layer, respectively. Using equations (2.16)-(2.17) and equations (2.23)-(2.24), solutions for the amplitudes α and β may be expressed in terms of the forward propagating amplitude in the load, α_L. Initially rearranging equation (2.16) to be in terms of β_L and substituting this expression into equation (2.23), yields

$$pZ_L(\alpha + \beta - 2\alpha_L) = pZ_T(-\alpha + \beta) - h\bar{Q}. \qquad (2.25)$$

This can then be rearranged resulting in

$$p\alpha(Z_T + Z_L) - p\beta(Z_T - Z_L) = 2p\alpha_L - h\bar{Q}, \qquad (2.26)$$

and dividing by $p(Z_T + Z_L)$ gives

$$\alpha - \frac{\beta(Z_T - Z_L)}{(Z_T + Z_L)} = \frac{2\alpha_L}{(Z_T + Z_L)} - \frac{h\bar{Q}}{p(Z_T + Z_L)}. \qquad (2.27)$$

The reflection coefficient, R_F, at the front face of the transducer is useful here since this is given by

$$R_F = \frac{(Z_T - Z_L)}{(Z_T + Z_L)}. \qquad (2.28)$$

Thus, substituting this into equation (2.27) gives

$$\alpha - \beta R_F = \alpha_L(1 - R_F) - \frac{h\bar{Q}}{p(Z_T + Z_L)}. \qquad (2.29)$$

Equivalently, substituting equation (2.17) into equation (2.24) gives

$$pZ_T(-\alpha e^{-p\tau} + \beta e^{p\tau}) - h\bar{Q} = pZ_B(-\alpha e^{-p\tau} - \beta e^{p\tau}). \qquad (2.30)$$

This is then rearranged as

$$p\beta e^{p\tau}(Z_T + Z_B) = p\alpha e^{-p\tau}(Z_T - Z_B) + h\bar{Q}, \qquad (2.31)$$

and then

$$
\begin{aligned}
\beta e^{p\tau} &= \alpha e^{-p\tau} \frac{(Z_T - Z_B)}{(Z_T + Z_B)} + \frac{h\bar{Q}}{p(Z_T + Z_B)} \\
&= \alpha e^{-p\tau} R_B + \frac{h\bar{Q}}{p(Z_T + Z_B)},
\end{aligned}
\tag{2.32}
$$

where R_B is the reflection coefficient at the back face of the transducer given by

$$
R_B = \frac{(Z_T - Z_B)}{(Z_T + Z_B)}.
\tag{2.33}
$$

Multiplying by $e^{-p\tau}$ then gives an expression for β as

$$
\beta = \alpha e^{-2p\tau} R_B + \frac{h\bar{Q}e^{-p\tau}}{p(Z_T + Z_B)}.
\tag{2.34}
$$

An expression for α can be found by substituting equation (2.34) into equation (2.29) and rearranging to give

$$
\alpha = \frac{\frac{h\bar{Q}R_F e^{-p\tau}}{p(Z_T + Z_B)} + \alpha_L(1 - R_F) - \frac{h\bar{Q}}{p(Z_T + Z_L)}}{1 - R_F R_B e^{-2p\tau}}.
\tag{2.35}
$$

In a similar manner, β is obtained through the substitution of equation (2.35) into equation (2.29),

$$
\beta = \left(\frac{\frac{h\bar{Q}}{p(Z_T + Z_B)} + \alpha_L(1 - R_F)R_B e^{-p\tau} - \frac{h\bar{Q}R_B e^{-p\tau}}{p(Z_T + Z_L)}}{1 - R_F R_B e^{-2p\tau}} \right) e^{-p\tau}.
\tag{2.36}
$$

Now that α and β are explicitly known (in terms of the forward propagating amplitude in the load, α_L), the expression for the voltage, found in equation (2.13), can be rewritten as

$$
\bar{V} = h \left(\bar{K}_F \left(\alpha_L(1 - R_F) - \frac{h\bar{Q}}{(Z_T + Z_L)p} \right) - \frac{\bar{K}_B h\bar{Q}}{(Z_T + Z_B)p} \right) \bar{U},
\tag{2.37}
$$

where

$$
\bar{K}_F = \frac{(1 - e^{-p\tau})(1 - R_B e^{-p\tau})}{(1 - R_F R_B e^{-2p\tau})},
\tag{2.38}
$$

and

$$
\bar{K}_B = \frac{(1 - e^{-p\tau})(1 - R_F e^{-p\tau})}{(1 - R_F R_B e^{-2p\tau})}.
\tag{2.39}
$$

21

The expressions K_F and K_B are the front and back face reverberation factors respectively, and these correspond to the occurrence of multiple reflections as a result of a mechanical wave incident on the front and back faces [71].

From the information obtained, expressions detailing the important operating characteristics of a monolithic piezoelectric transducer can be derived. The characteristics of interest are the electrical impedance, transmission and reception sensitivities. These are then plotted against the operating frequency. Electrical impedance profiles are important as they help determine the efficiency of the transducer. Experimental models of ultrasonic transducers can be very time consuming, particularly when concerning the operational capability of the device. An alternative is to measure the electrical impedance over a range of frequencies by connecting the transducer to an electrical circuit [7, 8]. The electrical impedance of the device is therefore very valuable to engineers as the outcome can help inform whether such devices should be pursued further. For the design engineer the features of interest from the electrical impedance plots are the occurrence of the electrical and mechanical resonant frequencies. The electrical resonant frequency f_e is the frequency at which there is the least amount of electrical resistance in the circuit and so is the frequency that should be used in transmission mode. The mechanical resonant frequency f_m is the frequency where the amplitude of the vibration is at a maximum and so this is the frequency that should be used in reception mode. The electrical and mechanical resonant frequencies are determined by locating in the plot, the first minimum and maximum respectively [7, 96, 98]. The main operating characteristics of the transducer are the transmission and reception sensitivities. These are of high importance as they identify the performance of a transducer when operating as a transmitter or receiver of ultrasound. The material presented in this section was previously published and is extended here to determine the useful figures of merit of the transducer.

When the transducer is transmitting there is no force incident at the front face of the transducer, and so there is no forward travelling wave in the load. Therefore,

$\alpha_L = 0$. Consequently, the previous expressions for α and β reduce to

$$\alpha = \frac{(R_F h\bar{Q}e^{-p\tau})/((Z_T + Z_B)p) - (h\bar{Q})/((Z_T + Z_L)p)}{1 - R_F R_B e^{-2p\tau}}, \tag{2.40}$$

$$\beta = \left(\frac{(h\bar{Q}e^{-p\tau})/((Z_T + Z_B)p) - (R_B h\bar{Q}e^{-2p\tau})/((Z_T + Z_L)p)}{1 - R_F R_B e^{-2p\tau}} \right). \tag{2.41}$$

Thus, it is possible to express the voltage in equation (2.37) as

$$\bar{V} = \frac{\bar{Q}}{C_0} \left(1 - h^2 C_0 \frac{(\bar{K}_F T_F + \bar{K}_B T_B)}{2pZ_T} \right), \tag{2.42}$$

where T_F and T_B are the front and back transmission coefficients given by

$$T_F = \frac{2Z_T}{Z_T + Z_L} \qquad \text{and} \qquad T_B = \frac{2Z_T}{Z_T + Z_B}. \tag{2.43}$$

An expression for the electrical impedance $Z = V/I$ can then be calculated as

$$\bar{Z} = \frac{1}{pC_0} \left(1 - h^2 C_0 \frac{(\bar{K}_F T_F + \bar{K}_B T_B)}{2pZ_T} \right). \tag{2.44}$$

Non-dimensionalising the electrical impedance results with

$$\hat{Z}_e = \frac{1}{pC_0 Z_0} \left(1 - h^2 C_0 \frac{(\bar{K}_F T_F + \bar{K}_B T_B)}{2pZ_T} \right), \tag{2.45}$$

where the subscript e denotes the electrical impedance of the Euclidean (standard) transducer. Moreover, this subscript will be attached to subsequent expressions for the operating characteristics of the device. When the transducer is transmitting, a voltage is applied to create a force at the front face, F_F. The current across the transducer, I, is defined in [96] and is given as

$$\bar{I} = \frac{a\bar{V}}{(Z + b)}, \tag{2.46}$$

where $a = Z_P/(Z_0 + Z_P)$ and $b = Z_0 Z_P/(Z_0 + Z_P)$. The terms Z_0 and Z_P correspond to the series and parallel electrical loads. Continuity of force at the front face gives

$$\bar{F}_F = pZ_T \frac{\partial \bar{u}}{\partial x}(0) - h\bar{Q} = pZ_T \left(-\alpha + \beta - \frac{h\bar{Q}}{pZ_T} \right). \tag{2.47}$$

By substituting equations (2.40) and (2.41) into the above equation, the following is obtained

$$\begin{aligned}
\bar{F}_F &= \frac{h\bar{Q}Z_T}{1 - R_F R_B e^{-2p\tau}} \\
&\times \left(\frac{1 - R_B e^{-2p\tau}}{(Z_T + Z_L)} + \frac{(1 - R_F)e^{-p\tau}}{(Z_T + Z_B)} - \frac{1 - R_F R_B e^{-2p\tau}}{Z_T} \right),
\end{aligned}$$

(2.48)

which simplifies to

$$\bar{F}_F = -\frac{h\bar{Q}\bar{K}_F Z_L}{Z_T + Z_L}.$$

(2.49)

Substituting equations (2.12) and (2.46) into equation (2.49) gives

$$\bar{F}_F = -\frac{ha\bar{V}\bar{K}_F Z_L}{p(\bar{Z} + b)(Z_T + Z_L)},$$

(2.50)

and therefore

$$\frac{\bar{F}_F}{\bar{V}} = -\frac{ha\bar{K}_F Z_L}{p(\bar{Z} + b)(Z_T + Z_L)} = -\frac{haA_F \bar{K}_F}{2p(\bar{Z} + b)},$$

(2.51)

where $A_F = 2Z_L/(Z_T + Z_L)$. An expression for the transmission sensitivity can then be found by substituting equation (2.44) into equation (2.51)

$$\bar{Z} + b = \frac{1 + bpC_0}{pC_0} - \frac{h^2(\bar{K}_F T_F + \bar{K}_B T_B)}{2p^2 Z_T},$$

(2.52)

and therefore

$$\frac{\bar{F}_F}{\bar{V}} = \frac{-ha(A_F/2)\bar{y}\bar{K}_F}{1 - h^2 \bar{y}(\bar{K}_F T_F + \bar{K}_B T_B)/2pZ_T},$$

(2.53)

where $\bar{y} = C_0/(1 + pC_0 b)$. The non-dimensionalised transmission sensitivity, ψ_e, is of the form

$$\psi_e = \frac{\bar{F}_F}{\bar{V}hC_0} = \frac{-a(A_F/2)\bar{y}\bar{K}_F/C_0}{(1 - h^2 \bar{y}(\bar{K}_F T_F + \bar{K}_B T_B))/2pZ_T}.$$

(2.54)

The incorporation of the piezoelectric material allows for the conversion of mechanical vibrations into electrical signals when the transducer is in receiving mode. In this instance $\alpha_L \neq 0$. An expression for the displacement amplitude at the front face is found using equation (2.23) and setting $\beta_L = 0$ since there would be no backward propagating wave in the load, hence

$$\alpha_L = -\frac{\bar{F}_F}{pZ_L}.$$

(2.55)

Thus the substitution of α_L together with equation (2.12) into equation (2.37) gives

$$
\begin{aligned}
\bar{V} &= -\frac{h\bar{F}_F\bar{K}_F(1-R_F)\bar{U}}{pZ_L} + \frac{h^2\bar{K}_F\bar{V}\bar{U}}{Z_P(Z_T+Z_L)p^2} + \frac{h^2\bar{K}_B\bar{V}\bar{U}}{Z_P(Z_T+Z_B)p^2} \\
&= \frac{-2h\bar{F}_F\bar{K}_F\bar{U}Z_T/(Z_T+Z_L)p}{Z_T - h^2\left(\frac{\bar{K}_FZ_T}{Z_T+Z_L} + \frac{\bar{K}_BZ_T}{Z_T+Z_B}\right)\bar{U}/p^2Z_P}.
\end{aligned}
\tag{2.56}
$$

An expression for the reception sensitivity is obtained from the rearrangement of equation (2.56)

$$
\frac{\bar{V}}{\bar{F}_F} = \frac{-2h\bar{K}_F\bar{U}Z_T/(Z_T+Z_L)p}{Z_T - h^2\left(\frac{\bar{K}_FZ_T}{Z_T+Z_L} + \frac{\bar{K}_BZ_T}{Z_T+Z_B}\right)\bar{U}/p^2Z_P}.
\tag{2.57}
$$

Thus the non-dimensionalised reception sensitivity, ϕ_e, is

$$
\phi_e = \frac{\bar{V}hC_0}{\bar{F}_F} = \frac{-h^2C_0T_F\bar{K}_F\bar{U}/pZ_T}{1 - h^2(\bar{K}_FT_F/2 + \bar{K}_BT_B/2)\bar{U}/p^2Z_TZ_P}.
\tag{2.58}
$$

Graphical representations for the electrical impedance, transmission sensitivity and reception sensitivity have been newly produced as they provide important information with regards to the transducer's operating characteristics. Each of these plots has been plotted as a function of the operating frequency where $p = i\omega = i2\pi f$. The graphs produced are based on a lead zirconate titanate ceramic transducer (PZT-5H). The material parameters of the ceramic are shown in Table 2.1.

Description	Constant	Value	Units
Elastic constant	c_{11}^c	12.6×10^{10}	N/m^2
Elastic constant	c_{12}^c	7.95×10^{10}	N/m^2
Elastic constant	c_{13}^c	8.41×10^{10}	N/m^2
Elastic constant	c_{33}^c	11.70×10^{10}	N/m^2
Dielectric constant	ϵ_{11}^c	$1700 \times 8.854 \times 10^{-12}$	F/m
Dielectric constant	ϵ_{33}^c	$1470 \times 8.854 \times 10^{-12}$	F/m
Piezoelectric stress coefficient	e_{31}	-6.50	C/m^2
Piezoelectric stress coefficient	e_{33}	23.30	C/m^2
Density	ρ^c	7.50×10^3	kg/m^3

Table 2.1: Material properties of the PZT-5H ceramic [138].

The electrical impedance, as shown in Figure 2.2, using equation (2.45), can give insight into how efficient the transducer is likely to be. The transducer is most effective when it transmits at the electrical resonant frequency f_e and receives at the mechanical resonant frequency f_m [96]. The electrical resonant frequency is
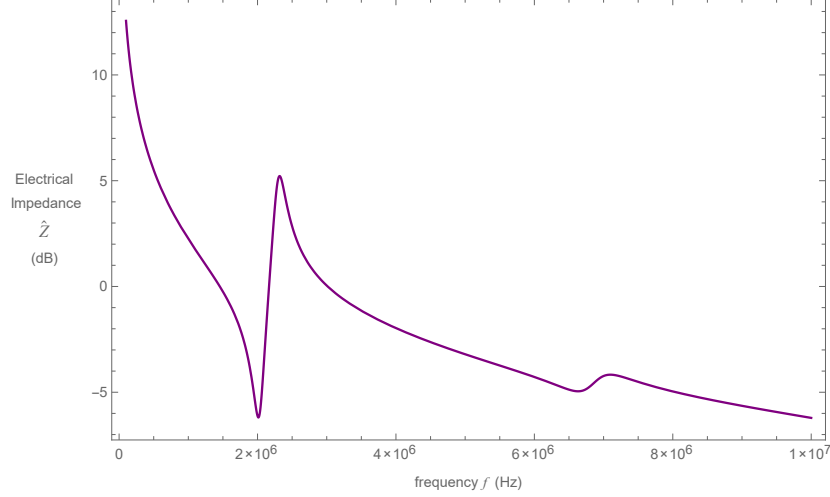
Figure 2.2: Non-dimensionalised electrical impedance $\hat{Z}_e$ (dB) versus frequency f (Hz) for a standard piezoelectric ceramic ultrasonic transducer.

determined by locating the first minimum in the graph and the mechanical resonant frequency is found by locating the first maximum. The electrical and mechanical resonant frequencies together with the corresponding electrical impedances for the device are given in Table 2.2.

Electrical Resonant Frequency		Mechanical Resonant Frequency	
f_e (MHz)	Z_e (dB)	f_m (MHz)	Z_e (dB)
2.063	−6.191	2.220	5.218

Table 2.2: Electrical and mechanical resonant frequencies for the Euclidean Transducer.

The transmission sensitivity of the device, illustrated in Figure 2.3 (equation (2.54)), can be seen to have a maximum peak at 2.063 MHz, and the re-

ception sensitivity, in Figure 2.4 (equation (2.58)), is shown to have its first peak at 2.220 MHz. In addition to previous research, the receiving and transmitting re-
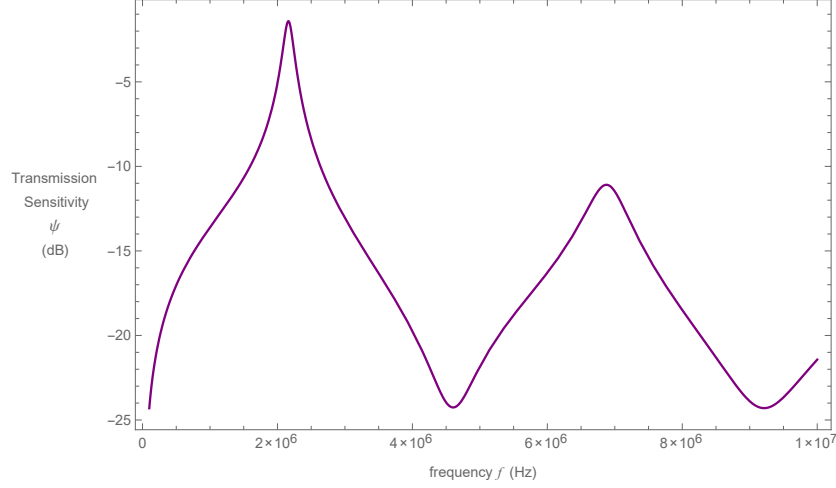
Figure 2.3: Non-dimensionalised transmission sensitivity ψ_e (dB) versus frequency f (Hz) for a standard piezoelectric ceramic ultrasonic transducer.

sponses were evaluated by determining the maximum amplitude, 3-dB bandwidth and the gain bandwidth product, which is the product of the maximum amplitude and bandwidth. High amplitude is a desirable attribute, since this relates to the production of energy; the higher the amplitude the greater the generation of energy [37]. Other authors have suggested that a useful measure of the effectiveness of a transducer is the 3-dB bandwidth [43, 77, 82, 84]. The bandwidth of the device is typically measured at the -3 dB point as this is the frequency range at which the transducers' efficiency in converting energies is at least half that of the maximum [51]. Consequently, it is often used as the cut-off frequency since this gives the range of frequencies over which the transducer operates efficiently.

Previous research has assessed the effectiveness of a transducer by determining its gain bandwidth product [43, 84]. This figure of merit is beneficial as it can provide an estimate for the range of frequencies around a particular centre frequency that attains a particular amplitude [42]. Using the amplitude, G, and defining the
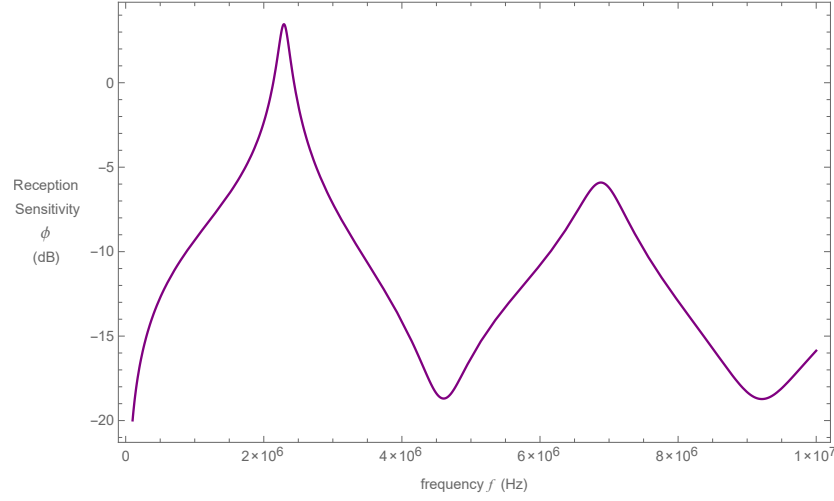
Figure 2.4: Non-dimensionalised reception sensitivity ϕ_e (dB) versus frequency f (Hz) for a standard piezoelectric ceramic ultrasonic transducer.

3-dB bandwidth, as BW,

$$BW = f_u - f_l, \tag{2.59}$$

where f_u is the upper frequency and f_l is the lower frequency respectively; see Figure 2.5. The gain bandwidth product, GBP, is given by [94, 95] as

$$GBP = G \times BW. \tag{2.60}$$

The bandwidth calculations were computed using Mathematica's FindPeaks command to initially find the positions (and values) at which the peaks occur. Prior to this, the operating functions were tabulated to three digit precision. Subsequently, the FindRoots command is utilised to determine upper and lower frequencies, by locating the position of values that intercept at the -3 dB point. These values are then substituted into equation (2.59) to obtain the bandwidths of the transmission and reception sensitivities.

The figures of merit for the transducer in both transmitting and receiving mode were calculated and the results are presented in Table 2.3.

28
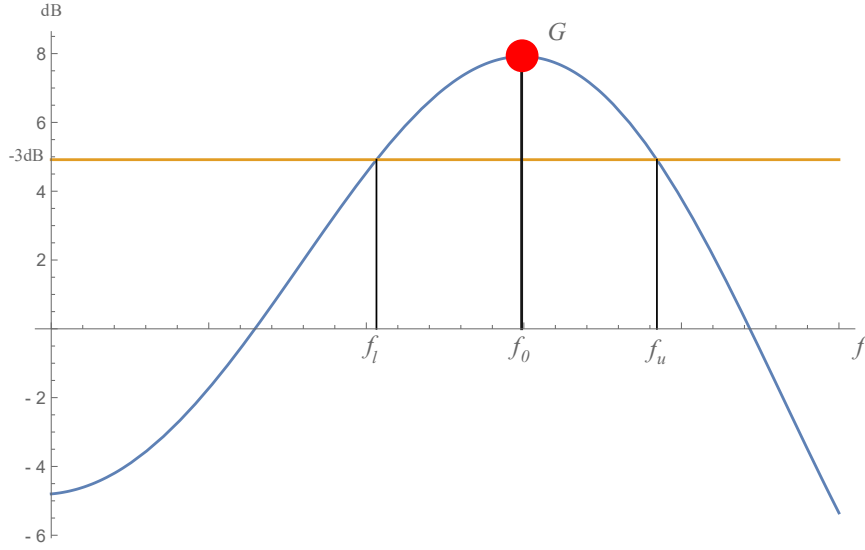
Figure 2.5: Graph illustrating the method for calculating the 3-dB bandwidth where f_0 is the centre frequency (maximum gain), f_u is the upper frequency and f_l is the lower frequency.

Euclidean Transducer	Maximum Amplitude (Gain) (dB)	3-dB Bandwidth (MHz)	Gain Bandwidth Product
Transmission	-1.414	0.259	0.187
Reception	3.463	0.263	0.584

Table 2.3: Figures of merit for the Euclidean transducer.

2.3   1-3 Composite Transducers

Composite transducers comprising a piezoelectric ceramic and passive polymer are superior to conventional monolithic transducers, in regards to a higher electromechanical coupling coefficient, reduced acoustic impedance and reduced lateral vibrations [52, 66, 96, 107]. It is due to these traits that composite transducers are widely used. In particular, they are the accepted choice within ultrasound imaging for medical diagnostics, which is the single largest market for 1-3 composite transducers [3, 52, 92, 96]. The majority of composite transducers produced

at present are the 1-3 and 2-2 connectivity transducers. This section considers the performance of a 1-3 composite transducer. This type of transducer consists of a piezoelectric material arranged into a grid of parallel pillars, with a passive polymer filling in the spaces.

In previous research [96], the linear systems model was utilised in order to describe the behaviour of the 1-3 composite transducer. However, this approach was initially used for a single phase device. To apply this technique to the composite device, it was necessary to derive the effective composite properties. Within this section the same methodology as used in [96] is applied to the composite and the research is extended to obtain the useful figures and merit. Furthermore, the impact of varying the volume fraction of the ceramic is performed to determine the effect this has on each figure of merit.

For elastic materials, Hooke's law states that a stress tensor T_i causes a proportional strain tensor S_j, related by an elastic modulus tensor c_{ij} [57],

$$T_i = c_{ij}S_j. \tag{2.61}$$

The electric displacement can be obtained by rearranging equation (2.2). For the composite structure, it is more convenient to express the electric displacement in tensor notation. This is defined as

$$D_i = e_{ij}S_j + \epsilon_{ij}E_j \quad \text{for} \quad i, j = 1, 2, 3, \tag{2.62}$$

where e_{ij} is the piezoelectric stress coefficient, ϵ_{ij} is the permittivity and E_j is the electric field. Equation (2.61) results in 6 equations consisting of 36 elastic constants if crystal symmetry, poling direction and differentiation order are not accounted for. The number of constants reduces significantly since the order of differentiation has no effect on the result, that is, $c_{ij} = c_{ji}$ [130]. Thus, the 36 constants reduce to 21. Furthermore, by considering the symmetries of the piezoelectric ceramic the number of independent constants will reduce further. The poling direction in this case is along the direction of the pillars and so there is

rotational symmetry around this direction [93]. Moreover, the ceramic is initially an isotropic material, and it is only during the poling process that the material is changed to become transversally isotropic. As mentioned, the piezoelectric ceramic is poled in the direction of the pillars, thus the piezoelectric equations within the ceramic phase are of the form [121],

$$T_1^c = c_{11}^c S_1^c + c_{12}^c S_2^c + c_{13}^c S_3^c - e_{31} E_3^c, \tag{2.63}$$

$$T_2^c = c_{12}^c S_1^c + c_{11}^c S_2^c + c_{13}^c S_3^c - e_{31} E_3^c, \tag{2.64}$$

$$T_3^c = c_{13}^c S_1^c + c_{13}^c S_2^c + c_{33}^c S_3^c - e_{33} E_3^c, \tag{2.65}$$

$$T_4^c = c_{44}^c S_4^c - e_{15} E_2^c, \tag{2.66}$$

$$T_5^c = c_{44}^c S_5^c - e_{15} E_1^c, \tag{2.67}$$

$$T_6^c = c_{66}^c S_6^c, \tag{2.68}$$

$$D_1^c = e_{15} S_5^c + \epsilon_{11}^c E_1^c, \tag{2.69}$$

$$D_2^c = e_{15} S_4^c + \epsilon_{11}^c E_2^c, \tag{2.70}$$

$$D_3^c = e_{31} S_1^c + e_{31} S_2^c + e_{33} S_3^c + \epsilon_{33}^c E_3^c, \tag{2.71}$$

and

$$T_1^p = c_{11} S_1^p + c_{12} S_2^p + c_{12} S_3^p, \tag{2.72}$$

$$T_2^p = c_{12} S_1^p + c_{11} S_2^p + c_{12} S_3^p, \tag{2.73}$$

$$T_3^p = c_{12} S_1^p + c_{12} S_2^p + c_{11} S_3^p, \tag{2.74}$$

$$T_4^p = c_{44} S_4^p, \tag{2.75}$$

$$T_5^p = c_{44} S_5^p, \tag{2.76}$$

$$T_6^p = c_{44} S_6^p, \tag{2.77}$$

$$D_1^p = \epsilon_{11} E_1^p, \tag{2.78}$$

$$D_2^p = \epsilon_{11} E_2^p, \tag{2.79}$$

$$D_3^p = \epsilon_{11} E_3^p, \tag{2.80}$$

within the polymer phase [121]. Equations (2.63)-(2.80) are of much simpler forms as a result of the reduction in the independent variables. Consequently, the piezo-electric constitutive equations for the ceramic and polymer phases can be given respectively as

$$T_i^c = c_{ij}^c S_j^c - e_{ij}^{c\top} E_j^c, \tag{2.81}$$

$$D_i^c = e_{ij}^c S_j^c + \epsilon_{ij}^c E_j^c, \tag{2.82}$$

and

$$T_i^p = c_{ij}^p S_j^p, \tag{2.83}$$

$$D_i^p = \epsilon_{ij}^p E_j^p. \tag{2.84}$$

See Appendix A for the corresponding tensor forms for equations (2.81)-(2.84). These tensor equations help illustrate the reduction in the number of independent variables.

In [121], it was stated that assumptions in the model are sufficient in extracting the essential physics. Additionally they serve to simplify the analysis considerably while still providing accurate results. In [121] six simplifying assumptions were made to the model to reduce equations (2.81)-(2.84) into the one-dimensional expressions for the composite. In these works the initial assumption is that the strain and electric field are dependent only upon the spatial variable z in both the piezo-electric material and polymer. It was also assumed that both the piezoelectric ceramic and polymer moved uniformly in the poling direction, that is

$$\tilde{S}_3 = S_3^p = S_3^c, \tag{2.85}$$

where the tilde refers to an average value for the composite, the superscripts p and c denote the polymer and ceramic phase respectively, and the subscript 3 refers to the z-direction (the vertical pillars in Figure 1.2 (a)). Moreover, the electric fields in each phase are assumed to be equal,

$$\tilde{E}_3 = E_3^p = E_3^c. \tag{2.86}$$

32

Furthering the simplification of the model, it was assumed that the transducer is a large, thin, electrode plate where symmetry is exhibited in the $x-y$ plane. This leads to the following simplifications of the model,

$$\tilde{E}_1 = \tilde{E}_2 = 0, \tag{2.87}$$

$$\tilde{T}_1 = \tilde{T}_2 \text{ and } \tilde{S}_1 = \tilde{S}_2, \tag{2.88}$$

where the subscripts 1 and 2 represent the x- and y- directions, respectively. The fifth assumption concerns the equivalence of the lateral stresses in each phase, more precisely it is given that

$$T_1^p = T_1^c = \tilde{T}_1. \tag{2.89}$$

Similarly lateral strains are addressed, whereby it is assumed that a complimentary lateral strain in the polymer is used to compensate the lateral strain in the ceramic. This is necessary in order for the composite to be wholly clamped along the lateral directions [96, 121]. This can be expressed as

$$\tilde{S}_1 = v_f S_1^c + \check{v}_f S_1^p = 0, \tag{2.90}$$

where v_f is the volume fraction of the ceramic and $\check{v}_f = (1 - v_f)$ is the volume fraction of the polymer. Using these assumptions, the piezoelectric constitutive equations can be reduced to three equations for both the ceramic and polymer phases. That is,

$$\tilde{T}_1 = (c_{11}^c + c_{12}^c)S_1^c + c_{13}^c \tilde{S}_3 - e_{31}\tilde{E}_3, \tag{2.91}$$

$$T_3^c = 2c_{13}^c S_1^c + c_{33}^c \tilde{S}_3 - e_{33}\tilde{E}_3, \tag{2.92}$$

$$D_3^c = 2e_{31}S_1^c + e_{33}\tilde{S}_3 + \epsilon_{33}^c \tilde{E}_3, \tag{2.93}$$

within the ceramic phase and

$$\tilde{T}_1 = (c_{11} + c_{12})S_1^p + c_{12}\tilde{S}_3, \tag{2.94}$$

$$T_3^p = 2c_{12}S_1^p + c_{11}\tilde{S}_3, \tag{2.95}$$

$$D_3^p = \epsilon_{11}\tilde{E}_3, \tag{2.96}$$

33

within the polymer phase. Combining equations (2.91) and (2.94), an expression for S_1^c is obtained,

$$S_1^c = \frac{((c_{11} + c_{12})S_1^p + (c_{12} - c_{13}^c)\tilde{S}_3 + e_{31}\tilde{E}_3)}{(c_{11}^c + c_{12}^c)}. \tag{2.97}$$

In equation (2.90) it can be shown that

$$S_1^c = -\frac{\check{v}_f S_1^p}{v_f}, \tag{2.98}$$

and

$$S_1^p = -\frac{v_f S_1^c}{\check{v}_f}. \tag{2.99}$$

Thus substituting equations (2.98) and (2.99) individually into equation (2.97) gives

$$S_1^c = \check{v}_f \left(\frac{-(c_{13}^c - c_{12})\tilde{S}_3 + e_{31}\tilde{E}_3}{v_f(c_{11} + c_{12}) + \check{v}_f(c_{11}^c + c_{12}^c)} \right), \tag{2.100}$$

and

$$S_1^p = v_f \left(\frac{(c_{13}^c - c_{12})\tilde{S}_3 - e_{31}\tilde{E}_3}{v_f(c_{11} + c_{12}) + \check{v}_f(c_{11}^c + c_{12}^c)} \right). \tag{2.101}$$

The mean elastic constants $\tilde{c}_{13}$, $\tilde{c}_{33}$, average piezoelectric stress coefficients $\tilde{e}_{31}$, $\tilde{e}_{33}$ and the average dielectric constant $\tilde{\epsilon}_{33}$ were given in [121] as

$$\tilde{c}_{13} = \frac{v_f c_{13}^c(c_{11} + c_{12}) + \check{v}_f c_{12}(c_{11}^c + c_{12}^c)}{v_f(c_{11} + c_{12}) + \check{v}_f(c_{11}^c + c_{12}^c)}, \tag{2.102}$$

$$\tilde{c}_{33} = v_f \left(c_{33}^c - \frac{2\check{v}_f(c_{13}^c - c_{12})^2}{v_f(c_{11} + c_{12}) + \check{v}_f(c_{11}^c + c_{12}^c)} \right) + \check{v}_f c_{11}, \tag{2.103}$$

$$\tilde{e}_{31} = \frac{v_f e_{31}(c_{11} + c_{12})}{v_f(c_{11} + c_{12}) + \check{v}_f(c_{11}^c + c_{12}^c)}, \tag{2.104}$$

$$\tilde{e}_{33} = v_f \left(e_{33} - \frac{2\check{v}_f e_{31}(c_{13}^c - c_{12})}{v_f(c_{11} + c_{12}) + \check{v}_f(c_{11}^c + c_{12}^c)} \right), \tag{2.105}$$

$$\tilde{\epsilon}_{33} = v_f \left(\epsilon_{33}^c + \frac{2\check{v}_f(e_{31})^2}{v_f(c_{11} + c_{12}) + \check{v}_f(c_{11}^c + c_{12}^c)} \right) + \check{v}_f \epsilon_{11}. \tag{2.106}$$

The inclusion of equation (2.100) into equation (2.91) gives

$$
\begin{aligned}
\tilde{T}_1 &= \check{v}_f(c_{11}^c + c_{12}^c)\left(\frac{(c_{12} - c_{13}^c)\tilde{S}_3 + e_{31}\tilde{E}_3}{v_f(c_{11} + c_{12}) + \check{v}_f(c_{11}^c + c_{12}^c)}\right) \\
&+ c_{13}^c\tilde{S}_3 - e_{31}\tilde{E}_3 \\
&= \frac{(v_f c_{13}^c(c_{11} + c_{12}) + \check{v}_f c_{12}(c_{11}^c + c_{12}^c))\tilde{S}_3}{v_f(c_{11} + c_{12}) + \check{v}_f(c_{11}^c + c_{12}^c)} \\
&- \frac{v_f e_{31}(c_{11} + c_{12})\tilde{E}_3}{v_f(c_{11} + c_{12}) + \check{v}_f(c_{11}^c + c_{12}^c)}.
\end{aligned}
\tag{2.107}
$$

Thus using equations (2.102) and (2.104) reduces equation (2.107) to the form

$$
\tilde{T}_1 = \tilde{c}_{13}\tilde{S}_3 - \tilde{e}_{31}\tilde{E}_3.
\tag{2.108}
$$

Similarly, expressions for T_3^c, T_3^p and D_3^c can be obtained by substituting equations (2.100) and (2.101) into equations (2.92), (2.93) and (2.95) to give

$$
\begin{aligned}
T_3^c &= \left(c_{33}^c - \frac{2\check{v}_f(c_{13}^c - c_{12})c_{13}^c}{v_f(c_{11} + c_{12}) + \check{v}_f(c_{11}^c + c_{12}^c)}\right)\tilde{S}_3 \\
&- \left(e_{33} - \frac{2\check{v}_f c_{13}^c e_{31}}{v_f(c_{11} + c_{12}) + \check{v}_f(c_{11}^c + c_{12}^c)}\right)\tilde{E}_3,
\end{aligned}
\tag{2.109}
$$

$$
\begin{aligned}
T_3^p &= \left(c_{11} + \frac{2v_f(c_{13}^c - c_{12})c_{12}}{v_f(c_{11} + c_{12}) + \check{v}_f(c_{11}^c - c_{12}^c)}\right)\tilde{S}_3 \\
&- \frac{2v_f c_{12} e_{31}\tilde{E}_3}{v_f(c_{11} + c_{12}) + \check{v}_f(c_{11}^c - c_{12}^c)},
\end{aligned}
\tag{2.110}
$$

$$
\begin{aligned}
D_3^c &= \left(e_{33} - \frac{2\check{v}_f(c_{13}^c - c_{12})e_{31}}{v_f(c_{11} + c_{12}) + \check{v}_f(c_{11}^c - c_{12}^c)}\right)\tilde{S}_3 \\
&+ \left(\epsilon_{33}^c + \frac{2\check{v}_f(e_{31})^2}{v_f(c_{11} + c_{12}) + \check{v}_f(c_{11}^c - c_{12}^c)}\right)\tilde{E}_3.
\end{aligned}
\tag{2.111}
$$

Lastly, it is assumed that the lateral periodicity is sufficiently fine. That is to say, there is an appropriate amount of spacing between the ceramic pillars. However, too fine of a structure, although effective, is challenging and costly to manufacture.

Thus, by assuming the scale is sufficiently fine, long ring-down times are prevented and the composite can be represented as an effective homogeneous medium [61, 120, 121, 122]. Once the piezoelectric ceramic has a pulse of electricity applied to it, it will cause the material to vibrate. The continual vibration of the ceramic is referred to as the ring-down time. Long ring-down times are undesirable as they increase the spatial pulse length. Thus, reducing the ring-down time will help to reduce the pulse of ultrasound. This is particularly significant in improving axial resolution [37]. Following on, the effective total stress and electric displacement can be expressed by volume averaging the constituent phases, namely,

$$\tilde{T}_3 = v_f T_3^c + \check{v}_f T_3^p, \tag{2.112}$$

$$\tilde{D}_3 = v_f D_3^c + \check{v}_f D_3^p. \tag{2.113}$$

Thus, substituting equations (2.109) and (2.110) into (2.112), as well as equations (2.111) and (2.96) into (2.113), gives

$$\tilde{T}_3 = \tilde{c}_{33}\tilde{S}_3 - \tilde{e}_{33}\tilde{E}_3, \tag{2.114}$$

and

$$\tilde{D}_3 = \tilde{e}_{33}\tilde{S}_3 + \tilde{\epsilon}_{33}\tilde{E}_3, \tag{2.115}$$

where $\tilde{c}_{33}$, $\tilde{e}_{33}$ and $\tilde{\epsilon}_{33}$ are given in equations (2.103), (2.105) and (2.106), respectively.

Considering the consecutive piezoelectric equations for the thickness mode transducer, it is possible to rewrite equations (2.114) and (2.115) to be of a similar form to equations (2.1)-(2.2). Rearranging equation (2.115) gives an expression for the electric field, given by

$$\tilde{E}_3 = \frac{1}{\tilde{\epsilon}_{33}}\left(\tilde{D}_3 - \tilde{e}_{33}\tilde{S}_3\right) = -\tilde{h}_{33}\tilde{S}_3 + \frac{\tilde{D}_3}{\tilde{\epsilon}_{33}}. \tag{2.116}$$

Using this expression, equation (2.114) can be rewritten to give

$$\tilde{T}_3 = \tilde{c}_{33}\tilde{S}_3 - \frac{\tilde{e}_{33}}{\tilde{\epsilon}_{33}}(\tilde{D}_3 - \tilde{e}_{33}\tilde{S}_3) = \tilde{Y}_{33}\tilde{S}_3 - \tilde{h}_{33}\tilde{D}_3, \tag{2.117}$$

36

where $\tilde{h}_{33} = \tilde{e}_{33}/\tilde{\epsilon}_{33}$ and $\tilde{Y}_{33} = \tilde{c}_{33} + (\tilde{e}_{33})^2/\tilde{\epsilon}_{33}$. These expressions for the electric field and stress must also be accompanied by the expression for the composite density, $\tilde{\rho}$, [121],

$$\tilde{\rho} = v_f \rho^c + \check{v}_f \rho^p, \tag{2.118}$$

where the density for the composite is dependent on the density of the ceramic, ρ^c, and the density of the polymer, ρ^p [72].

With these equations now derived, the analysis used previously on a monolithic plate transducer may now be applied to conventional 1-3 composite device to obtain the relevant operating characteristics, through substitution of these effective material parameters. Previous research [121] was carried out to determine the transducer parameters of interest. In particular authors obtained expressions for the composite's specific acoustic impedance, longitudinal velocity and thickness-mode electromechanical coupling constant. In this thesis, it is of interest to determine the transmitting and receiving abilities of novel ultrasonic transducers. Thus, for comparison, expressions for the non-dimensionalized electrical impedance and the transmission and reception sensitivities as a function of the operating frequency are determined for the previously investigated 1-3 composite device. The 1-3 composite transducer has been modelled on the PZT-5H ceramic and the polymer filler is the HY1300/CY1301 hard setting epoxy [96]. Material parameters for the polymer resin are shown in Table 2.4.

Description	Constant	Value	Units
Elastic constant	c_{11}	7.20×10^9	-
Elastic constant	c_{44}	1.57×10^9	-
Dielectric constant	ϵ	4	-
Density	ρ^p	1.15×10^3	$\mathrm{kg/m^3}$
Shear modulus	G'	1.57×10^9	$\mathrm{kg/m\,s^2}$
Young's modulus	Y'	4.28×10^9	$\mathrm{kg/m\,s^2}$

Table 2.4: Material properties for polymer phase HY1300/CY1301 [96].

Figure 2.6 illustrates the non-dimensionalised electrical impedance for a 1-3

composite transducer, with a ceramic volume fraction of $v_f = 0.5$. The electrical and mechanical resonant frequencies of the device have been calculated and are presented in Table 2.5.
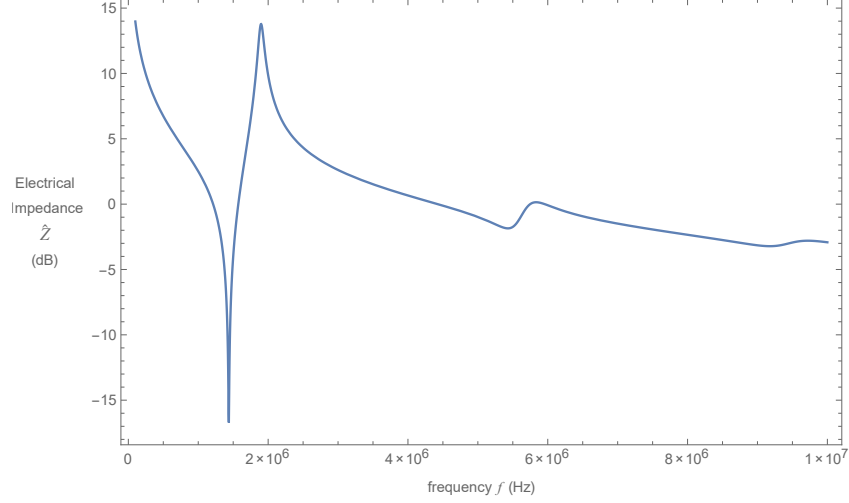
Figure 2.6: Non-dimensionalised electrical impedance $\hat{Z}_c$ (dB) versus frequency f (Hz) for a 1-3 composite transducer.

Electrical Resonant Frequency		Mechanical Resonant Frequency	
f_e (MHz)	Z_c (dB)	f_m (MHz)	Z_c (dB)
1.338	-16.8191	1.800	13.780

Table 2.5: Electrical and mechanical resonant frequencies for a 1-3 composite Transducer

Figure 2.7 shows the transmission sensitivity of the 1-3 composite device plotted against the operating frequency. Similar to the electrical impedance, the ceramic volume fraction was taken to be $v_f = 0.5$. This value was also used for the reception sensitivity which is plotted in Figure 2.8. The inclusion of the polymer shows there to be a substantial benefit when considering the figures of merit in transmission mode. In particular there is more than a two-fold increase in both the 3-dB bandwidth and gain bandwidth product at the device's resonant frequencies.
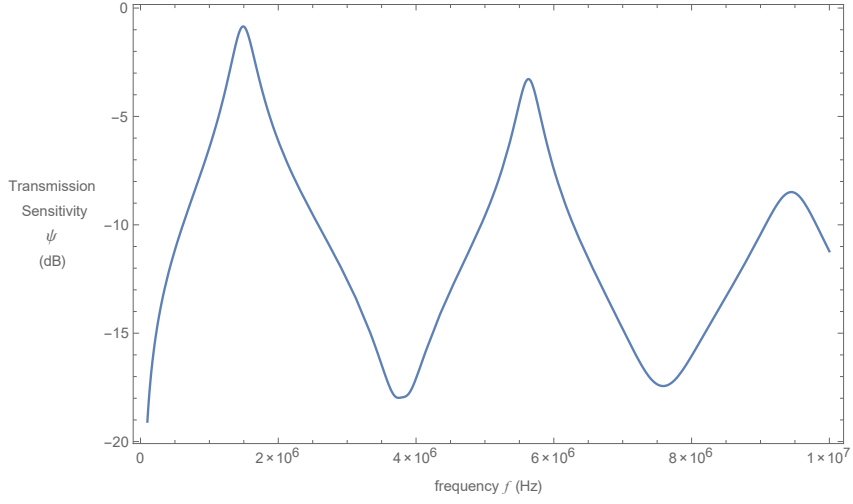
Figure 2.7: Non-dimensionalised transmission sensitivity ψ_c (dB) versus frequency f (Hz) for a 1-3 composite transducer.

Additionally, in reception mode there is an increase of 81% in the peak amplitude, when comparing the composite device to the monolithic transducer. However, in this operating function the increased amplitudes have likely resulted in reduced bandwidths and gain bandwidth product. Each figure of merit for the 1-3 composite transducer have been calculated in both operating modes and these are shown
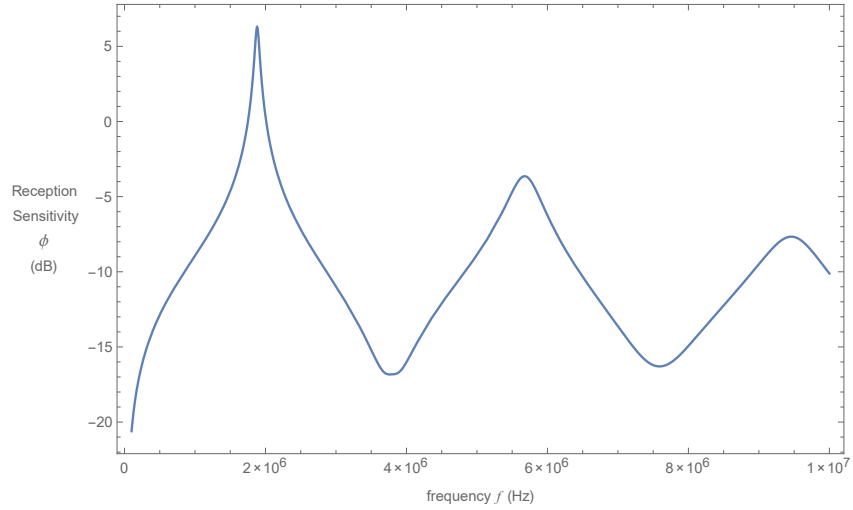
Figure 2.8: Non-dimensionalised reception sensitivity ϕ_c (dB) versus frequency f (Hz) for a 1-3 composite transducer.

in Table 2.6.

1-3 Composite Transducer	Maximum Amplitude (Gain) (dB)	3-dB Bandwidth (MHz)	Gain Bandwidth Product
Transmission	−0.839	0.542	0.446
Reception	6.268	0.109	0.463

Table 2.6: Figures of merit for a 1-3 composite transducer.

Further results on the electrical impedance and transmission and reception sensitivities have been gathered to determine the effect of varying the ceramic volume fraction. These results are illustrated in Figures 2.9, 2.10 and 2.11, respectively. High values at the mechanical resonant frequency are achieved by lowering the ceramic volume fraction, in particular the highest magnitude appears to be at a volume fraction around $v_f = 0.2$ or $v_f = 0.3$. Low amplitudes for the electrical resonant frequency are desirable in the electrical impedance profiles, since this relates to the peak amplitudes of the transmission sensitivity profiles. From observing Figure 2.9 (b) the lowest value seems to occur at a volume fraction of $v_f = 0.5$. When increasing the ceramic volume fraction the sensitivity of the device in transmission mode is reduced. Furthermore, the peak amplitudes occur at higher frequencies with the increase of the volume fraction. Initially increasing the volume fraction in reception mode will also increase sensitivity of the device. Yet this is only true up until a ceramic volume fraction of $v_f = 0.3$. Similar to transmission sensitivity, increasing the volume fraction also increases the resonant frequencies. The electrical and mechanical resonant frequencies with the corresponding electrical impedances for the composite device are tabulated in Table 2.7. In this table, the values for varying the volume fraction between 0.1 and 0.9 are presented. It can be established that the sought after minimum in electrical resonant frequency occurs at a volume fraction of $v_f = 0.5$, and the greatest amplitude in mechanical resonant frequency arises at a volume fraction of $v_f = 0.3$.

(a)

(b)
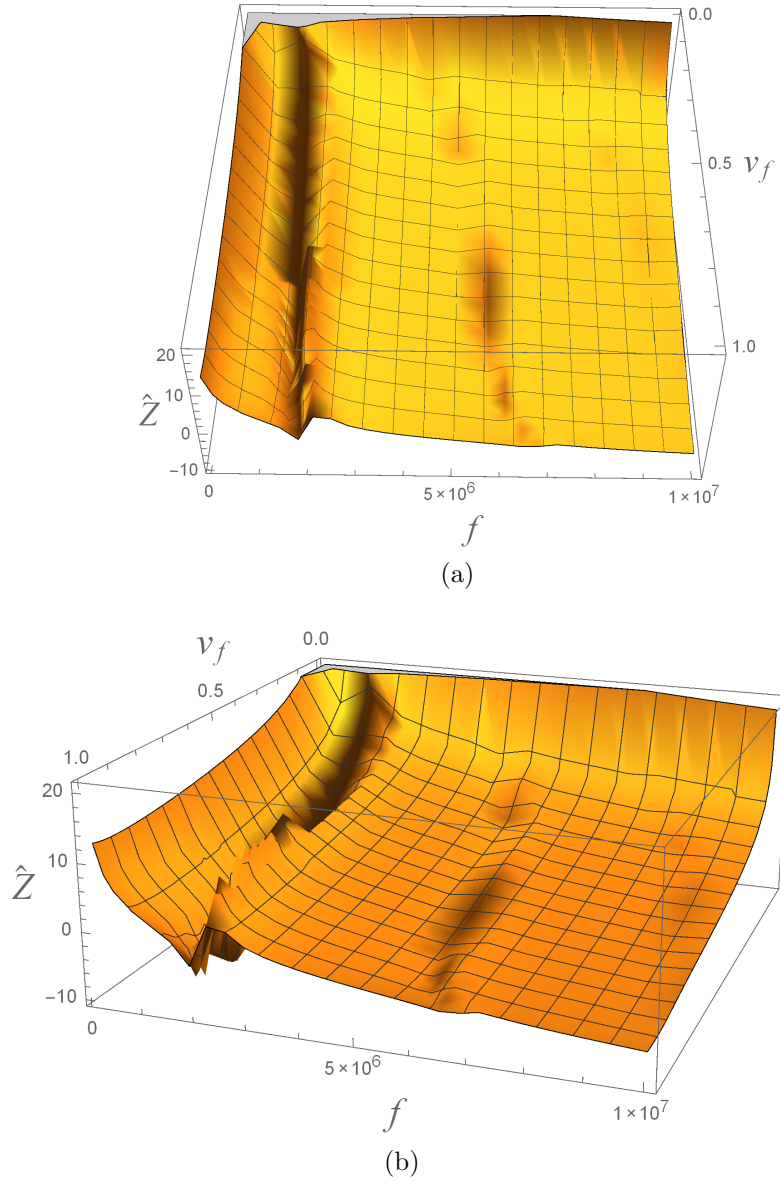
Figure 2.9: Non-dimensionalised electrical impedance $\hat{Z}_c$ (dB) versus frequency f (Hz) and ceramic volume fraction v_f (dimensionless) for a 1-3 composite transducer.

The performance of a 1-3 composite device has been analysed with varying ceramic volume fractions. The results of these are illustrated in Figures 2.12-2.14 in the form of gain, 3-dB bandwidth and gain bandwidth product, for both operating modes. Figure 2.12 clearly agrees with the observation that was made from

41

Figure 2.10, in that the sensitivity of the device in transmission mode reduces with
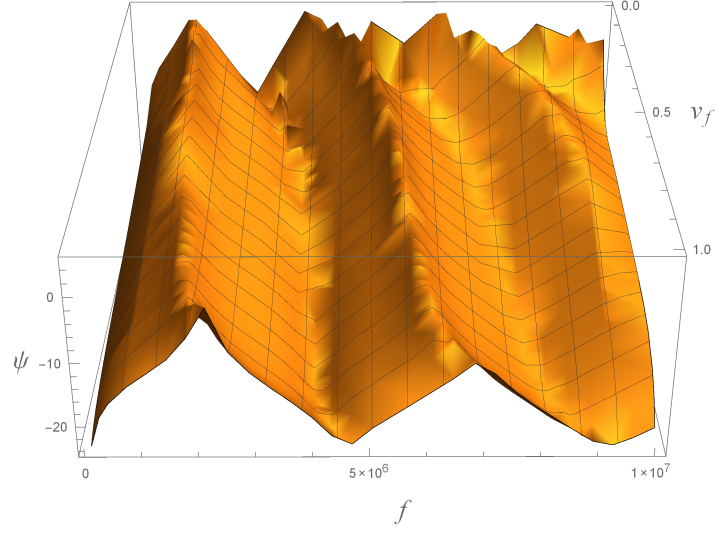
Figure 2.10: Non-dimensionalised transmission sensitivity ψ_c (dB) versus frequency f (Hz) and ceramic volume fraction v_f (dimensionless) for a 1-3 composite transducer.
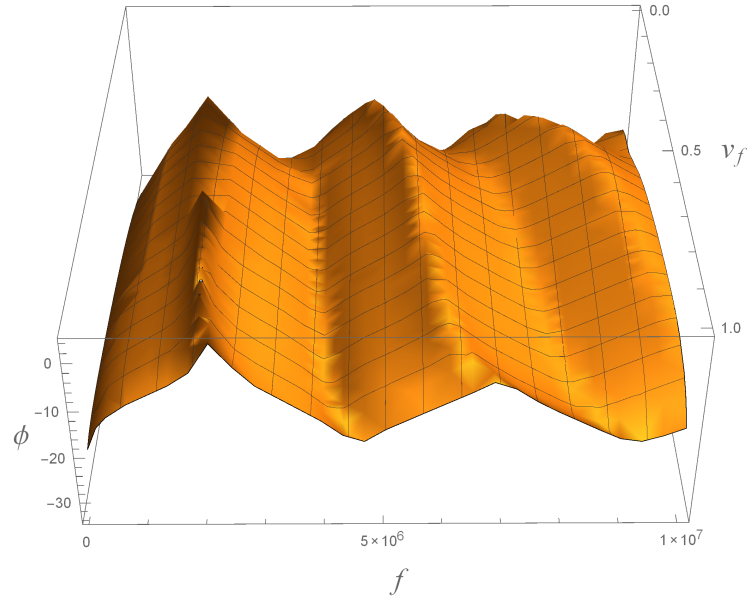
Figure 2.11: Non-dimensionalised reception sensitivity ϕ_c (dB) versus frequency f (Hz) and ceramic volume fraction v_f (dimensionless) for a 1-3 composite transducer.

the increasing ceramic volume fraction. Therefore, this would suggest that transducers embedded with a composite outperform the ceramic plate devices ($v_f = 1$). The highest gain in reception mode is achieved at a volume fraction of $v_f = 0.3$. Akin to the transmission sensitivity, the composite devices have greater sensitivity than the ceramic plate devices.

Volume Fraction (v_f)	Electrical Resonant Frequency		Mechanical Resonant Frequency	
	f_e (MHz)	Z_c (dB)	f_m (MHz)	Z_c (dB)
0.1	1.215	7.099	1.501	17.605
0.2	1.270	0.023	1.630	21.350
0.3	1.298	-5.430	1.707	21.389
0.4	1.318	-11.772	1.760	16.225
0.5	1.338	-16.819	1.800	13.780
0.6	1.361	-12.112	1.834	12.112
0.7	1.391	-10.762	1.867	10.804
0.8	1.441	-9.954	1.906	9.615
0.9	1.542	-8.992	1.974	8.272

Table 2.7: Electrical and mechanical resonant frequencies for a 1-3 composite transducer with varying volume fractions.

The 3-dB bandwidth of the 1-3 composite in transmission mode shows an increase in this value as the volume fraction is increased. Yet the introduction of the pure ceramic shows there to be a significant drop in value. A volume fraction of $v_f = 0.8$ offers the highest value for this figure of merit. Evidence would suggest through the data analysed that it is the pure ceramic case which provides the greatest value for the 3-dB bandwidth in reception mode, and that the value of this metric decreases at lower volume fractions. The lowest value is at a volume fraction of $v_f = 0.3$. However, this would be expected since at this volume fraction there is a substantial peak in the device's gain. Since there is generally a tradeoff between device amplitude and bandwidth, this has consequently led to the reduction in the bandwidth.
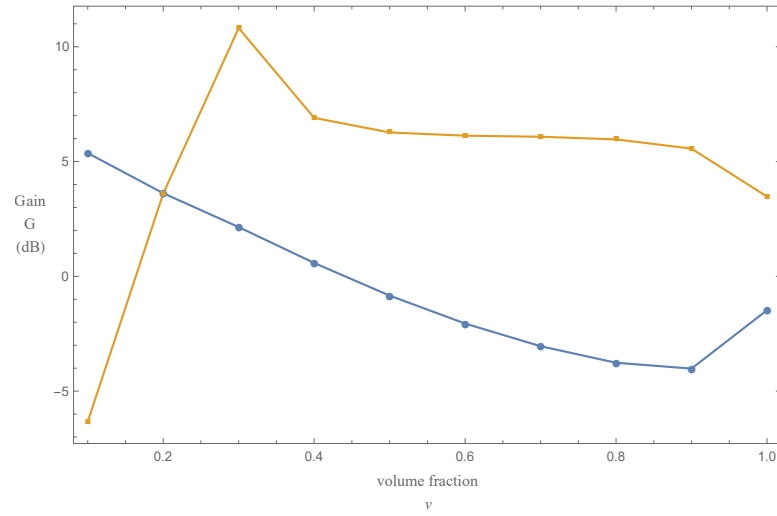
Figure 2.12: Gain (dB) versus volume fraction for the transmission sensitivity (blue) and reception sensitivity (orange) for a 1-3 composite transducer.
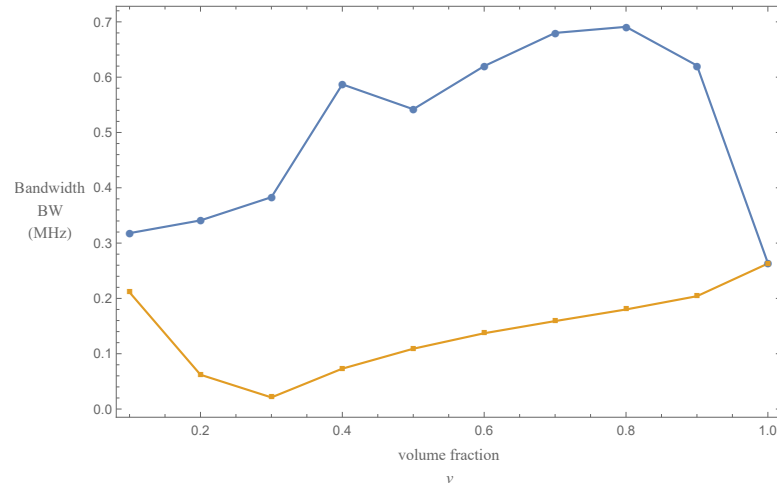
Figure 2.13: Bandwidth (MHz) versus volume fraction for the transmission sensitivity (blue) and reception sensitivity (orange) for a 1-3 composite transducer.

Figure 2.14 illustrates the transmission and reception sensitivities in terms of its gain bandwidth product over varying ceramic volume fraction. By comparing the behaviour of the operating modes it is clear that increasing the volume fraction has opposing results. In transmission mode an increase in volume fraction has a negative effect on the device's performance, whilst an increase in volume fraction

44

improves reception performance. Thus, for single devices requiring both modes of operation a mixture of both the ceramic and polymer materials would likely provide the most suitable composition. That is, when the ceramic volume fraction is $v_f = 0.5$.
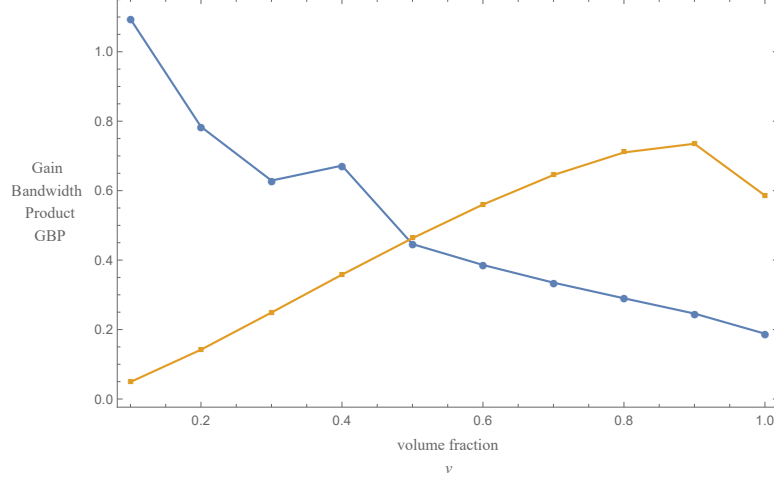
Figure 2.14: Gain bandwidth product versus volume fraction for the transmission sensitivity (blue) and reception sensitivity (orange) for a 1-3 composite transducer.

As a whole, the addition of a polymer phase into the design of ultrasonic transducers was found to present better operational characteristics than the single piezoelectric plate devices. Although presented with greater amplitudes, the values of the 3-dB bandwidth and gain bandwidth product of the composite device are both lower in reception mode than single-phase transducers. Additionally, both devices are regular in their design with simple periodic resonances. Consequently, these transducers operate effectively over relatively narrow bandwidths due to their designs consisting of a single length scale. Therefore, novel designs incorporating a range of length scales with the aim of improving device bandwidths will be investigated.

2.4 Sierpinski Gasket Transducer

To assist the construction of devices that operate efficiently over a larger range of frequencies, the implementation of fractal-like structures into the design of new ultrasonic transducers has been considered. Research into the topic of fractal-inspired transducers is still emerging. Yet, fractals used within the design of antennas are more widespread. In particular, Sierpinski carpet inspired antennas have previously been investigated [6, 22, 87]. These papers have highlighted that the performance of antennas inspired by fractal-like structures have resulted in the design of a multiband antenna. Furthermore, fractal-like geometries have allowed for the design of miniature antennas. This is as a result of the iterative process to form the fractal structure. That is, a specific fractal generation level may be chosen to allow the size of the antenna to be reduced with no affect to its performance [6]. Due to the continuing progression of the technological industry, there is the further opportunity to investigate other fractal-inspired transducers. Previous authors have demonstrated the benefits of implementing pre-fractal transducers [7, 83, 86, 97]. It was shown in these papers that ultrasonic transducers with multiple length scales benefited from more resonances and improved operation over a larger range of frequencies. This section explores the performance of a Sierpinski gasket inspired transducer, which has previously been investigated [86] using a finite difference model. The fractal-inspired device was further investigated using a finite element approach [7] and a prototype for a fourth generation pre-fractal device was constructed [83]. The analysis on the Sierpinski gasket inspired model is also extended here to determine the important figures of merit which are crucial in understanding device performance.

The construction of the fractal upon which this type of transducer is designed begins with an equilateral triangle. The next generation is obtained by replacing the original triangle by three copies of itself at half its height and width. The subsequent generations are then found by repeatedly applying this procedure to give the Sierpinski gasket (see Figure 2.15). The structures formed from the iterative

process are known as pre-fractals as the physical fractal is only formed after an infinite number of iterations [25]. For the purpose of manufacturing such designs, it is only the low generation pre-fractals that are of interest.
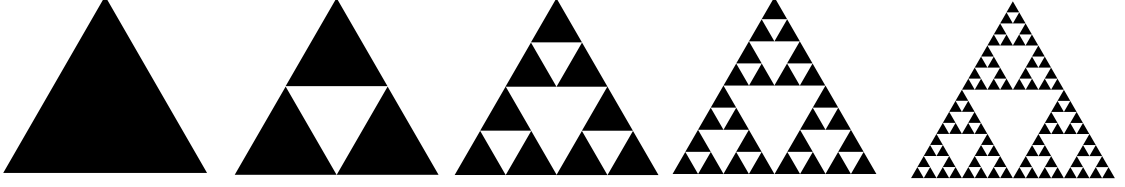
Figure 2.15: The sequence of Sierpinski gasket inspired transducers where the piezoelectric element is shown in black and the polymer in white.

A lattice equivalent of the Sierpinski gasket can be obtained by regarding the fractal structure as a sequence of graphs $\left\{ \mathcal{G}^{(n)} \right\}$ parameterised with respect to the order of generation n [41, 86]. The graph $\mathcal{G}^{(n+1)}$ is then obtained by connecting together three copies of $\mathcal{G}^{(n)}$, where each node in the sequence of graphs is the centre of a triangle of piezoelectric material. This allows for a self-similar structure as the sequence progresses [111]. A lattice counterpart of the Sierpinski gasket will be used to investigate the propagation of an ultrasonic wave. The lattice represents the vibrations of the piezoelectric material of the Sierpinski gasket [7]. By observing the graphs in Figure 2.16 it is possible to derive the total number of vertices for any given graph in the sequence. Let N_n denote the total number of vertices
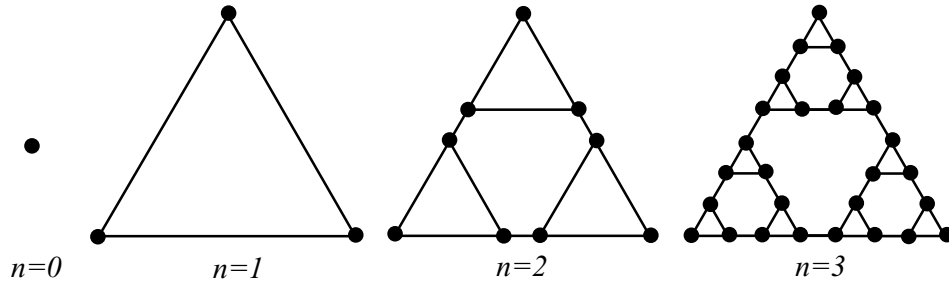
Figure 2.16: Graphical representations of generations 0 to 3 for the sequence of Sierpinski lattices.

of $\mathcal{G}^{(n)}$, then the nth generation has $N_n = 3^n$ vertices. The side length of the structure L_s is assumed to be fixed throughout the construction process [86]. As

a result of this condition, the edge length between adjacent vertices will reduce to zero, as the generation level is increased [40, 82]. For each graph in the sequence (with the exception of generation level $n = 0$) the vertex degree is three, excluding the corner vertices which have degree two. These corner vertices act as the input and output vertices which will be responsible for interacting with external loads and so fictitious vertices A, B and C are introduced to accommodate these boundary conditions [86], see Figure 2.17.
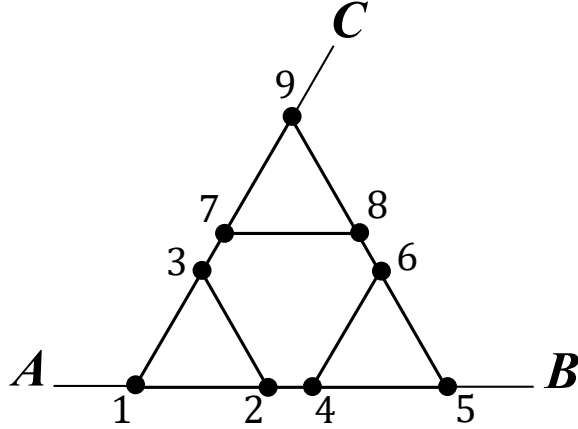
Figure 2.17: Sierpinski gasket lattice at generation $n = 2$, with fictitious vertices A, B and C.

Each graph of the sequence can be completely described by its adjacency matrix $H^{(n)}$, where the $(i, j)^{\text{th}}$ element gives the number of edges connecting vertex i to j by assigning the value one to connected vertices and zero otherwise. The recursive relationship of the graphs is then given as

$$H^{(n+1)} = \bar{H}^{(n)} + V^{(n)}, \tag{2.119}$$

where $\bar{H}^{(n)}$ is a block diagonal matrix which represents the connectivity properties of the individual sub-graphs of $\mathcal{G}^{(n)}$, i.e. its v blocks are equal to $H^{(n)}$. The connection of these sub-graphs is given by $V^{(n)}$ which is a sparse matrix that assigns the number one to the connection of sub-graphs. To illustrate this, the corresponding adjacency matrix for the lattice graph of $n = 2$ is given by

$$H^{(2)} = \begin{pmatrix} 0 & 1 & 1 & 0 & 0 & 0 & 0 & 0 & 0 \\ 1 & 0 & 1 & 1 & 0 & 0 & 0 & 0 & 0 \\ 1 & 1 & 0 & 0 & 0 & 0 & 1 & 0 & 0 \\ 0 & 1 & 0 & 0 & 1 & 1 & 0 & 0 & 0 \\ 0 & 0 & 0 & 1 & 0 & 1 & 0 & 0 & 0 \\ 0 & 0 & 0 & 1 & 1 & 0 & 0 & 1 & 0 \\ 0 & 0 & 1 & 0 & 0 & 0 & 0 & 1 & 1 \\ 0 & 0 & 0 & 0 & 0 & 1 & 1 & 0 & 1 \\ 0 & 0 & 0 & 0 & 0 & 0 & 1 & 1 & 0 \end{pmatrix}, \tag{2.120}$$

where

$$\bar{H}^{(1)} = \begin{pmatrix} 0 & 1 & 1 & 0 & 0 & 0 & 0 & 0 & 0 \\ 1 & 0 & 1 & 0 & 0 & 0 & 0 & 0 & 0 \\ 1 & 1 & 0 & 0 & 0 & 0 & 0 & 0 & 0 \\ 0 & 0 & 0 & 0 & 1 & 1 & 0 & 0 & 0 \\ 0 & 0 & 0 & 1 & 0 & 1 & 0 & 0 & 0 \\ 0 & 0 & 0 & 1 & 1 & 0 & 0 & 0 & 0 \\ 0 & 0 & 0 & 0 & 0 & 0 & 0 & 1 & 1 \\ 0 & 0 & 0 & 0 & 0 & 0 & 1 & 0 & 1 \\ 0 & 0 & 0 & 0 & 0 & 0 & 1 & 1 & 0 \end{pmatrix} \quad \text{and} \quad V^{(1)} = \begin{pmatrix} 0 & 0 & 0 & 0 & 0 & 0 & 0 & 0 & 0 \\ 0 & 0 & 0 & 1 & 0 & 0 & 0 & 0 & 0 \\ 0 & 0 & 0 & 0 & 0 & 0 & 1 & 0 & 0 \\ 0 & 1 & 0 & 0 & 0 & 0 & 0 & 0 & 0 \\ 0 & 0 & 0 & 0 & 0 & 0 & 0 & 0 & 0 \\ 0 & 0 & 0 & 0 & 0 & 0 & 0 & 1 & 0 \\ 0 & 0 & 1 & 0 & 0 & 0 & 0 & 0 & 0 \\ 0 & 0 & 0 & 0 & 0 & 1 & 0 & 0 & 0 \\ 0 & 0 & 0 & 0 & 0 & 0 & 0 & 0 & 0 \end{pmatrix}. \tag{2.121}$$

As with standard ultrasonic transducers, the Sierpinski gasket transducer also relies on the piezoelectric constitutive equations shown in equations (2.1) and (2.2). The analysis of a propagating ultrasonic wave within the Sierpinski gasket lattice requires the use of the discretized wave equation [86]

$$\rho_T \frac{\partial^2 \underline{u}}{\partial t^2} = \frac{Y_T}{\Delta x^2}(A^{(n)}\underline{u} + B^{(n)}\underline{u} + \underline{c}^{(n)}), \tag{2.122}$$

where ρ_T and Y_T are the density and Young's modulus for the piezoelectric material respectively, Δx is the distance between neighbouring vertices, $A^{(n)}$ is the matrix representing the discretized Laplacian and $B^{(n)}$ and $\underline{c}^{(n)}$ are a matrix and vector containing the boundary conditions at the input and output vertices. In order to maintain the overall size of the pre-fractal transducer, as the generation level is increased, the side length of the structure, L_s, is fixed throughout the construction process. Furthermore, $\Delta x^{(n)} = L_s/(2^n - 1)$ and so the distance between neighbouring vertices will decrease to zero as the generation level increases. In equation (2.122) the discretized Laplacian matrix is obtained using the second order central difference approximation. Thus $A^{(n)}$ is given by

$$A^{(n)} = H^{(n)} - qI_n, \tag{2.123}$$

49

where q is the vertex degree, and I_n denotes the identity matrix for generation level n.

2.4.1 Green Function Renormalization

Research into the construction of a transducer based on a Sierpinski gasket inspired design relies on renormalization analysis [83, 86, 111]. Previous research [38, 40, 86, 110] has identified a strategy in solving equations of a similar form to equation (2.122) by initially ignoring boundary conditions. These boundary conditions are then re-introduced later in the analysis, via suitable matrix transformations. Thus, by introducing a dimensionless variable

$$\theta = \frac{\sqrt{(Y_T/\rho_T)}t}{\Delta x}, \tag{2.124}$$

equation (2.122) takes the form

$$\frac{\partial^2 \underline{u}}{\partial \theta^2} = (A^{(n)}\underline{u} + B^{(n)}\underline{u} + \underline{c}^{(n)}). \tag{2.125}$$

Transforming equation (2.125) into the Laplace domain gives

$$p^2 I_n \underline{u} = (A^{(n)} + B^{(n)})\underline{u} + \underline{c}^{(n)}. \tag{2.126}$$

Thus, rearranging gives

$$(p^2 I_n - A^{(n)} - B^{(n)})\underline{u} = \underline{c}^{(n)},$$

$$\underline{u} = G^{(n)}\underline{c}^{(n)}, \tag{2.127}$$

where $G^{(n)}$ is the Green function matrix given by

$$G^{(n)} = (p^2 I_n - A^{(n)} - B^{(n)})^{-1}. \tag{2.128}$$

The bare Green function matrix is given as

$$\hat{G}^{(n)} = (p^2 I_n - A^{(n)})^{-1}, \tag{2.129}$$

since boundary conditions are neglected. The recursion relationship equation may be obtained by firstly utilising equations (2.123) and (2.129) to give,

$$\hat{G}^{(n+1)} = ((p^2 + q)I_{n+1} - H^{(n+1)})^{-1}. \tag{2.130}$$

Substituting equation (2.119) into the above expression then gives

$$\begin{aligned}
\hat{G}^{(n+1)} &= ((p^2 + q)I_{n+1} - \bar{H}^{(n)} - V^{(n)})^{-1}, \\
&= (\bar{F}^{(n)} - V^{(n)})^{-1},
\end{aligned} \tag{2.131}$$

where $\bar{F}^{(n)} = (p^2 + q)I_{n+1} - \bar{H}^{(n)}$, $(\bar{F}^{(n)})^{-1} = \bar{G}^{(n)}$ and $\bar{G}^{(n)}$ is a block diagonal matrix whose v blocks equal $\hat{G}^{(n)}$. Thus, using equation (2.131) along with the matrix property that $(\boldsymbol{A} - \boldsymbol{B})^{-1} = \boldsymbol{A}^{-1} + \boldsymbol{A}^{-1}\boldsymbol{B}(\boldsymbol{A} - \boldsymbol{B})^{-1}$, where $\boldsymbol{A}$ and $\boldsymbol{B}$ are two arbitrary matrices, the following recursion relationship is obtained [41]

$$\begin{aligned}
\hat{G}^{(n+1)} &= (\bar{F}^{(n)})^{-1} + (\bar{F}^{(n)})^{-1}V^{(n)}(\bar{F}^{(n)} - V^{(n)})^{-1}, \\
&= \bar{G}^{(n)} + \bar{G}^{(n)}V^{(n)}\hat{G}^{(n+1)}.
\end{aligned} \tag{2.132}$$

Similarly equations (2.119) and (2.128) are used with the same matrix identity to obtain the following

$$G^{(n)} = \hat{G}^{(n)} + \hat{G}^{(n)}B^{(n)}G^{(n)}. \tag{2.133}$$

Due to the symmetries of the lattice structure, it is of interest only to obtain the pivotal Green functions. The pivotal Green functions are the minimum number of independent elements required to develop a recursion [41]. Thus in the case of the Sierpinski gasket there are two pivotal Green functions, $\hat{G}_{11}^{(n)}$ and $\hat{G}_{15}^{(n)}$, where for ease of notation these will be labelled $\hat{x}_g = \hat{G}_{11}^{(n)}$ and $\hat{y}_g = \hat{G}_{15}^{(n)}$. The subscripts attached refer to vertices connecting the lattice structure to the fictitious vertices A, B and C [86] and the subscript g relates to the Sierpinski gasket model. While this method can be used at any generation level, the vertex labelling as illustrated in Figure 2.17 refers specifically to generation level $n = 2$. For instance, $G_{15}^{(n)}$ represents the same matrix Green function element at generation level two to $G_{1\,14}^{(n)}$ at generation level three. So for simplicity it is possible to denote both these

terms as $G_{15}^{(n)}$. Equally, subsequent chapters will denote Green function elements using the second generation notation. From symmetry $\hat{G}_{11}^{(n)} = \hat{G}_{55}^{(n)} = \hat{G}_{99}^{(n)}$ and $\hat{G}_{15}^{(n)} = \hat{G}_{19}^{(n)} = \hat{G}_{59}^{(n)}$, however it should be noted that this does not hold true when boundary conditions are re-introduced. These pivotal elements arise due to the sparsity of the connection matrix $V^{(n)}$. As a result, it is possible to employ only for the Green function elements associated with external vertices. That is, the vertices corresponding to the input/ output vertices. Similarly, the boundary matrix $B^{(n)}$ and vector $\underline{c}^{(n)}$ are also very sparse since the only non-zero entries occur at the input/ output vertices. Furthermore, only displacements at the input/ output vertices, u_1, u_5 and u_9 are of relevance and thus only pivotal Green functions, $G_{11}^{(n)}$, $G_{15}^{(n)}$, $G_{55}^{(n)}$ and $G_{59}^{(n)}$ are required. Using equation (2.132) it is possible to obtain a recursion for the corresponding pivotal Green functions. The recursion equations for the Sierpinski gasket inspired transducer are represented with capital letters, $\hat{X}_g$ and $\hat{Y}_g$. Since there are two pivotal elements when boundary conditions are neglected, these relate to $\hat{X}_g = \hat{G}_{11}^{(n+1)}$ and $\hat{Y}_g = \hat{G}_{15}^{(n+1)}$. Thus, application of equation (2.132) results in

$$\hat{X}_g = \hat{x}_g + \frac{2\hat{y}_g^2(\hat{x}_g - \hat{x}_g^2 + \hat{y}_g^2)}{(1 - \hat{x}_g - \hat{y}_g)(1 - \hat{x}_g^2 + \hat{y}_g + \hat{y}_g^2)}, \qquad (2.134)$$

$$\hat{Y}_g = \frac{\hat{y}_g^2(1 - \hat{x}_g + \hat{y}_g)}{(1 - \hat{x}_g - \hat{y}_g)(1 - \hat{x}_g^2 + \hat{y}_g + \hat{y}_g^2)}. \qquad (2.135)$$

The inclusion of boundary conditions suggests that $G_{15}^{(n)} = G_{19}^{(n)} = G_{51}^{(n)} = G_{91}^{(n)}$, $G_{55}^{(n)} = G_{99}^{(n)}$, $G_{59}^{(n)} = G_{95}^{(n)}$, $G_{11}^{(n)} \neq G_{55}^{(n)}$ and $G_{15}^{(n)} \neq G_{59}^{(n)}$. Thus the pivotal Green functions for this case are $G_{11}^{(n)}$, $G_{15}^{(n)}$, $G_{55}^{(n)}$ and $G_{59}^{(n)}$ which will be labelled respectively as x_g, y_g, z_g and w_g. Using equation (2.133) the following four equations are obtained

$$x_g = \frac{\hat{x}_g + 2\hat{y}_g y_g b_2}{1 - \hat{x}_g b_1}, \qquad (2.136)$$

$$y_g = \frac{\hat{y}_g}{(1 - \hat{x}_g b_1)(1 - b_2(\hat{x}_g + \hat{y}_g)) - 2\hat{y}_g^2 b_1 b_2}, \qquad (2.137)$$

$$z_g = \frac{\hat{x}_g + \hat{y}_g b_1 y_g + \hat{y}_g b_2 w_g}{1 - \hat{x}_g b_2}, \tag{2.138}$$

$$w_g = \frac{\hat{y}_g(1 + b_1 y_g(1 + b_2(\hat{y}_g - \hat{x}_g)))}{(\hat{x}_g b_2 - 1 + \hat{y}_g b_2)(\hat{x}_g b_2 - 1 - \hat{y}_g b_2)}, \tag{2.139}$$

where $b_1 = B_{11}^{(n)}$ and $b_2 = B_{55}^{(n)} = B_{99}^{(n)}$.

Equations (2.134)-(2.139) are all recalculations of the ones presented in [86]. This was performed to familiarise with and understand the renormalization technique. However, this highlighted an error in the previous research in regards to equation (2.137). Thus the corrected form of equation (2.137) has been presented in this thesis and has been subsequently used hereafter.

2.4.2 Application of Boundary Conditions

Given that the transducer is governed by the discretized wave equation, it follows that the mechanical load at the front face of the device is equally governed by the wave equation,

$$\rho_L \frac{\partial^2 u_L}{\partial t^2} = Y_L \frac{\partial^2 u_L}{\partial x_L^2}, \tag{2.140}$$

where ρ_L, u_L and Y_L are the density, particle displacement and Young's modulus in the mechanical load, respectively. Similarly the backing layer is governed by the wave equation. A solution to equation (2.140) is found by re-introducing the non-dimensional variable shown in equation (2.124) to give,

$$\frac{\partial^2 u_L}{\partial \theta^2} = \left(\frac{v_L}{v_T}\Delta x\right)^2 \frac{\partial^2 u_L}{\partial x_L^2}, \tag{2.141}$$

and then taking Laplace transforms of equation (2.141) gives

$$\frac{\partial^2 \bar{u}_L}{\partial x_L^2} - \left(\frac{pv_T}{\Delta x v_L}\right)^2 \bar{u}_L = 0, \tag{2.142}$$

where v_T is the wave velocity in the piezoelectric material and v_L is the wave velocity in the load. Expressions for the displacement in the load and backing material are given as

$$\bar{u}_L = \alpha_L \exp\left(\frac{-pv_T x_L}{\Delta x v_L}\right) + \beta_L \exp\left(\frac{pv_T x_L}{\Delta x v_L}\right), \tag{2.143}$$

and

$$\bar{u}_B = \alpha_B \exp\left(\frac{-pv_T x_B}{\Delta x v_B}\right) + \beta_B \exp\left(\frac{pv_T x_B}{\Delta x v_B}\right). \tag{2.144}$$

Similar to the standard device, it is assumed that the reflected wave within the backing layer is damped out, i.e. $\beta_B = 0$. Applying the conditions of continuity of displacement at the transducer boundaries gives

$$\bar{u}_L(0) = \alpha_L + \beta_L, \tag{2.145}$$

$$\bar{u}_B(0) = \alpha_B. \tag{2.146}$$

The fractal-inspired transducer will have a backing layer set at vertex A and two mechanical loads set at vertices B and C. Hence, due to the symmetry of the Green transfer matrix, equations (2.145) and (2.146) become

$$u_5 = u_9 = u_B = u_C = \alpha_L + \beta_L, \tag{2.147}$$

$$u_1 = u_A = \alpha_B, \tag{2.148}$$

where the subscripts attached to the displacement refers to a specific vertex of the graph. The force on each vertex is given by the same expression found in equation (2.18). It is possible to re-write the expression of the force as

$$\bar{F} = A_r Y \frac{\partial \bar{u}}{\partial x} - h\bar{Q}. \tag{2.149}$$

Hence, continuity of force gives

$$u_B - u_5 - \frac{h\bar{Q}}{Y_T \xi} = \frac{Z_L}{Z_T} p(-\alpha_L + \beta_L), \tag{2.150}$$

$$u_1 - u_A - \frac{h\bar{Q}}{Y_T \xi} = \frac{Z_B}{Z_T} p(-\alpha_B), \tag{2.151}$$

where $\xi = A_r/\Delta x$ is the ratio of the cross-sectional area of each edge to its length [86]. Combining equations (2.148) and (2.151) gives an expression for the mechanical displacement at the fictitious vertex A,

$$u_A = \left(\frac{1}{1 - p\frac{Z_B}{Z_T}}\right) u_1 - \frac{h\bar{Q}}{Y_T \xi} \left(\frac{1}{1 - p\frac{Z_B}{Z_T}}\right). \tag{2.152}$$

Similarly, the mechanical displacement at fictitious vertices B and C are obtained by combining equations (2.147) and (2.150) to give

$$u_B = \left(\frac{1}{1 - p\frac{Z_L}{Z_T}} \right) u_5 - \frac{h\bar{Q}}{Y_T\xi} \left(\frac{1}{1 - p\frac{Z_L}{Z_T}} \right) - 2\alpha_L p \frac{Z_L}{Z_T} \left(\frac{1}{1 - p\frac{Z_L}{Z_T}} \right) = u_C. \quad (2.153)$$

Thus, using equations (2.152) and (2.153), it is possible to determine elements of the boundary condition matrix, $B^{(n)}$,

$$B_{ij} = \begin{cases} \frac{1}{1 - p\frac{Z_B}{Z_T}}, & \text{for } B_{ij} = B_{11} \\ \frac{1}{1 - p\frac{Z_L}{Z_T}}, & \text{for } B_{ij} = B_{55} = B_{99} \\ 0, & \text{otherwise} \end{cases} , \quad (2.154)$$

and the vector $\underline{c}^{(n)}$

$$c_i = \begin{cases} -\frac{h\bar{Q}}{Y_T\xi} \left(\frac{1}{1 - p\frac{Z_B}{Z_T}} \right), & \text{for } c_i = c_1 \\ \left(\frac{1}{1 - p\frac{Z_L}{Z_T}} \right) \left(\frac{h\bar{Q}}{Y_T\xi} - 2\alpha_L p \frac{Z_L}{Z_T} \right), & \text{for } c_i = c_5 = c_9 \\ 0, & \text{otherwise} \end{cases} . \quad (2.155)$$

The derivations in equations (2.154) and (2.155) will be used to determine the expressions for the electrical impedance and transmission and reception sensitivities for the Sierpinski gasket inspired transducer.

2.4.3 Transducer Characteristics

Expressions detailing the electrical impedance and transmission and reception sensitivities for the fractal-inspired transducer can be derived. By utilising equation (2.11), the voltage for this fractal transducer may be described as

$$\bar{V} = -h(u_5 - u_1) + \frac{\bar{Q}}{C_0}, \quad (2.156)$$

where $u_5 = G_{15}^{(n)}c_1 + G_{55}^{(n)}c_5 + G_{59}^{(n)}c_9$ and $u_1 = G_{11}^{(n)}c_1 + G_{15}^{(n)}c_5 + G_{19}^{(n)}c_9$ since $\underline{u} = G^{(n)}\underline{c}$. Substituting u_5 and u_1 into equation (2.156) gives the voltage as

$$\bar{V} = \frac{h^2\bar{Q}}{Y_T\xi}(\mu_g + \nu_g) - 2\alpha_L \frac{Z_L}{Z_T} p h \mu_g + \frac{\bar{Q}}{C_0}, \quad (2.157)$$

55

where

$$\mu_g = \frac{2G_{15}^{(n)} - G_{59}^{(n)} - G_{55}^{(n)}}{1 - p\frac{Z_L}{Z_T}}, \tag{2.158}$$

and

$$\nu_g = \frac{G_{15}^{(n)} - G_{11}^{(n)}}{1 - p\frac{Z_B}{Z_T}}. \tag{2.159}$$

The current of the transducer is given by [86]

$$\bar{I} = \frac{p\bar{Q}Y_T\xi}{Z_T}. \tag{2.160}$$

By recalling that $\alpha_L = 0$ in transmission mode, and that the electrical impedance of the device is given as $Z = V/I$, it can be shown that,

$$\bar{Z}_g = \frac{Z_T}{pC_0Y_T\xi}\left(1 + \frac{h^2 C_0(\mu_g + \nu_g)}{Y_T\xi}\right). \tag{2.161}$$

Thus, non-dimensionalizing the electrical impedance results in

$$\hat{Z}_g = \frac{Z_T}{pC_0Y_T\xi Z_0}\left(1 + \frac{h^2 C_0(\mu_g + \nu_g)}{Y_T\xi}\right). \tag{2.162}$$

Since $\alpha_L = 0$, equations (2.147) and (2.150) reduce respectively to

$$u_5 = u_9 = u_B = u_C = \beta_L, \tag{2.163}$$

$$u_B - u_5 - \frac{h\bar{Q}}{Y_T\xi} = \beta_L \frac{Z_L}{Z_T}p. \tag{2.164}$$

Substituting these new expressions into equation (2.149) gives

$$\bar{F} = \frac{Y_L p v_T h\bar{Q}}{Y_T v_L}\left(\frac{1}{1 - p\frac{Z_L}{Z_T}}\right)\left(1 + \frac{G_{55}^{(n)} + G_{59}^{(n)}}{1 - p\frac{Z_L}{Z_T}} - \frac{G_{15}^{(n)}}{1 - p\frac{Z_B}{Z_T}}\right). \tag{2.165}$$

Using equations (2.46) and (2.160), gives

$$\bar{Q} = \frac{Z_T a\bar{V}}{p(Z_g + b)Y_T\xi}. \tag{2.166}$$

Hence, an expression for the transmission sensitivity can be found by substituting equation (2.166) into equation (2.165), giving

$$\frac{\bar{F}}{\bar{V}} = \frac{haZ_L K_g^{(n)}}{(\bar{Z}_g + b)Y_T\xi}, \tag{2.167}$$

56

where

$$K_g^{(n)} = \frac{1}{1 - p\frac{Z_L}{Z_T}} \left(1 + \frac{G_{55}^{(n)} + G_{59}^{(n)}}{1 - p\frac{Z_L}{Z_T}} - \frac{G_{15}^{(n)}}{1 - p\frac{Z_B}{Z_T}} \right). \tag{2.168}$$

Hence, the non-dimensionalized transmission sensitivity is

$$\psi_g = \frac{\bar{F}}{\bar{V}hC_0} = \frac{aZ_L K_g^{(n)}}{(\bar{Z}_g + b)Y_T\xi C_0}. \tag{2.169}$$

In reception mode the transducer generates an electric charge when its front face is subjected to external loads, that is, when the output vertices B and C (which correspond to vertex nodes 5 and 9) receive an external load. The expression for amplitude of the forward propagating wave is given by [86]

$$\alpha_L = -\frac{\bar{F}}{pv_T Z_s\xi}, \tag{2.170}$$

where Z_s is the specific acoustic impedance. Using this expression for α_L, it is possible to rewrite the expression for the voltage in equation (2.157) to be of the form

$$\bar{V} = \frac{h^2\bar{Q}}{Y_T\xi}(\mu_g + \nu_g) + \frac{2h\bar{F}\mu_g A_r}{Z_T v_T\xi} + \frac{\bar{Q}}{C_0}. \tag{2.171}$$

An expression for the reception sensitivity can be found by substituting the expression for the electrical charge found in equation (2.166) into the above expression for the voltage

$$\frac{\bar{V}}{\bar{F}} = \frac{2h\mu_g}{Y_T\xi \left(1 - \frac{aZ_T}{pC_0 Y_T\xi(\bar{Z}_g + b)} \left(1 + \frac{h^2C_0(\mu_g + \nu_g)}{Y_T\xi} \right) \right)}, \tag{2.172}$$

The non-dimensionalized expression is thus given by

$$\phi_g = \frac{\bar{V}hC_0}{\bar{F}} = \frac{2h^2C_0\mu_g}{Y_T\xi \left(1 - \frac{aZ_T}{pC_0 Y_T\xi(\bar{Z}_g + b)} \left(1 + \frac{h^2C_0(\mu_g + \nu_g)}{Y_T\xi} \right) \right)}. \tag{2.173}$$

The graphs displayed in Figures 2.18, 2.19 and 2.20, are of the electrical impedance, and transmission and reception sensitivities for the Sierpinski gasket inspired transducer at generation level five (equations (2.162), (2.169) and (2.173),

57

respectively) compared to the ceramic plate and 1-3 composite transducers. For the Sierpinski gasket inspired and standard piezoelectric block transducers, it is assumed that the ceramic volume fraction is the same for both devices ($v_f = 1$) to allow for a fair comparison. In later chapters, all novel designs will also have a ceramic volume fraction of $v_f = 1$. Although the investigation of a Sierpinski gasket inspired transducer has previously been achieved, the graph depicting generation level five in this thesis differs to its illustration in [86]. This is as a result of the amendment made to the lattice Green function that represents vertex 5 (where this vertex is in reference to one of the output vertices at generation level $n = 2$) connecting to the fictitious vertex B, i.e. y_g. Similar to the standard devices, this model has been further extended to obtain the figures of merit at interest for the pre-fractal devices at generation levels one to five.
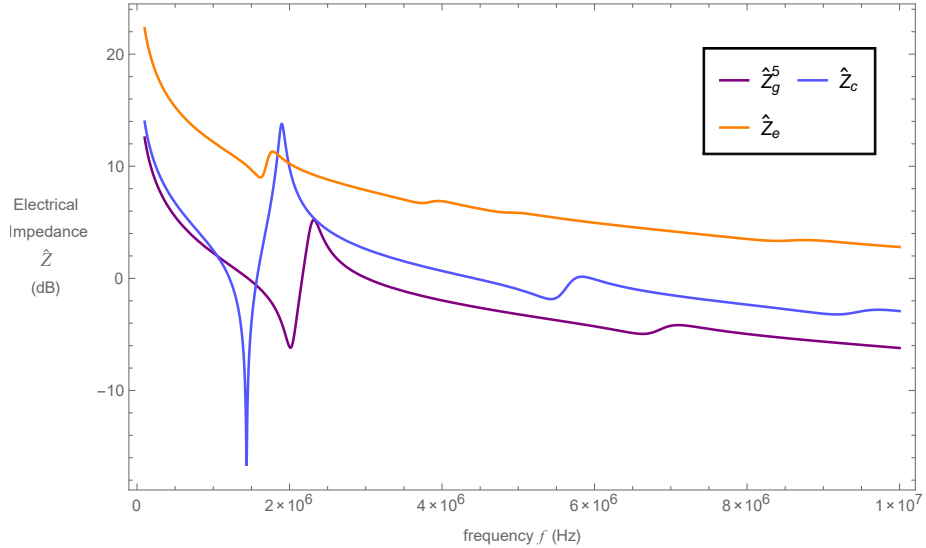
Figure 2.18: Non-dimensionalised electrical impedance $\hat{Z}$ (dB) versus frequency f (Hz) for the Sierpinski gasket ($\hat{Z}_g^5$ orange full line) transducer at fractal generation level $n = 5$, ceramic plate device ($\hat{Z}_e$ purple full line) and composite transducer ($\hat{Z}_c$ light blue full line).

Comparisons of the electrical impedance for the three devices are shown in Figure 2.18. The electrical and mechanical resonant frequencies and corresponding electrical impedances for the Sierpinski gasket inspired device for fractal generation

levels one to five are shown in Table 2.8. By observing the table of values, it is clear that the increasing the fractal generation level increases the electrical impedance magnitudes. Thus, with fractal-inspired devices it is possible to select an appropriate fractal generation level design, with the specific characteristics which are best suited to a particular application.

Generation (n)	Electrical Resonant Frequency		Mechanical Resonant Frequency	
	f_e (MHz)	Z_g (dB)	f_m (MHz)	Z_g (dB)
1	1.027	-6.306	1.195	-0.166
2	1.564	-2.591	1.780	2.157
3	1.689	1.331	1.896	4.990
4	1.638	5.204	1.822	8.082
5	1.519	9.011	1.680	11.304

Table 2.8: Electrical and mechanical resonant frequencies for the first five fractal generation levels for the Sierpinski gasket transducer.
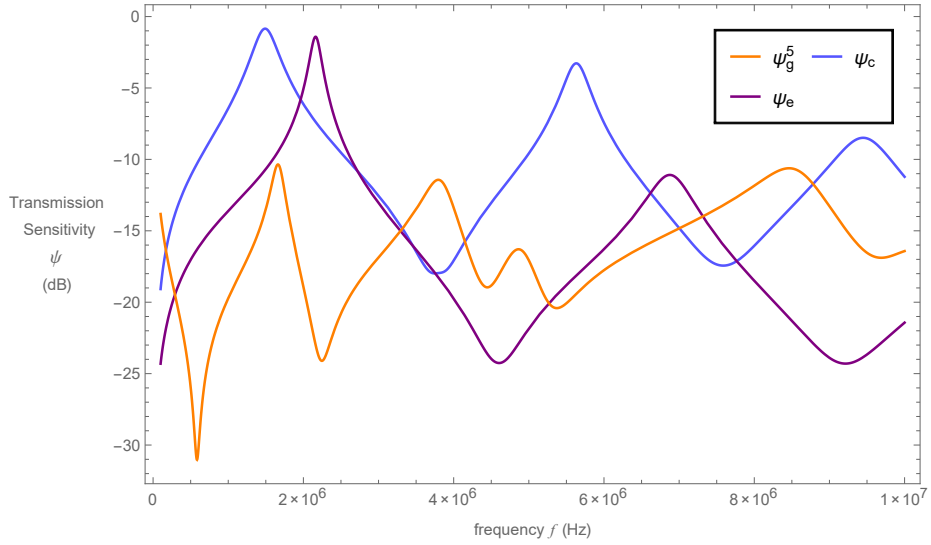
Figure 2.19: Non-dimensionalised transmission sensitivities ψ (dB) versus frequency f (Hz) for the Sierpinski gasket (ψ_g^5 orange full line) transducer at fractal generation level $n = 5$, ceramic plate device (ψ_e purple full line) and composite transducer (ψ_c light blue full line).

The transmission sensitives for the three devices are plotted in Figure 2.19. Unfortunately the results for the fractal device are relatively disappointing, at least in terms of its maximum amplitude. In regards to this figure of merit, there is a discouraging effect on the value as the fractal generation level is increased. Additionally, even at its highest peak the fractal device is still outperformed by the standard devices. However, the device outperforms the standard ceramic plate transducer in terms of its bandwidth for fractal generation levels four and five. Furthermore, it should be noted that practical transducers fabricated on the design of the Sierpinski gasket, or any pre-fractal, would be a composition of a piezoelectric ceramic and polymer filler. For investigatory purposes, the Sierpinski gasket device explored here is composed entirely of the ceramic material. In reality therefore, it is expected that pre-fractal devices composed of both a ceramic and polymer material would provide better operational characteristics. Table 2.9 presents the metrics describing the transmission characteristics for generation levels one to five of the Sierpinski gasket pre-fractal transducers.

Generation (n)	Maximum Amplitude (Gain) (dB)	3-dB Bandwidth (MHz)	Gain Bandwidth Product
1	-5.517	0.077	0.022
2	-3.427	0.113	0.052
3	-6.166	0.217	0.053
4	-8.576	0.276	0.038
5	-10.357	0.280	0.026

Table 2.9: Figures of merit in transmitting mode for Sierpinski gasket transducer.

Evidently from Figure 2.20, which illustrates the reception sensitives of the devices, it is the pre-fractal transducer which outperforms standard designs. Moreover, the gain bandwidth product at fractal generation level five has increased almost 3-fold over the traditional designs. The fractal-inspired device also contains more resonances which is likely due to the pre-fractal structure containing

a wider range of length scales. Each of the figures of merit for the reception sensitivities at fractal generation levels one to five are formulated in Table 2.10.
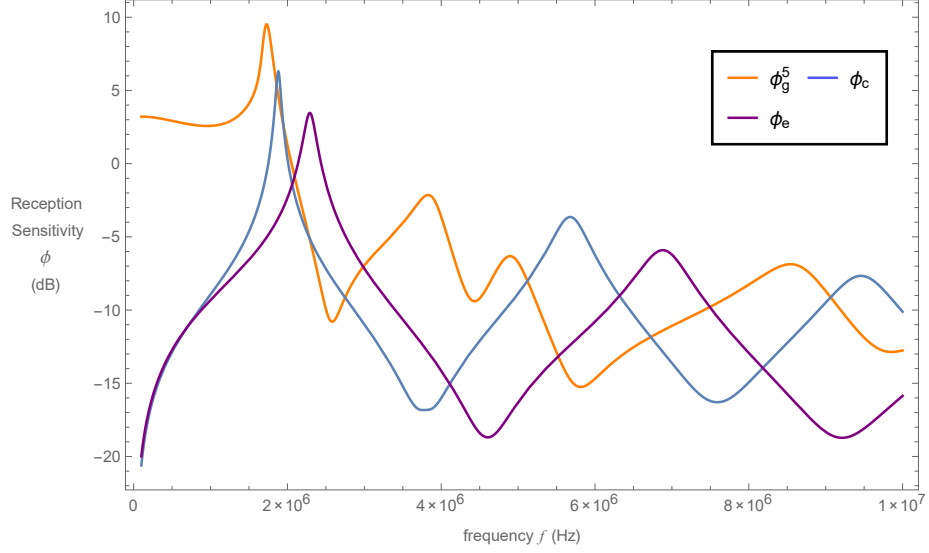
Figure 2.20: Non-dimensionalised reception sensitivities ϕ (dB) versus frequency f (Hz) for the Sierpinski gasket (ϕ_g^5 orange full line) transducer at fractal generation level $n = 5$, ceramic plate device (ϕ_e purple full line) and composite transducer (ϕ_c light blue full line).

Generation (n)	Maximum Amplitude (Gain) (dB)	3-dB Bandwidth (MHz)	Gain Bandwidth Product
1	0.807	0.331	0.399
2	1.735	0.220	0.265
3	4.098	0.213	0.547
4	6.882	0.200	0.976
5	9.520	0.185	1.657

Table 2.10: Figures of merit in receiving mode for Sierpinski gasket transducer.

In this section a pre-fractal design transducer was compared to traditional design transducers, one purely ceramic and the other of a ceramic-polymer composition. The analysis performed on the pre-fractal device accounted for only

ceramic properties, while in real-world applications it would also consist of a polymer material. It is understood that composite devices outperform single-phase transducers. So if pre-fractal single-phase devices outperform standard ceramic plated transducers, it can be presumed that fractal-inspired transducers composed of both ceramic and polymer materials would equally achieve better operating characteristics over tradition design composites.

2.5 Conclusions

In this chapter the performance of a single phase ceramic transducer and ceramic polymer composite transducer have been investigated. The operating characteristics for the two devices were derived and the analysis of the models was extended to obtain the figures of merit at interest. The metrics of significance were the maximum amplitude, 3-dB bandwidth and the gain bandwidth product. Furthering the analyses of the composite device, the ceramic volume fraction has been varied to determine its impact on each figure of merit, for the transmission, ψ_c, and reception, ϕ_c, sensitivities of the device. A Sierpinski gasket fractal inspired transducer was also investigated and the important output parameters, electrical impedance, $\hat{Z}_g$, transmission, ψ_g, and reception, ϕ_g, sensitivities were derived and plotted against the operating frequency. These operating characteristics help to determine how well the transducer is likely to perform. Therefore, the derivation of these parameters is essential for analysing the performance of each transducer model. The Sierpinski gasket inspired transducer was then compared against standard (Euclidean) devices. As with the standard devices the relevant figures of merit were calculated for the first five fractal generation levels. The research restricted the fractal generation level up to and including level five as a result of current manufacturing limitations. Pre-fractal devices benefit from a range of length scales and inherit more complexity in their designs than current industry used ultrasonic transducers. As the fractal generation level increases, the lengths between neighbouring vertices decrease and the resulting structure is of

a complicated multi scaled device, with diminutive length scales. Although these qualities are advantageous, it is due to these that construction of such devices is made problematic.

The results indicated an improvement in performance for the pre-fractal devices, with few figures of merit less than the industry standard. Importantly however, the fractal-inspired design only accounted for the ceramic phase. Thus it may be of use to further analyse such devices which incorporate the polymer filler. Research into a Sierpinski gasket inspired transducer that incorporates both ceramic and polymer phases is considered in [8]. Since pre-fractal transducers have been found to provide improved operational characteristics over standard designs, it is of relevance to further study new designs that incorporate other fractal-like geometries. This may assist in establishing the optimal design that could be used for ultrasonic transducers.

Chapter 3

The Sierpinski Carpet Transducer

3.1   Introduction

This chapter seeks to improve on current transducer design by assessing the benefits of incorporating fractal-like geometry into the design of ultrasonic transducers. This particular research is important as it contributes relevant information on methods to improve transducer efficiency, furthering the exchange of design ideas between the theoreticians and experimentalists.

There has been extensive research conducted on piezoelectric ultrasonic transducers [52, 71, 75, 84, 92, 94, 95, 98, 101, 125, 127]. However, only a small portion of this is based on fractal-designed transducers [7, 83, 86, 97]. In previous works [7, 86], Green function renormalization has been applied to fractal structures with the aim of obtaining recursion relations to facilitate expressions for the transducers' operating characteristics. In each case the fractal-like designs used to simulate the features of natural occurring ultrasonic transducers were limited to finitely ramified structures. Finitely ramified fractals are structures that can be separated into subparts through the removal of a finite and constant number of vertices, which is independent of the generation level [17, 40]. Infinitely ramified Sierpinski carpet antennas have previously been investigated [4, 23, 58, 136]. However, very few have studied its potential use in the design of ultrasonic transducers. In particular the plane wave expansion (PWE) model was employed to

64

study the performances of a Sierpinski carpet like and Cantor set transducers [97]. The connection process of the Sierpinski carpet prohibits the isolation of subgraphs through the removal of a finite and constant number of vertices and so does not satisfy the conditions of finitely ramified structures. For this reason the Sierpinski carpet is classified as an infinitely ramified fractal. The renormalization approach previously used on a Sierpinski gasket inspired transducer [86] is limited to finitely ramified fractals. However, this form of analysis can be extended to investigate infinitely ramified structures [40]. Therefore, the renormalization method is adapted to obtain expressions for the electrical impedance, transmission and reception responses for a transducer inspired by an infinitely ramified fractal [19].

In this chapter, three models based on the design of the Sierpinski carpet pre-fractal are investigated to determine the most appropriate device for ultrasonic applications. The differences between these models are dependent on the number of output nodes, i.e. the number of boundary conditions. For each of these models this chapter will show, that increasing the fractal generation level would result in an increase in the device's bandwidth and gain bandwidth product.

Section 3.2 outlines the construction of the Sierpinski carpet pre-fractal along with the derivation of its lattice counterpart. In Section 3.3, the Green function renormalization method is tailored to obtain the relevant relations for each transducer model. In Section 3.4 boundary conditions are obtained to aid the derivation of the expressions for the important output parameters; these are electrical impedance, $\hat{Z}$, transmission and reception sensitivities (ψ, ϕ) as outlined in Section 3.5. In Section 3.6, the results for the individual Sierpinski carpet transducer models are compared with the standard Euclidean transducer and the Sierpinski gasket inspired transducer. The findings are summarised and future research is discussed in Section 3.7.

3.2 Formulation of the Model

The fractal used to here imitate the complex geometry found in natural ultrasonic transducers is the Sierpinski carpet. The structure of this fractal begins with a square, which is then copied and scaled into nine congruent sub-squares with the centre square eliminated. The following generation is then achieved by replacing the initial square with this newly formed shape. Subsequent generations are then found by repeatedly applying this procedure to give the Sierpinski carpet [27, 28, 115], see Figure 3.1. The fractal known as the Sierpinski carpet was
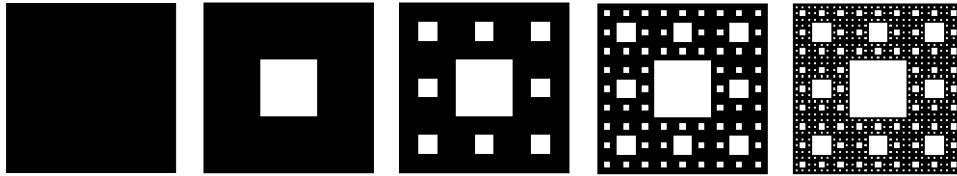
Figure 3.1: The initial square and first four iterations of the Sierpinski carpet.

first described in 1916 by mathematician Waclaw Sierpinski, a year after he first introduced the Sierpinski gasket [29]. The fractional dimension may also be defined using equation (1.1). Since the squares are scaled by a factor of three into eight sub-squares, the dimension for this fractal is $D_f = \log(8)/\log(3)$.

The sequence of graphs shown in Figure 3.2 are the lattice counterparts for the Sierpinski carpet. To study the behaviour of a propagating ultrasonic wave in the pre-fractal device, the fractal lattices are required. Analogous to the Sierpinski gasket pre-fractal transducer, the lattice counterpart represents the vibrations of the piezoelectric material. Thus, the structures are obtained in a similar method to the Sierpinski gasket lattices, whereby each graph in the sequence is obtained by connecting together eight copies of the previous one. Unlike the Sierpinski gasket however, the connection of subgraphs does not only exist at the boundary vertices. In the instance of the Sierpinski gasket it was possible to make the vertex degree constant and equal to $q = 3$ by introducing fictitious vertices at its input/output

vertices. Although the Sierpinski carpet inspired transducer will also position fictitious vertices at the input/output nodes, it should be noted that this will not make the vertex degrees constant and independent of the fractal generation level. This is as a result of there being an exponential increase in the number of connection vertices as the generation level is increased. The nth generation
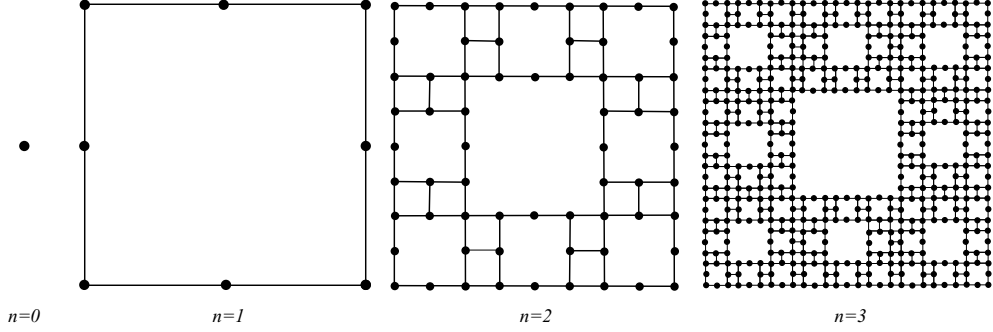
Figure 3.2: Graphical representations of generations 0 to 3 for the sequence of Sierpinski carpet lattices.

graph has $N_n = 2^{3n}$ vertices, and the side length of the structure L_s is once again assumed to be fixed throughout the construction process. For this lattice structure the vertex degree, is dependent on the number of sub-graphs it connects. For any fractal lattice, a single vertex will not connect more than three sub-graphs. Thus, the Sierpinski carpet lattice has vertex degree equal to four for vertices connecting three sub-graphs, three for vertices connecting two sub-graphs and two for non-connecting vertices. As a result, the input/output vertices have a vertex degree of two, which remains constant throughout the iteration process. Similar to the work presented in [86], fictitious vertices A, B, C and D are attached to these vertices to accommodate the boundary conditions, see Figure 3.3.

In the works proceeding, three models will be investigated, all of which are based on the design of the Sierpinski carpet. It is thought that the number of output vertices the transducer exhibits will have a direct effect on its performance, and as such it is desirable to obtain individual models which encompass these different numbers of output vertices, i.e. the number of boundary conditions. In

transmission mode, each model will contain a single input vertex that is connected to fictitious vertex A. At this vertex ultrasonic waves are generated through the application of an electric field and dependent on the model, one, two or three output vertices will be required. These output vertices will produce the mechanical vibrations once the wave has passed through the transducer. The graph in Figure 3.3 (a) defines model η at generation level two. As illustrated, model η contains two boundary conditions; an input vertex placed at vertex A and a single output vertex placed at vertex C. The second generation graph of model δ is shown in Figure 3.3 (b). This model will include three boundary conditions, again with the input vertex positioned at vertex A and two symmetric output vertices positioned at vertices B and D. Model γ will refer to the inclusion of four boundary conditions, see Figure 3.3 (c), where an input vertex is placed at vertex A, two symmetric vertices are to be placed at vertices B and D and an additional output vertex is placed at vertex C.
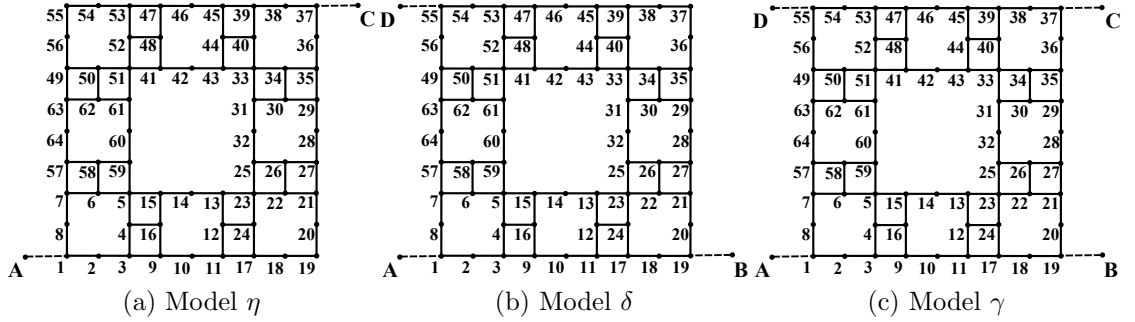
Figure 3.3: Sierpinski carpet lattice at generation $n = 2$. Fictitious vertices A, B, C and D are introduced to accommodate the boundary conditions. (a) Representation of Model η with fictitious vertices A and C. (b) Representation of Model δ with fictitious vertices A, B and D. (c) Representation of Model γ with fictitious vertices A, B, C and D.

3.3 Renormalization Analysis: Model Recursive Relations

Research into a Sierpinski carpet inspired device will utilise a similar analysis to the Sierpinski gasket inspired transducer. The method used previously has generally only been applied to finitely ramified fractals; very little has been studied on infinitely ramified fractals. Such structures have briefly been explored in [39, 40, 111]. In these papers, the entries of the Green function matrix are achieved by obtaining the Cartesian product of two lattices, with the purpose of assisting the study of much more complicated structures with spectral dimension greater than two. In Chapter 5, the possible performance of two new transducers are analysed by obtaining the Cartesian product of two pre-fractal lattices.

This section develops the Green function renormalization to an infinitely ramified Sierpinski carpet. In the following sections, the derivation of the recursion equations needed to derive any subsequent generation Green functions will be presented.

3.3.1 Model η: Single Output Vertex

It is important to obtain the Green functions at the input/output vertices of the structure for each of the three models as shown is Figure 3.3. Model η requires the following pivotal elements: $G_{11}^{(n)}$, $G_{1\,37}^{(n)}$ and $G_{37\,37}^{(n)}$. These can more conveniently be expressed as x_η, z_η and v_η, respectively, where the subscript η relates to the transducer model rather than to the vertices of the lattice. For this particular case, fictitious vertices A and C will be connected to vertices 1 and 37 respectively. Model η refers to the case in which there are two boundary conditions at vertices 1 and 37, and so it is assumed that vertices 19 and 55 are to be insulated. Since model η only takes into account boundary conditions placed at vertices 1 and 37, it only requires the recursion relations $\hat{x}$ and $\hat{z}$ since vertices 19 and 55 are presumed to have no interaction with external loads. By utilising equation (2.133),

the following set of equations for the pivotal Green functions are obtained

$$x_\eta = \hat{x}_\eta + \hat{x}_\eta b_1 x_\eta + \hat{z}_\eta b_2 z_\eta, \tag{3.1}$$

$$z_\eta = \hat{z}_\eta + \hat{z}_\eta b_1 x_\eta + \hat{x}_\eta b_2 z_\eta, \tag{3.2}$$

$$v_\eta = \hat{x}_\eta + \hat{z}_\eta b_1 z_\eta + \hat{x}_\eta b_2 v_\eta, \tag{3.3}$$

where $\hat{x}_\eta = \hat{G}_{11}^{(n)}$ and $\hat{z}_\eta = \hat{G}_{1\,37}^{(n)}$ correspond to the boundary matrix, $B^{(n)}$, being set to zero, and $b_1 = B_{11}^{(n)}$ and $b_2 = B_{37\,37}^{(n)}$ relate to the boundary conditions set at fictitious vertices A and C. Thus solving these three equations solely in terms of $\hat{x}_\eta$, $\hat{z}_\eta$, b_1, and b_2, yields

$$x_\eta = \frac{(\hat{z}_\eta^2 - \hat{x}_\eta^2)b_2 + \hat{x}_\eta}{\Delta_A}, \tag{3.4}$$

$$z_\eta = \frac{\hat{z}_\eta}{\Delta_A}, \tag{3.5}$$

$$v_\eta = \frac{(\hat{z}_\eta^2 - \hat{x}_\eta^2)b_1 + \hat{x}_\eta}{\Delta_A}, \tag{3.6}$$

where

$$\Delta_A = ((\hat{x}_\eta^2 - \hat{z}_\eta^2)b_1 - \hat{x}_\eta)b_2 + 1 - \hat{x}_\eta b_1. \tag{3.7}$$

In [40], one of the conditions in order to apply this renormalization method to a family of graphs is that the process of obtaining $G^{(n+1)}$ from $G^{(n)}$ consists of connecting together v copies of $G^{(n)}$ solely through the input/output vertices. As the Sierpinski carpet is an infinitely ramified fractal, the connection process to form the nth generation level graph consists of connecting v copies of $G^{(n)}$ at the input/output vertices in addition to internal vertices. Thus the method for obtaining the subsequent generations of Green functions is not achieved in the same manner as for the Sierpinski gasket. Since the vertex degrees are fixed for the Sierpinski gasket, it was possible to use the recursion relation equation, given in equation (2.132), which connects $G^{(n+1)}$ and $G^{(n)}$ as a way of obtaining the exact $(i,j)^{\text{th}}$ element of the Green function matrix for any given generation level. As a result of the non-constant vertex degrees in the Sierpinski carpet lattices, it is not possible to use the relation equation, and only equation (2.133) will be used for

70

each model to develop the recursion relationships. Furthermore, it is necessary to obtain the Green function matrices. Consequently, results for higher generation levels are computationally intensive and therefore only low generation levels have been computed. Previous papers have analysed infinitely ramified fractals using methods such as percolation, random walks and Brownian motion [13, 14, 45]. These give alternative methods for studying the propagation of an ultrasonic wave within a Sierpinski carpet pre-fractal.

3.3.2 Model δ: Two Symmetric Output Vertices

Model δ is concerned with the inclusion of three boundary conditions; an input vertex at site 1 and two output vertices at sites 19 and 55. Due to the symmetries of this lattice, it can be shown that $G_{1\,19}^{(n)}$ and $G_{1\,55}^{(n)}$ are equal. For this model it is necessary to determine the relations for $\hat{x}_\delta$, $\hat{y}_\delta$, $\hat{t}_\delta$ and $\hat{w}_\delta$, as it is assumed that vertex 37 is to be insulated from the external loads. The need for the addition of $\hat{t}_\delta$ and $\hat{w}_\delta$ is due to the symmetry of this lattice, see Figure 3.3(b). In this instance $\hat{G}_{1\,1}^{(n)} \neq \hat{G}_{19\,19}^{(n)}$. Thus using analysis similar to that with model η results with

$$x_\delta = \frac{\left(1 - b_2 \left(\hat{t}_\delta + \hat{w}_\delta\right)\right) \hat{x}_\delta + 2b_2 \hat{y}_\delta^2}{\Delta_B}, \tag{3.8}$$

$$y_\delta = \frac{\hat{y}_\delta}{\Delta_B}, \tag{3.9}$$

$$w_\delta = \frac{b_1 \left(1 + 2b_2 \left(\hat{t}_\delta - \hat{w}_\delta\right)\right) \hat{y}_\delta^2 - \left(\hat{w}_\delta + b_2 \left(\hat{t}_\delta - \hat{w}_\delta\right) \left(\hat{t}_\delta + \hat{w}_\delta\right)\right) \left(b_1 \hat{x}_\delta - 1\right)}{\Delta_C}, \tag{3.10}$$

$$t_\delta = \frac{\hat{t}_\delta - b_1 \hat{t}_\delta \hat{x}_\delta + b_1 \hat{y}_\delta^2}{\Delta_C}, \tag{3.11}$$

where

$$\Delta_B = \left(b_2 \left(\hat{t}_\delta + \hat{w}_\delta\right) - 1\right) \left(b_1 \hat{x}_\delta - 1\right) - 2b_1 b_2 \hat{y}_\delta^2, \tag{3.12}$$

$$\Delta_C = \left(1 + b_2 \left(\hat{t}_\delta - \hat{w}_\delta\right)\right) \left(\left(b_2 \left(\hat{t}_\delta + \hat{w}_\delta\right) - 1\right) \left(b_1 \hat{x}_\delta - 1\right) - 2b_1 b_2 \hat{y}_\delta^2\right) \tag{3.13}$$

and x_δ, y_δ, w_δ and t_δ correspond to the pivotal elements $G_{1\,1}^{(n)}$, $G_{1\,19}^{(n)}$, $G_{19\,19}^{(n)}$ and $G_{19\,55}^{(n)}$ respectively.

3.3.3 Model γ: Three Output Vertices

In the case of model γ there are seven pivotal elements, $G_{11}^{(n)}$, $G_{119}^{(n)}$, $G_{137}^{(n)}$, $G_{1919}^{(n)}$, $G_{3737}^{(n)}$, $G_{1937}^{(n)}$ and $G_{1955}^{(n)}$, where for ease of notation these will be labelled respectively as x_γ, y_γ, z_γ, w_γ, v_γ, u_γ and t_γ. From lattice symmetry

$$\hat{G}_{11}^{(n)} = \hat{G}_{1919}^{(n)} = \hat{G}_{3737}^{(n)} = \hat{G}_{5555}^{(n)}, \tag{3.14}$$

$$\hat{G}_{119}^{(n)} = \hat{G}_{155}^{(n)} = \hat{G}_{1937}^{(n)} = \hat{G}_{3755}^{(n)}, \tag{3.15}$$

$$\hat{G}_{137}^{(n)} = \hat{G}_{1955}^{(n)}, \tag{3.16}$$

however it should be noted that this does not hold true when boundary conditions are reintroduced. These Green function elements are associated with the internal structure of the lattice and as a result it is possible to set these elements equal to one another, as shown in equations (3.14)-(3.16). The introduction of the boundary conditions transforms the bare Green function matrix to take into account the backing layer and mechanical loads set at the input/output vertices. This therefore alters the Green function matrix, and thus the inclusion of boundary conditions suggests that

$$G_{119}^{(n)} = G_{155}^{(n)}, \tag{3.17}$$

$$G_{1937}^{(n)} = G_{3755}^{(n)}, \tag{3.18}$$

$$G_{11}^{(n)} \neq G_{1919}^{(n)} \neq G_{3737}^{(n)}, \tag{3.19}$$

$$G_{119}^{(n)} \neq G_{137}^{(n)}. \tag{3.20}$$

The use of equation (2.133) results in seven equations,

$$x_\gamma = \frac{\begin{pmatrix} 2b_2\left(\hat{x}_\gamma^2 - \hat{y}_\gamma^2\right) + b_2\left(\hat{x}_\gamma - \hat{z}_\gamma\right)\left(4\hat{y}_\gamma^2 b_2 - \hat{z}_\gamma\left(\hat{x}_\gamma b_2 - 1\right)\right) \\ - b_2^2\left(\hat{x}_\gamma^3 - \hat{z}_\gamma^3\right) - \hat{x}_\gamma \end{pmatrix}}{\Delta_1}, \tag{3.21}$$

$$y_\gamma = \frac{\hat{y}_\gamma\left(1 - b_2\left(\hat{x}_\gamma - \hat{z}_\gamma\right)\right)}{\Delta_1}, \tag{3.22}$$

$$z_\gamma = \frac{2\hat{y}_\gamma^2 b_2 + \hat{z}_\gamma\left(1 - b_2\left(\hat{x}_\gamma + \hat{z}_\gamma\right)\right)}{\Delta_1}, \tag{3.23}$$

$$w_\gamma = \big((2\hat{x}_\gamma^2(\hat{x}_\gamma b_1 - 1) - 2(2\hat{y}_\gamma^2 + \hat{z}_\gamma^2)b_1\hat{x}_\gamma + \hat{y}_\gamma^2(1 + 4\hat{z}_\gamma b_1) + \hat{z}_\gamma^2)b_2$$
$$- \big(\hat{x}_\gamma(\hat{x}_\gamma^2 b_1 + \hat{x}_\gamma(\hat{z}_\gamma b_1 - 1) - (4\hat{y}_\gamma^2 + \hat{z}_\gamma^2)b_1 - \hat{z}_\gamma) + \hat{z}_\gamma b_1$$
$$\times \; (4\hat{y}_\gamma^2 - \hat{z}_\gamma^2) + 2\hat{y}_\gamma^2\big)\,(\hat{x}_\gamma - \hat{z}_\gamma)b_2{}^2 - b_1(\hat{x}_\gamma^2 - \hat{y}_\gamma^2) + \hat{x}_\gamma\big)\,(\Delta_2)^{-1} \tag{3.24}$$

$$v_\gamma = \frac{\left(\begin{array}{c} (\hat{x}_\gamma - \hat{z}_\gamma)\,(\hat{x}_\gamma + 2\hat{y}_\gamma + \hat{z}_\gamma)\,(\hat{x}_\gamma - 2\hat{y}_\gamma + \hat{z}_\gamma)\,b_1 b_2 \\ -\,(\hat{x}_\gamma\,(\hat{x}_\gamma + \hat{z}_\gamma) + 2\hat{y}_\gamma^2)\,b_2 - (\hat{x}_\gamma^2 - \hat{z}_\gamma^2)\,b_1 + \hat{x}_\gamma \end{array} \right)}{\Delta_1}, \tag{3.25}$$

$$u_\gamma = \frac{\hat{y}_\gamma\,(b_1\,(\hat{x}_\gamma - \hat{z}_\gamma) - 1)}{\Delta_1}, \tag{3.26}$$

$$t_\gamma = \frac{\hat{z}_\gamma - (\hat{x}_\gamma\hat{z}_\gamma - \hat{y}_\gamma^2)(b_1 + b_2) + b_1 b_2(\hat{z}_\gamma(\hat{x}_\gamma^2 - \hat{z}_\gamma^2) - 2\hat{y}_\gamma^2(\hat{x}_\gamma - \hat{z}_\gamma))}{\Delta_2}, \tag{3.27}$$

where

$$\Delta_1 \;=\; b_1 b_2^2\,(\hat{x}_\gamma - \hat{z}_\gamma)\,(\hat{x}_\gamma\hat{z}_\gamma - 4\hat{y}_\gamma^2) + (2\hat{y}_\gamma^2 b_1 + \hat{x}_\gamma)\,(b_1 + b_2)$$
$$+ \; b_1 b_2\,(b_2\,(\hat{x}_\gamma^3 - \hat{z}_\gamma^3) - (2\hat{x}_\gamma - \hat{z}_\gamma)\,(\hat{x}_\gamma + \hat{z}_\gamma)) - 1, \tag{3.28}$$

$$\Delta_2 \;=\; ((\hat{x}_\gamma - \hat{z}_\gamma)b_2 - 1)(((\hat{x}_\gamma - \hat{z}_\gamma)(\hat{x}_\gamma + 2\hat{y}_\gamma + \hat{z}_\gamma)(\hat{x}_\gamma - 2\hat{y}_\gamma + \hat{z}_\gamma)$$
$$- \; \hat{x}_\gamma(\hat{x}_\gamma + \hat{z}_\gamma) + 2\hat{y}_\gamma^2)b_2^2(((\hat{z}_\gamma(\hat{z}_\gamma - \hat{x}_\gamma) - 2(\hat{x}_\gamma^2 - \hat{y}_\gamma^2))b_1 + 2\hat{x}_\gamma$$
$$+ \; \hat{z}_\gamma)b_2 + \hat{x}_\gamma b_1 - 1)), \tag{3.29}$$

with $b_1 = B_{1\,1}^{(n)}$ and $b_2 = B_{19\,19}^{(n)} = B_{37\,37}^{(n)} = B_{55\,55}^{(n)}$. For brevity, the system of equations used to derive the pivotal Green functions for models δ and γ is presented in Appendix B.

As the pivotal elements for each of the carpet models have been determined, expressions detailing the electrical impedance and transmission and reception sensitivities for each device can now be calculated.

3.4 Application of Boundary Conditions

Chapter 2 presents the constitutive equations (2.1)-(2.2) required to describe the interaction between electrical and mechanical properties of the piezoelectric material. For each model, mechanical loads are placed at the output vertices and an

electrical load is positioned at the input vertex. To find the governing equation for these loads, stress, T, can be expressed as [88]

$$T = \frac{F}{A_r},$$ (3.30)

where F is the force on each vertex and A_r is the cross-sectional area of each fractal lattice edge. Using Newton's Second Law of Motion which describes force to be the product of mass and acceleration and making the appropriate substitution for mass, the force may be defined as

$$F = A_r l \rho \frac{\partial^2 u}{\partial t^2}.$$ (3.31)

Substituting this into equation (3.30) gives

$$T = l \rho \frac{\partial^2 u}{\partial t^2},$$ (3.32)

where l is transducer thickness, ρ is the density and u is the particle displacement. Thus

$$\frac{\partial T}{\partial x} = \rho \frac{\partial^2 u}{\partial t^2},$$ (3.33)

which is the stress equation of motion, given previously in equation (2.4). Using the definition of Hooke's law in equation (2.61), the governing equation is found to be

$$\rho_i \frac{\partial^2 u_i}{\partial t^2} = Y_i \frac{\partial^2 u_i}{\partial x_i^2},$$ (3.34)

where the subscript i will be suitably substituted with L when concerning the mechanical load and with B when referring to the backing layer. A solution to the above is found by re-introducing the non-dimensional variable shown in equation (2.124)

$$\frac{\partial^2 u_i}{\partial \theta^2} = \left(\frac{v_i}{v_T} \Delta x \right)^2 \frac{\partial^2 u_i}{\partial x_i^2},$$ (3.35)

and taking Laplace transforms of equation (3.35) to give

$$\frac{\partial^2 \bar{u}_i}{\partial x_i^2} - \left(\frac{p v_T}{\Delta x v_i} \right)^2 \bar{u}_i = 0,$$ (3.36)

74

where v_T is the wave velocity in the piezoelectric material and v_i is the wave velocity in the mechanical load or backing layer. As with earlier devices it is assumed that the wave only propagates away from the ceramic phase. Thus, a solution for the displacement in the load and backing layer are given respectively as

$$\bar{u}_L = \alpha_L \exp\left(\frac{-pv_T x_L}{\Delta x v_L}\right) + \beta_L \exp\left(\frac{pv_T x_L}{\Delta x v_L}\right), \tag{3.37}$$

and

$$\bar{u}_B = \alpha_B \exp\left(\frac{-pv_T x_B}{\Delta x v_B}\right). \tag{3.38}$$

The solution for the wave equation, found in equations (3.37) and (3.38), is fundamental in transducer analysis as the equations are used to obtain the voltage across the transducer and the force acting on each vertex. The calculation for the voltage is presented in the following section. Applying the conditions of continuity of displacement at the transducer boundaries gives

$$\bar{u}_L(0) = \alpha_L + \beta_L, \tag{3.39}$$

$$\bar{u}_B(0) = \alpha_B. \tag{3.40}$$

There is a possibility to avail of a variety of transducers here, with the option of having one, two or three mechanical loads. Each of the models being investigated will have the backing material set at vertex A, and one, two or three mechanical loads (depending on the model) placed at vertices B, C and/or D. To be more specific, model γ is the fractal transducer that will have the three mechanical loads at vertices B, C and D. Hence, due to the symmetry of the Green transfer matrix, equations (3.39) and (3.40) become

$$u_{19} = u_{37} = u_{55} = u_B = u_C = u_D = \alpha_L + \beta_L, \tag{3.41}$$

$$u_1 = u_A = \alpha_B, \tag{3.42}$$

where the subscripts attached to the displacement u refer to a specific vertex of the graph. Equation (3.41) can be rewritten for models η and δ respectively as

$$u_{37} = u_C = \alpha_L + \beta_L \quad \text{and} \tag{3.43}$$

75

$$u_{19} = u_{55} = u_B = u_D = \alpha_L + \beta_L. \tag{3.44}$$

In equation (3.30), stress is given in terms of force and area. Using equation (2.1) and rearranging in terms of force gives

$$\bar{F} = A_r \bar{T} = A_r Y \frac{\partial \bar{u}}{\partial x} - h\bar{Q}, \tag{3.45}$$

where $\bar{S} = \partial \bar{u}/\partial x$ and $\bar{D} = \bar{Q}/A_r$ [86]. The derivative in the above equation can be defined as

$$\frac{\partial \bar{u}}{\partial x} = \lim_{\Delta x \to 0} \frac{u(x + \Delta x) - u(x)}{\Delta x}. \tag{3.46}$$

This can then be approximated to give

$$\frac{\partial \bar{u}_i}{\partial x} \approx \frac{u(x_i + \Delta x) - u(x_i)}{\Delta x} = \frac{u_{i+1} - u_i}{\Delta x}. \tag{3.47}$$

Substituting this into equation (3.45) gives an expression for the force, $\bar{F}_T$, in the piezoelectric layer as

$$\bar{F}_T = A_r Y_T \frac{u_{i+1} - u_i}{\Delta x} - h\bar{Q}, \tag{3.48}$$

To obtain the expressions for the force in the backing layer and load the derivative in equation (3.45) is replaced to give

$$\bar{F}_B = -A_r Y_B \left(\frac{p v_T}{\Delta x v_B} \right) \alpha_B, \tag{3.49}$$

for the backing layer and

$$\bar{F}_L = A_r Y_L \left(\frac{p v_T}{\Delta x v_L} \right) (-\alpha_L + \beta_L), \tag{3.50}$$

for the load. Hence, continuity of force gives

$$
\begin{aligned}
\bar{F}_T = \bar{F}_B &= A_r Y_T \left(\frac{u_1 - u_A}{\Delta x} \right) - h\bar{Q} = -A_r Y_B \left(\frac{p v_T}{\Delta x v_B} \right) \alpha_B \\
&= (u_1 - u_A) - \frac{h\bar{Q}\Delta x}{A_r Y_T} = -\frac{p v_T Y_B}{Y_T v_B} \alpha_B \\
&= u_1 - u_A - \frac{h\bar{Q}}{Y_T \xi} = -\frac{Z_B}{Z_T} p\alpha_B, \tag{3.51}
\end{aligned}
$$

$$\bar{F}_T = \bar{F}_L = A_r Y_T \left(\frac{u_B - u_{19}}{\Delta x} \right) - h\bar{Q} = A_r Y_L \left(\frac{p v_T}{\Delta x v_L} \right) (-\alpha_L + \beta_L)$$

$$= u_B - u_{19} - \frac{h\bar{Q}}{Y_T \xi} = \frac{Z_L}{Z_T} p(-\alpha_L + \beta_L), \tag{3.52}$$

where $\xi = A_r / \Delta x$ is the ratio of the cross-sectional area of each edge to its length [86]. Combining equations (3.42) and (3.51) gives an expression for the mechanical displacement at the fictitious vertex A,

$$u_1 - u_A - \frac{h\bar{Q}}{Y_T \xi} = -p \frac{Z_B}{Z_T} u_A,$$

$$u_1 - \frac{h\bar{Q}}{Y_T \xi} = u_A \left(1 - p \frac{Z_B}{Z_T} \right),$$

$$u_A = u_1 \left(\frac{1}{1 - p \frac{Z_B}{Z_T}} \right) - \frac{h\bar{Q}}{Y_T \xi} \left(\frac{1}{1 - p \frac{Z_B}{Z_T}} \right). \tag{3.53}$$

Similarly, the mechanical displacement at fictitious vertices B, C and D is obtained by combining equation (3.41) with equation (3.52) to give

$$u_B - u_{19} - \frac{h\bar{Q}}{Y_T \xi} = p \frac{Z_L}{Z_T} (-2\alpha_L + u_B),$$

$$u_B \left(1 - p \frac{Z_L}{Z_T} \right) = u_{19} + \frac{h\bar{Q}}{Y_T \xi} - 2p\alpha_L \frac{Z_L}{Z_T},$$

$$u_B = u_{19} \left(\frac{1}{1 - p \frac{Z_L}{Z_T}} \right) + \left(\frac{h\bar{Q}}{Y_T \xi} - 2p\alpha_L \frac{Z_L}{Z_T} \right) \left(\frac{1}{1 - p \frac{Z_L}{Z_T}} \right) = u_C = u_D. \tag{3.54}$$

Thus, using equations (3.53) and (3.54) it is possible to determine elements of the boundary condition matrix $B^{(n)}$,

$$B_{ij} = \begin{cases} \frac{1}{1 - p \frac{Z_B}{Z_T}} & \text{if } i = j = 1 \\ \frac{1}{1 - p \frac{Z_L}{Z_T}} & \text{if } i = j = 19,\ 37 \text{ or } 55, \\ 0 & \text{otherwise} \end{cases} \tag{3.55}$$

and the vector $\underline{c}^{(n)}$

$$
c_i = \begin{cases} -\frac{h\bar{Q}}{Y_T\xi}\left(\frac{1}{1-p\frac{Z_B}{Z_T}}\right) & \text{if } i = 1 \\[2ex] \left(\frac{h\bar{Q}}{Y_T\xi} - 2pA_L\frac{Z_L}{Z_T}\right)\left(\frac{1}{1-p\frac{Z_L}{Z_T}}\right) & \text{if } i = 19, 37 \text{ or } 55. \\[2ex] 0 & \text{otherwise} \end{cases} \tag{3.56}
$$

Within this section, expressions detailing the mechanical displacements at the boundary vertices were derived, and from this the boundary matrix elements as well as the vector $\underline{c}^{(n)}$ elements were obtained. The following section will utilise these calculations to determine expressions for the electrical impedance and transmission and reception sensitivities for the three devices.

3.5 Electrical Impedance, Transmission and Reception Sensitivities

An expression for the voltage may be obtained by firstly expressing equation (2.2) as

$$
\bar{E} = -h\frac{\partial \bar{u}}{\partial x} + \frac{\bar{Q}}{A_r\epsilon}. \tag{3.57}
$$

Integrating, and utilising equation (2.7) then gives

$$
\begin{aligned}
\bar{V} &= \int_0^{L_s}\left(-h\frac{\partial \bar{u}}{\partial x} + \frac{\bar{Q}}{A_r\epsilon}\right)dx, \\
&= -h\int_a^b\left(\frac{\partial \bar{u}}{\partial x} + \frac{\bar{Q}}{C_0}\right)dx, \tag{3.58}
\end{aligned}
$$

where a and b are any two points in space. In this instance, a and b are any two points in the lattice structure. Three cases are being investigated for the theoretical Sierpinski carpet transducer, each differ from one another depending on the number of boundary conditions and the location of these boundaries. A charge Q is applied to the transducer at vertex A and passes through in the direction of the electric field. The voltage for model η is measured between fictitious vertices A

and C, thus implementing these parameters into equation (3.58) and using Gauss'
law gives the voltage as

$$\bar{V} = -h\left(u_{37} - u_1\right) + \frac{\bar{Q}}{C_0}. \tag{3.59}$$

In a similar way, the voltage for model δ is found to be

$$\bar{V} = -h\left(u_{19} - u_1\right) + \frac{\bar{Q}}{C_0}, \tag{3.60}$$

since the path taken from A to B (or A to D) is parallel to the electric field;
see Figure 3.4. For model γ the voltage consists of two contributions, one for each
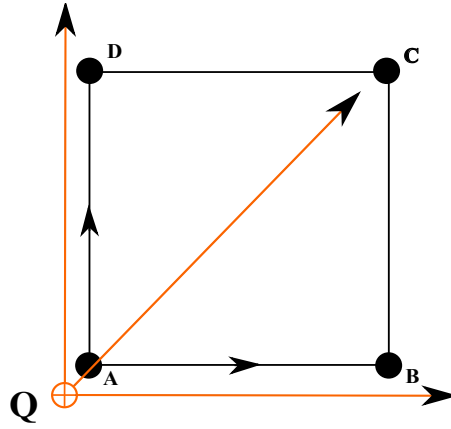
Figure 3.4: Electric field lines emanating from a point positive electric charge Q.

lattice edge of the path, these being the path A to B and the path B to C. Since
a positive charge is applied to the transducer at vertex A, electric field lines would
emanate in all directions away from this point. So when moving from vertex A to
B the voltage in this case would just be the difference between vertices u_{19} and u_1
since the path taken is parallel to the electric field. However, the path from vertex
B to C would result in zero voltage as the path in this case is perpendicular to
the direction of the electric field. Thus the voltage for model γ is given as

$$\begin{aligned}
\bar{V} &= \bar{V}_{BA} + \bar{V}_{CB} \\
&= \left(\bar{V}_B - \bar{V}_A\right) + \left(\bar{V}_C - \bar{V}_B\right) \\
&= \bar{V}_B - \bar{V}_A \\
&= -h\left(u_{19} - u_1\right) + \frac{\bar{Q}}{C_0}. \tag{3.61}
\end{aligned}$$

A general term for the voltage can be given by

$$\bar{V} = -h\left(u_b - u_a\right) + \frac{\bar{Q}}{C_0}. \tag{3.62}$$

It is stated in Chapter 2 that the electrical charge is given by

$$Q = \int I \, dt. \tag{3.63}$$

For a transducer based on the design of the Sierpinski carpet, the charge is obtained by introducing the non-dimensional variable θ in equation (2.124)

$$Q = \Delta x \sqrt{\rho_T / Y_T} \int I \, d\theta, \tag{3.64}$$

and then taking Laplace transforms to give

$$\bar{Q} = \frac{\sqrt{\rho_T / Y_T} \Delta x \bar{I}}{p}. \tag{3.65}$$

Rearranging in terms of the current gives

$$\bar{I} = \frac{p \bar{Q} Y_T \xi}{Z_T}, \tag{3.66}$$

where $Z_T = \sqrt{Y_T \rho_T} A_r$. The electrical impedance of the device is given by $Z = V/I$, so using equations (3.62) and (3.66) results in

$$\bar{Z} = \frac{Z_T}{p C_0 Y_T \xi} \left(1 - \frac{h C_0 (u_b - u_a)}{\bar{Q}}\right). \tag{3.67}$$

As there are three independent models, it is important to obtain the electrical impedance for each. So to begin with, the electrical impedance for model η is found by solving $u_{37} - u_1$ and substituting this in place of the $u_b - u_a$ term found in equation (3.67). Since $\underline{u} = G^{(n)} \underline{c}$ then $u_{37} = G^{(n)}_{1\,37} c_1 + G^{(n)}_{37\,37} c_{37}$ and $u_1 = G^{(n)}_{1\,1} c_1 + G^{(n)}_{1\,37} c_{37}$. Utilising equation (3.56) results in

$$
\begin{aligned}
u_{37} - u_1 = -\frac{h\bar{Q}}{Y_T \xi} \left(\frac{G^{(n)}_{1\,37} - G^{(n)}_{37\,37}}{1 - p\frac{Z_L}{Z_T}} + \frac{G^{(n)}_{1\,37} - G^{(n)}_{1\,1}}{1 - p\frac{Z_B}{Z_T}}\right) \\
+ \frac{2p\alpha_L Z_L}{Z_T} \left(\frac{G^{(n)}_{1\,37} - G^{(n)}_{37\,37}}{1 - p\frac{Z_L}{Z_T}}\right).
\end{aligned} \tag{3.68}
$$

80

Denoting $\mu_\eta = \frac{G_{1\,37}^{(n)} - G_{37\,37}^{(n)}}{1 - p\frac{Z_L}{Z_T}}$ and $\nu_\eta = \frac{G_{1\,37}^{(n)} - G_{11}^{(n)}}{1 - p\frac{Z_B}{Z_T}}$ as well as substituting equation (3.68) into equation (3.67) gives the electrical impedance for model η as

$$\bar{Z}_\eta = \frac{Z_T}{pC_0 Y_T \xi}\left(1 + \frac{h^2 C_0(\mu_\eta + \nu_\eta)}{Y_T \xi} - \frac{2hC_0 p\mu_\eta \alpha_L Z_L}{\bar{Q} Z_T}\right). \tag{3.69}$$

The non-dimensionalized electrical impedance for model η is then found by dividing through a series electrical load, Z_0, resulting in

$$\hat{Z}_\eta = \frac{Z_T}{pC_0 Y_T \xi Z_0}\left(1 + \frac{h^2 C_0(\mu_\eta + \nu_\eta)}{Y_T \xi} - \frac{2hC_0 p\mu_\eta \alpha_L Z_L}{\bar{Q} Z_T}\right). \tag{3.70}$$

For models δ and γ their respective electrical impedance only differs to model η in regards to their μ and ν expressions. For model δ these terms are found through the solution of $u_{19} - u_1$,

$$
\begin{aligned}
u_{19} - u_1 &= -\frac{h\bar{Q}}{Y_T \xi}\left(\frac{2G_{1\,19}^{(n)} - G_{19\,19}^{(n)} - G_{19\,55}^{(n)}}{1 - p\frac{Z_L}{Z_T}} + \frac{G_{1\,19}^{(n)} - G_{11}^{(n)}}{1 - p\frac{Z_B}{Z_T}}\right) \\
&\quad + \frac{2p\alpha_L Z_L}{Z_T}\left(\frac{2G_{1\,19}^{(n)} - G_{19\,19}^{(n)} - G_{19\,55}^{(n)}}{1 - p\frac{Z_L}{Z_T}}\right),
\end{aligned} \tag{3.71}
$$

where

$$u_{19} = G_{1\,19}^{(n)}c_1 + G_{19\,19}^{(n)}c_{19} + G_{19\,55}^{(n)}c_{55} = G_{1\,19}^{(n)}c_1 + (G_{19\,19}^{(n)} + G_{19\,55}^{(n)})c_{19}, \tag{3.72}$$

$$u_1 = G_{11}^{(n)}c_1 + G_{1\,19}^{(n)}c_{19} + G_{1\,55}^{(n)}c_{55} = G_{11}^{(n)}c_1 + 2G_{1\,19}^{(n)}c_{19}, \tag{3.73}$$

thus

$$\mu_\delta = \frac{2G_{1\,19}^{(n)} - G_{19\,19}^{(n)} - G_{19\,55}^{(n)}}{1 - p\frac{Z_L}{Z_T}}, \tag{3.74}$$

$$\nu_\delta = \frac{G_{1\,19}^{(n)} - G_{11}^{(n)}}{1 - p\frac{Z_B}{Z_T}}. \tag{3.75}$$

Therefore, the non-dimensionalized electrical impedance for model δ is given by

$$\hat{Z}_\delta = \frac{Z_T}{pC_0 Y_T \xi Z_0}\left(1 + \frac{h^2 C_0(\mu_\delta + \nu_\delta)}{Y_T \xi} - \frac{2hC_0 p\mu_\delta \alpha_L Z_L}{\bar{Q} Z_T}\right). \tag{3.76}$$

Similarly, finding the electrical impedance for model γ requires the solution of $u_{19} - u_1$. Although this gives the impression of having the same solution as model δ,

81

it is in fact different due to the addition of a boundary condition set at vertex 37. In this instance

$$
\begin{aligned}
u_{19} &= G_{1\,19}^{(n)}c_1 + G_{19\,19}^{(n)}c_{19} + G_{19\,37}^{(n)}c_{37} + G_{19\,55}^{(n)}c_{55} \\
&= G_{1\,19}^{(n)}c_1 + (G_{19\,19}^{(n)} + G_{19\,37}^{(n)} + G_{19\,55}^{(n)})c_{19},
\end{aligned}
\tag{3.77}
$$

$$
\begin{aligned}
u_1 &= G_{1\,1}^{(n)}c_1 + G_{1\,19}^{(n)}c_{19} + G_{1\,37}^{(n)}c_{37} + G_{1\,55}^{(n)}c_{55} \\
&= G_{1\,1}^{(n)}c_1 + (2G_{1\,19}^{(n)} + G_{1\,37}^{(n)})c_{19},
\end{aligned}
\tag{3.78}
$$

hence,

$$
\begin{aligned}
u_{19} - u_1 &= -\frac{h\bar{Q}}{Y_T\xi}\left(\frac{2G_{1\,19}^{(n)} + G_{1\,37}^{(n)} - G_{19\,19}^{(n)} - G_{19\,37}^{(n)} - G_{19\,55}^{(n)}}{1 - p\frac{Z_L}{Z_T}}\right) \\
&\quad - \frac{h\bar{Q}}{Y_T\xi}\left(\frac{G_{1\,19}^{(n)} - G_{1\,1}^{(n)}}{1 - p\frac{Z_B}{Z_T}}\right) \\
&\quad + \frac{2p\alpha_L Z_L}{Z_T}\left(\frac{2G_{1\,19}^{(n)} + G_{1\,37}^{(n)} - G_{19\,19}^{(n)} - G_{19\,37}^{(n)} - G_{19\,55}^{(n)}}{1 - p\frac{Z_L}{Z_T}}\right).
\end{aligned}
\tag{3.79}
$$

Thus, the non-dimensionalized electrical impedance for model γ is

$$
\hat{Z}_\gamma = \frac{Z_T}{pC_0 Y_T \xi Z_0}\left(1 + \frac{h^2 C_0(\mu_\gamma + \nu_\gamma)}{Y_T\xi} - \frac{2hC_0 p\mu_\gamma \alpha_L Z_L}{\bar{Q}Z_T}\right),
\tag{3.80}
$$

where

$$
\mu\gamma = \frac{2G_{1\,19}^{(n)} + G_{1\,37}^{(n)} - G_{19\,19}^{(n)} - G_{19\,37}^{(n)} - G_{19\,55}^{(n)}}{1 - p\frac{Z_L}{Z_T}},
\tag{3.81}
$$

and

$$
\nu_\gamma = \frac{G_{1\,19}^{(n)} - G_{1\,1}^{(n)}}{1 - p\frac{Z_B}{Z_T}} \neq \beta_\delta.
\tag{3.82}
$$

Now that the electrical impedances for each of the transducer models have been calculated, these analytical expressions will be used to derive the necessary transmission and reception sensitivities for each device.

3.5.1 Transmission Sensitivity

This section derives the equations detailing the transmission sensitivities for each model for the carpet inspired transducer. These equations, along with the expressions for the electrical impedance (found in the previous section) and the reception sensitivities, are very significant as they can give useful insight as to the performance of the device. The reception sensitivity is derived in the following section.

In transmission mode, the conversion of electrical signal to mechanical vibration is achieved from the application of an applied voltage [51, 88, 114]. When the transducer is transmitting there is no force incident at the front face of the transducer, and so there is no forward travelling wave in the load, i.e. $\alpha_L = 0$ [86, 96]; see Figure 3.5. The current across the transducer can be derived by examining Figure 3.5 and making use of the generalized Ohm's law. This form of Ohm's
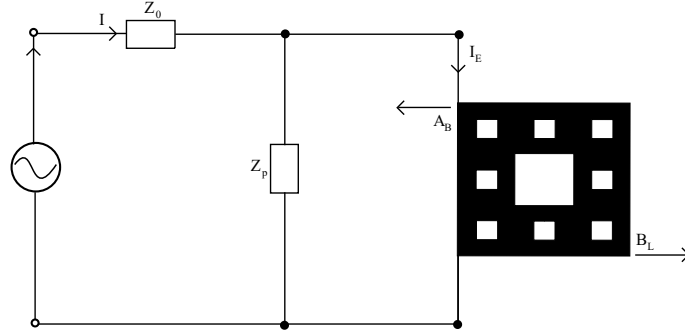
Figure 3.5: Potential transducer arrangement in transmission mode where Z_0 represents the series electrical load, Z_p is the parallel electrical load and I_E is the current across the transducer.

law states that the current, I, is expressed to be the voltage, V, divided by the impedance, Z. The total impedance is calculated using the rules for combining impedances in series and parallel circuits. That is,

$$Z_{eq} = \sum_{r=1}^{n} Z_r, \tag{3.83}$$

for series combination and

$$\frac{1}{Z_{eq}} = \sum_{r=1}^{n} \frac{1}{Z_r}, \tag{3.84}$$

for parallel combination. The series combination is $Z_{eq} = Z_0$ and the parallel combination is $1/Z_{eq} = 1/Z_p + 1/\bar{Z} = (\bar{Z} + Z_p)/Z_p\bar{Z}$. Thus, the total impedance is

$$Z_I = Z_0 + \frac{Z_p\bar{Z}}{\bar{Z} + Z_p}, \tag{3.85}$$

resulting in

$$\bar{I} = \frac{\bar{V}}{Z_0 + \frac{Z_p\bar{Z}}{\bar{Z}+Z_p}}, \tag{3.86}$$

since $I = V/Z_I$. By defining the voltage across the transducer as

$$\begin{aligned}
\bar{V}_E &= \bar{I}\bar{Z} = \frac{\bar{V}}{Z_0 + \frac{Z_p\bar{Z}}{\bar{Z}+Z_p}} \times \frac{Z_p\bar{Z}}{\bar{Z} + Z_p}, \\
&= \frac{\bar{V}Z_p\bar{Z}}{Z_0\left(\bar{Z} + Z_p\right) + Z_p\bar{Z}},
\end{aligned} \tag{3.87}$$

an expression for the current across the transducer is determined as

$$\bar{I}_E = \frac{\bar{V}_E}{\bar{Z}} = \frac{\bar{V}Z_p}{Z_0\left(\bar{Z} + Z_p\right) + Z_p\bar{Z}}. \tag{3.88}$$

After some rearrangement, this can be written in the form of

$$\bar{I}_E = \frac{a\bar{V}}{\left(\bar{Z} + b\right)}, \tag{3.89}$$

where $a = Z_p/(Z_0 + Z_p)$ and $b = Z_0 Z_p/(Z_0 + Z_p)$. Equations (3.85)-(3.89) have been derived previously in [86, 96]. Theoretically, this transducer is placed in a circuit similar to that of the Sierpinski gasket and monolithic transducers, and as a result, the expressions for the voltage, impedances and current would be the same. In particular, equation (3.89) was seen earlier in equation (2.46). Thus, using the two expressions for the current in equations (3.66) and (3.89), the input voltage can be defined as

$$\begin{aligned}
\frac{p\bar{Q}Y_T\xi}{Z_T} &= \frac{a\bar{V}}{\left(\bar{Z} + b\right)}, \\
\bar{V} &= \frac{p\bar{Q}Y_T\xi(\bar{Z} + b)}{Z_T a}.
\end{aligned} \tag{3.90}$$

84

The electrical impedance is redefined as

$$\bar{Z}_i = \frac{Z_T}{pC_0 Y_T \xi} \left(1 + \frac{h^2 C_0 (\mu_i + \nu_i)}{Y_T \xi} \right), \tag{3.91}$$

where the subscript i will be appropriately substituted with η, δ or γ dependent on the model. In order to obtain an expression for the transmission sensitivity of the device it is important to derive the output force, so from continuity of force at the front face,

$$\bar{F} = \bar{F}_L = A_r Y_L \beta_L \left(\frac{p v_T}{\Delta x v_L} \right) = \xi Y_L \beta_L p \frac{v_T}{v_L}. \tag{3.92}$$

Using equations (3.41) and (3.54) the above equation is re-written as

$$\begin{aligned}
\bar{F} &= \xi Y_L p \frac{v_T}{v_L} u_C \\
&= \frac{\xi Y_L p v_T}{v_L} \left(\frac{1}{1 - p\frac{Z_L}{Z_T}} \right) \left(u_{37} + \frac{h\bar{Q}}{Y_T \xi} \right),
\end{aligned} \tag{3.93}$$

and substituting for u_{37} gives

$$\bar{F} = \frac{h\bar{Q} Y_L p v_T}{v_L Y_T} \left(\frac{1}{1 - p\frac{Z_L}{Z_T}} \right) \left(1 + \frac{G_{37\,37}^{(n)}}{1 - p\frac{Z_L}{Z_T}} - \frac{G_{1\,37}^{(n)}}{1 - p\frac{Z_B}{Z_T}} \right). \tag{3.94}$$

This can be simplified by setting

$$K_\eta^{(n)} = \left(\frac{1}{1 - p\frac{Z_L}{Z_T}} \right) \left(1 + \frac{G_{37\,37}^{(n)}}{1 - p\frac{Z_L}{Z_T}} - \frac{G_{1\,37}^{(n)}}{1 - p\frac{Z_B}{Z_T}} \right), \tag{3.95}$$

and hence,

$$\bar{F} = \frac{h\bar{Q} Y_L p v_T K_\eta^{(n)}}{v_L Y_T}. \tag{3.96}$$

In equations (3.93) - (3.96) the parameters used correspond to model η thus, the expression for the output force for any given model is given by

$$\bar{F} = \frac{h\bar{Q} Y_L p v_T K_i^{(n)}}{v_L Y_T}, \tag{3.97}$$

where

$$K_\delta^{(n)} = \left(\frac{1}{1 - p\frac{Z_L}{Z_T}} \right) \left(1 + \frac{G_{19\,19}^{(n)} + G_{19\,55}^{(n)}}{1 - p\frac{Z_L}{Z_T}} - \frac{G_{1\,19}^{(n)}}{1 - p\frac{Z_B}{Z_T}} \right), \tag{3.98}$$

and

$$K_\gamma^{(n)} = \left(\frac{1}{1 - p\frac{Z_L}{Z_T}} \right) \left(1 + \frac{G_{19\,19}^{(n)} + G_{19\,37}^{(n)} + G_{19\,55}^{(n)}}{1 - p\frac{Z_L}{Z_T}} - \frac{G_{1\,19}^{(n)}}{1 - p\frac{Z_B}{Z_T}} \right), \qquad (3.99)$$

correspond to models δ and γ respectively. Since both the input voltage and output force have been derived, an expression for the transmission sensitivity is given by

$$\frac{\bar{F}}{\bar{V}} = \frac{hY_L v_T Z_T a K_i^{(n)}}{v_L Y_T^2 \xi(\bar{Z}_i + b)} = \frac{haZ_L K_i^{(n)}}{Y_T \xi(\bar{Z}_i + b)}. \qquad (3.100)$$

For this device the non-dimensionalized transmission sensitivity is given by

$$\psi_i = \frac{\bar{F}}{\bar{V}hC_0} = \frac{aZ_L K_i^{(n)}}{Y_T \xi C_0(\bar{Z}_i + b)}. \qquad (3.101)$$

3.5.2 Reception Sensitivity

In reception mode, the piezoelectric material converts mechanical energy into electrical energy through the contact of sound waves resulting in the production of an electrical signal [51, 88, 114]. The front face of the transducer will be subjected to external forces when in receiving mode, hence $\alpha_L \neq 0$. The expression for amplitude of the forward propagating wave can be obtained using equation (3.50) and applying continuity of force at the load to get

$$\bar{F} = \bar{F}_L = A_r Y_L \left(\frac{pv_T}{\Delta x v_L} \right)(-\alpha_L + \beta_L), \qquad (3.102)$$

setting $\beta_L = 0$ gives

$$\bar{F} = Y_L \xi p \left(\frac{v_T}{v_L} \right)(-\alpha_L),$$
$$\alpha_L = -\frac{Fv_L}{pY_L \xi v_T}. \qquad (3.103)$$

Substituting this into equation (3.69) gives an expression for the electrical impedance as

$$\bar{Z}_i = \frac{Z_T}{pC_0 Y_T \xi} \left(1 + \frac{h^2 C_0(\mu_i + \nu_i)}{Y_T \xi} + \frac{2hC_0 \mu_i Z_L \bar{F} v_L}{v_T \bar{Q} Z_T Y_L \xi} \right). \qquad (3.104)$$

Since $Z = V/I$ and using equation (3.66) the voltage may expressed as

$$
\begin{aligned}
\bar{V} &= \frac{\bar{Q}}{C_0} + \frac{h^2\bar{Q}(\mu_i + \nu_i)}{Y_T\xi} + \frac{2h\mu_i Z_L F v_L}{v_T Z_T Y_L \xi} \\
&= \frac{\bar{Q}}{C_0} + \frac{h^2\bar{Q}(\mu_i + \nu_i)}{Y_T\xi} + \frac{2h\mu_i A_r F}{v_T Z_T \xi}.
\end{aligned}
\tag{3.105}
$$

Equation (3.90) can then be rearranged to give an expression for the charge as

$$
\bar{Q} = \frac{a Z_T \bar{V}}{p Y_T \xi (\bar{Z}_i + b)}.
\tag{3.106}
$$

Using equations (3.105) and (3.106) gives the voltage as

$$
\begin{aligned}
\bar{V} &= \frac{2h\mu_i A_r \bar{F}}{v_T Z_T \xi \left(1 - \frac{aZ_T}{pC_0 Y_T \xi(\bar{Z}_i+b)} - \frac{h^2(\mu_i+\nu_i)aZ_T}{p(Y_T\xi)^2(\bar{Z}_i+b)} \right)} \\
&= \frac{2h\mu_i \bar{F}}{Y_T\xi \left(1 - \frac{aZ_T}{pC_0 Y_T\xi(\bar{Z}_i+b)} \left(1 + \frac{h^2 C_0(\mu_i+\nu_i)}{Y_T\xi} \right) \right)}.
\end{aligned}
\tag{3.107}
$$

Thus, an expression for the reception sensitivity is given by

$$
\frac{\bar{V}}{\bar{F}} = \frac{2h\mu_i}{Y_T\xi \left(1 - \frac{aZ_T}{pC_0 Y_T\xi(\bar{Z}_i+b)} \left(1 + \frac{h^2 C_0(\mu_i+\nu_i)}{Y_T\xi} \right) \right)},
\tag{3.108}
$$

where again i will be substituted accordingly for each model. A description for the non-dimensionalized reception sensitivity is then given by

$$
\phi_i = \frac{\bar{V} h C_0}{\bar{F}} = \frac{2h^2 C_0 \mu_i}{Y_T\xi \left(1 - \frac{aZ_T}{pC_0 Y_T\xi(\bar{Z}_i+b)} \left(1 + \frac{h^2 C_0(\mu_i+\nu_i)}{Y_T\xi} \right) \right)}.
\tag{3.109}
$$

Equations (3.101) and (3.109) are similar to those found previously in Chapter 2 for the Sierpinski gasket inspired device. The only differences being in regards to the μ and ν terms, which account for the Green function elements. With the re-derivation of the relevant operating characteristics now determined, computer simulation models can be utilised in order to determine the possible benefits of a transducer based on the design of the Sierpinski carpet. The electrical impedance, transmission and reception sensitivities for each of the models are presented in the following section.

3.6 Computer Simulation Results

To minimise time and costs involved in manufacturing new ultrasonic transducers, mathematical computer models are employed to test the performances of hypothetical designs. These models can give an insight as to what benefit, if any, can be achieved from altering current designs or can suggest the most effective configuration of new designs. In regards to a Sierpinski carpet-like transducer it is only realistically viable to consider the lower generation levels when it comes to potential manufacture. Incrementing the fractal generation level increases the complexity of the transducer model, and it is for this reason that constructing higher generation levels would currently prove to be infeasible. The work presented in this chapter allows for comparison of the three Sierpinski carpet models with the Sierpinski gasket and Euclidean transducers, where the ceramic properties are modelled on a PZT-5H ceramic and each device has a ceramic volume fraction of $v_f = 1$. This section details the results attained through the computer simulations for each of the three transducer models.

3.6.1 Model η: Single Output Vertex

To recap, model η is the simplest of the three transducer models in regards to the number of boundary vertices it incorporates. This model will interact with electrical loads at vertex A and mechanical loads at vertex C (which is the fictitious vertex placed at node u_{37}); see Figure 3.3 (a).

Figure 3.6 shows the comparison for the electrical impedance between the standard (Euclidean) device, and the Sierpinski gasket and Sierpinski carpet devices at generation level one. To recap, in regards to the electrical impedance, the device is considered most efficient when it transmits at the electrical resonant frequency and receives at the mechanical resonant frequency. These are located at the first minimum and first maximum in the plot respectively. Thus, using this approach the location of the electrical resonant frequency for the carpet device is at $0.945\,\mathrm{MHz}$ with an electrical impedance of $-3.534\,\mathrm{dB}$ and the location of the
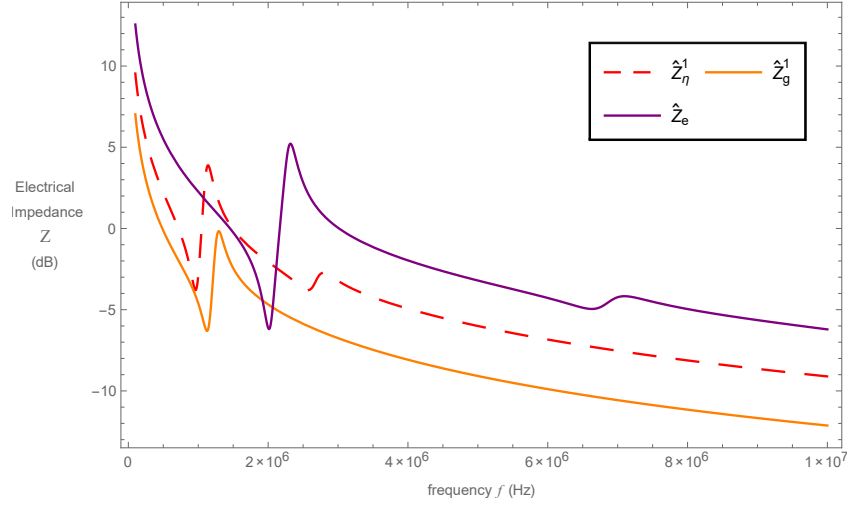
Figure 3.6: Non-dimensionalised electrical impedance $\hat{Z}$ (dB) versus frequency f (Hz) for the Sierpinski carpet model η ($\hat{Z}_\eta^1$ red dashed line, equation (3.70)) and Sierpinski gasket ($\hat{Z}_g^1$ orange full line, equation (2.162)) fractal inspired transducers at generation $n = 1$ and the traditional Euclidean transducer ($\hat{Z}_e$ purple full line, equation (2.45)).

mechanical resonant frequency is at 1.039 MHz with an electrical impedance of 3.687 dB. In comparison to the standard and gasket devices, it can be noted that the carpet transducer follows a similar trend and resonates at lower frequencies. Additionally, it may be noted that the Sierpinski gasket device has fewer resonances in comparison to the other devices, suggesting that at fractal generation level $n = 1$, the gasket transducer has only one length scale; hence the presence of a single resonance. In the case of the Sierpinski gasket the location of the electrical resonant frequency is at 1.027 MHz with an electrical impedance of -6.306 dB and the location of the mechanical resonant frequency is at 1.195 MHz with an electrical impedance of -0.166 dB. The standard device has its electrical resonant frequency at 2.063 MHz with an electrical impedance of -6.191 dB and the location of the mechanical resonant frequency is at 2.220 MHz with an electrical impedance of 5.218 dB. For each generation level considered, the electrical and mechanical resonant frequencies, together with the corresponding electrical impedances, for the three Sierpinski carpet models are further tabulated in Appendix C.

89

Figure 3.7: Non-dimensionalised transmission sensitivity ψ (dB) versus frequency f (Hz) for the Sierpinski carpet model η (ψ_η^1 red dashed line, equation (3.101)) and Sierpinski gasket (ψ_g^1 orange full line, equation (2.169)) fractal inspired transducers at generation $n = 1$ and the traditional Euclidean transducer (ψ_e purple full line, equation (2.54)).

Figure 3.7 illustrates the comparison in transmission sensitivity for the Sierpinski carpet model η device against the standard and Sierpinski gasket ($n = 1$) devices. Two important parameters when studying the transmitting and receiving capabilities of any ultrasonic transducer are the 3-dB bandwidth and maximum amplitude (gain). To be an efficient transmitter and/or receiver of ultrasound it is necessary for the transducer to have high amplitude and a wide bandwidth [16, 24, 36]. It was previously mentioned in earlier chapters that the effectiveness of a transducer can be determined by calculating its gain bandwidth product. The gain bandwidth product, in this chapter, is used as the principle figure of merit to establish the optimal device. To distinguish between fractal generation levels, a superscript is attached to each figure of merit. Likewise a subscript e, g, η, δ and γ will denote the Euclidean, Sierpinski gasket and Sierpinski carpet model devices, respectively. By examining Figure 3.7 it is evident that the transmission sensitivity for the carpet device has greater maximum amplitude, $G_\eta^1 = 1.218$ dB, in comparison to the other two devices. Furthermore this peak

90

is achieved at a frequency of 0.945 MHz. While the gasket device has maximum amplitude $G_g^1 = -5.517\,\text{dB}$ at a frequency of 1.027 MHz and the standard device has $G_e = -1.414\,\text{dB}$ at a frequency of 2.063 MHz. The limitation, however, to the carpet device is its 3-dB bandwidth. This was calculated at $BW_\eta^1 = 0.041\,\text{MHz}$, whereas the gasket was estimated at $BW_g^1 = 0.077\,\text{MHz}$ and the standard device was $BW_e = 0.259$ MHz. Thus, it may be established that the standard device in this case is more capable at operating over a larger range of frequencies. In the same way it is the standard device which has the highest value for the gain bandwidth product and the gasket device in this instance has the lowest value. The values for the figures of merit in both transmitting and receiving mode, for each Sierpinski carpet model, are also presented in Appendix C. The standard and Sierpinski gasket inspired transducer values were previously tabulated in Tables 2.3, 2.9 and 2.10.
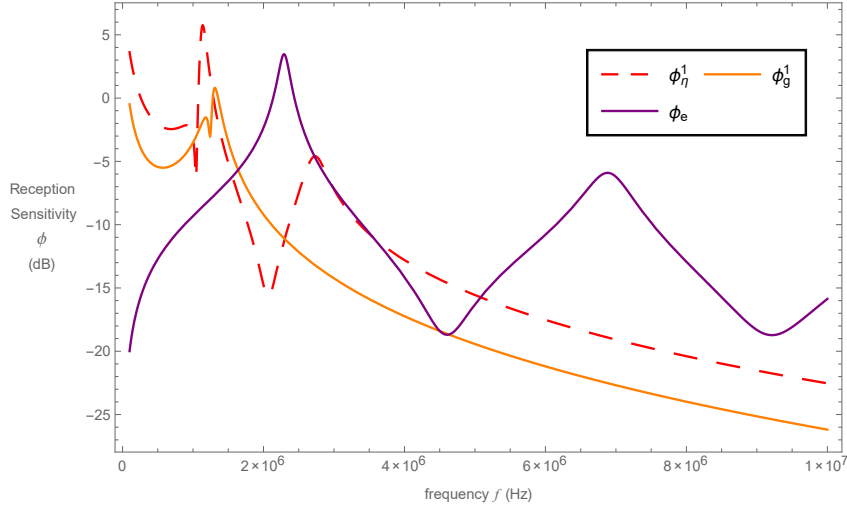
Figure 3.8: Non-dimensionalised reception sensitivity $\phi\,(\text{dB})$ versus frequency $f\,(\text{Hz})$ for the Sierpinski carpet model η (ϕ_η^1 red dashed line, equation (3.109)) and Sierpinski gasket (ϕ_g^1 orange full line, equation (2.173)) fractal inspired transducers at generation $n = 1$ and the traditional Euclidean transducer (ϕ_e purple full line, equation (2.58)).

Figure 3.8 is the comparison plot of the reception sensitivities for the carpet device against the gasket device at the same generation level and the standard

device. The reception sensitivity has a maximum amplitude $G_\eta^1 = 5.751\,\text{dB}$ at a frequency of $1.039\,\text{MHz}$, in a similar manner to the transmission sensitivity this again is higher than both the gasket, $G_g^1 = 0.807\,\text{dB}$ at $1.195\,\text{MHz}$ and the standard device, $G_e = 3.463\,\text{dB}$ at $2.220\,\text{MHz}$. In this instance it is the gasket device which outperforms both the carpet and standard device in terms of its bandwidth, which has been calculated at $BW_g^1 = 0.331\,\text{MHz}$. The carpet model has the smallest bandwidth in comparison and was calculated at $BW_\eta^1 = 0.126\,\text{MHz}$, and for the standard device was calculated at $BW_e = 0.263\,\text{MHz}$. In terms of the gain bandwidth product for each of the devices, the standard device is the greatest at $GBP_e = 0.584$, with the gasket and carpet devices $GBP_g^1 = 0.399$ and $GBP_\eta^1 = 0.473$ respectively. Thus, in regards to device bandwidth it is the gasket device which has the most promising results and that this particular carpet device is the poorest in performance. One way of potentially improving device bandwidth is from the inclusion of two or multiple matching layers [49, 51], as the presence of these layers increases the amount of energy transmitted into the object. There-
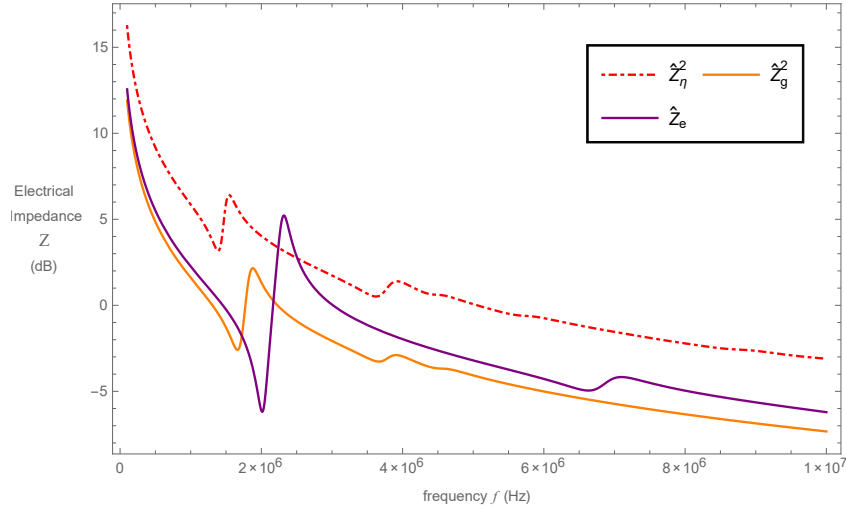
Figure 3.9: Non-dimensionalised electrical impedance $\hat{Z}$ (dB) versus frequency f (Hz) for the Sierpinski carpet model η ($\hat{Z}_\eta^2$ red dot-dashed line, equation (3.70)) and Sierpinski gasket ($\hat{Z}_g^2$ orange full line, equation (2.162)) fractal inspired transducers at generation $n = 2$ and the traditional Euclidean transducer ($\hat{Z}_e$ purple full line, equation (2.45)).

fore, it may be possible to increase the operational bandwidth of the device by the inclusion of these front matching layers.

For generation level two the location of the electrical resonant frequency is at $1.332\,\mathrm{MHz}$ with an electrical impedance of $3.112\,\mathrm{dB}$ and the location of the mechanical resonant frequency is at $1.418\,\mathrm{MHz}$ with an electrical impedance of $6.393\,\mathrm{dB}$. The electrical resonant frequency for the gasket device is $1.564\,\mathrm{MHz}$ with an electrical impedance of $-2.591\,\mathrm{dB}$ and the mechanical resonant frequency is $1.780\,\mathrm{MHz}$ with an electrical impedance of $2.157\,\mathrm{dB}$.
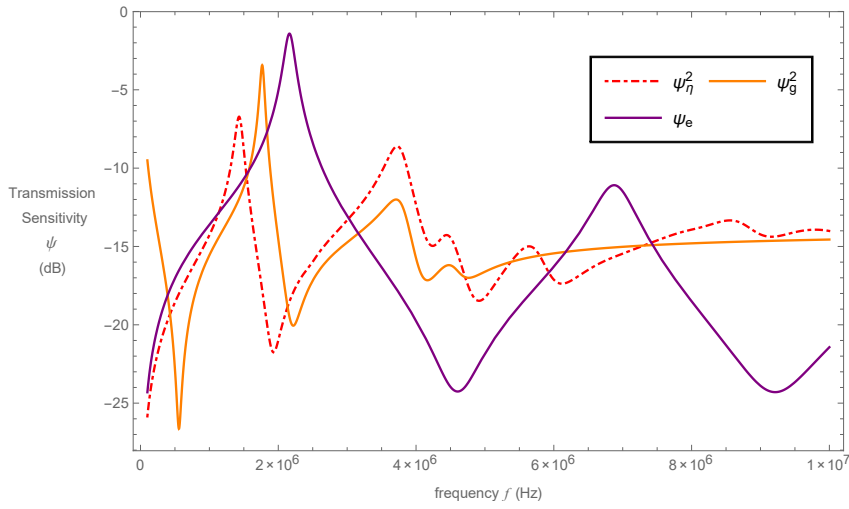
Figure 3.10: Non-dimensionalised transmission sensitivity ψ (dB) versus frequency f (Hz) for the Sierpinski carpet model η (ψ_η^2 red dot-dashed line, equation (3.101)) and Sierpinski gasket (ψ_g^2 orange full line, equation (2.169)) fractal inspired transducers at generation $n = 2$ and the traditional Euclidean transducer (ψ_e purple full line, equation (2.54)).

Figure 3.10 plots the transmission sensitivities for the carpet and gasket devices at $n = 2$ as well as the standard device. The result for the transmission sensitivity for the carpet device at this generation level gives the maximum amplitude $G_\eta^2 = -6.717\,\mathrm{dB}$. Unfortunately this is below both the standard and gasket devices, where the maximum amplitude for the gasket at the same generation level is $G_g^2 = -3.427\,\mathrm{dB}$. The same can be said regarding the device's gain bandwidth product in that the value for this was lower than the gasket and standard devices.

This was calculated as $GBP_\eta^2 = 0.043$, whereas the gasket and standard devices were $GBP_g^2 = 0.052$ and $GBP_e = 0.187$ respectively. However, there is a significant improvement to the transducer's 3-dB bandwidth. This was calculated at $BW_\eta^2 = 0.203\,\mathrm{MHz}$ and for the gasket device was calculated at $BW_g^2 = 0.113\,\mathrm{MHz}$. When comparing the carpet and gasket devices, there is a relatively good match, with the carpet device presenting more resonances. This is to be expected as the carpet device features more complexity in its design, i.e. there is a wider range of length scales.
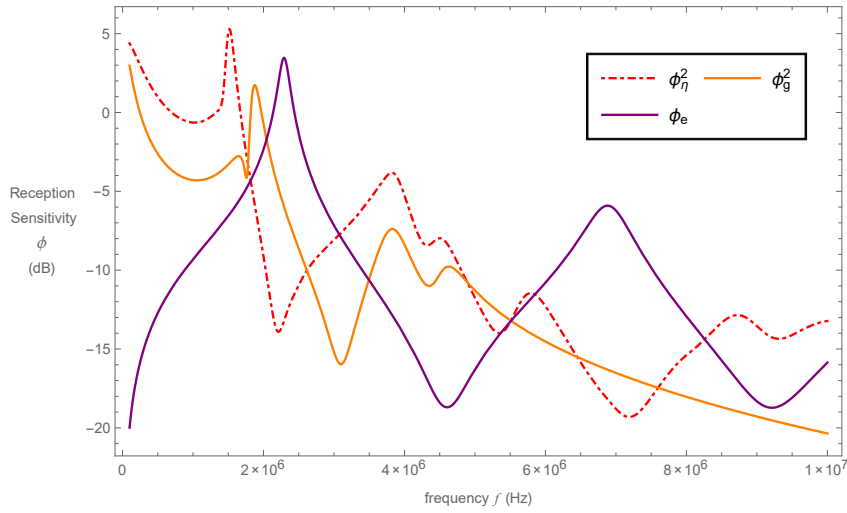
Figure 3.11: Non-dimensionalised reception sensitivity ϕ (dB) versus frequency f (Hz) for the Sierpinski carpet model η (ϕ_η^2 red dot-dashed line, equation (3.109)) and Sierpinski gasket (ϕ_g^2 orange full line, equation (2.173)) fractal inspired transducers at generation $n = 2$ and the traditional Euclidean transducer (ϕ_e purple full line, equation (2.58)).

Figure 3.11 displays the reception sensitivities plotted against operation frequency for the carpet, gasket and standard devices. Looking at this figure, the maximum amplitude for the carpet device at generation level two is $G_\eta^2 = 5.286\,\mathrm{dB}$. This is again higher than that of the standard and gasket devices, where the maximum amplitude for the gasket at the same generation level is $G_g^2 = 1.735\,\mathrm{dB}$. The bandwidths at these peaks were given at $BW_\eta^2 = 0.162\,\mathrm{MHz}$

and $BW_g^2 = 0.220\,\text{MHz}$. In terms of the gain bandwidth product, there is an improvement in this figure of merit when comparing against the Sierpinski gasket, but is lower than that for the standard device. These figures of merit were calculated as $GBP_g^2 = 0.265$, $GBP_\eta^2 = 0.547$ and $GBP_e = 0.584$.

Figure 3.12 plots the electrical impedances for the standard, gasket and carpet devices at generation level three. The electrical resonant frequency was calculated as $1.416\,\text{MHz}$ with an electrical impedance of $9.261\,\text{dB}$ for the carpet device and $1.689\,\text{MHz}$ with an electrical impedance of $1.331\,\text{dB}$ for the gasket device. Similarly the mechanical resonant frequency for the carpet device is $1.456\,\text{MHz}$ with electrical impedance of 10.380 dB and 1.896 MHz with an electrical impedance of $4.990\,\text{dB}$ for the gasket device.
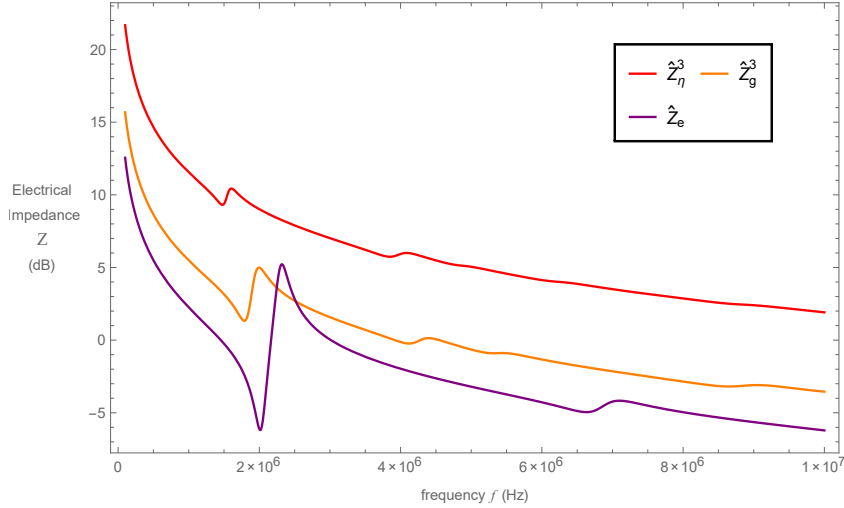
Figure 3.12: Non-dimensionalised electrical impedance $\hat{Z}$ (dB) versus frequency f (Hz) for the Sierpinski carpet model η ($\hat{Z}_\eta^3$ red full line, equation (3.70)) and Sierpinski gasket ($\hat{Z}_g^3$ orange full line, equation (2.162)) fractal inspired transducers at generation $n = 3$ and the traditional Euclidean transducer ($\hat{Z}_e$ purple full line, equation (2.45)).

The transmission sensitivity at this generation has its maximum amplitude $G_\eta^3 = -11.441\,\text{dB}$ with a bandwidth at this peak of $BW_\eta^3 = 0.752\,\text{MHz}$. The gasket's maximum amplitude at this same level is $G_g^3 = -6.166\,\text{dB}$ with a bandwidth of $BW_g^3 = 0.217\,\text{dB}$. It appears that as the generation level is increased the

bandwidth of the device widens but at the expense of the maximum amplitude. The gain bandwidth product of the device was calculated as $GBP_\eta^3 = 0.054$. This is unfortunately considerably less than the gain bandwidth product value of the standard device. Figure 3.13 illustrates the transmission sensitives of the devices at this generation level.
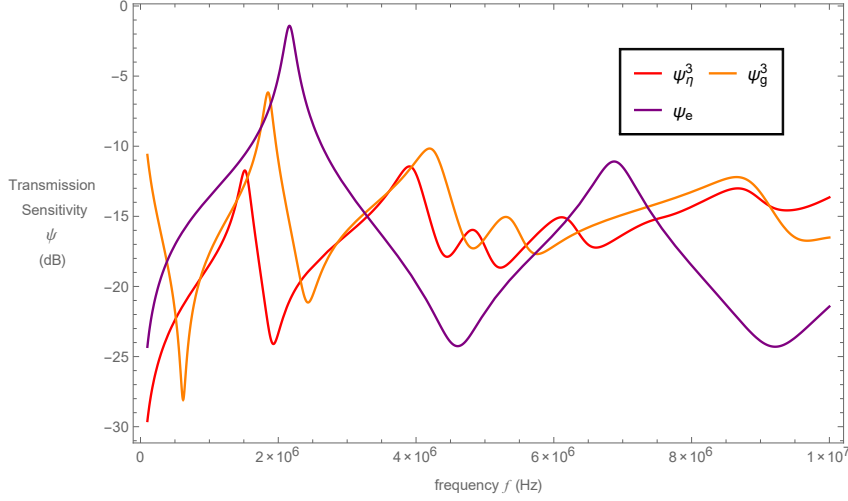
Figure 3.13: Non-dimensionalised transmission sensitivity ψ (dB) versus frequency f (Hz) for the Sierpinski carpet model η (ψ_η^3 red full line, equation (3.101)) and Sierpinski gasket (ψ_g^3 orange full line, equation (2.169)) fractal inspired transducers at generation $n = 3$ and the traditional Euclidean transducer (ψ_e purple full line, equation (2.54)).

There are much more encouraging results when studying the reception sensitivity of the carpet device at generation level three. From Figure 3.14 the gain bandwidth product, maximum amplitude and the 3-dB bandwidth at this peak were obtained. These were given as $GBP_\eta^3 = 0.917$, $G_\eta^3 = 5.723\,\mathrm{dB}$ and $BW_\eta^3 = 0.246\,\mathrm{MHz}$. At this fractal generation level the Sierpinski carpet device surpasses the Sierpinski gasket transducer in all three metrics. Furthermore there is a substantial improvement in terms of the maximum amplitude and gain bandwidth product over standard designs, where this value has increased by 65% and 57% respectively. The gasket device had a calculated gain bandwidth product of $GBP_g^3 = 0.547$, maximum amplitude $G_g^3 = 4.098\,\mathrm{dB}$ and 3-bandwidth

$BW_g^3 = 0.213\,\text{MHz}$. From these results it can be deduced that higher fractal generation levels would improve even further.
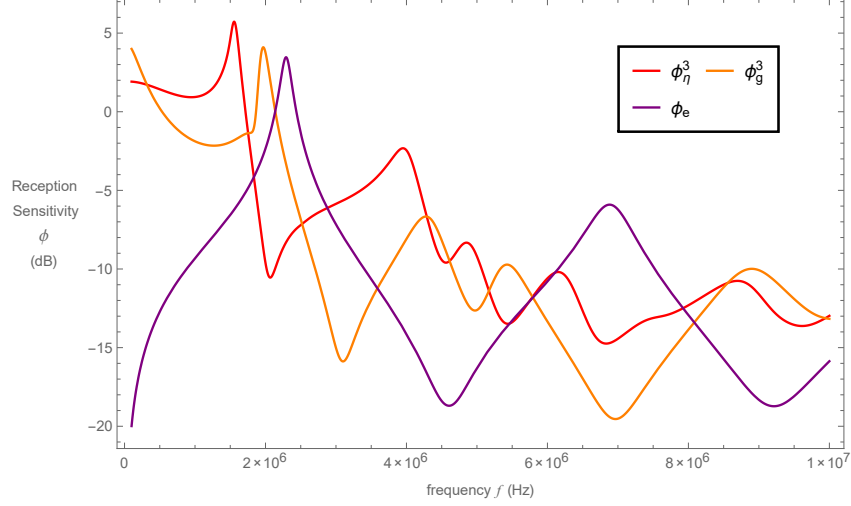
Figure 3.14: Non-dimensionalised reception sensitivity ϕ (dB) versus frequency f (Hz) for the Sierpinski carpet model η (ϕ_η^3 red full line, equation (3.109)) and Sierpinski gasket (ϕ_g^3 orange full line, equation (2.173)) fractal inspired transducers at generation $n = 3$ and the traditional Euclidean transducer (ϕ_e purple full line, equation (2.58)).

Figures 3.15 to 3.17 show the comparisons between fractal generation levels for each of the operating characteristics of interest. In Figure 3.15 there is a notable increase in magnitude of the electrical impedance as the generation level is increased. This is likely due to a reduction in size of the length scales and by referring back to Figure 3.2, it is clear to see the length between adjacent vertices will decrease as the fractal generation level increases.

In terms of the transmission and reception sensitivities, Figures 3.16 and 3.17 suggest higher fractal generation will result in much lower amplitudes. Nevertheless, this generally results in an increased bandwidth allowing the transducer to perform more efficiently over a larger range of frequencies. Furthermore, an increase in the gain bandwidth product is evident in the potential transducer's receiving mode. This also appears to be the case in transmission mode, although analysis of higher fractal generation levels would be required to back up this claim.

Thus, it may be assumed that if the fractal generation level was increased further still, the operational bandwidth of the device would only improve.

Figure 3.15: Non-dimensionalised electrical impedance $\hat{Z}$ (dB) (equation (3.70)) versus frequency f (Hz) for the Sierpinski carpet model η transducer at fractal generation levels one ($\hat{Z}_\eta^1$ dashed line), two ($\hat{Z}_\eta^2$ dot-dashed line) and three ($\hat{Z}_\eta^3$ full line).
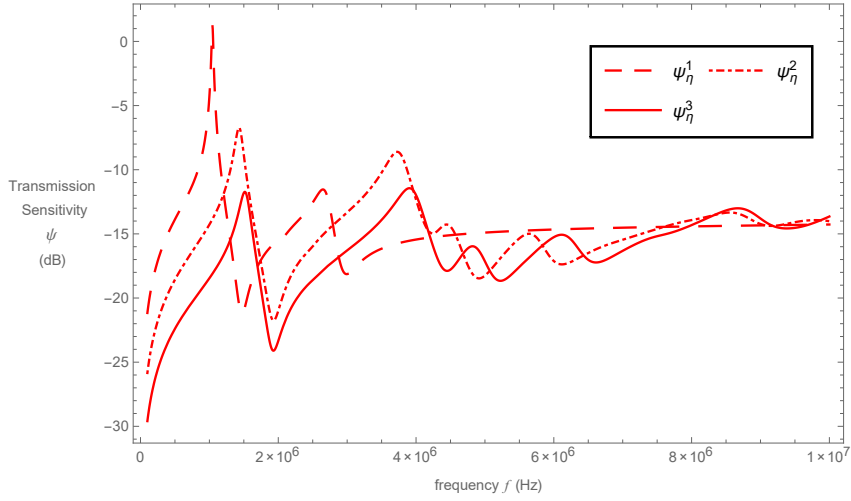
Figure 3.16: Non-dimensionalised transmission sensitivity ψ (dB) (equation (3.101)) versus frequency f (Hz) for the Sierpinski carpet model η transducer at fractal generation levels one (ψ_η^1 dashed line), two (ψ_η^2 dot-dashed line) and three (ψ_η^3 full line).
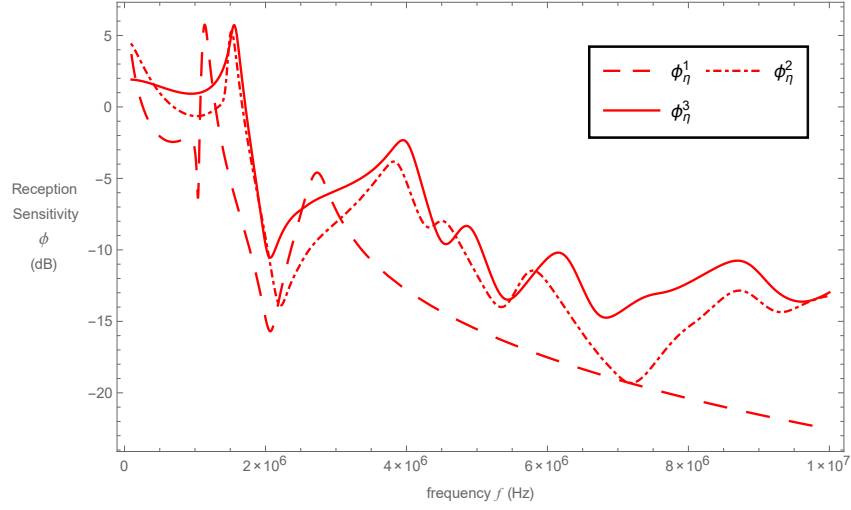
Figure 3.17: Non-dimensionalised reception sensitivity ϕ (dB) (equation (3.109)) versus frequency f (Hz) for the Sierpinski carpet model η transducer at fractal generation levels one (ϕ_η^1 dashed line), two (ϕ_η^2 dot-dashed line) and three (ϕ_η^3 full line).

In general the carpet device displays more resonances in the same frequency range when comparing against the gasket and standard devices. This is to be expected due to a greater range of length scales present in the carpet device. With the exception of the first fractal generation level, the carpet device outperforms the gasket and standard devices in terms of its bandwidth when acting as a transmitter of ultrasound. In the case of reception mode, it is only when the carpet device is at its third fractal generation level that an improvement in the bandwidth is achieved.

3.6.2 Model δ: Two Symmetric Output Vertices

Model δ refers to the device incorporating three boundary conditions where there is a single input vertex placed at site A and two symmetric output vertices positioned at sites B and D; see Figure 3.3 (b). Continuing in the same procedure as model η, a discussion of the theoretical transducer's operating characteristics is presented below.

99

Figure 3.18 illustrates the electrical impedance at generation level one for carpet model δ device with comparison to the gasket device at the same generation level and the standard device. In the case of this model the electrical resonant frequency is $0.995\,\mathrm{MHz}$ with an electrical impedance of $-1.431\,\mathrm{dB}$ and the mechanical resonant frequency is $1.153\,\mathrm{MHz}$ with an electrical impedance of $0.835\,\mathrm{dB}$.

Figure 3.18: Non-dimensionalised electrical impedance $\hat{Z}$ (dB) versus frequency f (Hz) for the Sierpinski carpet model δ ($\hat{Z}_\delta^1$ blue dashed line, equation (3.76)) and Sierpinski gasket ($\hat{Z}_g^1$ orange full line, equation (2.162)) fractal inspired transducers at generation $n = 1$ and the traditional Euclidean transducer ($\hat{Z}_e$ purple full line, equation (2.45)).

The transmission sensitivities for each device are shown in Figure 3.19. The maximum amplitude for the carpet model δ device is $G_\delta^1 = -6.986\,\mathrm{dB}$ with a 3-dB bandwidth at this peak of $BW_\delta^1 = 0.273\,\mathrm{MHz}$ and a gain bandwidth product of $GBP_\delta^1 = 0.055$. The bandwidth is larger than that of both the Sierpinski gasket and standard devices. In particular there is more than a 3-fold increase over the Sierpinski gasket pre-fractal device at the same fractal generation level. This significant increase in bandwidth indicates that the Sierpinski carpet pre-fractal device is more efficient at operating over a larger range of frequencies when acting as a transmitter of ultrasound. This gives motive to explore a prototype of a Sierpinski carpet-like transducer.

100
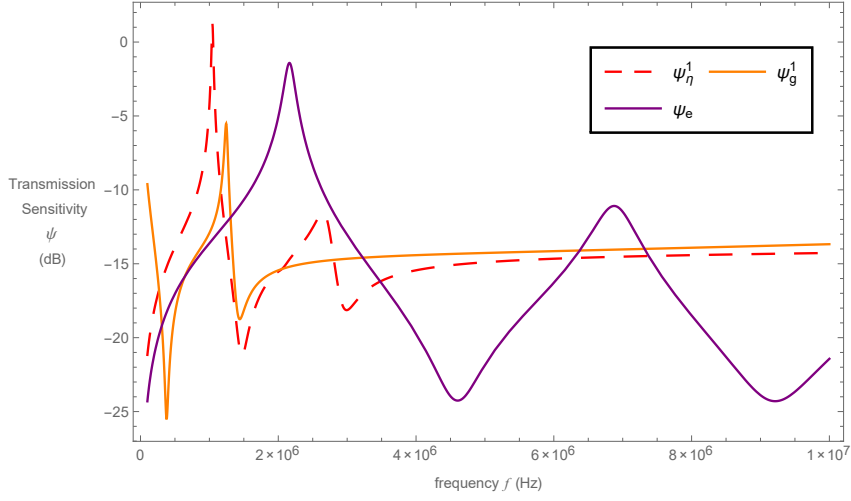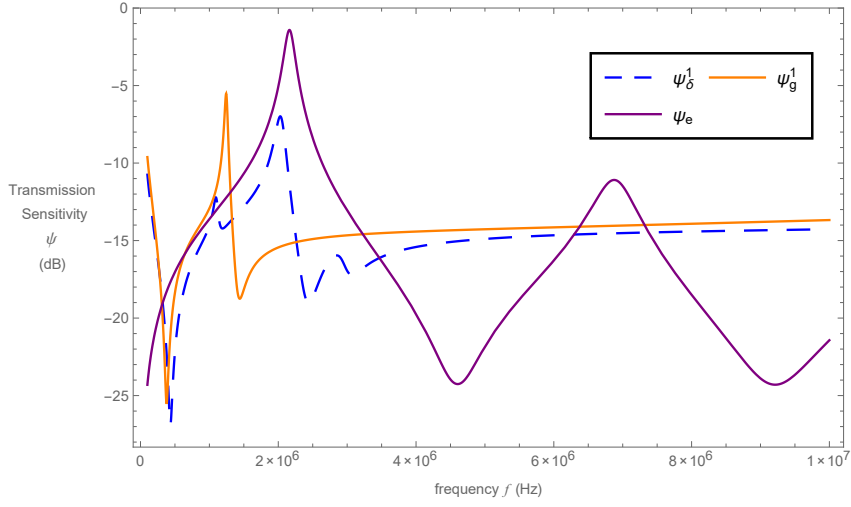
Figure 3.19: Non-dimensionalised transmission sensitivity ψ (dB) versus frequency f (Hz) for the Sierpinski carpet model δ (ψ_δ^1 blue dashed line, equation (3.101)) and Sierpinski gasket (ψ_g^1 orange full line, equation (2.169)) fractal inspired transducers at generation $n = 1$ and the traditional Euclidean transducer (ψ_e purple full line, equation (2.54)).

Figure 3.20: Non-dimensionalised reception sensitivity ϕ (dB) versus frequency f (Hz) for the Sierpinski carpet model δ (ϕ_δ^1 blue dashed line, equation (3.109)) and Sierpinski gasket (ϕ_g^1 orange full line, equation (2.173)) fractal inspired transducers at generation $n = 1$ and the traditional Euclidean transducer (ϕ_e purple full line, equation (2.58)).

101

In Figure 3.20 the reception sensitivities are plotted as a function of operation frequency. From this the maximum amplitude for the carpet device is $G_\delta^1 = -0.182\,\text{dB}$. Although lower than both the comparative devices it achieves a substantial increase in terms of its bandwidth at its resonant frequency; $BW_\delta^1 = 0.553\,\text{MHz}$. Furthermore there is a 33% increase in its gain bandwidth product when comparing against the previously investigated Sierpinski gasket inspired transducer.

In Figure 3.21 the electrical impedance of model δ at generation level two is plotted as a comparison against the gasket at the same fractal generation level and the standard device. From this the electrical resonant frequency is $2.301\,\text{MHz}$ with an electrical impedance of $4.200\,\text{dB}$ and the mechanical resonant frequency is $2.401\,\text{MHz}$ with an electrical impedance of $4.853\,\text{dB}$.
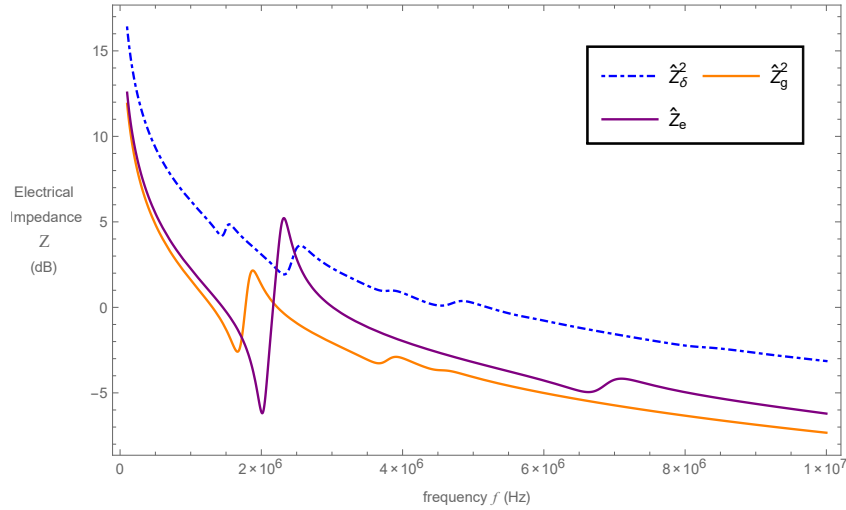
Figure 3.21: Non-dimensionalised electrical impedance $\hat{Z}$ (dB) versus frequency f (Hz) for the Sierpinski carpet model δ ($\hat{Z}_\delta^2$ blue dot-dashed line, equation (3.76)) and Sierpinski gasket ($\hat{Z}_g^2$ orange full line, equation (2.162)) fractal inspired transducers at generation $n = 2$ and the traditional Euclidean transducer ($\hat{Z}_e$ purple full line, equation (2.45)).

Figure 3.22 shows the transmission sensitivities plotted against the operating frequency. From this plot the maximum amplitude for the carpet device is $G_\delta^2 = -7.525\,\text{dB}$ with a 3-dB bandwidth range of $BW_\delta^2 = 0.381\,\text{MHz}$. This gives

a percentage bandwidth of 46%, while the percentage bandwidth for the gasket and standard devices are 12% and 13% respectively. This clearly shows a sizable improvement in regards to the device's bandwidth when comparing against the Euclidean transducer and the experimental Sierpinski triangle prototype. This presents a remarkable improvement on device operating performance when comparing against the other two devices. For this reason, fabricating a prototype
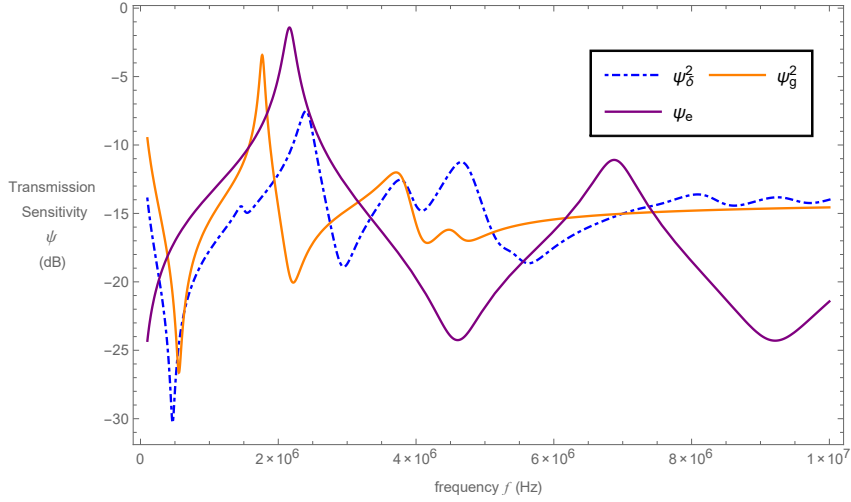
Figure 3.22: Non-dimensionalised transmission sensitivity ψ (dB) versus frequency f (Hz) for the Sierpinski carpet model δ (ψ_δ^2 blue dot-dashed line, equation (3.101)) and Sierpinski gasket (ψ_g^2 orange full line, equation (2.169)) fractal inspired transducers at generation $n = 2$ and the traditional Euclidean transducer (ψ_e purple full line, equation (2.54)).

based the configuration of model δ for the Sierpinski carpet would be worthwhile, and in doing so it could possibly verify this hypothetical conclusion. Another relevant measure is in regards to the gain bandwidth product. This was found to be $GBP_\delta^2 = 0.067$, which is greater than that for the gasket device, but is still less than for the standard device.

Figure 3.23 shows the reception sensitivity against frequency for the carpet and gasket devices at generation level two, as well as the standard device. Comparison of the maximum amplitude shows that the carpet device has the lowest amplitude of $G_\delta^2 = 1.226$ dB. The 3-dB bandwidth for the carpet device is $BW_\delta^2 = 0.468$ MHz.
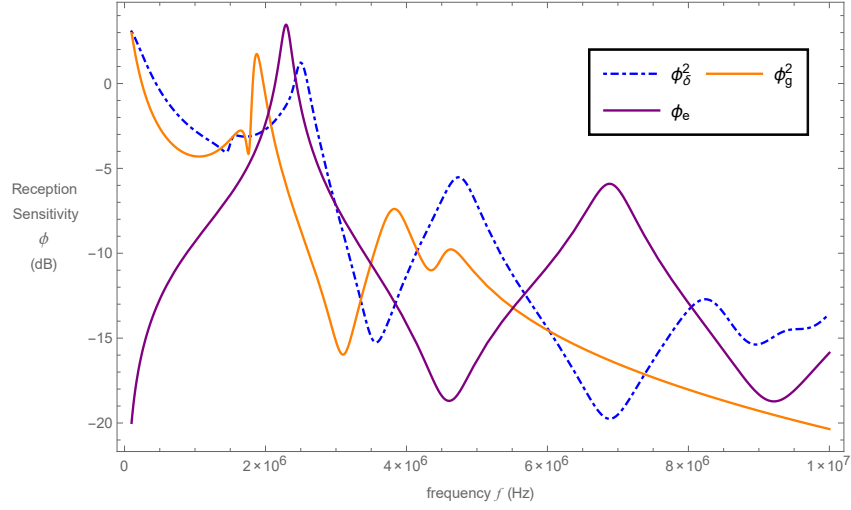
Figure 3.23: Non-dimensionalised reception sensitivity ϕ (dB) versus frequency f (Hz) for the Sierpinski carpet model δ (ϕ_δ^2 blue dot-dashed line, equation (3.109)) and Sierpinski gasket (ϕ_g^2 orange full line, equation (2.173)) fractal inspired transducers at generation $n = 2$ and the traditional Euclidean transducer (ϕ_e purple full line, equation (2.58)).

This is a significant increase over the two devices. The lessened amplitude is a possible reason for the increase in device bandwidth. The principle figure of merit of the carpet model, in receiving mode was calculated as $GBP_\delta^2 = 0.620$, which is more than 2-fold increase against the previously investigated pre-fractal transducer, and a 6% increase against industry used transducers.

In Figure 3.24 the electrical impedances of each of the devices, at generation level three, are plotted. For the carpet device, the electrical resonant frequency is 2.381 MHz with an electrical impedance of 9.718 dB and the mechanical resonant frequency is 2.433 MHz with an electrical impedance of 9.758 dB.

Figure 3.25 plots the comparison in transmission sensitivities for the carpet and gasket devices at the third generation level and the standard device as a function of frequency. Looking at this figure the maximum amplitude for the carpet device is at 2.381 MHz with $G_\delta^3 = -11.558$ dB. The 3-dB bandwidth at this peak is $BW_\delta^3 = 0.467$ MHz, which is a significant improvement from the other two devices. Its negative amplitude however, is somewhat discouraging and it

is considerably lower than its comparable devices. There are also concerns over the value of its principle figure of merit, as there is a significant drop in value, $GBP_\delta^3 = 0.033$, from its previous fractal generation levels. Additionally, it is much lower than the values of the gasket and standard devices. Yet this could simply be an anomaly in its third fractal generation level. This suggests a need to compute higher fractal generation level results.
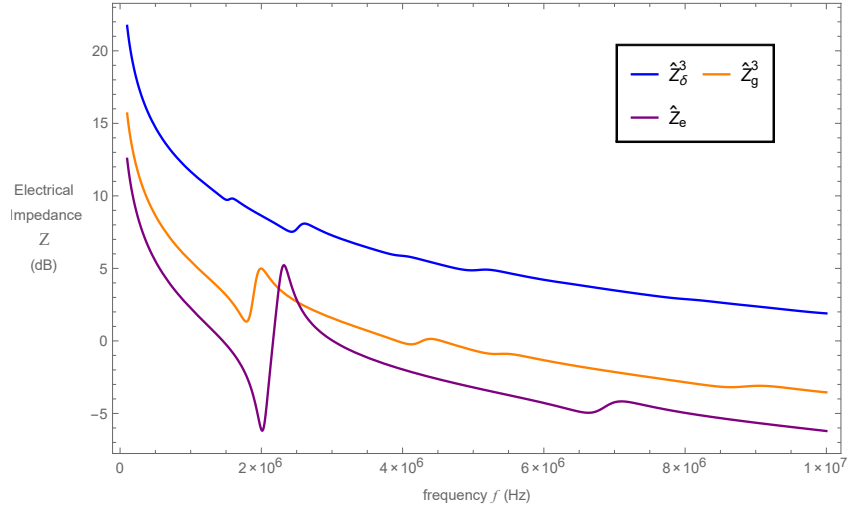
Figure 3.24: Non-dimensionalised electrical impedance $\hat{Z}$ (dB) versus frequency f (Hz) for the Sierpinski carpet model δ ($\hat{Z}_\delta^3$ blue full line, equation (3.76)) and Sierpinski gasket ($\hat{Z}_g^3$ orange full line, equation (2.162)) fractal inspired transducers at generation $n = 3$ and the traditional Euclidean transducer ($\hat{Z}_e$ purple full line, equation (2.45)).

In Figure 3.26 the reception sensitivities of the devices are plotted as a function of the operating frequency. From this plot, the maximum amplitude of the carpet device is at $2.433\,\mathrm{MHz}$ with $G_\delta^3 = 2.660\,\mathrm{dB}$. This gives a decrease in the amplitude of 35% compared to the gasket and a decrease of 23% compared to the standard device. However at this peak, the 3-dB bandwidth is considerably greater than both the standard and gasket devices. Furthermore this increase in bandwidth has resulted in a 75% and 64% increase in the value of the gain bandwidth value over the Sierpinski gasket pre-fractal and Euclidean transducers.
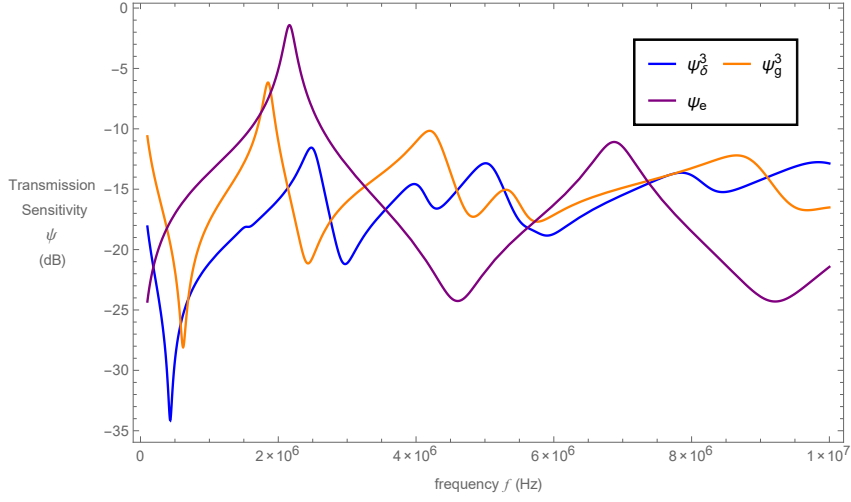
Figure 3.25: Non-dimensionalised transmission sensitivity ψ (dB) versus frequency f (Hz) for the Sierpinski carpet model δ (ψ_δ^3 blue full line, equation (3.101)) and Sierpinski gasket (ψ_g^3 orange full line, equation (2.169)) fractal inspired transducers at generation $n = 3$ and the traditional Euclidean transducer (ψ_e purple full line, equation (2.54)).
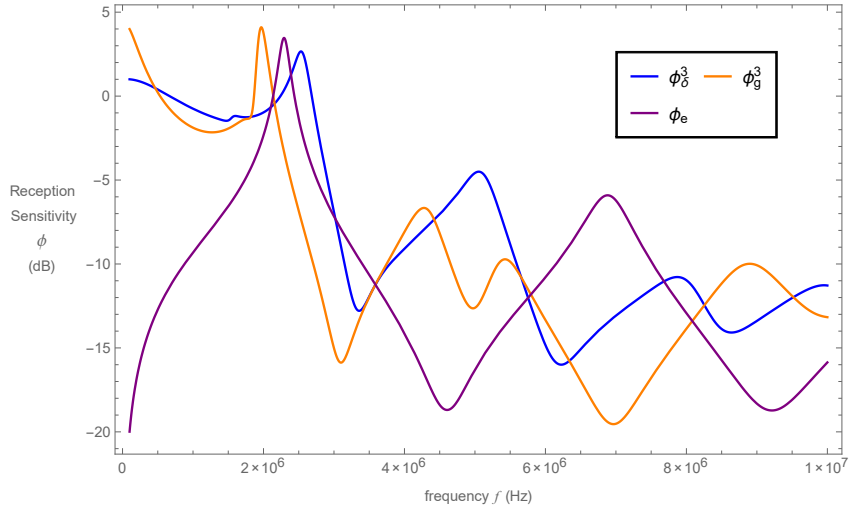
Figure 3.26: Non-dimensionalised reception sensitivity ϕ (dB) versus frequency f (Hz) for the Sierpinski carpet model δ (ϕ_δ^3 blue full line, equation (3.109)) and Sierpinski gasket (ϕ_g^3 orange full line, equation (2.173)) fractal inspired transducers at generation $n = 3$ and the traditional Euclidean transducer (ϕ_g purple full line, equation (2.58)).

Comparison plots between fractal generation levels for each operating characteristic are shown in Figures 3.27, 3.28 and 3.29. In a similar way to model η it was found that by increasing the fractal generation level, higher electrical and mechanical resonant frequencies would occur. This effect can be seen in Figure 3.27. In
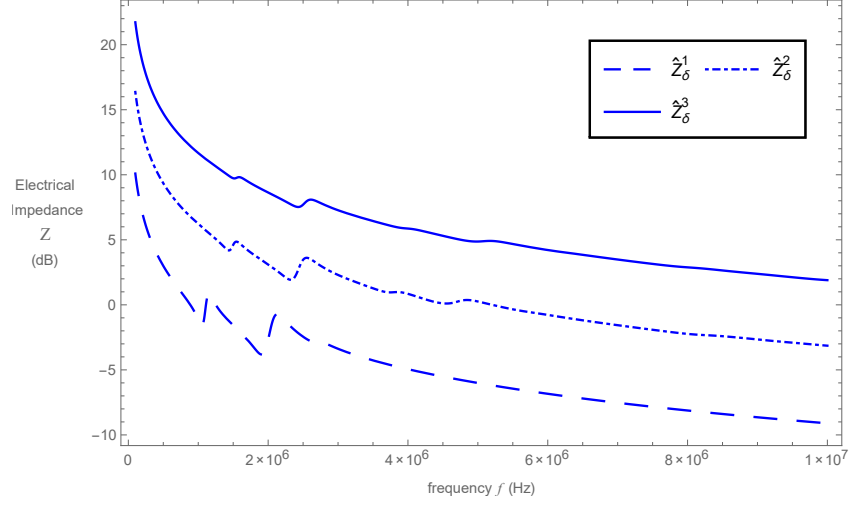
Figure 3.27: Non-dimensionalised electrical impedance $\hat{Z}$ (dB) (equation (3.76)) versus frequency f (Hz) for the Sierpinski carpet model δ transducer at fractal generation levels one ($\hat{Z}_\delta^1$ dashed line), two ($\hat{Z}_\delta^2$ dot-dashed line) and three ($\hat{Z}_\delta^3$ full line).

transmission mode the effect of increasing the fractal generation level resulted in a wider bandwidth. However, this increase in bandwidth consequently resulted in a reduction in the device's amplitude. It would be beneficial to obtain more analysis at higher fractal generation levels to ascertain whether there is usually a compromise between the transducer's bandwidth and peak amplitude. It was assumed that by increasing the fractal generation level, an improvement in the model's gain bandwidth product would be certain. This was the case when increasing the generation level from one to two, but at generation level three the value of this figure of merit fell below the value at generation level one. Again, this highlights the benefits of obtaining results for the higher fractal generation levels, to see the effect on the gain bandwidth product. In contrast to transmission mode, the ef-
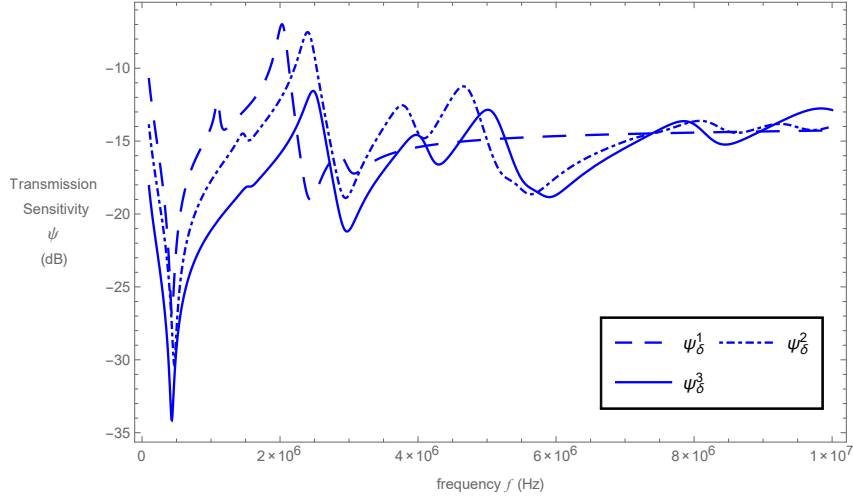
Figure 3.28: Non-dimensionalised transmission sensitivity ψ (dB) (equation (3.101)) versus frequency f (Hz) for the Sierpinski carpet model δ transducer at fractal generation levels one (ψ_δ^1 dashed line), two (ψ_δ^2 dot-dashed line) and three (ψ_δ^3 full line).

fect of increasing the fractal generation level in reception mode resulted with an improvement in the devices maximum amplitude. This consequently reduced the value of the operational bandwidth, at least in terms of the first two fractal generation levels. There was subsequently an increase from generation level two to three, yet this value is still lower than the initial value (fractal generating level one). Although the value of the operational bandwidth decreased with increasing fractal generation level, the opposite happens for the principle figure of merit. Additionally these values were substantially greater than the Sierpinski gasket pre-fractal and Euclidean transducers. However the analysis performed here only reflects on the first three fractal generation levels. It would therefore be worthwhile to study the performance of a Sierpinski carpet-like transducer at higher fractal generation levels. This can then determine what fractal generation level (if any) outperforms the standard and gasket devices in terms of maximum amplitude.

As with model η, the model δ device results demonstrate more resonances than the gasket and standard transducers. Overall it would appear that the carpet device outperforms the standard and gasket devices in transmission and reception

108
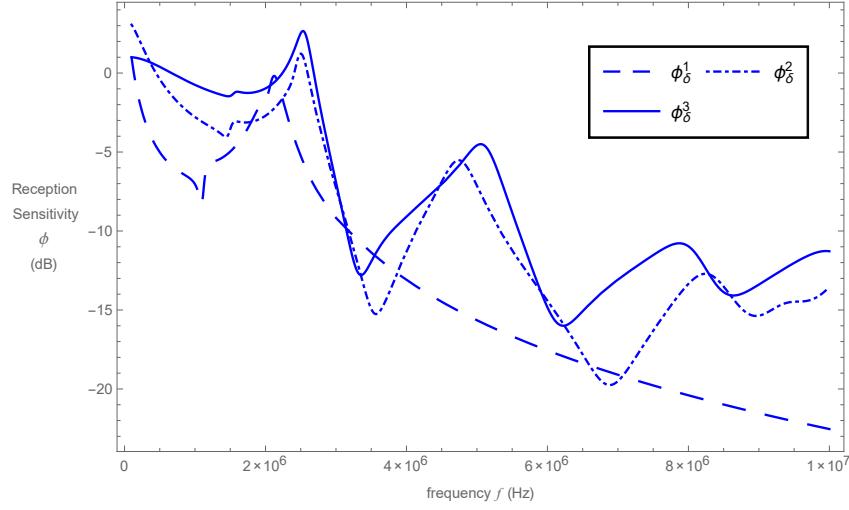
Figure 3.29: Non-dimensionalised reception sensitivity ϕ (dB) (equation (3.109)) versus frequency f (Hz) for the Sierpinski carpet model δ transducer at fractal generation levels one (ϕ_δ^1 dashed line), two (ϕ_δ^2 dot-dashed line) and three (ϕ_δ^3 full line).

mode, when evaluating its operational bandwidth. This is most likely due to an increase in the range of length scales within the Sierpinski carpet's geometry. Furthermore its gain bandwidth product supersedes the previous devices when the transducer is acting as a receiver of ultrasound.

3.6.3 Model γ: Three Output Vertices

Model γ refers to the device having boundary conditions set at each of its four corners. The input vertex is placed at the fictitious site A, and has three output vertices at fictitious sites B, C and D, where B and D are the two symmetric output vertices; see Figure 3.3 (c). This section details the likely performance of a theoretical transducer based on the parameters of model γ.

Figure 3.30 plots the electrical impedance against operating frequency for the carpet model γ device and its comparisons to the gasket and standard devices. There is a good match between all three transducers with further resonances occurring in the carpet device. This is likely due to a wider range of length scales

presented in carpet structure. For the carpet device the electrical resonant frequency is 0.906 MHz with an electrical impedance of -2.517 dB and the mechanical resonant frequency is 1.033 MHz with an electrical impedance of 1.132 dB.
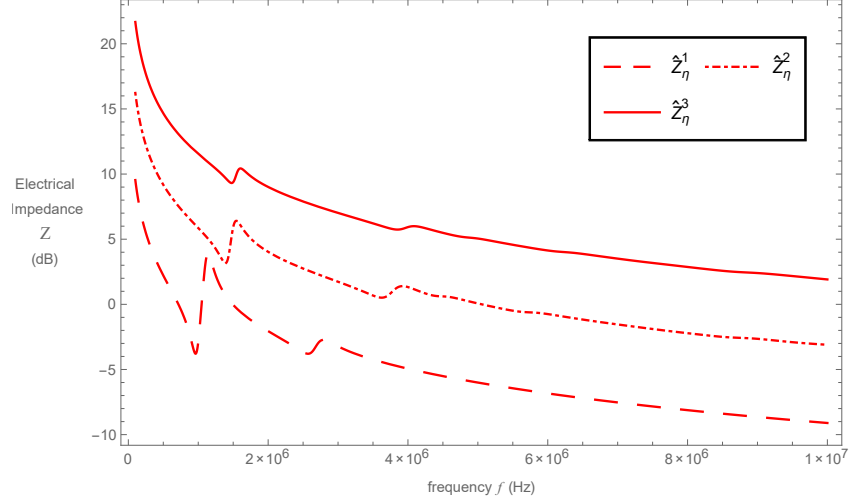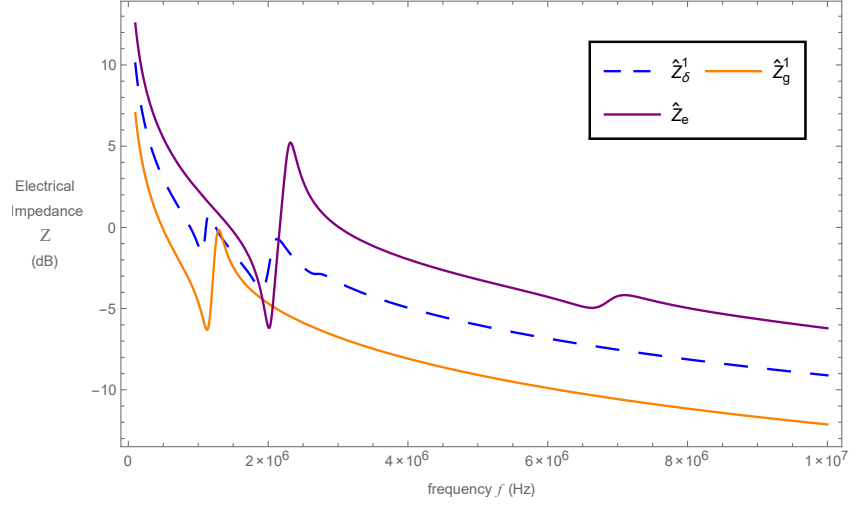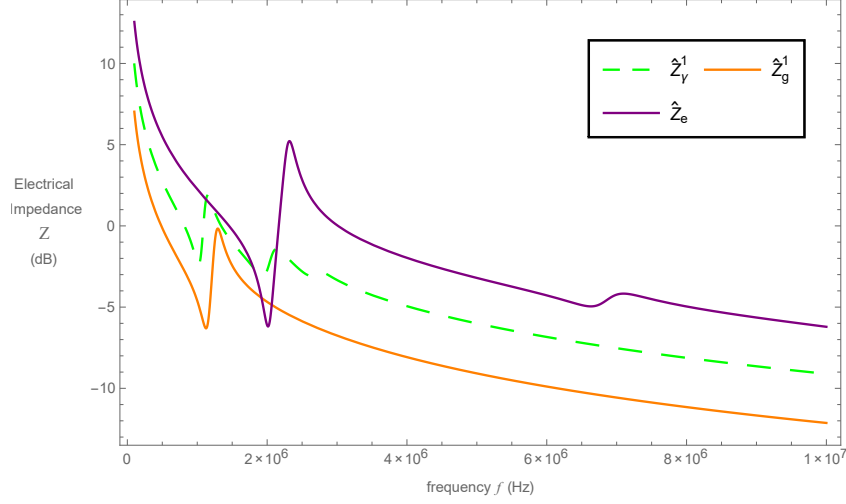

Figure 3.30: Non-dimensionalised electrical impedance $\hat{Z}$ (dB) versus frequency f (Hz) for the Sierpinski carpet model γ ($\hat{Z}_\gamma^1$ green dashed line, equation (3.80)) and Sierpinski gasket ($\hat{Z}_g^1$ orange full line, equation (2.162)) fractal inspired transducers at generation $n = 1$ and the traditional Euclidean transducer ($\hat{Z}_e$ purple full line, equation (2.45)).

Figure 3.31 illustrates that the transmission sensitivity for model γ of the carpet transducer has maximum amplitude of $G_\gamma^1 = -9.621$ dB. This shows a significant decrease in amplitude against the standard transducer, as well as a reduction in amplitude compared to the gasket transducer. However, the bandwidth at this peak is considerably greater than the gasket and standard transducers, and found as $BW_\gamma^1 = 0.424$ MHz. Additionally the gain bandwidth product was $GBP_\gamma^1 = 0.046$ which is more than twice of that of the gasket device.

In regards to the reception sensitivity of the device, Figure 3.32 shows a slight reduction in amplitude against the other two devices, with $G_\gamma^1 = 0.583$ dB. The bandwidth at this peak is $BW_\gamma^1 = 0.130$ MHz. This is a decrease of 61% when comparing against the Sierpinski gasket and a decrease of 50% compared to the standard device. Furthermore, the carpet model was outperformed in terms of

110
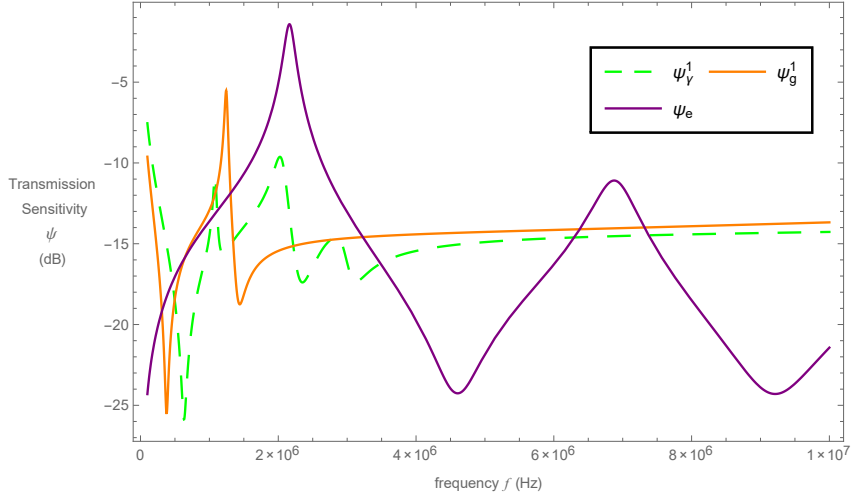
Figure 3.31: Non-dimensionalised transmission sensitivity ψ (dB) versus frequency f (Hz) for the Sierpinski carpet model γ (ψ_γ^1 green dashed line, equation (3.101)) and Sierpinski gasket (ψ_g^1 orange full line, equation (2.169)) fractal inspired transducers at generation $n = 1$ and the traditional Euclidean transducer (ψ_e purple full line, equation (2.54)).
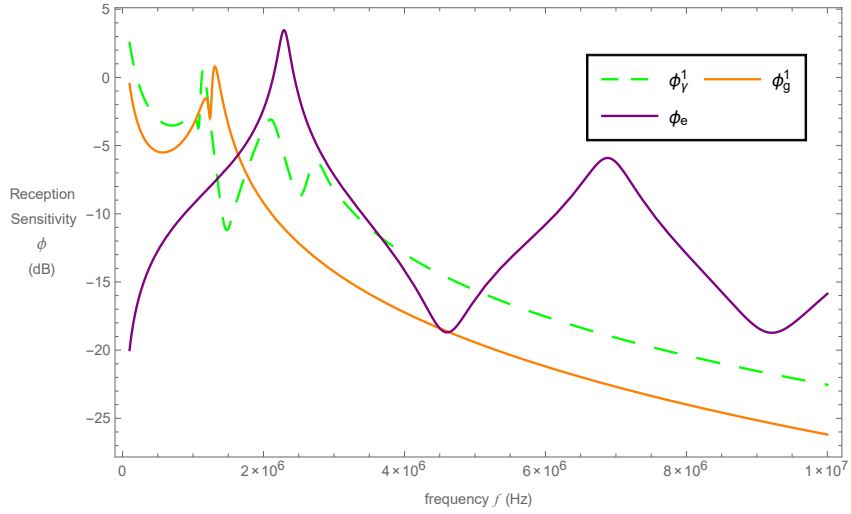
Figure 3.32: Non-dimensionalised reception sensitivity ϕ (dB) versus frequency f (Hz) for the Sierpinski carpet model γ (ϕ_γ^1 green dashed line, equation (3.109)) and Sierpinski gasket (ϕ_g^1 orange full line, equation (2.173)) fractal inspired transducers at generation $n = 1$ and the traditional Euclidean transducer (ϕ_e purple full line, equation (2.58)).

111

its gain bandwidth product by both the gasket and standard devices. This was calculated as $GBP^1_\gamma = 0.149$.

In Figure 3.33 the electrical resonant frequency for the carpet model γ device at generation level two was taken as $1.347\,\text{MHz}$ with an electrical impedance of $3.828\,\text{dB}$. Since this value of the electrical impedance is greater than those for the gasket and standard devices it may be assumed that the maximum amplitude in the carpet's transmission sensitivity would be less than for these two devices. This is for the reason that, the lower the value of the electrical impedance the greater the peak will be in the transmission sensitivity [7]. The mechanical resonant frequency is expected to be the optimal operating frequency in receiving mode, and from Figure 3.33 this is $1.408\,\text{MHz}$ with an electrical impedance of $5.350\,\text{dB}$.
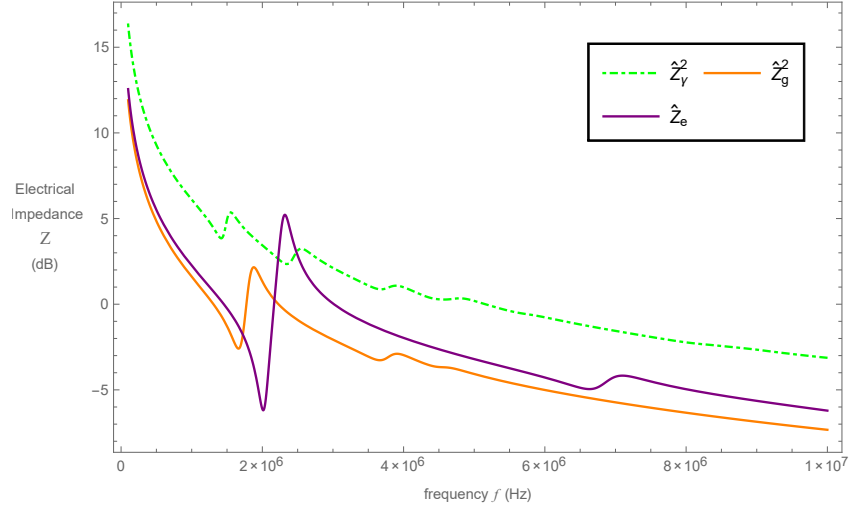
Figure 3.33: Non-dimensionalised electrical impedance $\hat{Z}$ (dB) versus frequency f (Hz) for the Sierpinski carpet model γ ($\hat{Z}^2_\gamma$ green dot-dashed line, equation (3.80)) and Sierpinski gasket ($\hat{Z}^2_g$ orange full line, equation (2.162)) fractal inspired transducers at generation $n = 2$ and the traditional Euclidean transducer ($\hat{Z}_e$ purple full line, equation (2.45)).

Figure 3.34 shows the transmission sensitivities of the devices plotted as a function of operating frequency and Figure 3.35 is the plotted reception sensitives against frequency. As expected, from the results of the electrical impedance, the
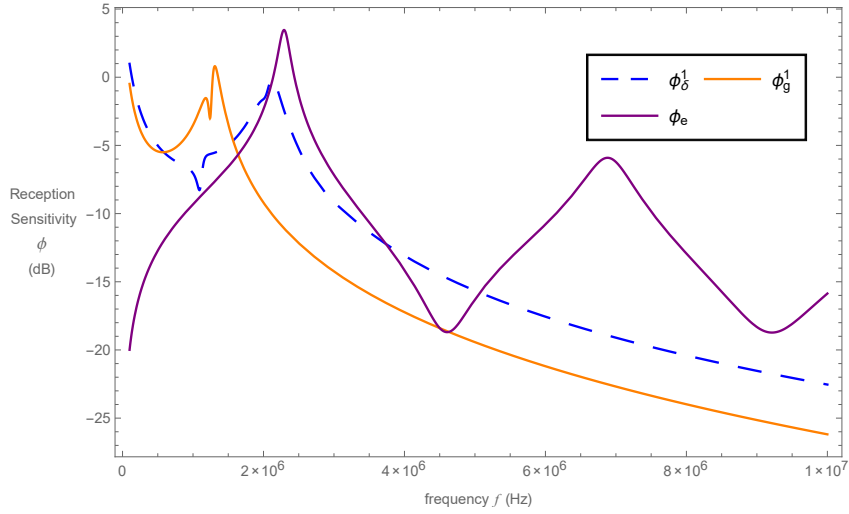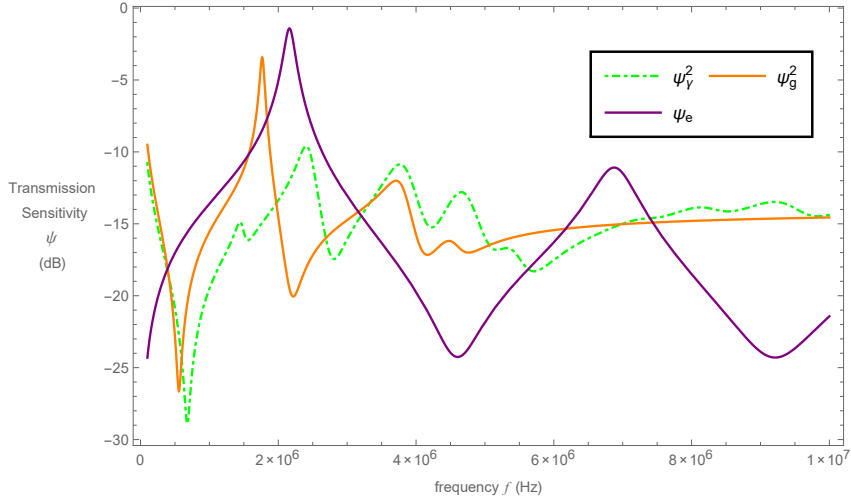
Figure 3.34: Non-dimensionalised transmission sensitivity ψ (dB) versus frequency f (Hz) for the Sierpinski carpet model γ (ψ_γ^2 green dot-dashed line, equation (3.101)) and Sierpinski gasket (ψ_g^2 orange full line, equation (2.169)) fractal inspired transducers at generation $n = 2$ and the traditional Euclidean transducer (ψ_e purple full line, equation (2.54)).
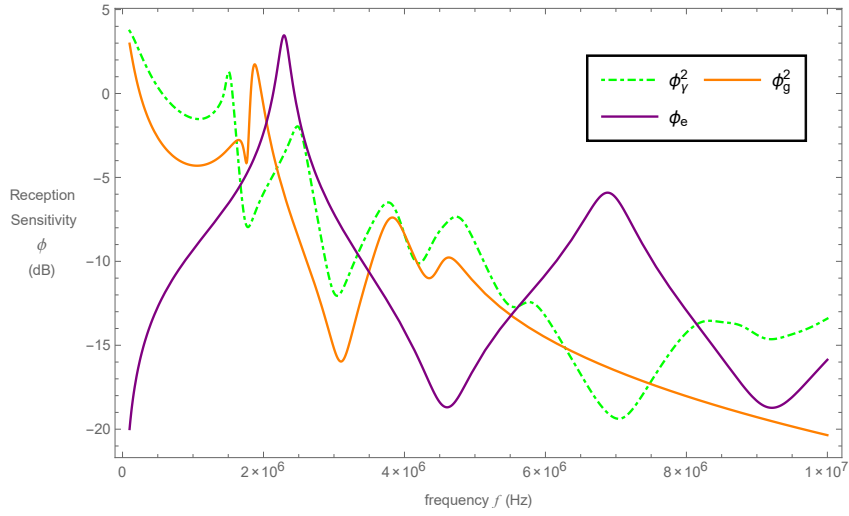
Figure 3.35: Non-dimensionalised reception sensitivity ϕ (dB) versus frequency f (Hz) for the Sierpinski carpet model γ (ϕ_γ^2 green dot-dashed line, equation (3.109)) and Sierpinski gasket (ϕ_g^2 orange full line, equation (2.173)) fractal inspired transducers at generation $n = 2$ and the traditional Euclidean transducer (ϕ_e purple full line, equation (2.58)).

maximum amplitude of the carpet device is lower than both the gasket and standard devices, $G_\gamma^2 = -9.597$ dB, with the 3-dB bandwidth around this peak of $BW_\gamma^2 = 0.465$ MHz. As with the first fractal generation level this is again greater than the gasket and standard devices. Its gain bandwidth product at this generation level was calculated as $GBP_\gamma^2 = 0.051$, which is an improvement from its last fractal generation. However this is less than that of the standard and Sierpinski gasket pre-fractal transducer. In reception mode, the maximum amplitude for the carpet device is $G_\gamma^2 = 1.288$ dB. Although this is lower than the gasket and standard devices, the 3-dB bandwidth at this peak covers a larger range of frequencies. This was calculated as $BW_\gamma^2 = 0.511$ MHz. There is a huge improvement in gain bandwidth product to that of both the gasket and standard devices where its value of $GPB_\gamma^2 = 0.688$ is more than double that of the gasket device.

In Figure 3.36 the electrical impedance for the standard, Sierpinski gasket and Sierpinski carpet transducers at the third generation level is plotted. For the car-
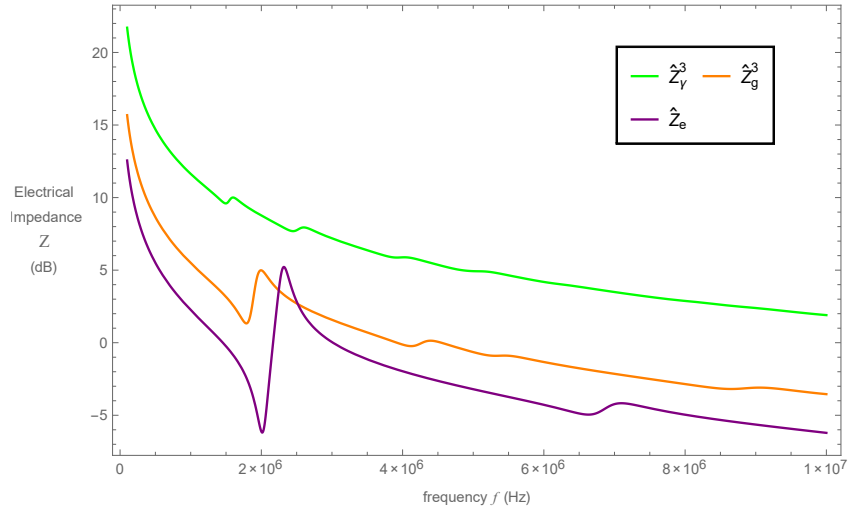
Figure 3.36: Non-dimensionalised electrical impedance $\hat{Z}$ (dB) versus frequency f (Hz) for the Sierpinski carpet model γ ($\hat{Z}_\gamma^3$ green full line, equation (3.80)) and Sierpinski gasket ($\hat{Z}_g^3$ orange full line, equation (2.162)) fractal inspired transducers at generation $n = 3$ and the traditional Euclidean transducer ($\hat{Z}_g$ purple full line, equation (2.45)).

pet transducer, the electrical resonant frequency is 1.416 MHz with an electrical

impedance of 9.609 dB and the mechanical resonant frequency is 1.438 MHz with an electrical impedance of 10.030 dB. As with the previous two generation levels the maximum amplitude of the Sierpinski carpet is significantly less than the other two comparable transducers. From Figure 3.37 this was found at $G_\gamma^3 = -13.030$ dB. Though, the 3-dB bandwidth at this peak was estimated at $BW_\gamma^3 = 0.850$ MHz, leading to a percentage bandwidth of 22%, which compares to just 12% for the Sierpinski gasket and 13% for the standard device. This represents a substantial improvement on device performance over both the currently used Euclidean transducer and the Sierpinski gasket prototype [83]. The results suggest strongly that it
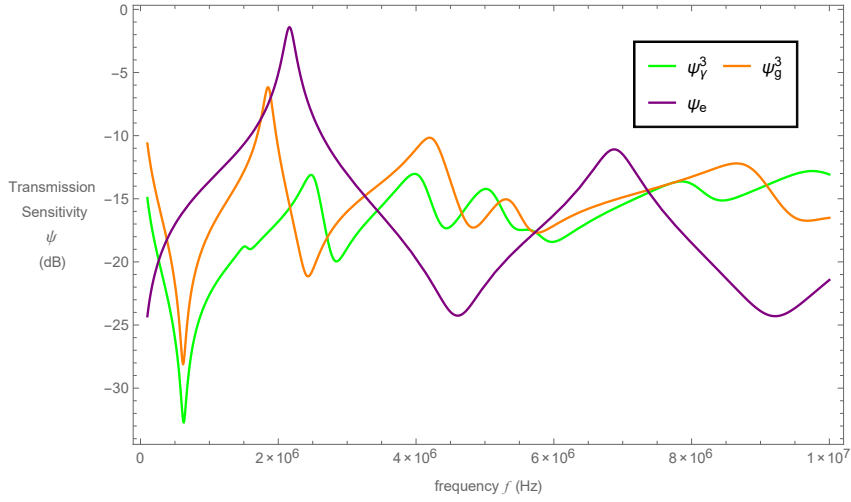
Figure 3.37: Non-dimensionalised transmission sensitivity ψ (dB) versus frequency f (Hz) for the Sierpinski carpet model γ (ψ_γ^3 green full line, equation (3.101)) and Sierpinski gasket (ψ_g^3 orange full line, equation (2.169)) fractal inspired transducers at generation $n = 3$ and the traditional Euclidean transducer (ψ_g green full line, equation (2.54)).

would be worthwhile for a prototype based on the Sierpinski carpet to be built, to determine whether experimental results corroborate with these theoretical results. Furthermore, it would be interesting to explore results at higher fractal generation levels, to determine whether the Sierpinski carpet still outperforms the other two devices.
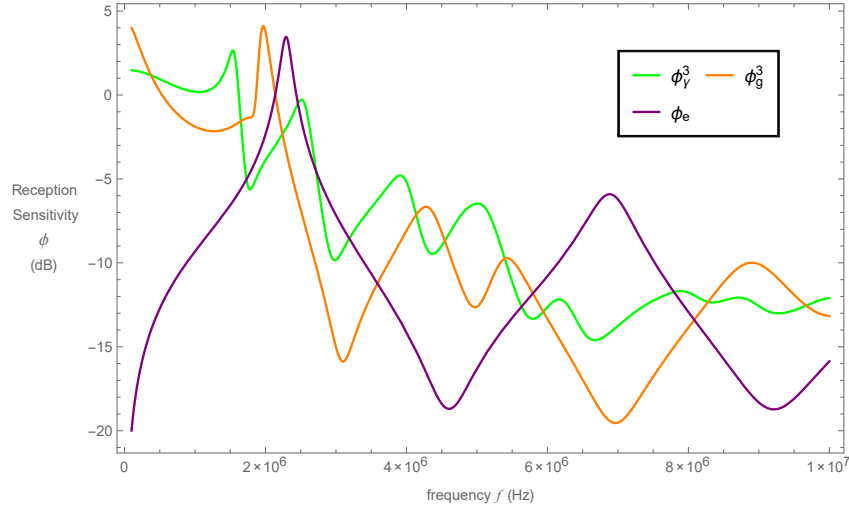
Figure 3.38: Non-dimensionalised reception sensitivity ϕ (dB) versus frequency f (Hz) for the Sierpinski carpet model γ (ϕ_γ^3 green full line, equation (3.109)) and Sierpinski gasket (ϕ_g^3 orange full line, equation (2.173)) fractal inspired transducers at generation $n = 3$ and the traditional Euclidean transducer (ϕ_e purple full line, equation (2.58)).

Figure 3.38 graphically represents the reception sensitivity against the operating frequency of the third generation level Sierpinski carpet and gasket transducers and the standard transducer. Comparison between the gasket and carpet transducers shows a good match with the carpet transducer resonating at lower frequencies. From this figure the maximum amplitude for the carpet device is $G_\gamma^3 = 2.648$ dB with the 3-dB bandwidth at this peak of $BW_\gamma^3 = 1.528$ MHz and a gain bandwidth product of $GBP_\gamma^3 = 2.812$. These results for the two metrics are significantly higher than those for both the gasket and standard devices, and so would suggest that a transducer based on the design of carpet model γ at fractal generation level three would perform efficiently in reception mode.

As previously discussed, it was observed that by increasing the fractal generation level, the bandwidth and gain bandwidth product of the device would also increase. This, however, led to a reduction in the amplitude in transmission mode. In addition, this increase in generation level widens the range of length scales and so results with a more resonant device.

116
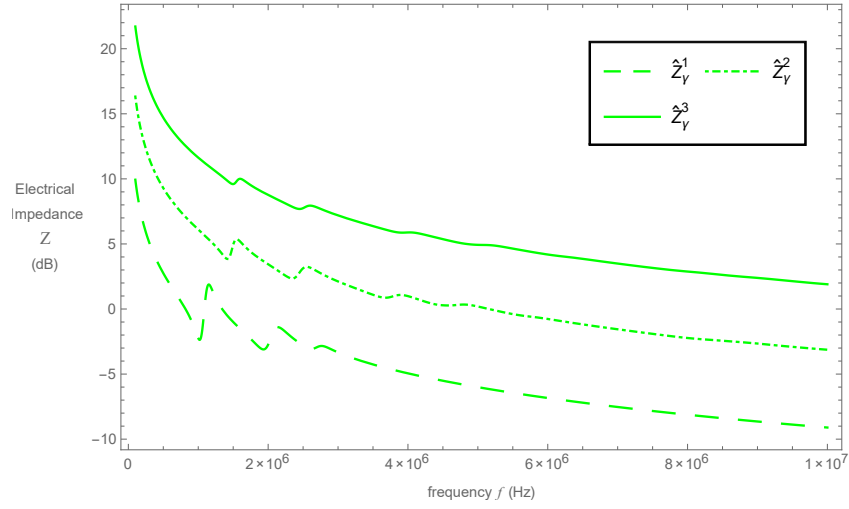
Figure 3.39: Non-dimensionalised electrical impedance $\hat{Z}$ (dB) (equation (3.80)) versus frequency f (Hz) for the Sierpinski carpet model γ transducer at fractal generation levels one ($\hat{Z}_\gamma^1$ dashed line), two ($\hat{Z}_\gamma^2$ dot-dashed line) and three ($\hat{Z}_\gamma^3$ full line).

Figures 3.39 to 3.41 illustrate the effect of increasing the fractal generation level for the transducer's operating characteristics.
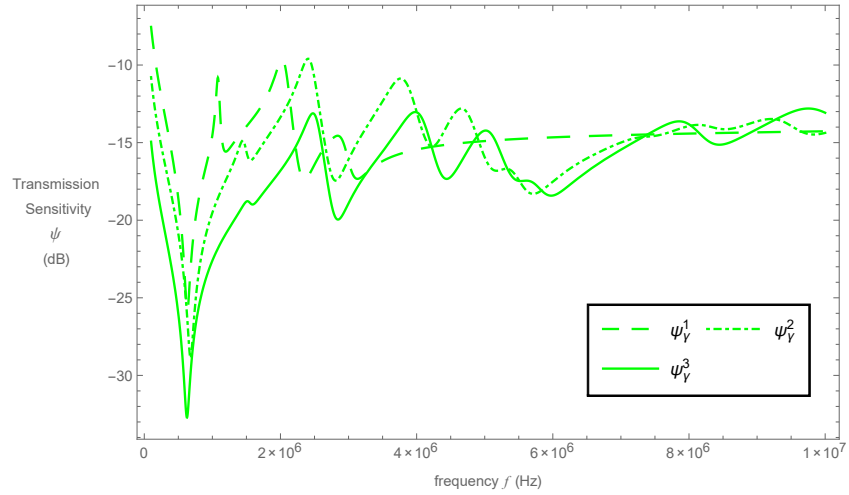
Figure 3.40: Non-dimensionalised transmission sensitivity ψ (dB) (equation (3.101)) versus frequency f (Hz) for the Sierpinski carpet model γ transducer at fractal generation levels one (ψ_γ^1 dashed line), two (ψ_γ^2 dot-dashed line) and three (ψ_γ^3 full line).

117
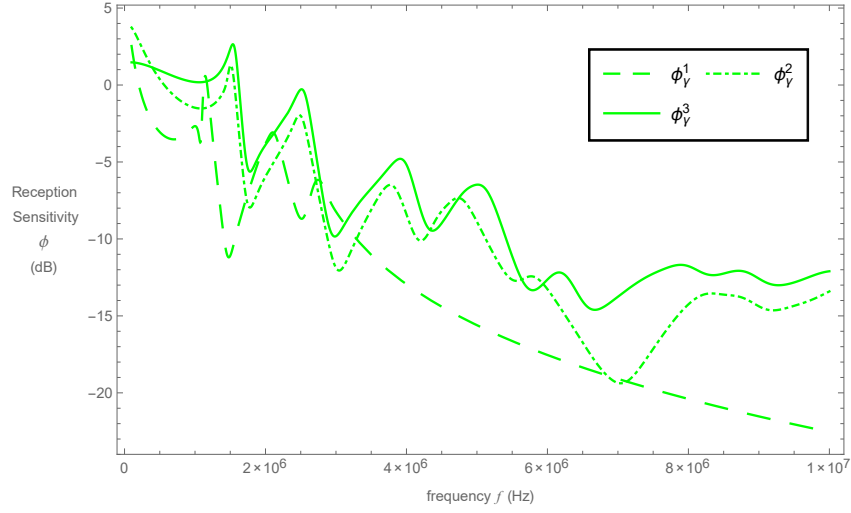
Figure 3.41: Non-dimensionalised reception sensitivity ϕ (dB) (equation (3.109)) versus frequency f (Hz) for the Sierpinski carpet model γ transducer at fractal generation levels one (ϕ_γ^1 dashed line), two (ϕ_γ^2 dot-dashed line) and three (ϕ_γ^3 full line).

The results for model γ suggest that the Sierpinski carpet transducer contains more resonances than the Sierpinski gasket and standard transducers. It was also established that the carpet transducer outperformed the other two devices at almost all fractal generation levels in terms of its bandwidth, in both transmission and reception modes, further reinforcing the notion of implementing this particular design as a workable prototype.

3.6.4 Model Comparisons

In addition to the comparison of the standard, Sierpinski gasket and individual model Sierpinski carpet transducers, it is also important to ascertain the optimal device amongst the three carpet models. Starting with the first fractal generation level, one particular feature that can be observed when studying Figure 3.42 is the good agreement between the three models. The models follow closely in relation to their profiles and are resonant at around the same frequencies.

Figure 3.43 shows a comparison between the three carpet transducer models
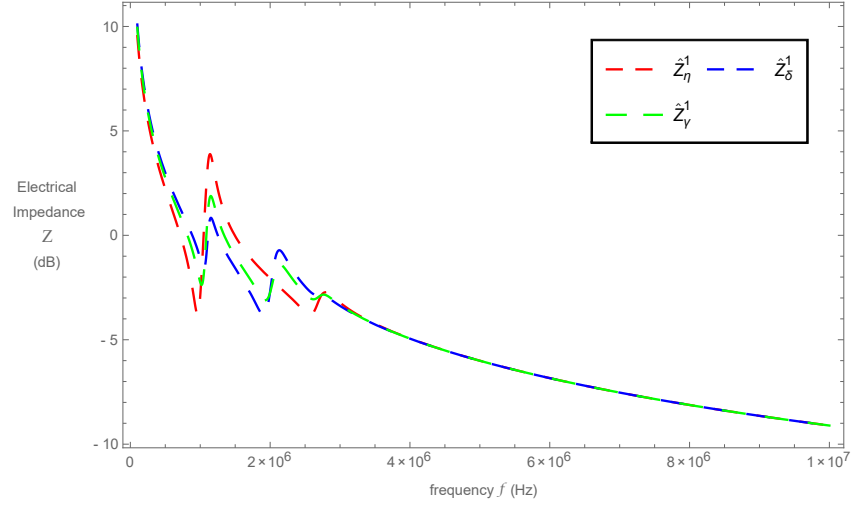
Figure 3.42: Non-dimensionalised electrical impedance $\hat{Z}$ (dB) versus frequency f (Hz) for models η ($\hat{Z}_\eta^1$ red dashed line, equation (3.70)), δ ($\hat{Z}_\delta^1$ blue dashed line, equation (3.76)) and γ ($\hat{Z}_\gamma^1$ green dashed line, equation (3.80)) at fractal generation level $n = 1$.
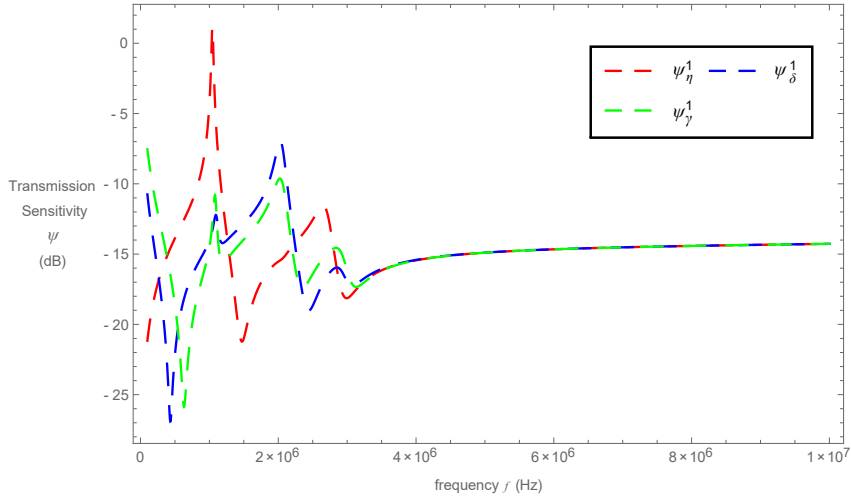
Figure 3.43: Non-dimensionalised transmission sensitivity ψ (dB) (equation (3.101)) versus frequency f (Hz) for models η (ψ_η^1 red dashed line), δ (ψ_δ^1 blue dashed line) and γ (ψ_γ^1 green dashed line) at fractal generation level $n = 1$.

in transmission mode at fractal generation level one. The highest peak amplitude is present in model η and the lowest (in comparison) in model γ, where there is a difference of 10.839 dB. However, the bandwidth of the device suffers with larger

peaks, resulting with model γ having a more desirable bandwidth. This would potentially allow the device to perform more efficiently over a larger range of frequencies. On the other hand, the principal figure of merit used to determine the
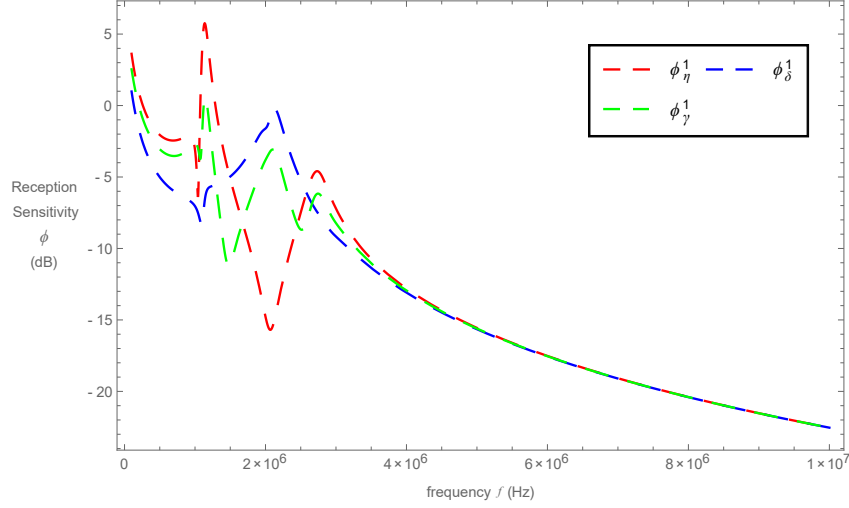
Figure 3.44: Non-dimensionalised reception sensitivity ϕ (dB) (equation (3.101)) versus frequency f (Hz) for models η (ϕ_η^1 red dashed line), δ (ϕ_δ^1 blue dashed line) and γ (ϕ_γ^1 green dashed line) at fractal generation level $n = 1$.

optimal transducer design is the gain bandwidth product, GBP and this suggests models η and δ to be the ideal transducer. See Appendix C for the GBP results. Similarly in reception mode, model η has the highest peak amplitude and is greater than model δ by 0.5993 dB and by 5.168 dB against model γ. As with the transmission sensitivity, the largest bandwidth is attained in the device which has the lowest amplitude. Therefore, on this occasion model δ has the largest bandwidth. The results from the gain bandwidth product suggest that model δ outperforms models η and γ when operating as a sensor of ultrasound.

Following on from these results is a discussion on the next fractal generation level. In Figure 3.45 the electrical impedance of each model device is plotted against the operating frequency. Each transducer model follows a similar profile to their earlier fractal generation level although at a higher decibel and frequency range. Another observation that may be noted is the narrowing between the sepa-

ration of the electrical and mechanical resonant frequencies. For the transmission
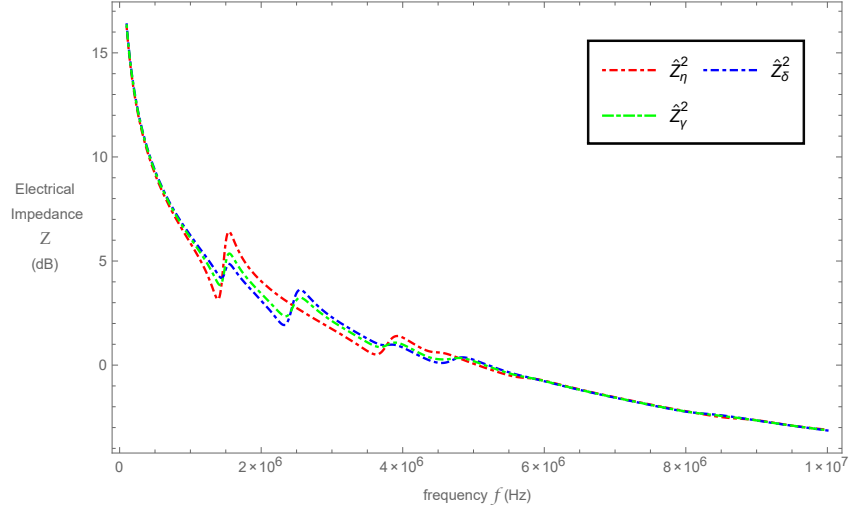
Figure 3.45: Non-dimensionalised electrical impedance $\hat{Z}$ (dB) versus frequency f (Hz) for models η ($\hat{Z}_\eta^2$ red dot-dashed line, equation (3.70)), δ ($\hat{Z}_\delta^2$ blue dot-dashed line, equation (3.76)) and γ ($\hat{Z}_\gamma^2$ green dot-dashed line, equation (3.80)) at fractal generation level $n = 2$.
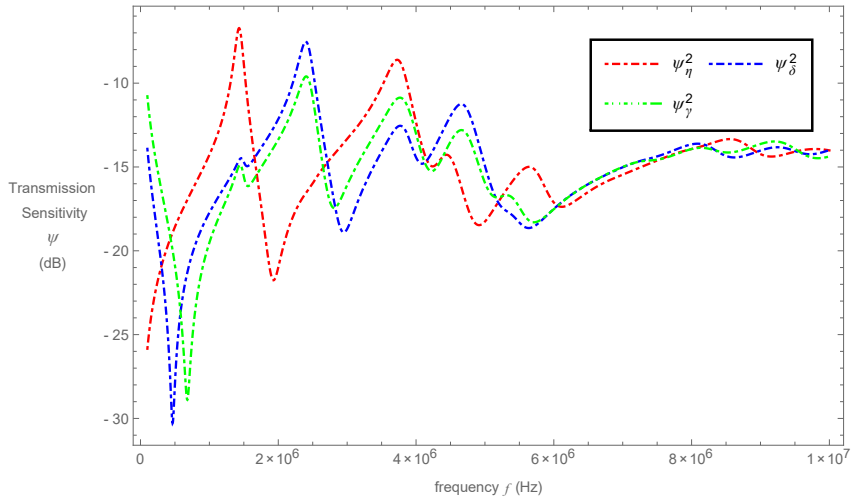
Figure 3.46: Non-dimensionalised transmission sensitivity ψ (dB) (equation (3.101)) versus frequency f (Hz) for models η (ψ_η^2 red dot-dashed line), δ (ψ_δ^2 blue dot-dashed line) and γ (ψ_γ^2 green dot-dashed line) at fractal generation level $n = 2$.

sensitivities at the second fractal generational level a notable shift in the ampli-

tude is clearly evident, particularly when concerning model η, where there is a drop of 7.935 dB in its maximum peak. Yet for models δ and γ there is only a small reduction in amplitude. However, it is still a reduction and their initial negative amplitudes are nevertheless discouraging. On the other hand, model γ has
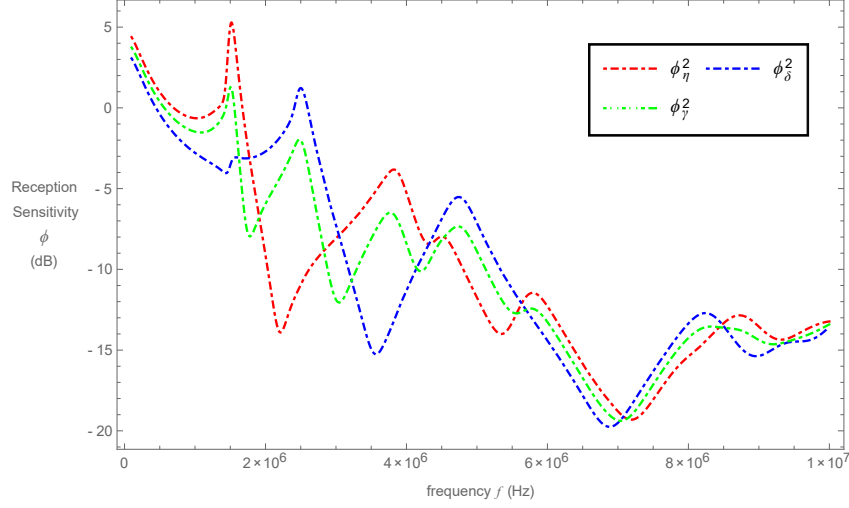
Figure 3.47: Non-dimensionalised reception sensitivity ϕ (dB) (equation (3.109)) versus frequency f (Hz) for models η (ϕ_η^2 red dot-dashed line), δ (ϕ_δ^2 blue dot-dashed line) and γ (ϕ_γ^2 green dot-dashed line) at fractal generation level $n = 2$.

the widest bandwidth and model δ achieves the greatest gain bandwidth product of $GBP_\delta^2 = 0.067$, while models η and γ are $GBP_\eta^2 = 0.055$ and $GBP_\gamma^2 = 0.046$, respectively. Figure 3.47 shows the reception sensitivity against frequency for the three Sierpinski carpet models at fractal generation level two. Comparison of the maximum peaks between the first and second generation levels shows that a device based on model η has a reduction in its maximum amplitude of 8% while the other two have an increase in amplitude of 1.408 dB for model δ and 0.705 dB for model γ. In regards to the gain bandwidth product model γ has the highest at a value of $GBP_\gamma^2 = 0.688$, whilst model η has $GBP_\eta^2 = 0.547$ and model δ has $GBP_\delta^2 = 0.620$.

Figure 3.48 shows the plotted electrical impedance of the three models as a function of frequency for the third fractal generation level. By observing the be-
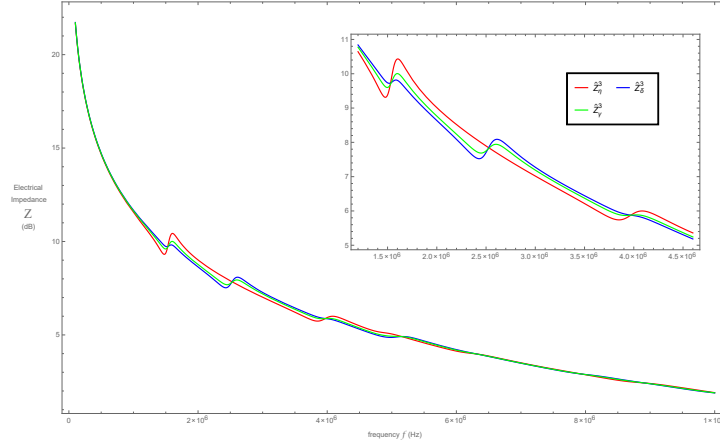
Figure 3.48: Non-dimensionalised electrical impedance $\hat{Z}$ (dB) versus frequency f (Hz) for models η ($\hat{Z}_\eta^3$ red full line, equation (3.70)), δ ($\hat{Z}_\delta^3$ blue full line, equation (3.76)) and γ ($\hat{Z}_\gamma^3$ green full line, equation (3.80)) at fractal generation level $n = 3$. Insert figure is a close up of the resonances.

haviour of Figures 3.42, 3.45 and 3.48 it appears that as the fractal generation level is increased, the electrical and mechanical resonant frequencies approach towards a closer decibel value. The effect of increasing the generation level results in an increase in both the electrical and mechanical resonant frequencies. Consequently,
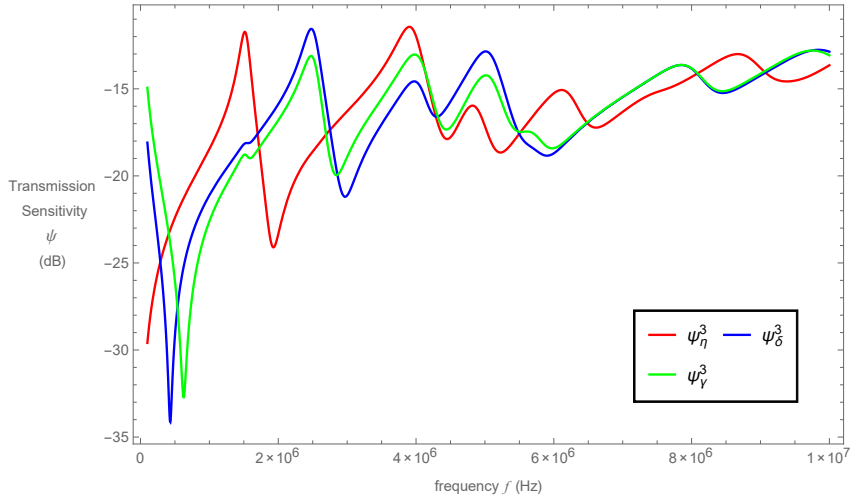
Figure 3.49: Non-dimensionalised transmission sensitivity ψ (dB) (equation (3.101)) versus frequency f (Hz) for models η (ψ_η^3 red full line), δ (ψ_δ^3 blue full line) and γ (ψ_γ^3 green full line) at fractal generation level $n = 3$.

this could suggest a decrease in amplitude for the transmission sensitivity, but an increase in amplitudes for the reception sensitivities. This assumption can be validated by examining the transmission and reception sensitivities for the third fractal generation level. These are plotted in Figures 3.49 and 3.50, respectively
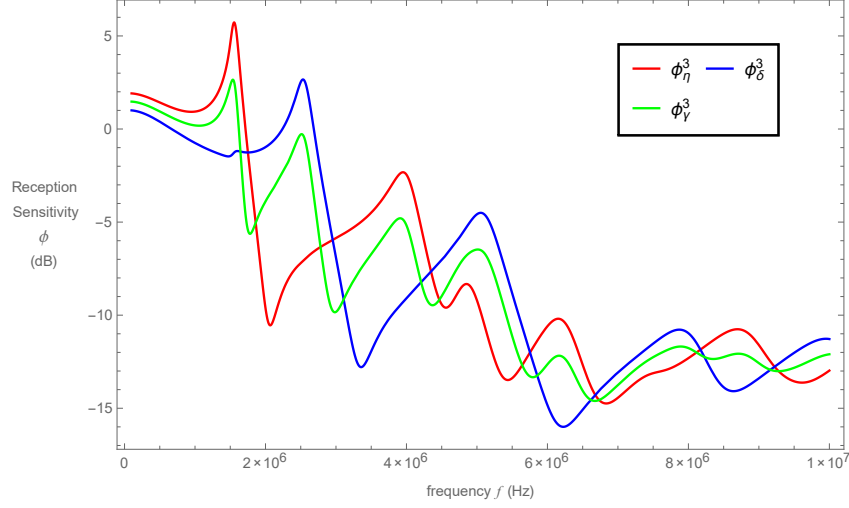
Figure 3.50: Non-dimensionalised reception sensitivity ϕ (dB) (equation (3.109)) versus frequency f (Hz) for models η (ϕ_η^3 red full line), δ (ϕ_δ^3 blue full line) and γ (ϕ_γ^3 green full line) at fractal generation level $n = 3$.

As expected, the maximum amplitude for each of the carpet models has decreased from its previous fractal generation level, this effect can be seen in Figure 3.51. Model η has the highest gain bandwidth product in transmission mode. This was calculated as $GBP_\eta^3 = 0.054$ which is 64% greater than model δ, and 29% greater than model γ. Similarly, the maximum amplitudes in reception sensitivities have generally increased for all models from their previous generation level. This behaviour can be observed in Figure 3.52. The gain bandwidth product values were calculated as $GBP_\eta^3 = 0.917$ for model η, $GBP_\delta^3 = 0.959$ for model δ and $GBP_\gamma^3 = 2.812$ for model γ. Evidence would suggest through the data analysed that generation level one of model η provides the greatest amplitude and that the value of the amplitude decreases as the generation level is increased. This trend is also reflected in the model structures, in that model η amplitude surpasses mod-

els δ and γ at all fractal generation levels. Likewise, model δ exceeds models γ amplitude in all fractal generation levels. Figure 3.51 and tables C.2, C.5 and C.8 confirms this conclusion. In regards to the amplitude in reception mode, the data
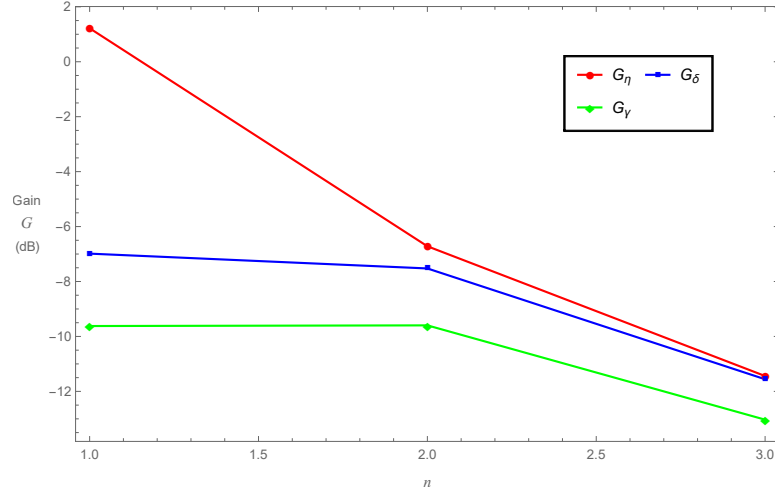
Figure 3.51: Gain (dB) for transmission sensitivity ψ versus fractal generation level n for the Sierpinski carpet transducer models η (G_η red full line), δ (G_δ blue full line) and γ (G_γ green full line).
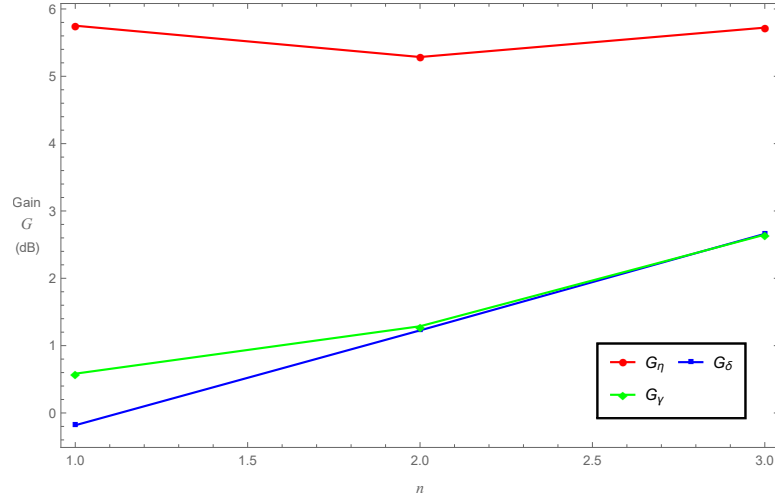
Figure 3.52: Gain (dB) for reception sensitivity ϕ versus fractal generation level n for the Sierpinski carpet transducer models η (G_η red full line), δ (G_δ blue full line) and γ (G_γ green full line).

plotted in Figure 3.52 suggests that the increasing fractal generation level improves the value of the amplitude; with model η once more exceeding models δ and γ at all generation levels.

The 3-dB bandwidth for transmission sensitivity is plotted against the fractal generation level in Figure 3.53. From this plot it is evident that the bandwidth of
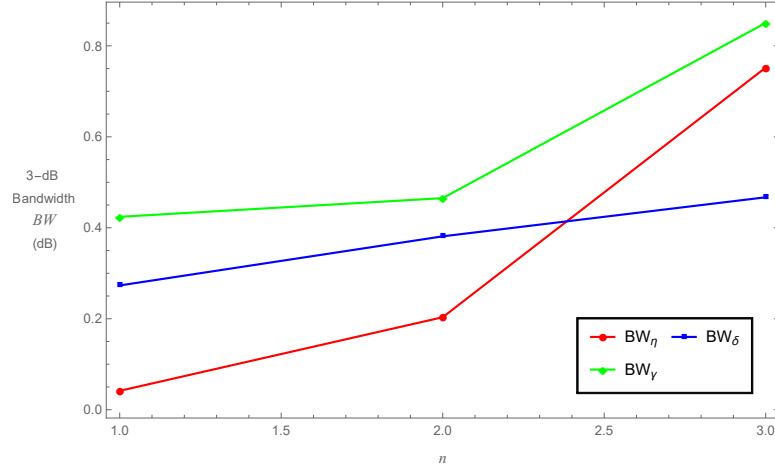
Figure 3.53: The 3-dB bandwidth (MHz) for transmission sensitivity ψ versus fractal generation level n for the Sierpinski carpet transducer models η (BW_η red full line), δ (BW_δ blue full line) and γ (BW_γ green full line).

each device improves from increasing the fractal generation. In particular, there is a significant increase from generation level two to three in models η and γ, while model δ appears to have a more steady increase. Furthermore the best results are present in model γ. Based on the gradient of the increase it would appear that future generation levels of model η could surpass both models δ and γ. However, as this is only speculative further research on future generation would need to be conducted. The 3-dB bandwidth in reception mode, plotted in Figure 3.54, illustrates that model γ outperforms in this figure of merit for generation levels two and three, and that model δ outperforms the other two models at generation level one. In this instance, there is a substantial increase in value when increasing the generation level for model γ. Therefore, it is presumed that this model would

exceed models η and δ at higher generation levels. Still this is an only assumption and for this reason the analysis of higher fractal generation levels is necessary.
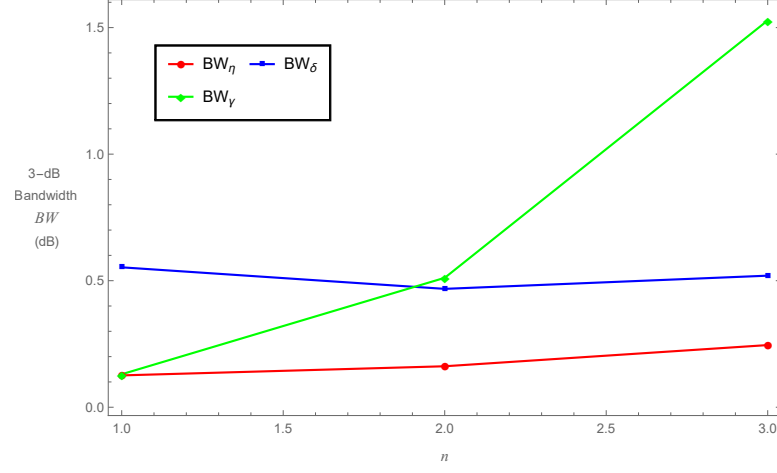
Figure 3.54: The 3-dB bandwidth (MHz) for reception sensitivity ϕ versus fractal generation level n for the Sierpinski carpet transducer models η (BW_η red full line), δ (BW_δ blue full line) and γ (BW_γ green full line).
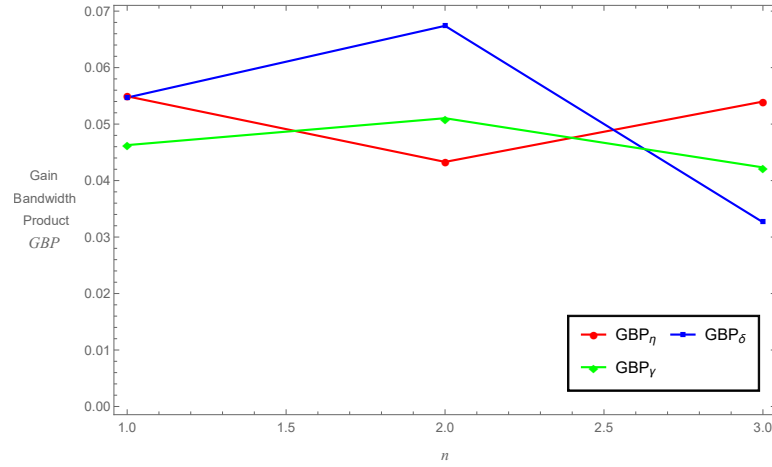
Figure 3.55: The gain bandwidth product for transmission sensitivity ψ versus fractal generation level n for the Sierpinski carpet transducer models η (GBP_η red full line), δ (GBP_δ blue full line) and γ (GBP_γ green full line).

Figures 3.55 and 3.56 illustrate the gain bandwidth product against fractal generation level for the three models for the transmission and reception sensitivities

respectively. By observing the behaviour of each device in Figure 3.55, it would appear that models η and γ have the opposite effect to one another. Due to these profiles it would be difficult to determine the effect of higher fractal generation levels. Similar to model γ, model δ mimics this behaviour but with much steeper gradients.

In Figure 3.56 it is clear to see that model γ overall outperforms models η and δ. In regards to models η and δ, their values for this figure of merit are very close to one another at each generation level. As such, it is possible that model η may exceed model δ at higher fractal generation levels. Although, these assumptions have not been verified and so this warrants the need to analyse the performance at higher fractal generation levels.
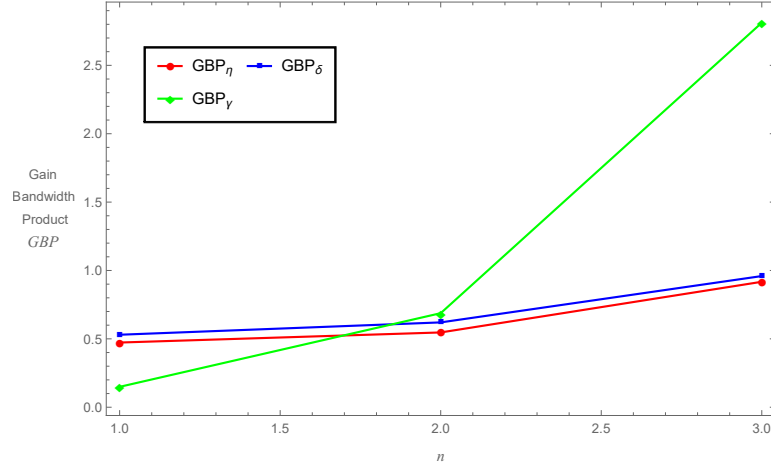
Figure 3.56: The gain bandwidth product for reception sensitivity ϕ versus fractal generation level n for the Sierpinski carpet transducer models η (GBP_η red full line), δ (GBP_δ blue full line) and γ (GBP_γ green full line).

3.7 Conclusions

The analysis presented in this section extended earlier research on incorporating fractal geometry into ultrasonic transducer design. As with previous works, a renormalisation technique was used to investigate the potential performance of

a fractal-inspired transducer. The fractal used as inspiration for the transducer design was the Sierpinski carpet. This was examined by constructing three individual transducer models all influenced by the design of the Sierpinski carpet. The variations in models corresponded to the number of the boundary conditions and for each of the models a lattice counterpart was used to analyse the transducers' operating characteristics. Although all three models are relatively similar in their form, the symmetries of the lattice for model δ resulted with the need for additional independent Green functions.

Due to the limitations of the computing power available that was used to produce the results for the theoretical Sierpinski carpet-like transducer, only the first three fractal generation levels were investigated. Each model has been executed in Mathematica on a laptop computer. The run times for model γ were 12.453 seconds, 2.698 minutes and 49.713 minutes for generation levels one, two and three respectively. Whilst only the first three fractal generation levels have been generated, the computer program used allows for the computation at any fractal generation level. This opens up the possibility of further investigation for transducers which incorporate higher generation levels. Alternatively, higher performance computers are more than capable at producing these operational characteristics for higher fractal generation levels. However, due to current manufacturing limitations it may not prove to be viable to construct a fractal transducer beyond generation level three.

To assess the performance of each transducer model the electrical impedance, and transmission and reception sensitivities were plotted as a function of operating frequency. These were then compared to a previously investigated Sierpinski gasket transducer as well as standard design transducers that are commonly used in industry. As expected it was the carpet devices which experienced more resonance at a wider range of frequencies. In regards to the transmission sensitivities, an increase in the fractal generation level resulted in an increase in the devices bandwidth. Unfortunately this also led to a reduction in the device's amplitude. For the

129

reception sensitivities, an increase in fractal generation level was generally followed by an increase in both its amplitude and bandwidth. The principal figure of merit that was used to determine the most efficient transducer was the gain bandwidth product. The three carpet models were then compared to one another in regards to their transmitting and receiving capabilities, using this figure of merit. Thus in transmission mode, it was model η which in general presented the best results. In reception mode, model γ had overall the highest value, with an average gain bandwidth product almost two times higher than model δ. On the other hand, the 3-dB bandwidth signifies that model γ outperforms models η and δ at all fractal generation levels for both transmission and reception. This suggests that model γ would be suitable in ultrasonic design to enhance current transducer performance, especially when considering the results in reception mode. Furthermore, increasing the fractal generation resulted in an increase in the principle figure of merit for all the carpet models, in reception mode. This was to be expected since the range of length scales increased with the fractal generation level. Similarly, the same could be said in transmitting mode, although with a few discrepancies. Thus, given the opportunity to access greater computing power it would be interesting to see how this figure of merit changes with increasing fractal generation levels. In addition to obtaining these results, given the required computing power it would be ideal to be able compare the convergence of the transmission and reception sensitivities using the L_2 norm, in similar way to the research presented in [86] for the Sierpinski gasket transducer.

This research investigates the theoretical performance of a Sierpinski carpet inspired transducer by utilising the Green function renormalization method. For a comparison it would be beneficial to investigate the carpet structure using the finite element analysis akin to that done on the Sierpinski gasket pre-fractal in [7]. Another area of interest would be in transducer performance optimization. A technique for increasing the values for each of the figures of merit at interest (amplitude, bandwidth and gain bandwidth product) could be achieved by sampling

130

different material parameters. For instance, it is possible to vary the material parameters such as the piezoelectric constant and Young's modulus, since these are simply properties taken from PZT-5H ceramic. This may assist in establishing the optimal material that could be used for ultrasonic transducers. As this chapter has investigated the propagation of an ultrasonic wave within an infinitely ramified fractal-like structure, it would be of added interest to analyse a similar structure by the means of the Cartesian product. The Cartesian product is a method for extending the Green function renormalization to infinitely ramified structures, where the Cartesian product of two graphs can be considered as the sum of the two graphs [111]. In Chapter 5, this extension will be applied to two Sierpinski carpet-like structures with the aim of obtaining the potential transducer characteristics. Additionally, the Cartesian product of two Sierpinski gasket lattices will be investigated.

Chapter 4

Modelling the Effects of a Sierpinski Tetrix-Like Transducer

4.1   Introduction

This chapter extends the Green function renormalization method to study the potential performance of a transducer inspired by the Sierpinski tetrix [20]. Expressions for the transducer's operating characteristics are derived and plotted against the operating frequency. These profiles are then compared against the standard (Euclidean) and the Sierpinski gasket fractal inspired transducers.

This is an interesting design that may now be considered for potential manufacturing, as a result of the development in rapid prototyping techniques. For example 3-D printers could be used in the manufacturing of the composite filler. Additionally, research into 3-D printing of ceramic materials has been performed [68, 69, 81, 137] and the results indicated that the ceramic materials still retained their piezoelectric functionality, which is of utmost importance for ceramic materials used in electronics.

The Sierpinski tetrix can be classified as the three dimensional equivalent of the Sierpinski gasket on account of its construction [60, 63, 100]. Its structure is achieved in a similar way as the Sierpinski gasket but replaces the newly formed tetrahedrons with four copies of itself at half its original height and width. Therefore, the dimension for this fractal is $D_f = \log(4)/\log(2) = 2$. Similarly, the
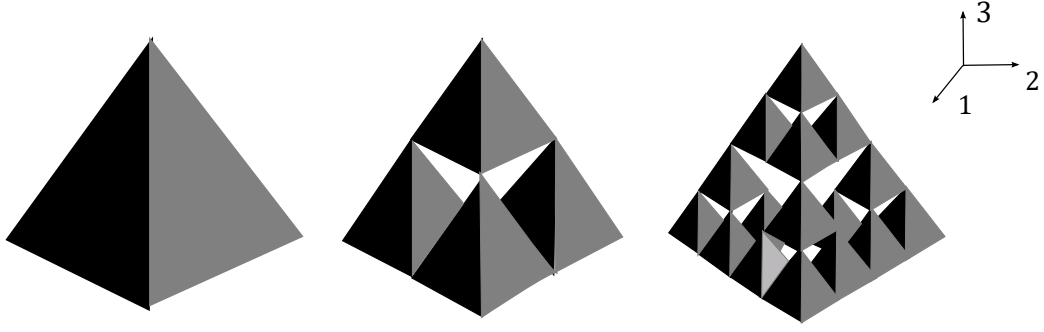
Figure 4.1: Schematic representation of a Sierpinski tetrix transducer at fractal generation levels zero, one and two, where the piezoelectric element is shown in black with a centre filled polymer in white.

lattice equivalents are obtained using the technique mentioned previously for the Sierpinski gasket and carpet pre-fractals, and are once again used to investigate the propagation of an ultrasonic wave. The interaction between the electrical and mechanical behaviour of the lattice vertices is described by [138] and is detailed further in Section 4.2. Figure 4.1 represents the Sierpinski tetrix at fractal at generation levels zero, one and two and Figure 4.2 illustrates the lattice counterpart. For the lattice structure, the nth generation graph has $N_n = 4^n$ vertices, and is constructed by assigning a vertex to the centre of the piezoelectric tetrahedrons and joining these vertices by an edge. The vertex degree for this fractal lattice is $q = 4$. However, the vertex degree is not consistent since the corner vertices have a vertex degree $q = 3$. These vertices correspond to the input/output vertices as they will interact with external loads. Analogous to the previous fractal-inspired transducers, fictitious vertices A, B, C and D are attached to these input/output vertices, thereby resolving the inconsistency of the vertex degrees. This is of importance since it simplifies the process of obtaining subsequent lattice Green functions. For the Sierpinski gasket and tetrix fractal inspired transducers it is possible to obtain the exact $(i, j)^{th}$ element of the Green function matrix using the recursion relationship given in equation (2.132).

The investigation of the Sierpinski tetrix fractal inspired transducer will begin by deriving the governing wave equation from tensor equations. This is pre-
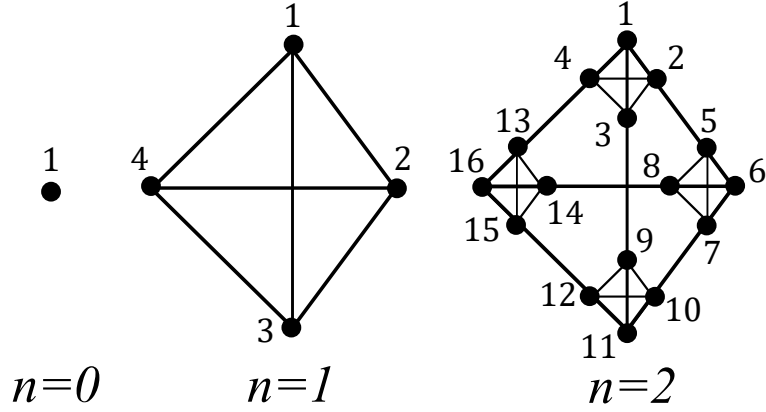
Figure 4.2: Graphical representations of generations 0 to 2 for the sequence of Sierpinski tetrix lattices.

sented in Section 4.2. In Section 4.3, the Green function renormalization method is utilised to obtain the relevant relations for the transducer model. Boundary conditions are obtained to aid the derivation of the expressions for the important output parameters, electrical impedance and transmission and reception sensitivities in Section 4.4. The steady-state solution of the transducer design is discussed in Section 4.5. In Section 4.6, the results for the Sierpinski tetrix fractal inspired transducer are compared with standard Euclidean design and the previously investigated Sierpinski gasket fractal inspired transducer. The findings are then summarized in Section 4.7.

4.2 Wave Propagation in the Sierpinski Tetrix

This section analyses the propagation of an ultrasonic wave within the Sierpinski tetrix lattice. The movement of a wave through the piezoelectric material can be described using the stress equation of motion

$$\rho_T \frac{\partial^2 u_i}{\partial t^2} = \sum_{i,j=1}^{3} \frac{\partial T_{ij}}{\partial x_j},$$

(4.1)

where ρ_T is the density of the piezoelectric material, u_i is the displacement tensor and T_{ij} is the stress tensor. The three-dimensional constitutive equations describ-

134

ing the coupling between electrical and mechanical behaviour of the lattice vertices
are given by

$$T_{ij} = c_{ijkl}S_{kl} - e_{kij}E_k, \tag{4.2}$$

$$D_i = e_{ikl}S_{kl} + \epsilon_{ik}E_k. \tag{4.3}$$

In these equations c_{ijkl} denotes the stiffness tensor, S_{kl} is the strain tensor, e_{kij}
is the piezoelectric tensor, E_k is the electric field, D_i is the displacement and ϵ_{ik}
denotes the permittivity tensor. The relationship between the strain tensor and
mechanical displacement is given by

$$S_{kl} = \frac{1}{2}\left(\frac{\partial u_l}{\partial x_k} + \frac{\partial u_k}{\partial x_l}\right). \tag{4.4}$$

Additionally a relationship between electric field and electric potential, Φ, is ex-
pressed as

$$E_k = -\frac{\partial \Phi}{\partial x_k}. \tag{4.5}$$

The poling direction of the piezoelectric material is parallel to the direction
of the x_3-axis and it is assumed that an electric field is only applied in this direc-
tion [30, 139]. This is to ensure that the orientation of the dipoles of the piezoelec-
tric ceramic are aligned and not left in their randomly oriented state. If left in their
original state the piezoelectric effect is disabled. Previous experimental research
on the Sierpinski gasket [83] has shown the dependence of the transducer's perfor-
mance on the poling direction (which can be chosen in the manufacture process).
Consequently, the assumption made above on the poling direction and from the
electric field essentially allows for the reduction of the three-dimensional coupling
equations in (4.2) and (4.3) to reduce to one dimension. Hence,

$$E_1 = E_2 = 0, \ E_3 \neq 0 \ \text{ and } D_1 = D_2 = 0, \ D_3 \neq 0. \tag{4.6}$$

Consequently, from equation (4.1)

$$
\begin{aligned}
\sum_{i,j=1}^{3} \frac{\partial T_{ij}}{\partial x_j} = \sum_{j=1}^{3} \frac{\partial T_{3j}}{\partial x_j} &= \frac{\partial T_{33}}{\partial x_3} + \frac{\partial T_{32}}{\partial x_2} + \frac{\partial T_{31}}{\partial x_1} \\
&= \frac{\partial T_3}{\partial x_3} + \frac{\partial T_4}{\partial x_2} + \frac{\partial T_5}{\partial x_1},
\end{aligned}
\tag{4.7}
$$

where the components with $i = j$ relate to longitudinal stresses and with $i \neq j$ indicate the shear stresses. Equation (4.1) can be reduced further since it is assumed that the wave travelling within the transducer is wholly longitudinal along the x_3-axis, that is, the shear waves are negligible in comparison to that of the longitudinal waves. This assumption can be made due to the poling direction and the direction of the applied electric field and simplifies the algebra considerably. Longitudinal waves in the x_1- and x_2-directions are also neglected due to the direction of the poling and the applied electric field. Hence,

$$
\rho_T \frac{\partial^2 u_3}{\partial t^2} = \frac{\partial T_3}{\partial x_3},
\tag{4.8}
$$

where $u_3 = u_3(x_3, t)$. Electric charges do not flow easily within the piezoelectric ceramic as a result of it being a good insulator. Thus, from Gauss' law,

$$
\frac{\partial D_3}{\partial x_3} = 0.
\tag{4.9}
$$

Using equations (4.2)-(4.6) and (4.9) together with equation (4.8) yields

$$
\begin{aligned}
\rho_T \frac{\partial^2 u_3}{\partial t^2} &= \frac{\partial}{\partial x_3} \left(c_{33} \frac{\partial u_3}{\partial x_3} - e_{33} E_3 \right) \\
&= c_{33} \frac{\partial^2 u_3}{\partial x_3^2} + \frac{e_{33}^2}{\epsilon_{33}} \frac{\partial^2 u_3}{\partial x_3^2} \\
&= c_{33} \left(1 + \frac{e_{33}^2}{\epsilon_{33} c_{33}} \right) \frac{\partial^2 u_3}{\partial x_3^2}.
\end{aligned}
\tag{4.10}
$$

Equation (4.10) can be reduced into the one-dimensional form by setting the Young's modulus of the piezoelectric material, $Y_T = c_{33} + e_{33}^2/\epsilon_{33}$, and temporarily dropping the subscript attached to the displacement tensor. Thus,

$$
\rho_T \frac{\partial^2 u_3}{\partial t^2} = Y_T \frac{\partial^2 u_3}{\partial x_3^2}.
\tag{4.11}
$$

The one-dimensional equation is subsequently used to derive the boundary conditions and the transducer operating characteristics. It is discretized and by introducing the non-dimensionalized variable θ, can be written in the form shown in equation (2.125).

The derivation of the effective one-dimensional model was the technique for simplifying the analysis of wave propagation within the fractal-like lattice. Longitudinal waves can propagate in all three forms, solid, liquid and gases, while shear waves can only propagate through solids [73, 93, 106]. This effective one-dimensional model accounts only for longitudinal waves in the x_3-direction since the shear waves and longitudinal waves in the x_1- and x_2-directions are considered negligible in comparison. This form of analysis, in effect, treats elastic solids as liquids, simplifying the model while still providing useful results on the likely performance of this transducer. Furthermore, this simplification provides a reasonable comparison against the previously investigated Sierpinski gasket fractal inspired transducer which was also modelled using this analysis [86]. Nevertheless, reducing the system to a one-dimensional model will result in the loss of some nonlinear information. This could be resolved by using a fully three-dimensional finite element analysis on the wave propagation. Previously [7], a finite element approach was applied to a Sierpinski gasket inspired device to analytically produce the discretised equations which underwent a renormalization approach. Additionally, a finite element model for the same design was built to determine the behaviour of the device [32]. However, while such models proposed for the Sierpinski gasket will be more accurate, they are computationally expensive and the finite differences model proposed previously for the same structure [83] produced similar results without the computational overheads. Hence, a similar approach was taken here.

4.3 Renormalization

The Green function renormalization method is applied to the Sierpinski tetrix lattice in the same manner as the Sierpinski gasket. This is enabled as a result

of it being another example of a finitely ramified fractal. The Sierpinski gasket and tetrix are of the $S(q)$ family of graphs, whereby the tetrix is simply the three dimensional Sierpinski gasket. Thus they can be described in terms of a constant vertex degree, $q = 3$ for the gasket and $q = 4$ for the tetrix [40, 41, 110, 112]. In regards to the number of input/output vertices, both the gasket and tetrix lattices have this equal to the vertex degree. Hence for the Sierpinski tetrix it is assumed that there is single input vertex at vertex A and three output vertices; vertices B, C and D, see Figure 4.3. Similar to the previous fractal transducer models, fictitious vertices A, B, C and D are attached to the input/ output vertices to accommodate the boundary conditions.
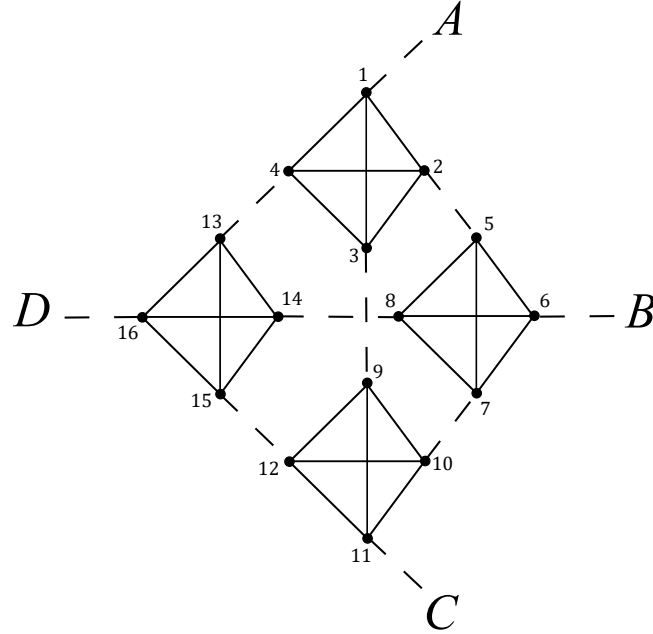
Figure 4.3: Sierpinski tetrix lattice at generation $n = 2$. Fictitious vertices A, B, C and D are introduced to accommodate the boundary conditions.

Figure 4.3 shows the second generation level fractal lattice from the connection of four copies of the first generation level lattice, i.e. the process of forming $\mathcal{G}^{(n+1)}$ is made from the connection of four copies of $\mathcal{G}^{(n)}$. Taking into account symmetry of the tetrix lattice, there are two pivotal Green functions, where for ease of notation these will be labelled as $\hat{x}_t = \hat{G}_{11}^{(n)}$ and $\hat{y}_t = \hat{G}_{66}^{(n)}$. The corresponding Green

functions at the next fractal generation level, $\hat{X}_t = \hat{G}_{11}^{(n+1)}$ and $\hat{Y}_t = \hat{G}_{66,}^{(n+1)}$ are found by applying equation (2.132)

$$\hat{X}_t = \hat{x}_t + 3\hat{y}_t \hat{G}_{51}^{(n+1)}, \tag{4.12}$$

$$\hat{Y}_t = \hat{y}_t \left(\hat{G}_{21}^{(n+1)} + \hat{G}_{71}^{(n+1)} \right). \tag{4.13}$$

To obtain $\hat{X}_t$ and $\hat{Y}_t$ in terms of $\hat{x}_t$ and $\hat{y}_t$ solely, expressions for $\hat{G}_{21,}^{(n+1)}$ $\hat{G}_{51}^{(n+1)}$ and $\hat{G}_{71}^{(n+1)}$ are required, utilising equation (2.132) results in

$$\hat{G}_{21}^{(n+1)} = \hat{y}_t + (\hat{x}_t + 2\hat{y}_t) \hat{G}_{51}^{(n+1)}, \tag{4.14}$$

$$\hat{G}_{51}^{(n+1)} = \hat{x}_t \hat{G}_{21}^{(n+1)} + 2\hat{y}_t \hat{G}_{71}^{(n+1)}, \tag{4.15}$$

$$\hat{G}_{71}^{(n+1)} = \hat{y}_t \hat{G}_{21}^{(n+1)} + (\hat{x}_t + \hat{y}_t) \hat{G}_{71}^{(n+1)}. \tag{4.16}$$

Solving equations (4.12)-(4.16) for the corresponding Green functions gives [112, 113]

$$\hat{X}_t = \hat{x}_t - \frac{3\hat{y}_t^2 (\hat{x}_t^2 - \hat{x}_t + \hat{x}_t\hat{y}_t - 2\hat{y}_t^2)}{(1 - \hat{x}_t - 2\hat{y}_t)(1 - \hat{x}_t^2 + \hat{y}_t - \hat{x}_t\hat{y}_t + 2\hat{y}_t^2)}, \tag{4.17}$$

$$\hat{Y}_t = \frac{\hat{y}_t^2 (1 - \hat{x}_t + \hat{y})}{(1 - \hat{x}_t - 2\hat{y}_t)(1 + \hat{y}_t - (\hat{x}_t - \hat{y}_t)(\hat{x}_t + 2\hat{y}_t))}. \tag{4.18}$$

To account for boundary conditions, equation (2.133) is utilised in a similar manner,

$$x_t = \hat{x}_t + \hat{x}_t b_1 x_t + 3\hat{y}_t b_2 y_t, \tag{4.19}$$

$$y_t = \hat{y}_t + \hat{y}_t b_1 x_t + \hat{x}_t b_2 y_t + 2\hat{y}_t b_2 y_t, \tag{4.20}$$

$$z_t = \hat{x}_t + \hat{y}_t b_1 y_t + \hat{x}_t b_2 z_t + 2\hat{y}_t b_2 w_t, \tag{4.21}$$

$$w_t = \hat{y}_t + \hat{y}_t b_1 y_t + \hat{x}_t b_2 w_t + \hat{y}_t b_2 w_t + \hat{y}_t b_2 y_z. \tag{4.22}$$

Solving these equations simultaneously results in

$$x_t = \frac{\hat{x}_t - b_2(\hat{x}_t - \hat{y}_t)(\hat{x}_t + 3\hat{y}_t)}{\Delta_t}, \tag{4.23}$$

$$y_t = \frac{\hat{y}_t}{\Delta_t}, \tag{4.24}$$

139

$$z_t = \frac{(1 - \hat{x}_t b_1)(1 - b_2(\hat{x}_t - \hat{y}_t)) - \Delta_t(1 - 3b_2(\hat{x}_t - \hat{y}_t))}{3b_2(1 - b_2(\hat{x}_t - \hat{y}_t))\Delta_t}, \tag{4.25}$$

$$w_t = \frac{(1 - b_1(\hat{x}_t - \hat{y}_t))\hat{y}_t}{1 - (b_2(\hat{x}_t - \hat{y}_t))\Delta_t}, \tag{4.26}$$

where $x_t = G_{11}^{(n)}$, $y_t = G_{61}^{(n)}$, $z_t = G_{66}^{(n)}$, $w_t = G_{616}^{(n)}$ and $\Delta_t = (\hat{x}_t b_1 - 1)(\hat{x}_t b_2 - 1) + 2b_2(\hat{x}_t b_1 - 1)\hat{y}_t - 3\hat{y}_t^2 b_1 b_2$.

The pivotal elements calculated in this section can now be utilised to derive the relevant operating transducer characteristic. This is presented in the following section.

4.4   Boundary Conditions and Transducer Operating Characteristics

Similar to the Sierpinski gasket and carpet fractal inspired transducers, this model is arranged to have mechanical loads placed at the output vertices and an electrical load at the input vertex. In transmission mode it is assumed that there is only a wave travelling away from the piezoelectric material. Likewise it follows that the ultrasonic wave travels towards the transducer in reception mode. The elements of the boundary matrix $B^{(n)}$ and vector $\underline{c}^{(n)}$ were found to be the same as previous fractal-inspired transducers, though these require suitable substitutions in regards to the particular vertex of the graph. Equations (3.55) and (3.56) are thus re-derived as

$$B_{ij} = \begin{cases} \frac{1}{1 - p\frac{Z_B}{Z_T}} & \text{if } i = j = 1 \\ \frac{1}{1 - p\frac{Z_L}{Z_T}} & \text{if } i = j = 6, \ 11 \text{ or } 16, \\ 0 & \text{otherwise} \end{cases} \tag{4.27}$$

and

$$c_i = \begin{cases} -\frac{h\bar{Q}}{Y_T\xi}\left(\frac{1}{1 - p\frac{Z_B}{Z_T}}\right) & \text{if } i = 1 \\ \left(\frac{h\bar{Q}}{Y_T\xi} - 2p\alpha_L\frac{Z_L}{Z_T}\right)\left(\frac{1}{1 - p\frac{Z_L}{Z_T}}\right) & \text{if } i = 6, \ 11 \text{ or } 16. \\ 0 & \text{otherwise} \end{cases} \tag{4.28}$$

The derivations in equations (4.27) and (4.28) will be used to determine the expressions for the electrical impedance and transmission and reception sensitivities for the Sierpinski tetrix fractal inspired transducer. Again due to the arrangement of the transducer in the circuit, the expression for the non-dimensionalized electrical impedance was calculated previously in equation (3.70), where μ_η and ν_η are replaced with

$$\mu_t = \frac{3y_t - w_t - z_t}{1 - p\frac{Z_L}{Z_T}} \qquad \text{and} \qquad \nu_t = \frac{y_t - x_t}{1 - p\frac{Z_B}{Z_T}}, \qquad (4.29)$$

for the Sierpinski tetrix fractal inspired device. Following on from the electrical impedance, an expression for the transmission sensitivity is found by setting $\alpha_L = 0$ (since force is absent at the front face in transmission) and using the expression of force found in equation (3.92). For the tetrix device the force is given in equation (3.97) where $K^{(n)}$ is substituted with

$$K_t^{(n)} = \left(\frac{1}{1 - p\frac{Z_L}{Z_T}}\right)\left(1 + \frac{2w_t + z_t}{1 - p\frac{Z_L}{Z_T}} - \frac{y_t}{1 - p\frac{Z_B}{Z_T}}\right). \qquad (4.30)$$

Thus, the non-dimensionalized transmission sensitivity for the Sierpinski tetrix device is similar to that of equation (3.101) where the relevant substitutions are to be made for $K^{(n)}$ and Z. In reception mode the expression for amplitude of the forward propagating wave is given by equation (3.103) and so the non-dimensionalized reception sensitivity is given in equation (3.109) where μ, ν and Z are replaced accordingly.

Within this section a brief recap on the derivation of the relevant operating characteristics for a transducer based on the Sierpinski tetrix design has been outlined. This has been kept succinct due to the similarity to the output parameters found previously for the Sierpinski carpet and Sierpinski gasket fractal inspired transducers.

4.5   Steady-State and Exact Solutions

For manufacturing purposes it is only the pre-fractal designs that may be considered for ultrasonic applications. This is due to the complexity of true fractal

structures. However, from an analytical perspective it is of interest to consider a situation where a true fractal occurs. This fractal structure is only formed when the fractal generation level n tends to infinity [8, 25]. Furthermore it is assumed that the renormalization recursion relationships will converge to a steady state [8]. To distinguish steady state solutions a superscript s will be attached. Thus, the steady state is found by setting $\hat{x}_t = \hat{X}_t = \hat{x}_t^s$ and substituting this into equation (4.17) gives

$$0 = \frac{3\hat{y}_t^{s^2} \left(\hat{x}_t^s \left(1 - \hat{y}_t^s \right) - \hat{x}_t^{s^2} + 2\hat{y}_t^{s^2} \right)}{\left(1 - \hat{x}_t^s - 2\hat{y}_t^s \right) \left(1 + \hat{y}_t^s - \left(\hat{x}_t^s + \hat{y}_t^s \right) \left(\hat{x}_t^s + 2\hat{y}_t^{s^2} \right) \right)}. \tag{4.31}$$

From equation (4.31)

$$\hat{y}_t^s = 0, \tag{4.32}$$

or

$$\hat{x}_t^s - \hat{x}_t^s \hat{y}_t^s - \hat{x}_t^{s^2} + 2\hat{y}_t^{s^2} = 0. \tag{4.33}$$

If $\hat{y}_t^s = 0$ then equation (4.18) is satisfied since $\hat{y}_t = \hat{Y}_t = \hat{y}_t^s$. As for equation (4.33), this can be substituted into equation (4.18) to give

$$1 = \frac{\hat{y}_t^s \left(1 - \hat{x}_t^s + \hat{y}_t^s \right)}{\left(1 - \hat{x}_t^s - 2\hat{y}_t^s \right) \left(1 + \hat{y}_t^s - \hat{x}_t^{s^2} - \hat{x}_t^s \hat{y}_t^s + 2\hat{y}_t^{s^2} \right)}. \tag{4.34}$$

Rearranging equation (4.33) in terms of $\hat{y}_t^{s^2}$ and substituting this into equation (4.34) results in

$$
\begin{aligned}
1 &= \frac{\hat{y}_t^s \left(1 - \hat{x}_t^s + \hat{y}_t^s \right)}{\left(1 - \hat{x}_t^s - 2\hat{y}_t^s \right) \left(1 - \hat{x}_t^s + \hat{y}_t^s \right)}, \\
1 &= \frac{\hat{y}_t^s}{\left(1 - \hat{x}_t^s - 2\hat{y}_t^s \right)}. \tag{4.35}
\end{aligned}
$$

As a condition of equation (4.35) $\hat{y}_t^s \neq 0$, as this could otherwise imply that $1 = 0$. Thus, an expression for $\hat{y}_t^s$ is

$$\hat{y}_t^s = \frac{1}{3} \left(1 - \hat{x}_t^s \right). \tag{4.36}$$

Also from equation (4.33)

$$\hat{y}_t^s = \frac{\hat{x}_t^s \pm \sqrt{9\hat{x}^{s^2}_t - 8\hat{x}_t^s}}{4}, \tag{4.37}$$

hence

$$\frac{\hat{x}_t^s \pm \sqrt{9\hat{x}^{s^2}_t - 8\hat{x}_t^s}}{4} = \frac{1}{3}\left(1 - \hat{x}_t^s\right), \tag{4.38}$$

and so

$$\hat{x}_t^s = -\frac{1}{2} \text{ or } \hat{x}_t^s = 1. \tag{4.39}$$

However, a solution of $\hat{x}_t^s = 1$ is neglected since this would imply that $\hat{y}_t^s = 0$ and as previously mentioned this cannot be the case. If $\hat{x}_t^s = -\frac{1}{2}$ then from equation (4.36), $\hat{y}_t^s = \frac{1}{2}$ and so the recursion relations have two steady states; a line of stable fixed points at $(\hat{x}_t^s, 0)$ and an unstable fixed point at $\left(-\frac{1}{2}, \frac{1}{2}\right)$, where the stability of each fixed point was numerically determined by computing the Jacobian matrix to evaluate the eigenvalues of the matrix. These steady states can now be substituted into equations (4.23)-(4.26) to derive the boundary equations. So as follows, inserting $(\hat{x}_t^s, 0)$ into these equations gives

$$x = \frac{\hat{x}_t^s}{1 - \hat{x}_t^s b_1}, \tag{4.40}$$

$$y = 0, \tag{4.41}$$

$$z = \frac{\hat{x}_t^s}{1 - \hat{x}_t^s b_2} \tag{4.42}$$

$$w = 0. \tag{4.43}$$

Similarly, inserting $\left(-\frac{1}{2}, \frac{1}{2}\right)$ in these equations results in

$$x = \frac{1 - 2b_2}{2b_1 b_2 - b_1 + b_2 - 2}, \tag{4.44}$$

$$y = \frac{1}{2 + b_1 - b_2 - 2b_1 b_2}, \tag{4.45}$$

$$z = \frac{1 - (1 + 2b_1) b_2}{(1 + b_2)(2b_1 b_2 - b_1 + b_2 - 2)}, \tag{4.46}$$

$$w = -\frac{1 + b_1}{(1 + b_2)(2b_1 b_2 - b_1 + b_2 - 2)}. \tag{4.47}$$

143

The recursion relations given in equations (4.17) and (4.18) can be reduced into a simpler form by defining a new set of coordinates (a, u). If (a, u) denotes the nth generation level, capital letters (A, U) denote the corresponding values at generation level $n + 1$. The transformation $\zeta\!:\!(a, u) \to (\hat{x}_t, \hat{y}_t)$ for the $S(p)$ fractal lattice family is given in [113]. Thus for the tetrix lattices,

$$\hat{x}_t = \frac{3(1 + a - au) + u(a + u - au)}{4u}, \tag{4.48}$$

$$\hat{y}_t = \frac{(u - 1)(1 + a + u - au)}{4u}, \tag{4.49}$$

with inverse $\zeta^{-1}\!:\!(\hat{x}_t, \hat{y}_t) \to (a, u)$,

$$a = \frac{1 - \hat{x}_t^2 + \hat{x}_t\hat{y}_t - 3\hat{y}_t(\hat{x}_t - \hat{y}_t)}{4\hat{y}_t}, \tag{4.50}$$

$$u = \frac{1 + \hat{x}_t + 2\hat{y}_t}{1 + \hat{x}_t - \hat{y}_t}. \tag{4.51}$$

The recursion of these new coordinates, $Z\!:\!(a, u) \to (A, U)$ is attained using $Z = \zeta\kappa\zeta^{-1}$ [112, 113], where κ is the mapping of $(\hat{x}_t, \hat{y}_t) \to (\hat{X}_t, \hat{Y}_t)$. Therefore,

$$a \to A(a) = 4a^2 - 2a - 1, \tag{4.52}$$

$$u \to U(a, u) = \frac{(4a - 2)(a + 1 + (1 + 3a)u)}{(4a + 2)(a + 1 + 3(a - 1)u)}. \tag{4.53}$$

Thus, the recursion A is decoupled since it only depends on a. The initial conditions $\hat{x}_{t_0}$ and $\hat{y}_{t_0}$ are obtained using equation (2.129) with $n = 0$, that is

$$\hat{x}_{t_0} = \hat{y}_{t_0} = \frac{1}{p^2 + 4}, \tag{4.54}$$

since the renormalization maps begin with a single vertex.

The results for the electrical impedance, transmission and reception sensitivities for the Sierpinski tetrix model are presented in the following section.

4.6 Results

Similar to previously investigated fractal-like transducers, it is only realistically viable to consider the potential construction of designs based on low fractal generation levels. Current manufacturing limitations do not allow for the construction of a piezoelectric Sierpinski tetrix at high generation levels at the dimensions required for an operational frequency in the sub-megahertz range. This is a result of the increasing complexity in the design as the generation level is increased. (Of course, the scale of the prototype could be increased, in order to attain higher generation levels, but the corresponding operating frequency range would be significantly reduced). Thus, for manufacturing purposes this section discusses the results attained via a mathematical computer model, for the performance of a Sierpinski tetrix fractal inspired transducer for generation levels one to five. As a result of the consistent vertex degree ($q = 4$), the renormalization technique used provides an excellent method for obtaining the results for any fractal generation level design. A comparison of key operating characteristics between the Sierpinski tetrix and Sierpinski gasket designs at generation level five, and the currently used Euclidean device is presented. The three devices have been modelled on a PZT-5H ceramic with the material parameters shown in Table 2.1. The Sierpinski gasket was used for comparison due to it belonging to the same family of fractal lattices. Specifically, the Sierpinski gasket belongs to the $S(3)$ lattice family and the Sierpinski tetrix is part of the $S(4)$ family [41, 113]; where the 3 and 4 indicate the vertex degree of the fractal lattices.

4.6.1 Transducer Performance at Varying Fractal Generation Levels

Figure 4.4 shows a comparison in electrical impedance between the first five fractal generation levels of the Sierpinski tetrix fractal inspired transducer. In this plot all fractal generation levels show qualitatively similar results and adhere to similar patterns with higher fractal generation levels resonating at higher electrical

145
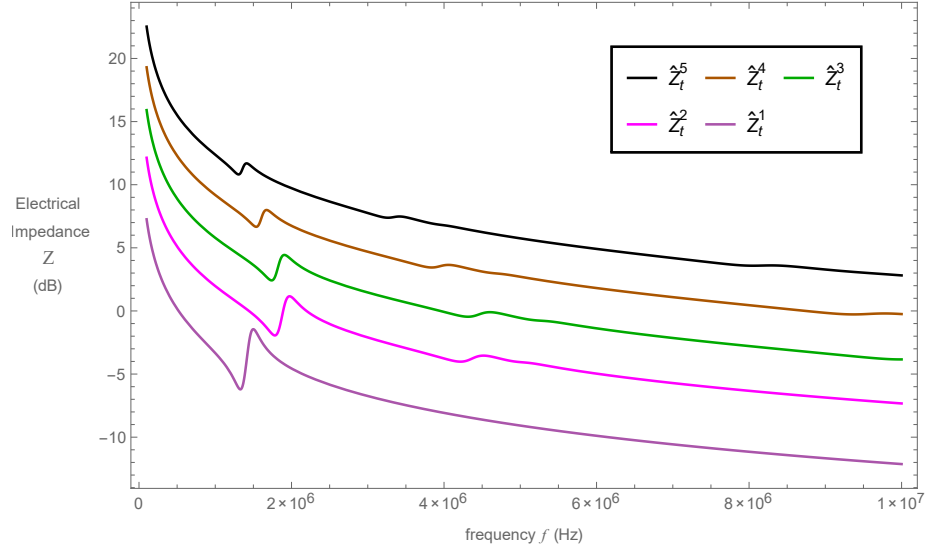
Figure 4.4: Non-dimensionalised electrical impedance $\hat{Z}$ (dB) (equation (3.70), with the appropriate substitutions) versus frequency f (Hz) for the Sierpinski tetrix fractal inspired transducer at fractal generation levels one to five.

impedances. This most likely relates to the reduction in the size of the length scales as the fractal generation level is increased. That is, at fractal generation level five the length scales within the device's internal structure would be considerably smaller than the ones present within the first fractal generation level. This would consequently result in higher values for the electrical impedance. Equally, the electrical impedance is sure to rise since increasing the fractal generation level results in the removal of more material. The electrical and mechanical resonant frequencies together with the corresponding electrical impedances for each fractal generation level are given in Table 4.1.

Comparison of transmission sensitives are shown in Figure 4.5. From these results it is evident that the transmission sensitivity for the fractal generation level two has the highest maximum amplitude and is greater by 3.434 dB than fractal generation level five, which offers the lowest. Consequently, this has resulted in a lower bandwidth of $BW_t^2 = 0.217$ MHz at its resonant frequency leading to a percentage bandwidth of 12%, while fractal generation level five has a percentage bandwidth of 21%. Additionally, there is a substantial improvement in terms of the

Generation (n)	Electrical Resonant Frequency		Mechanical Resonant Frequency	
	f_e (MHz)	Z_t (dB)	f_m (MHz)	Z_t (dB)
1	1.231	-6.211	1.400	-1.449
2	1.683	-1.939	1.875	1.160
3	1.640	2.421	1.807	4.434
4	1.438	6.666	1.573	7.995
5	1.207	10.815	1.312	11.690

Table 4.1: Electrical and mechanical resonant frequencies for the first five fractal generation levels for the Sierpinski tetrix transducer.
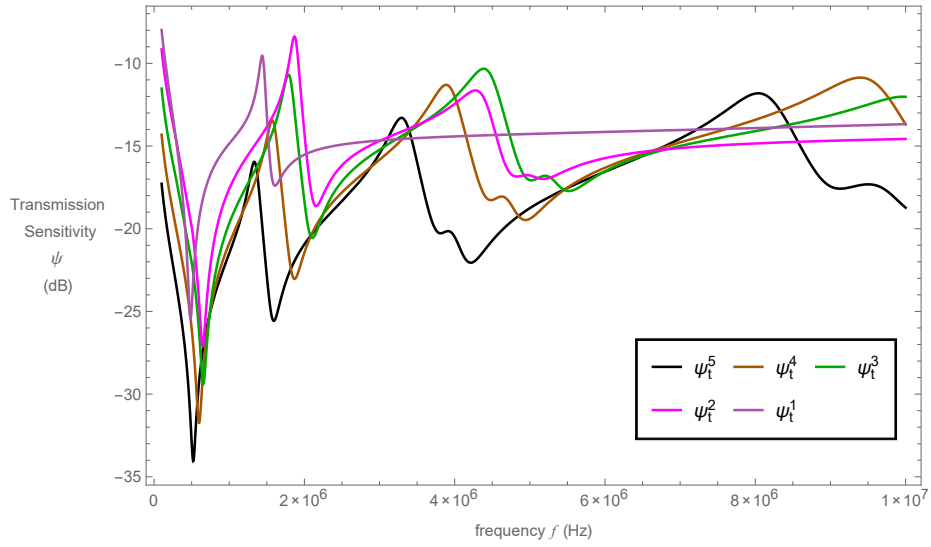
Figure 4.5: Non-dimensionalised transmission sensitivities ψ (dB) (equation (3.101), with the appropriate substitutions) versus frequency f (Hz) for the Sierpinski tetrix fractal inspired transducer at fractal generation levels one to five.

gain bandwidth product when increasing the fractal generation level. See Table 4.2 for all figures of merit in transmission mode. Table 4.2 only illustrates the effective figures of merit at the resonant frequency for the individual fractal generation levels. Additional calculations for the bandwidth and gain bandwidth product have been made using the amplitude of the first peak of fractal generation level five. This peak amplitude was then used to determine the figures of merit for each

147

Generation (n)	Maximum Amplitude (Gain) (dB)	3-dB Bandwidth (MHz)	Gain Bandwidth Product
1	−9.539	0.186	0.021
2	−8.378	0.217	0.032
3	−10.327	1.006	0.093
4	−10.861	2.334	0.191
5	−11.812	1.691	0.111

Table 4.2: Figures of merit in transmitting mode for Sierpinski tetrix transducer.

fractal generation level. In this instance fractal generation level two supersedes any other in terms of all three figures of merit, and incrementing the fractal generation level past this point proves not to be worthwhile since all metrics decrease with the increase of the fractal generation level. These results are presented in Table 4.3.

Generation (n)	First Peak Amplitude (dB)	3-dB Bandwidth (MHz)	Gain Bandwidth Product
1	−9.539	0.994	0.1105
2	−8.378	1.265	0.184
3	−10.680	0.953	0.081
4	−13.457	0.545	0.025
5	−15.954	0.242	0.006

Table 4.3: Figures of merit in transmitting mode for Sierpinski tetrix transducer using the first peak amplitude of fractal generation level five.

The reception sensitivity profiles for the proposed device based on the initial five fractal generations of the Sierpinski tetrix pre-fractals are shown in Figure 4.6. It is evident from this plot that an increase in the fractal generation level from one to five results with higher maximum amplitudes. Furthermore, it can be seen that fractal generation levels three, four and five produce reception sensitivity profiles with more resonances, within the frequency range, than their generation levels one and two counterparts. In fact, by increasing the fractal generation level beyond
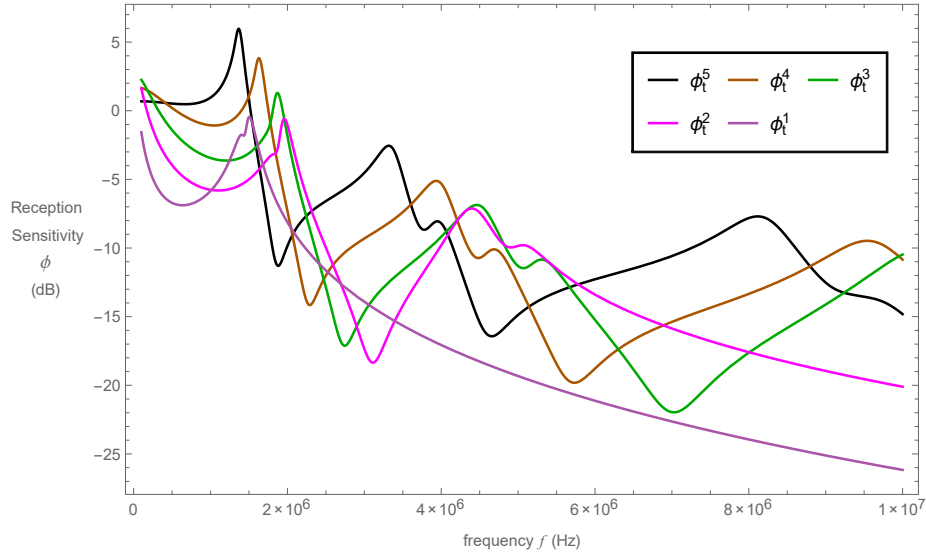
Figure 4.6: Non-dimensionalised reception sensitivities ϕ (dB) (equation (3.109), with the appropriate substitutions) versus frequency f (Hz) for the Sierpinski tetrix fractal inspired transducer at fractal generation levels one to five.

level five, it is found that the reception sensitivity profiles show evidence of more resonances, but this is offset with a reduced maximum amplitude.

The reception sensitivity profiles for the proposed device at generation levels one, five and fifteen are shown in Figure 4.7. As is evident from this plot, the initial fractal generation level has far fewer resonances in comparison to other two devices. This indicates that the device at this generation level has only a single length scale and hence the presence of a single resonance. The higher the fractal generation level, the greater the presence of resonances and this is attributed to increased complexity in the pre-fractal design; to be precise, there is a greater range of length scales. However, moving beyond a certain fractal generation level results in a compromise between increased resonances and maximum amplitude. This can be observed when comparing generation levels five to fifteen. As the generation level is increased, the size of the length scales decreases, and for very small length scales, the performance of the transducer, in reception mode, at higher frequencies is improved. This is expected since the designs of higher generation levels span a
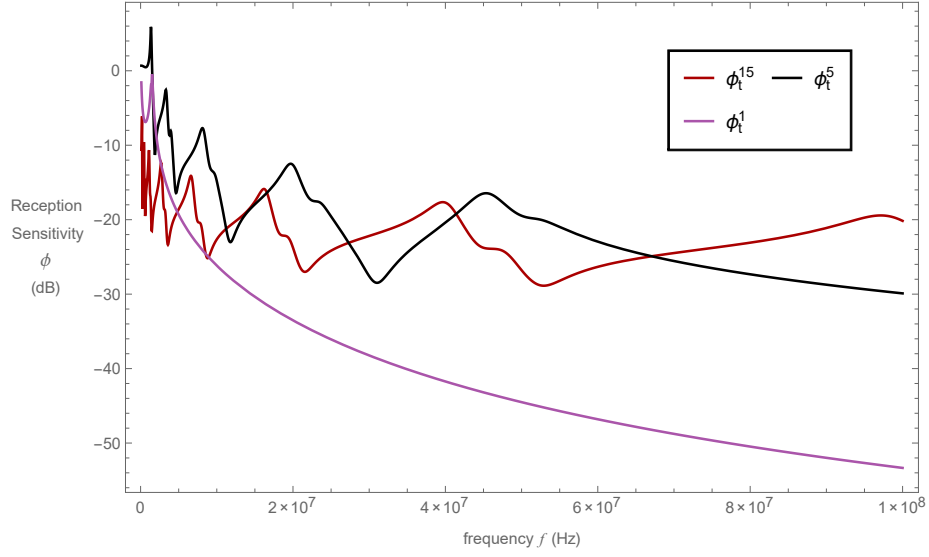
Figure 4.7: Non-dimensionalised reception sensitivities ϕ (dB) (equation (3.109), with the appropriate substitutions) versus frequency f (Hz) for the Sierpinski tetrix fractal inspired transducer at fractal generation levels one (ϕ_t^1 light purple full line), five (ϕ_t^5 black full line) and fifteen (ϕ_t^{15} burgundy full line).

greater range of length scales.

Generation (n)	Maximum Amplitude (Gain) (dB)	3-dB Bandwidth (MHz)	Gain Bandwidth Product
1	−0.448	0.397	0.358
2	−0.597	0.386	0.336
3	1.296	0.276	0.372
4	3.825	0.249	0.601
5	5.967	0.215	0.849

Table 4.4: Figures of merit in receiving mode for Sierpinski tetrix transducer.

The bandwidth and gain bandwidth product for each fractal generation level was initially calculated at the relative resonant frequency. These results are presented in Table 4.4. From this table it is clear to see that, while the amplitude and gain bandwidth product, in most instances, both increase with the fractal generation level, the same cannot be said for the 3-dB bandwidth. This reduc-

tion in bandwidth is likely a result of the increased sensitivity amplitude. Further calculations were made on these figures of merit using the same amplitude. That is, the peak amplitude was taken at the resonant frequency of fractal generation level two, since this generation level had the lowest maximum amplitude. In this respect the bandwidth is likely to increase with the fractal generation. To corroborate this, the metrics for each fractal generation level have been calculated and are tabulated in Table 4.5.

Generation (n)	First Peak Amplitude (dB)	3-dB Bandwidth (MHz)	Gain Bandwidth Product
1	−0.448	0.415	0.375
2	−0.597	0.386	0.336
3	1.296	0.941	1.269
4	3.825	1.765	4.259
5	5.967	1.521	6.010

Table 4.5: Figures of merit in receiving mode for Sierpinski tetrix transducer using the resonant frequency of fractal generation level two.

Additional resonances in the sensitivity profiles are desired as they increase the operational bandwidth of the device. Single length scale devices can only operate at a single frequency, whilst designs with a range of length scales have the potential to operate over a wide range of frequencies. Thus, to raise the entire reception sensitivity output, a device that presents multiple resonances is preferred. The desirable resonant behaviour of the device is clearly achieved by increasing the fractal generation level. Furthermore, these resonances occur at lower frequencies. The added advantage of higher fractal generation level devices is the effect it has on the reception sensitivity bandwidth. In certain instances, increasing the fractal generation level improves the operational bandwidth at the resonant frequency significantly. For example, due to the additional resonances of the fifth generation level design, the reception sensitivity outperforms the first generation device at almost every possible frequency. Additionally, the value of the gain bandwidth

151

product is much more encouraging, as there is a noticeable increase in this figure of merit as the fractal generation level is increased. In some instances, this figure of merit increased more than three-fold over the previous fractal generation level.

To summarise, increasing the fractal generation level resulted in greater electrical impedance magnitudes and more crucially developed the pre-fractal transducer into a multi-resonant device. When evaluating the figures of merit of the pre-fractal transducers at their particular resonant frequency in transmission mode, it was established that the bandwidth around these peaks increased but consequently reduced the peak amplitudes. Yet in reception mode it was found that the amplitudes increased with the fractal generation level but then the bandwidth around these peaks decreased. Comparison of fractal generation levels was then assessed at a particular frequency range. In transmission mode the amplitude was taken at the first peak of fractal generation level five. The results attained via this process showed that there was no benefits in increasing the fractal generation level beyond level two. This was simply for the reason that all other pre-fractal generation level devices were poorer in all figures of merit. The amplitude in reception mode was taken at the resonant frequency of fractal generation level two. For the reception sensitivities there was a substantial improvement in increasing the fractal generation level since all figures of merit improved. Thus, the receiving capabilities of a transducer inspired by the Sierpinski tetrix fractal appear to only improve with greater fractal generation levels.

4.6.2 Comparison between Standard and Pre-Fractal Devices

The effect of an additional vertex into the design of the Sierpinski gasket, i.e. the Sierpinski tetrix, on the electrical impedance at fractal generation level five is shown in Figure 4.8. This plot also illustrates the electrical impedance for the standard design. From this plot it can be seen that the inclusion of this extra vertex results with the electrical and mechanical resonant frequencies occurring
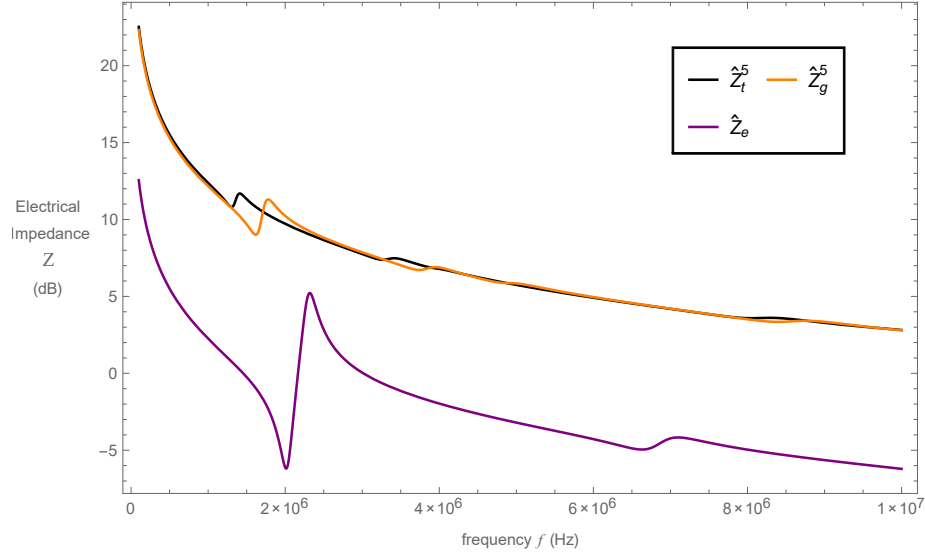
Figure 4.8: Non-dimensionalised electrical impedances $\hat{Z}$ (dB) versus frequency f (Hz) for the Sierpinski tetrix ($\hat{Z}_t^5$ black full line, equation (3.70), with the appropriate substitutions) and Sierpinski gasket ($\hat{Z}_g^5$ orange full line, equation (2.162)) fractal inspired transducers at fractal generation five and the traditional Euclidean transducer ($\hat{Z}_e$ purple full line, equation (2.45)).

at lower frequencies. Additionally this plot illustrates that there is the significant increase in magnitude of the electrical impedance when comparing the pre-fractal devices to the Euclidean transducer. See Tables 4.1, 2.8 and 2.2 for the electrical and mechanical resonant frequencies for the Sierpinski tetrix, gasket and standard transducers. The behavioural difference between the Sierpinski tetrix and gasket pre-fractal devices shows there is a slightly higher magnitude. As with the Sierpinski carpet models this was most likely a result of the pre-fractal lattice containing more length scales in its design than a transducer based on the design of the Sierpinski gasket. Furthermore, the minor rise in magnitude is to be expected since the key difference between the two devices is the vertex degree.

Comparison of the transmission sensitivities are illustrated in Figure 4.9 for the standard and pre-fractal devices. While the transducer designs vary in their construction, for a worthwhile comparison, care has been taken with regard to the construction variables to ensure that the designs have their first resonance around the

153
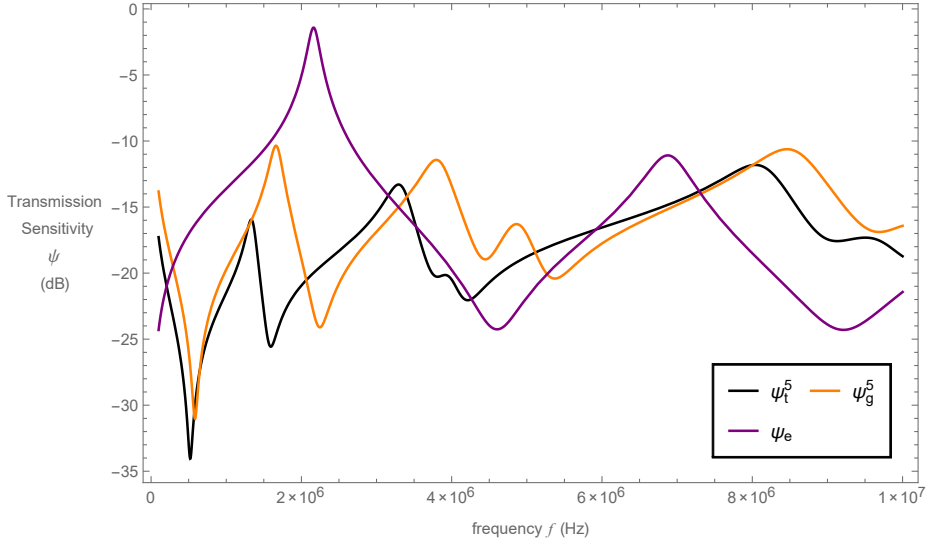
Figure 4.9: Non-dimensionalised transmission sensitivities ψ (dB) versus frequency f (Hz) for the Sierpinski tetrix (ψ_t^5 black full line, equation (3.101), with the appropriate substitutions) and Sierpinski gasket (ψ_g^5 orange full line, equation (2.169)) fractal inspired transducers at fractal generation five and the traditional Euclidean transducer (ψ_e purple full line, equation (2.54)).

same frequency. For instance the value for the cross-sectional area of the Euclidean device is $A_r = 10^{-4}$, while pre-fractal devices have $A_r = \xi \Delta x = \xi L_s/(2^n - 1)$. Therefore, the cross-sectional area will decrease as the fractal generation level is increased. Furthermore, the ceramic volume fractions for all devices are the same to maintain a fair comparison. As expected due to the range of length scales present, the pre-fractal designs demonstrate more resonances than the Euclidean transducer and hence are effective over a wider frequency range. The Sierpinski tetrix device shows that there is a reduction in peak amplitude when comparing against the Sierpinski gasket inspired transducer, and that the maximum amplitude occurs at a higher frequency. The Sierpinski gasket device has maximum amplitude $G_g^5 = -10.357 \, \text{dB}$ at a frequency of $1.519 \, \text{MHz}$ and the Sierpinski tetrix device has $G_t^5 = -11.812 \, \text{dB}$ at a frequency of $7.941 \, \text{MHz}$. As expected, the tetrix device has a larger bandwidth than the gasket device, at its resonant frequency, with an effective operating range of $BW_t^5 = 1.691 \, \text{MHz}$. The Sierpinski

154

gasket fractal inspired transducer has, at its resonant frequency, a 3-dB bandwidth of 0.280 MHz. Thus the percentage bandwidths of the two devices are 21% for the Sierpinski tetrix and 18% for the Sierpinski gasket. This increase in device bandwidth has led to an improvement in the gain bandwidth product, which is $GBP_t^5 = 0.111$ compared to that of $GBP_g^5 = 0.026$ for the gasket device. The Sierpinski tetrix fractal inspired device also outperforms the standard transducer in terms of the 3-dB bandwidth (at the related resonant frequencies), where the standard device only has a percentage bandwidth of 13%. However, comparisons at the first peak amplitudes suggest the Sierpinski tetrix fractal inspired device is considerably outperformed by both the standard and Sierpinski gasket fractal inspired transducers in regards to all the figures of merit. This is clearly evident from the results presented in Table 4.6.

	First Peak Amplitude (dB)	3-dB Bandwidth (MHz)	Gain Bandwidth Product
Sierpinski Tetrix	-15.954	0.242	0.006
Sierpinski Gasket	-10.357	0.933	0.086
Euclidean	-1.414	3.569	2.577

Table 4.6: Figures of merit for the Euclidean, Sierpinski gasket and tetrix pre-fractal transducers at generation level five in transmission mode. The figures of merit for all devices has been calculated using the amplitude of the first peak of the Sierpinski tetrix pre-fractal transducer.

Figure 4.10 illustrates the reception sensitivities of the three devices plotted as a function of the operating frequency. Again the profiles of the pre-fractal devices are qualitatively similar with the Sierpinski tetrix inspired device displaying lower amplitudes than the Sierpinski gasket inspired device at all frequencies. The lower amplitudes present in the tetrix device could suggest that there is a loss in signal as a result of the additional path the ultrasonic wave has to travel. The amplitude of the wave diminishes the further it travels through the lattice structure and thus results in greater attenuation. However, the tetrix device does resonate at lower

155
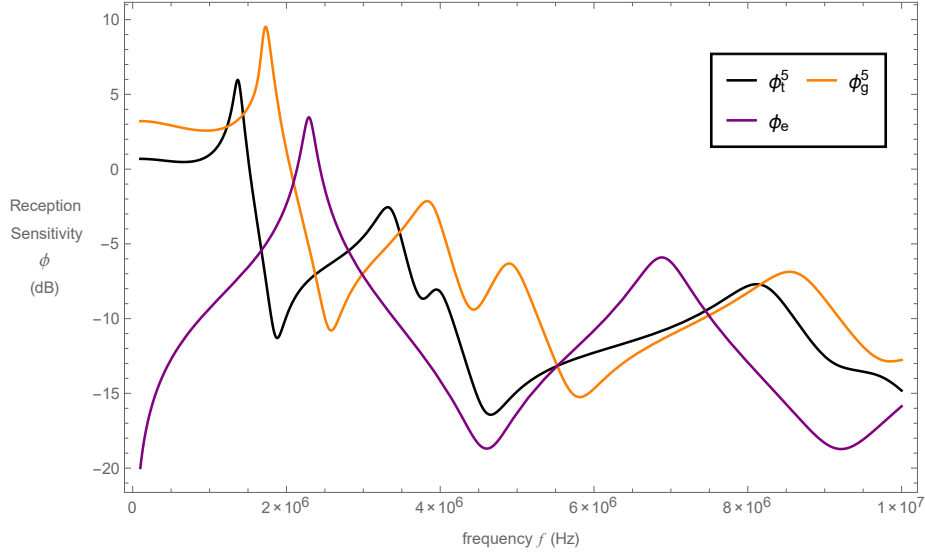
Figure 4.10: Non-dimensionalised reception sensitivities ϕ (dB) versus frequency f (Hz) for the Sierpinski tetrix (ϕ_t^5 black full line, equation (3.109), with the appropriate substitutions) and Sierpinski gasket (ϕ_g^5 orange full line, equation (2.173)) fractal inspired transducers at fractal generation five and the traditional Euclidean transducer (ϕ_e purple full line, equation (2.58)).

frequencies than the gasket device and therefore may allow for greater penetration depth. It was expected that the pre-fractal Sierpinski tetrix-inspired transducer would exhibit more resonances than the Sierpinski gasket pre-fractal device on account of its lattice structure covering more length scales. However, the results do not validate this initial assumption, since, in Figure 4.10, it is observed that the gasket device is equally as resonant. This may relate to the simplification of the tetrix model. The reduction of the three-dimensional model to the one-dimensional mode only accounts for wave propagation in one direction. Similarly, the model of the Sierpinski gasket device restricts attention to wave propagation in the same direction [86]. Performing three-dimensional wave analysis on the Sierpinski tetrix device may yield better performance characteristics in comparison to the Sierpinski gasket device. In regards to the maximum amplitude the tetrix device has $G_t^5 = 5.967$ dB and the gasket device has $G_g^5 = 9.520$ dB. These amplitudes suggests that the increase in vertex degree from 3, for the gasket lattice, to 4, for the tetrix lattice,

156

has reduced the maximum amplitude by 37%. Thus, at each of the transducers resonant frequencies their related 3-dB bandwidths means that the Sierpinski tetrix fractal inspired device has a greater bandwidth of $BW_g^5 = 0.215\,\mathrm{MHz}$ than that of the Sierpinski gasket fractal inspired device, which is $BW_t^5 = 0.185\,\mathrm{MHz}$. The gain bandwidth product of the Sierpinski tetrix fractal inspired device was calculated to be $GBP_t^5 = 0.849$ which is a decrease of 49% compared to the gasket device, where $GBP_g^5 = 1.657$. This is most likely a result of the lower amplitudes present in the tetrix device.

Comparisons between the Sierpinski tetrix fractal inspired transducer and Euclidean transducer are much more encouraging. Figure 4.10 shows that the prefractal device contains more resonances than the traditional design. This is to be expected since the Sierpinski tetrix device benefits from range of length scales while standard designs generally only have a single length scale. The maximum amplitude for the standard device is $G_e = 3.463\,\mathrm{dB}$, and thus the Sierpinski tetrix device outperforms the standard device by 72% in terms of this metric. Moreover, the reception sensitivity bandwidth surpasses standard designs by an additional $0.583\,\mathrm{MHz}$ (using the amplitude at the resonant frequency of the Euclidean device). As a result of the increased amplitudes and bandwidth exhibited in the Sierpinski tetrix device, the gain bandwidth product is also enhanced; see Table 4.7. Noting

	First Peak Amplitude (dB)	3-dB Bandwidth (MHz)	Gain Bandwidth Product
Sierpinski Tetrix	5.967	0.846	3.341
Sierpinski Gasket	9.520	2.022	11.811
Euclidean	3.463	0.263	0.584

Table 4.7: Figures of merit for the Euclidean, Sierpinski gasket and tetrix prefractal transducers at generation level five in reception mode. The figures of merit for all devices has been calculated using the amplitude at the resonant frequency of the Euclidean transducer.

Tables 4.5 and 4.7, all fractal generation levels surpass the standard device in terms

of bandwidth. Here, in order to get a fair comparison, the bandwidths for the pre-fractal devices have all been calculated using the 3-dB amplitude of the second generation level. The advantage of pre-fractal designs over Euclidean designs is the presence of more resonances. It has been observed that the initial three fractal generation levels are not as effective in at least one of the figures of merit as the standard device. However, as the generation level is increased, so does the presence of resonances, thus increasing the values of all figures of merit. It was found that higher fractal generation level devices exhibited additional resonances at higher frequencies, while such resonances were absent in lower generation levels. Thus, it may be established that devices designed on high fractal generation levels will most closely resemble those found in nature, for which these systems are far more efficient in operating over a wider range of frequencies, giving rise to improved bandwidths. Therefore, the improvement in these values as the generation level is increased demonstrates that multiple resonances enhance transducer performance. The amplitude at fractal generation level four exceeds the standard device, and fractal generation level three shows a significant improvement in regards to the gain bandwidth product. In particular, there is over a two fold increase at this fractal generation level over that of the standard device. Thus, the results in comparison to a standard design suggest strongly that it would be worthwhile for a prototype based on the Sierpinski tetrix to be built, in order to determine whether experimental results support these theoretical results, especially for fractal generation level five. Three-dimensional printing of electronic sensors and additively-manufactured piezoelectric devices are still emerging technologies [68, 69, 137]. However, the scope exists for tackling the construction of these three-dimensional piezoelectric structures.

The effect of increasing the fractal generation level resulted with an improvement in all three metrics with the exception of generation level two. In addition, there was a decrease in regards to the operational bandwidth and gain bandwidth product when increasing the fractal generation level from four to five. However,

there is concern over the Sierpinski tetrix device performance in comparison to the Sierpinski gasket device at the same fractal generation level. On the other hand, the tetrix device performs much more effectively than currently favoured designs.

4.6.3 Convergence of the Model

The convergence of the fractal generation level for the transmission and reception sensitives is presented in this section. This is achieved by computing the summation of the absolute value of the difference between successive fractal generations, integrated with respect to frequency, for up to 50 generation levels. That is

$$\bar{\psi}(n) = \frac{\|\psi(f;n) - \psi(f;n+1)\|_2}{\max \psi(f;n)}, \tag{4.55}$$

for the transmission sensitivities and for the reception sensitivities,

$$\bar{\phi}(n) = \frac{\|\phi(f;n) - \phi(f;n+1)\|_2}{\max \phi(f;n)}, \tag{4.56}$$

where $\psi(f;n)$ and $\phi(f;n)$ are the transmission and reception sensitivity, at frequency f and generation level n, respectively. Previous research [7, 86] has also applied this same technique in order to determine the point of convergence for the Sierpinski gasket fractal inspired transducer.

Figure 4.11 illustrates the points of convergence for the transmission sensitivities for both the Sierpinski tetrix and Sierpinski gasket transducers, and has been normalized between zero and one with respect to their maximum values. From this plot it is apparent that the Sierpinski tetrix device converges at a lower fractal generation level than the Sierpinski gasket device. Using a 5% tolerance level the Sierpinski tetrix device convergences by fractal generation level $n = 15$, while the Sierpinski gasket device converges by fractal generation level $n = 20$. At a 1% tolerance level the convergences are $n = 19$ and $n = 27$ for the Sierpinski tetrix and gasket devices respectively. Similarly Figure 4.12 shows the convergence of reception sensitivities of the Sierpinski tetrix and Sierpinski gasket devices and is again normalized between zero and one. It can be seen that significant improvements can be made on the reception sensitivity by increasing the generation level

159
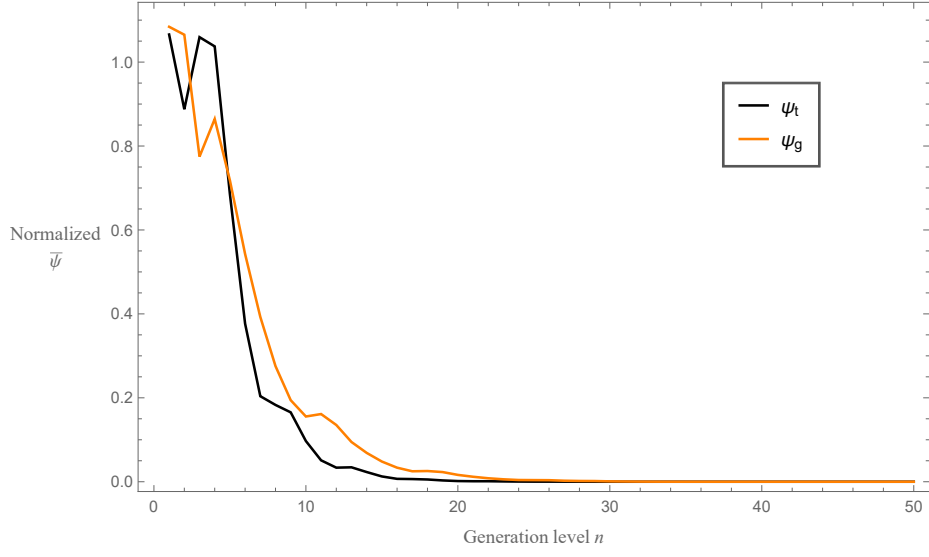
Figure 4.11: Normalized transmission sensitivity for the Sierpinski tetrix ($\bar{\psi}_t$ black full line) and Sierpinski gasket ($\bar{\psi}_g$ orange full line) devices as a function of fractal generation level n, over a frequency range of $0.1 - 10\,\text{MHz}$.

from one to five. Thereafter, the differences between each successive generation level decreases before converging. The Sierpinski tetrix device converges at a lower
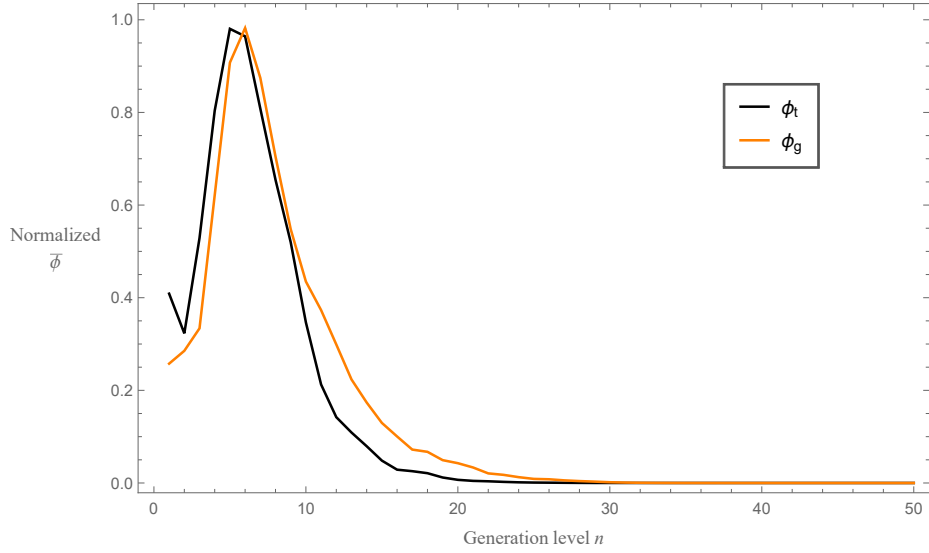
Figure 4.12: Normalized reception sensitivity for the Sierpinski tetrix ($\bar{\phi}_t$ black full line) and Sierpinski gasket ($\bar{\phi}_g$ orange full line) devices as a function of fractal generation level n, over a frequency range of $0.1 - 10\,\text{MHz}$.

fractal generation level when compared with the Sierpinski gasket device. At the 5% tolerance level, the Sierpinski tetrix device converges by fractal generation level $n = 25$, while the Sierpinski gasket device converges by fractal generation level $n = 32$. The 1% tolerance level shows the points of the convergences to be $n = 28$ for the Sierpinski tetrix device and $n = 34$ for the Sierpinski gasket device. From a manufacturing perspective, this is positive as it shows that a device which incorporates a pre-fractal with a high generation level is not required. The trade-off between design intricacy and device performance is maximised at around generation level five, which is possible with the current prototyping technology.

4.7 Conclusions

This chapter investigated a Sierpinski tetrix fractal inspired transducer using the Green function renormalization technique as a method for obtaining the transducer operating characteristics, modelled on a PZT-5H ceramic. The electrical impedance, transmission and reception sensitivities for a Sierpinski tetrix-like transducer were analysed by constructing the lattice equivalents, as was previously performed for the Sierpinski gasket and carpet devices [7, 19, 20, 86].

As a result of current manufacturing procedures, the construction of pre-fractal transducers would be restricted to low fractal generation levels. This is as a consequence of the reduction in the size of the length scales as the generation level is increased. Thus, in this chapter only the performance of the first five fractal generation levels have been discussed. However, fractal generation level fifteen has been included to determine what effect higher fractal generation levels have on the performance of the transducer. The point of convergence of the transducers performance was also studied. From this analysis it was shown that the transmission sensitivities converged at around fractal generation level $n = 15$ at the 5% tolerance level and at fractal generation level $n = 19$ at the 1% tolerance level. The reception sensitivities converged by fractal generation level $n = 25$ with a tolerance level of 5% and converged at $n = 28$ with a 1% tolerance level. However,

transducers based on the design of fractal generation levels beyond $n = 5$ would currently cause manufacturing difficulties.

To assess the performance of a Sierpinski tetrix fractal inspired transducer, a computer model was utilised to plot each of the operating characteristics as a function of the operating frequency. This was then compared to a previously investigated Sierpinski gasket fractal inspired transducer as well as a conventional designed transducer. As expected, the tetrix device experienced more resonances at a wider range of frequencies than the standard transducer. Furthermore, an increase in the fractal generation level led to a more resonant device with the presence of higher frequency resonances. Thus, fractal-inspired transducers demonstrate suitability for a various number of purposes. In transmission mode for the Sierpinski tetrix pre-fractal, an increase in the fractal generation level resulted in an increase in the device's bandwidth. However, the increase in device bandwidth resulted in a reduction in the corresponding maximum amplitudes. Additionally, the value of the gain bandwidth product also decreased as the fractal generation level increased. In comparison of the Sierpinski tetrix device with the Sierpinski gasket and Euclidean devices, it was found that a transducer inspired by the Sierpinski tetrix was less efficient in the transmission of ultrasound. This was concluded since all figures of merit for the Sierpinski tetrix device were calculated to be less than the other two devices when using the same amplitude. In regards to the reception sensitivities, an increase in fractal generation level was followed by an increase in the sensitivity amplitude and gain bandwidth product. Yet the increase in amplitudes resulted in reduced 3-dB bandwidths at the resonant frequencies. For fractal generation level five, these figures of merit were all reduced in comparison to the previously investigated Sierpinski gasket fractal inspired transducer. However, in regards to device performance over traditional designs, the analysis presented in this chapter indicates a substantial increase in each of these figures of merit. Comparisons between the Sierpinski tetrix, Sierpinski gasket and Euclidean devices were evaluated using the amplitude of the Euclidean device at

its resonant frequency. These results do therefore suggest the possibility that a Sierpinski tetrix fractal inspired transducer could be suitable in ultrasonic design to enhance current performance in reception mode.

Given the simplified nature of the model, it could be beneficial to investigate this structure using finite element analysis akin to that done on the Sierpinski gasket pre-fractal in [7, 32]. Utilising this method would allow for the re-introduction of longitudinal and shear propagating waves into the model. Transducer performance optimization could also be employed with the aim of improving the values of the bandwidth, amplitude and gain bandwidth product. This could be achieved by sampling different material parameters, such as the piezoelectric constant and Young's modulus [12]. This provides an opportunity to ascertain a range of materials that could be used in the creation of novel fractal-inspired ultrasonic transducers.

Chapter 5

Modelling of Product Lattice Inspired Transducers

5.1   Introduction

In this chapter, the Green function renormalization method is extended to investigate the performance of infinitely ramified structures. Previously, in Chapter 3, the effects of infinitely ramified Sierpinski carpet devices were studied using an adaptation of the renormalization method. The extension in this chapter obtains Green functions by considering the Cartesian product of two pre-fractal lattices. In particular, the Cartesian product of the Sierpinski gasket with itself and the Cartesian product of the Sierpinski carpet with itself are presented.

In previous research [7, 8, 12, 19, 20, 32, 83, 86, 97], it was concluded that fractal-inspired ultrasonic transducers were found to be superior to conventional Euclidean designs in terms of the operating characteristics of the device. This demonstrated the benefits of multi-length scaled devices. One potential method of increasing the range of length scales of these new designs is to consider the product design of two pre-fractal structures that is, the design obtained from the Cartesian product of two graphs. The results presented within this chapter are relevant in determining the potential performance of ultrasonic transducers that are significantly more complex in their design, and which possess a greater range of length scales. However, the results are merely theoretical, since only the

structures of the lattice counterparts are discussed. It is important to note that a lattice structure is used to derive the operating characteristics for a theoretical device, but it does not necessarily relate to a specific physical object. As such, it is difficult to illustrate the number of length scales, or even represent the design of the transducer. Nevertheless, this study is significant in deducing whether there is motive to investigate more intricate designs. To reiterate, the lattice structures are only used to study wave propagation. Thus, further research is required to determine the actual design of the transducer in order for a potential prototype to be fabricated. However, for the purpose of this chapter it is only of interest to determine the likely performance of such theoretical designs.

The Cartesian product of two graphs is obtained by employing the usual definition of the Cartesian product of two sets. The Cartesian product of two sets is the set that takes all ordered pairs, i.e. for the sets $\boldsymbol{A} = \{\boldsymbol{a_1}, \boldsymbol{a_2}, \cdots, \boldsymbol{a_n}\}$ and $\boldsymbol{B} = \{\boldsymbol{b_1}, \boldsymbol{b_2}, \cdots, \boldsymbol{b_m}\}$, the Cartesian product $\boldsymbol{A} \times \boldsymbol{B}$ is given by

$$\boldsymbol{A} \times \boldsymbol{B} = \{(\boldsymbol{a}, \boldsymbol{b}) | \boldsymbol{a} \in \boldsymbol{A}, \boldsymbol{b} \in \boldsymbol{B}\}. \tag{5.1}$$

Consequently, the Cartesian product of two graphs is achieved in a similar manner. For instance if $\mathcal{G}_1$ is a graph with the vertex set $V_S(\mathcal{G}_1) = \{u_1, u_2, ..., u_m\}$ and $\mathcal{G}_2$ is another graph with the vertex set $V_S(\mathcal{G}_2) = \{v_1, v_2, ..., v_n\}$ the Cartesian product, $\mathcal{G}_1 \otimes \mathcal{G}_2$, is the graph whose vertex set is $V_S(\mathcal{G}_1) \times V_S(\mathcal{G}_2)$. In addition, two vertices (u_i, v_j) and (u_k, v_l) are adjacent in $\mathcal{G}_1 \otimes \mathcal{G}_2$ if and only if

1. $u_i = u_k$ and v_j is adjacent to $v_l \in \mathcal{G}_2$, or

2. $v_j = v_l$ and u_i is adjacent to $u_k \in \mathcal{G}_1$.

To demonstrate this process, it is possible to consider the following simple example; $\mathcal{G}_1$ is a graph with vertex set $V_S(\mathcal{G}_1) = \{a, b\}$ and $\mathcal{G}_2$ is another graph with vertex set $V_S(\mathcal{G}_2) = \{1, 2, 3\}$. Thus, the Cartesian product is the graph whose vertex set is the set of ordered pairs, $V_S(\mathcal{G}_1) \times V_S(\mathcal{G}_2) = \{(a, 1), (a, 2), (a, 3), (b, 1), (b, 2), (b, 3)\}$. The initial graphs and resultant graph obtained from the Cartesian product are shown in Figure 5.1.
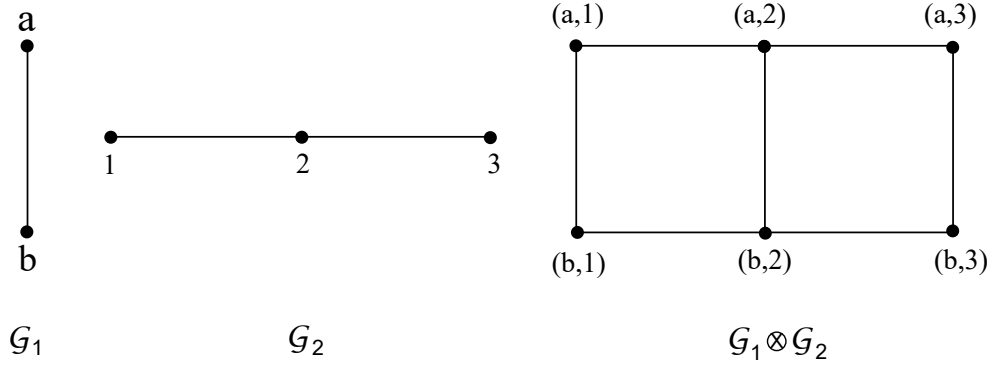
Figure 5.1: Representation of the Cartesian graph product of two one-dimensional lines, resulting in a rectangular structure.

While this extension to the Green function renormalization method has not previously been applied to evaluate the performance of product lattice transducers, it has previously been implemented to study the Green functions of infinitely ramified fractals [39, 40, 111], particularly to account for spectral dimensions greater than two. The spectral dimension of a fractal is different to the fractional dimension. The fractional dimension refers to the structural properties of the fractal, while the spectral dimension is in reference to the topological (dynamical) properties of the fractal [55, 123]. To demonstrate the spectral dimension it is possible to consider the spectral dimension of the Sierpinski gasket. Previously the fractional dimension was obtained using the Hausdorff Besicovitch description given in equation (1.1). Thus, for the Sierpinski gasket the fractional dimension is $D_f = \log(3)/\log(2)$. Equally the same result may be obtained using [55, 80, 89, 103, 104],

$$D_f = \frac{\log(d+1)}{\log(2)}, \tag{5.2}$$

where d is the dimension of embedding Euclidean space. For deterministic fractals the spectral dimension can be obtained exactly [89]. Hence, the spectral dimension for the Sierpinski gasket is [55, 89, 104]

$$d_s = 2\frac{\log(d+1)}{\log(d+3)} = 2\frac{\log(3)}{\log(5)}. \tag{5.3}$$

Furthermore, for the Sierpinski gasket the following relation holds [89, 103, 104],

$$d \geq D_f \geq d_s. \tag{5.4}$$

That is,

$$2 > 1.585 > 1.365. \tag{5.5}$$

For the Cartesian product graphs, the fractional and spectral dimensions are twice those of the fractal graphs [40, 111].

In this chapter the results of a theoretical transducer, whose product lattice is the Cartesian product of two Sierpinski gasket lattices for generation level one, is of interest. In addition, the result for the Cartesian product of two Sierpinski carpet lattices for the same generation level is explored. To begin this investigation, the product lattices need to be derived. Thus, by applying the definition of the Cartesian product of two graphs presented above, the resultant Sierpinski gasket and Sierpinski carpet product lattices can be formed. Figure 5.2 details
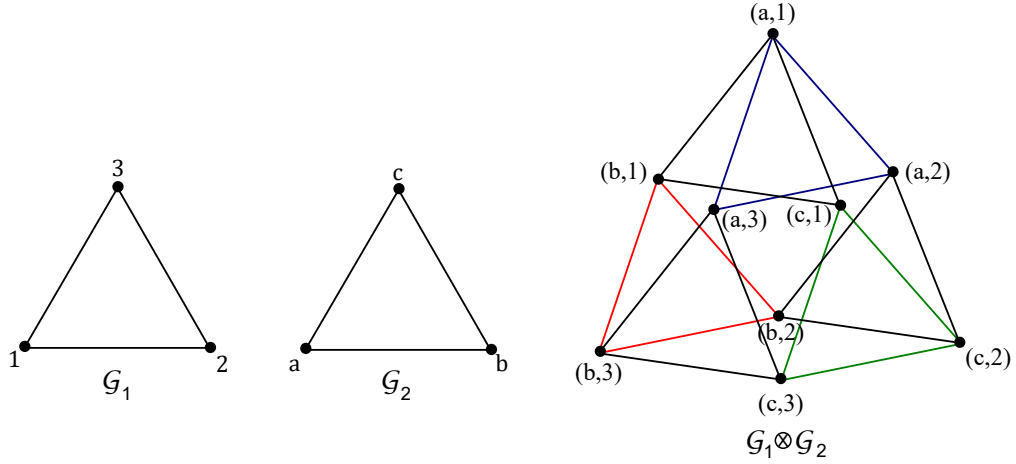
Figure 5.2: The Cartesian graph product $\mathcal{G}^{(p)} = \mathcal{G}_1 \otimes \mathcal{G}_2$, with the vertex set $\{(1, a), (1, b), (1, c), (2, a), (2, b), (2, c), (3, a), (3, b), (3, c)\}$, of two Sierpinski gasket lattices at fractal generation level $n = 1$, where $V_S(\mathcal{G}_1) = \{1, 2, 3\}$ and $V_S(\mathcal{G}_2) = \{a, b, c\}$.

the process of obtaining the Cartesian product of two Sierpinski gasket fractal lattices at generation level $n = 1$ and Figure 5.3 illustrates the resultant Sierpinski
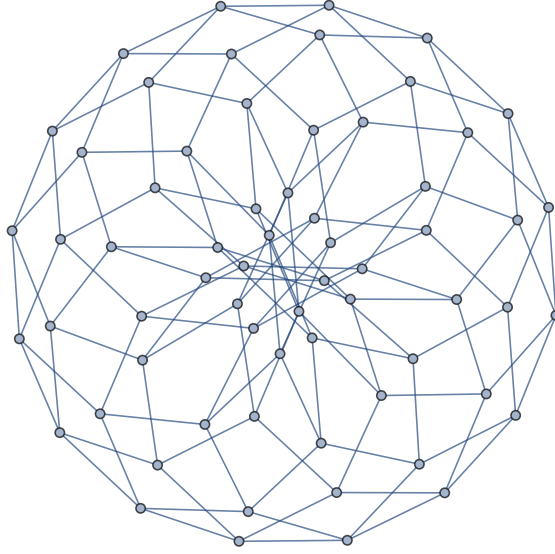
Figure 5.3: Schematic representation of the Cartesian product of the Sierpinski carpet lattice at fractal generation level $n = 1$ with itself.

carpet product lattice obtained from two first generation level lattices. For the Sierpinski gasket product lattice, the theoretical transducer is assumed to interact with input voltages at vertex $(a, 1)$ (and so a positive electric charge is applied to the transducer at this vertex in transmission mode) and mechanical loads at vertices $(a, 2)$ and $(a, 3)$. The input/output loads have been chosen specifically to be consistent with the original Sierpinski gasket inspired transducer. Similar to the Sierpinski gasket fractal lattice, at the first fractal generation level all vertex degrees are consistent and equal to four (for the Sierpinski gasket fractal lattice this is equal to two). However, as the generation level is increased the vertex degrees become inconsistent. In particular, the Cartesian product of two Sierpinski gasket lattices at fractal generation level two, have a vertex degree equal to six for internal vertices, a vertex degree of five for vertices on an edge and a vertex degree of four for corner vertices. However, the models considered here are only of the first generation level product graphs.

It should be borne in mind that a transducer configured on the Sierpinski carpet product lattice is likely to result in manufacturing difficulties. The lattice

168

structure, obtained as the Cartesian product of two Sierpinski carpet lattices at their first fractal generation level, has a total of 128 edges. In contrast, the structure of a single Sierpinski carpet lattice for the same generation level has only 8 edges. Nevertheless, the results presented in this chapter are included to further support the belief that devices with a range of length scales yield improved proficiency in the detection and generation of ultrasonic waves, specifically in comparison with the traditional designed devices. In contrast, it may be possible to construct a transducer whose lattice counterpart is the Sierpinski gasket product lattice prototype. However, this likely only achievable for its first lattice generation level, as a result of the significant increase in the amount of edges as the generation level is increased. Likewise, it is assumed that the amount of length scales, within higher generation levels, would increase considerably. Manufacturing constraints are therefore to be expected on the assembly of such prototypes.

5.2 Green Function Application to Product Lattices

Both structures investigated in this section are obtained by taking the Cartesian product of pre-fractal lattice with itself. Therefore, it follows that the product graph is given by [40]

$$\mathcal{G}^{(\pi)} = \mathcal{G} \otimes I_n + I_n \otimes \mathcal{G}, \tag{5.6}$$

where I_n is the N_n-vertex identity graph. As before, the graph $\mathcal{G}$ consists of Laplacian matrix $A^{(n)} = H^{(n)} - qI_n$ and boundary matrix $B^{(n)}$. Then by denoting $k^{(n)} = A^{(n)} + B^{(n)}$ the resulting Green function matrix is $G^{(n)} = (p^2 I_n - k^{(n)})^{-1}$, where p is a complex variable.

The product graph $\mathcal{G}^{(\pi)}$ has a total of $N_n \times N_n = N_\pi$ vertices. Thus, for the Sierpinski carpet and Sierpinski gasket product lattices, the total numbers of vertices are $N_\pi = 2^{6n}$ and $N_\pi = 3^{2n}$ respectively. Yet the side length of the Cartesian product lattices remains fixed. As a result of the dimensions of these new structures, representations of these three-dimensional lattices become extremely

difficult to represent. To attempt to illustrate this, the front face of the lattice structure depicted in Figure 5.2, would be the triangle whose vertex set is $\{(a, 1), (a, 2), (a, 3)\}$. The adjacency matrix associated with the Green function matrix of the product graph, $\hat{G}^{(\pi)}$ (where $\hat{G}^{(\pi)}$ indicates the matrix not accounting for boundary conditions), is expressed as [39, 40, 111]

$$H^{(\pi)} = H_1^{(n)} \otimes I_n + I_n \otimes H_2^{(n)}, \tag{5.7}$$

where $H_1^{(n)}$ and $H_2^{(n)}$ indicate individual lattice graphs. Of course the matrices $H_1^{(n)}$ and $H_2^{(n)}$ do not have to be the same. However, the results presented in this chapter are modelled on the Cartesian product of a graph with itself, and so the subscripts can be dropped. Thus,

$$H^{(\pi)} = H^{(n)} \otimes I_n + I_n \otimes H^{(n)}. \tag{5.8}$$

Similar to $H^{(\pi)}$, an expression for $k^{(\pi)}$ is given by

$$k^{(\pi)} = k^{(n)} \otimes I_n + I_n \otimes k^{(n)}. \tag{5.9}$$

The characteristic equation for the Laplacian matrix $A^{(n)}$ is

$$A^{(n)} \varphi^\sigma = \lambda_\sigma \varphi^\sigma, \tag{5.10}$$

where $\{\lambda_\sigma\}_{\sigma=1}^{N_n}$ is the set of eigenvalues of $A^{(n)}$ with corresponding eigenvectors $\{\varphi^\sigma\}_{\sigma=1}^{N_n}$ and N_n is the total number of vertices of the graph. Thus, the entries of the bare Green function matrix may be expressed as [40, 111]

$$\hat{G}_{(i,j)}^{(n)} = \sum_{\sigma=1}^{N_n} \frac{1}{p^2 - \lambda_\sigma} \varphi_i^\sigma \varphi_j^\sigma. \tag{5.11}$$

Equally it follows that $\{\lambda_\zeta\}_{\zeta=1}^{N_n}$ is the set of eigenvalues of a second matrix (i.e. $A_2^{(n)}$) with corresponding eigenvectors $\{\varphi^\zeta\}_{\zeta=1}^{N_n}$. Therefore, the eigenvectors of $A^{(\pi)}$ are obtained by taking the direct product of the eigenvectors of $A_1^{(n)}$ and $A_2^{(n)}$ (here $A_1^{(n)} = A_2^{(n)} = A^{(n)}$), $\varphi_{i,j}^{(\sigma+\zeta)} = \varphi_i^\sigma \varphi_j^\zeta$. Consequently, the corresponding eigenvalues are

$\lambda_\sigma + \lambda_\zeta$. Hence, the entries of the bare Green function matrix for the product lattice are given by [40, 111]

$$\hat{G}^{(\pi)}_{(i,h)(j,k)} = \sum_{\sigma=1}^{N_n} \sum_{\zeta=1}^{N_n} \frac{1}{p^2 - (\lambda_\sigma + \lambda_\zeta)} \varphi_i^\sigma \varphi_j^\sigma \varphi_h^\zeta \varphi_k^\zeta. \tag{5.12}$$

For the Sierpinski gasket product lattice, the eigenvalues and corresponding eigenvectors, when boundary conditions are neglected, are

$$\lambda_1 = -1, \qquad \varphi^1 = \begin{pmatrix} 1 \\ 1 \\ 1 \end{pmatrix}, \tag{5.13}$$

$$\lambda_2 = -4, \qquad \varphi^2 = \begin{pmatrix} 0 \\ 1 \\ -1 \end{pmatrix}, \tag{5.14}$$

$$\lambda_3 = -4, \qquad \varphi^3 = \begin{pmatrix} 1 \\ 0 \\ -1 \end{pmatrix}, \tag{5.15}$$

where $\lambda_\sigma = \lambda_\zeta$ and $\varphi^\sigma = \varphi^\zeta$ and equations (5.13)-(5.15) are the eigenvalues and eigenvectors of $A^{(1)}$. For a theoretical device modelled using the Cartesian product of two Sierpinski gasket fractal lattices at generation level one (Figure 5.2), the input vertex is at $(a, 1)$ and the output vertices are $(a, 2)$ and $(a, 3)$. Therefore, at the input vertex $(i, h) = (a, 1)$ the pivotal Green function according to equation (5.12) is

$$\begin{aligned} \hat{G}^{(\pi)}_{(a,1)(a,1)} &= \sum_{\sigma=1}^{N} \sum_{\zeta=1}^{N} \frac{1}{p^2 - (\lambda_\sigma + \lambda_\zeta)} \varphi_a^\sigma \varphi_a^\sigma \varphi_1^\zeta \varphi_1^\zeta \\ &= \sum_{\sigma=1}^{N} \left(\frac{1}{p^2 - (\lambda_\sigma - 1)} \varphi_a^\sigma \varphi_a^\sigma (1)(1) \right. \\ &\quad + \frac{1}{p^2 - (\lambda_\sigma - 4)} \varphi_a^\sigma \varphi_a^\sigma (0)(0) \\ &\quad \left. + \frac{1}{p^2 - (\lambda_\sigma - 4)} \varphi_a^\sigma \varphi_a^\sigma (1)(1) \right) \\ &= \frac{2(2p^4 + 20p^2 + 41)}{(p^2 + 8)(p^2 + 5)(p^2 + 2)}. \end{aligned} \tag{5.16}$$

171

To accommodate for boundary conditions at the input/output vertices, the pivotal Green functions are obtained similarly. That is, by deriving the eigenvalues and eigenvectors of $k^{(1)}$ and subsequently utilising equation (5.12). Thus, at the input vertex

$$
\begin{aligned}
G^{(\pi)}_{(a,1)(a,1)} &= \frac{2(p^2 - b_1 - b_2 + 5)}{p^4 - 2p^2(b_1 + b_2 - 5) + 4(b_1(b_2 - 2) - 3b_2 + 4)} \cdot \\
&+ \frac{2}{p^2 - b_1 - b_2 + 5}
\end{aligned}
\tag{5.17}
$$

In a similar manner, all remaining pivotal elements for both the Sierpinski gasket and Sierpinski carpet product lattices can be obtained through the application of equation (5.12). It follows that the required Green functions for the Sierpinski gasket product lattice are $G^{(\pi)}_{(a,1)(a,1)}$, $G^{(\pi)}_{(a,1)(a,2)}$, $G^{(\pi)}_{(a,2)(a,2)}$ and $G^{(\pi)}_{(a,2)(a,3)}$. However, the resultant expressions are large and so for brevity these are presented in Appendix D. Alternatively, a second model based on the Cartesian product of two Sierpinski gasket lattices is considered. For this model an input voltage is applied to the device at vertex $(a, 1)$ and two output vertices, $(b, 3)$ and $(c, 2)$, will convert the ultrasonic wave into mechanical vibrations. Thus, the required Green functions are $G^{(\pi)}_{(a,1)(a,1)}$, $G^{(\pi)}_{(a,1)(b,3)}$, $G^{(\pi)}_{(b,3)(b,3)}$ and $G^{(\pi)}_{(b,3)(c,2)}$. The differences between these models are the location of the output vertices. For the first model (hereafter will be denoted with a subscript $g1$), ultrasonic waves only enter and leave the system through a single triangle within the product lattice graph. Thus, the full effect of the product lattice my not be accounted for. To account for the entirety of the structure, the output vertices are repositioned onto two other sub-triangles in the product lattice graph; see Figure 5.2. This positioning describes model 2 and so will be indicated with a subscript $g2$.

In these instances it has been possible to determine the pivotal Green functions from inspection of the symmetries of the product lattice. However, for higher fractal generation levels, the resultant product graphs can be extremely complex and portrayal of them is difficult, even in 3-D [111]. In previous research [39, 40, 111],

the Green functions in equation (5.12) are further expressed as the convolution integrals, and the Green functions for $\mathcal{G}_1$ and $\mathcal{G}_2$ are assumed to be known.

5.3 Results

In this section, the operating performances of two Cartesian product fractal inspired transducers are investigated. The results for the two models of the Cartesian product of a Sierpinski gasket lattice with itself are presented in Section 5.3.1. Only generation level one is considered due to computer power limitations. Moreover, higher fractal generation level designs would currently present manufacturing difficulties. Analogous to earlier transducer models, a mathematical computer model is employed to test the performance of the Cartesian product of the Sierpinski gasket inspired transducer at its first generation level. Furthermore, a comparison of the transducer model between the previously investigated Sierpinski gasket inspired transducer, at fractal generation level one, and the standard Euclidean device is presented.

In Section 5.3.2, the Cartesian product of the Sierpinski carpet lattice with itself is also investigated. Although manufacturing of such a device is currently unlikely due to its complexity, it offers an insight into to the expected performance of ultrasonic transducers that have non-regular geometry and a wide range of length scales. Similar to previous chapters, the transducer model is compared with the standard Euclidean model as well as the Sierpinski carpet inspired transducer.

5.3.1 The Sierpinski Gasket Product Lattice Transducer

As previously mentioned two models are considered for which the Cartesian product of two Sierpinski gasket lattices, at generation level one, is used to investigate wave propagation. Firstly, the results obtained from model one is presented. Figure 5.4 illustrates a comparison in electrical impedance profiles between the Cartesian product of two Sierpinski gasket lattices (Figure 5.2), the Sierpinski gasket pre-fractal transducer and the conventional Euclidean transducer. As with

Figure 5.4: Non-dimensionalised electrical impedance $\hat{Z}$ (dB) versus frequency f (Hz) for the model 1 Sierpinski gasket product lattice inspired transducer ($\hat{Z}_{g1}^{(\pi)}$ dark blue full line, equation (2.162), with the appropriate substitutions), the Sierpinski gasket fractal inspired transducer at generation level $n = 1$ ($\hat{Z}_g^1$ orange full line, equation (2.162)) and the traditional Euclidean transducer ($\hat{Z}_e$ purple full line, equation (2.45)).

earlier results herein and the devices investigated here are modelled on a PZT-5H ceramic. The structure of the Cartesian product inspired device is the product graph of the Sierpinski gasket with itself at generation level $n = 1$. Therefore, the previously investigated Sierpinski gasket inspired transducer at generation level $n = 1$ has been used to provide an appropriate comparison. The electrical impedance profile of the Cartesian product design matches very closely to the profile of the Sierpinski gasket design with the addition of an extra resonance. This is as a result of the presence of a greater range of length scales in the modified gasket design. Furthermore, resonances at higher frequencies are absent. This is also the case in the design of the Sierpinski gasket inspired device and it is not until the fractal generation level is increased that higher frequency resonant modes occur. It is presumed that higher fractal generation level designs of the Cartesian product inspired device would adhere to similar profiles. Whilst it is possible to consider

analytically the results of higher fractal generation level Cartesian product designs, only the first fractal generation level has been studied. To some extent, this is as a consequence of manufacturing constraints that would be present in such designs. Although the predominate reason is as a result of computing limitations. The electrical and mechanical resonant frequencies together with the corresponding electrical impedances for Cartesian product, Sierpinski gasket inspired and Euclidean devices are given in Table 5.1.

	Electrical Resonant Frequency		Mechanical Resonant Frequency	
	f_e (MHz)	Z (dB)	f_m (MHz)	Z (dB)
Model 1 Sierpinski Gasket Product Lattice	0.926	-8.740	1.185	0.380
Sierpinski Gasket	1.027	-6.306	1.195	-0.166
Euclidean	2.063	-6.191	2.220	5.218

Table 5.1: Electrical and mechanical resonant frequencies for the Euclidean, Sierpinski gasket inspired (generation level one) and model 1 Sierpinski gasket product lattice inspired transducers.

As is evident in Figure 5.5, there is a substantial improvement in the transmission sensitivity, over the standard and fractal-inspired transducers. In particular, there is an improvement of 20.084 dB in the maximum amplitude when comparing against the previous Sierpinski gasket inspired transducer. However, this increase in amplitude has resulted in a reduced bandwidth. While the previously investigated fractal-inspired device had an operational bandwidth of 0.077 MHz, the Cartesian product of this pre-fractal structure achieves only a 3-dB bandwidth of 0.002 MHz. Yet in regards to the gain bandwidth product the Cartesian product device outperforms the Sierpinski gasket inspired device. Table 5.2 presents the figures of merit for the device in transmission and reception mode.

Comparison between the three transducers in reception mode is illustrated in Figure 5.6. Similar to the transmission sensitivity of the device, the reception sen-
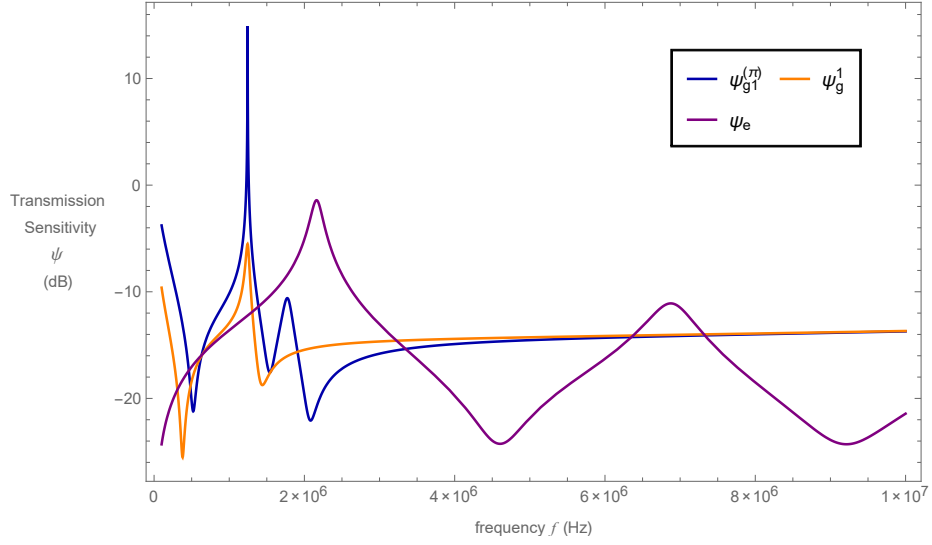
Figure 5.5: Non-dimensionalised transmission sensitivity ψ (dB) versus frequency f (Hz) for the model 1 Sierpinski gasket product lattice inspired transducer ($\psi_{g1}^{(\pi)}$ dark blue full line, equation (2.169), with the appropriate substitutions), the Sierpinski gasket fractal inspired transducer at generation level $n = 1$ (ψ_g^1 orange full line, equation (2.169)) and the traditional Euclidean transducer (ψ_e purple full line, equation (2.54)).

	Maximum Amplitude (Gain) (dB)	3-dB Bandwidth (MHz)	Gain Bandwidth Product
Transmission	14.567	0.002	0.070
Reception	1.059	0.157	0.201

Table 5.2: Figures of merit in for the model 1 Sierpinski gasket product lattice inspired transducer.

sitivity achieves greater amplitudes than the Sierpinski gasket inspired transducer. However, there is only a slight improvement in this instance. Furthermore, the potential operation of such a device in reception mode compares poorly in all figures of merit in comparison to the traditional design.

The results of the Cartesian product of two Sierpinski gasket lattices model suggest that there is a significant improvement in transmission amplitudes. However, the reception sensitivity of the device is outperformed in all figures of merit

176

Figure 5.6: Non-dimensionalised reception sensitivity ϕ (dB) versus frequency f (Hz) for the model 1 Sierpinski gasket product lattice inspired transducer ($\phi_{g1}^{(\pi)}$ dark blue full line, equation (2.173), with the appropriate substitutions), the Sierpinski gasket fractal inspired transducer at generation level $n = 1$ (ϕ_g^1 orange full line, equation (2.173)) and the traditional Euclidean transducer (ϕ_e purple full line, equation (2.58)).

in comparison to the Euclidean design, and in almost all when compared to the Sierpinski gasket inspired device. It appears that the additional edges within the pre-fractal lattice have resulted in more exaggerated resonances in the transmission and reception sensitives when comparing to the original Sierpinski gasket lattice.

The results presented thus far on the Cartesian product of two Sierpinski gasket lattices only considered an ultrasonic wave entering the system at the input vertex and exiting the lattice at the output vertices, all of which are positioned on the same triangle. As a result, this leads to narrow bandwidths in both operating functions compared to the standard and the Sierpinski gasket inspired designs. One way to increase the operational bandwidth for this theoretical device is to reposition the input/output vertices. In Section 5.2, the Green functions for an alternative model were defined and the results for this model are presented below.

The effect of repositioning the output vertices, that is having two output ver-

tices positioned at $(b, 3)$ and $(c, 2)$, where there remains a single input vertex at $(a, 1)$ i.e. model 2, on the electrical impedance of the device is illustrated in Figure 5.7. As shown in this figure, the change of output vertices has resulted in
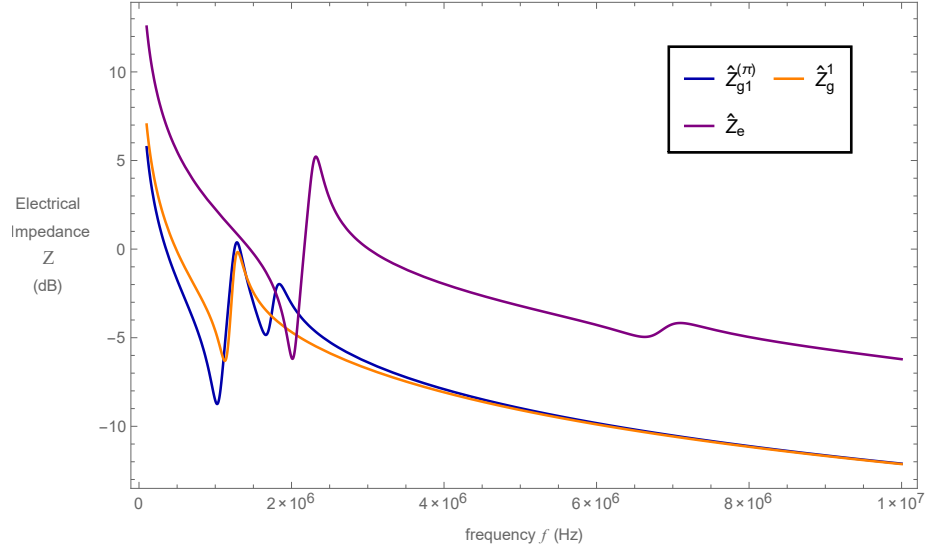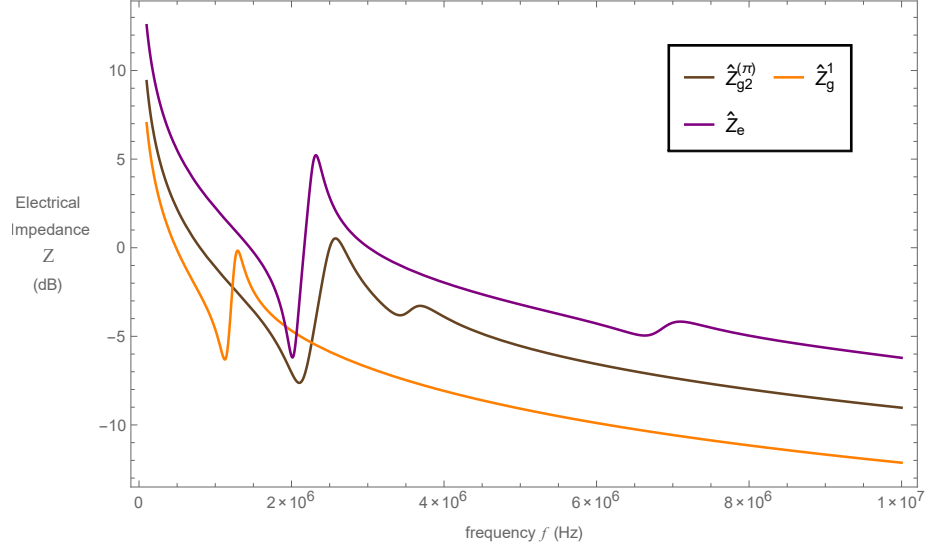

Figure 5.7: Non-dimensionalised electrical impedance $\hat{Z}$ (dB) versus frequency f (Hz) for the model 2 Sierpinski gasket product lattice inspired transducer (model two, $\hat{Z}_{g2}^{(\pi)}$ brown full line, equation (2.162), with the appropriate substitutions), the Sierpinski gasket fractal inspired transducer at generation level $n = 1$ ($\hat{Z}_g^1$ orange full line, equation (2.162)) and the traditional Euclidean transducer ($\hat{Z}_e$ purple full line, equation (2.45)).

the shift of the electrical and mechanical resonant frequencies. The occurrence of these frequencies is presented in Table 5.3 together with the corresponding electrical impedances. Since the electrical resonant frequency is less than the first

Electrical Resonant Frequency		Mechanical Resonant Frequency	
f_e (MHz)	$Z_{g2}^{(\pi)}$ (dB)	f_m (MHz)	$Z_{g2}^{(\pi)}$ (dB)
2.003	-7.626	2.478	0.525

Table 5.3: Electrical and mechanical resonant frequencies for the model 2 Sierpinski gasket product lattice inspired transducer.

model, it is assumed that the amplitude for the transmission sensitivity will be less for model 2. Whereas the mechanical resonant frequency attains higher electrical impedance than the earlier model and so the amplitudes for the reception sensitivity ought to be greater.

The transmission sensitivity for model 2 is plotted in Figure 5.8, together with the Sierpinski gasket inspired device and Euclidean transducer. Clearly, this fig-
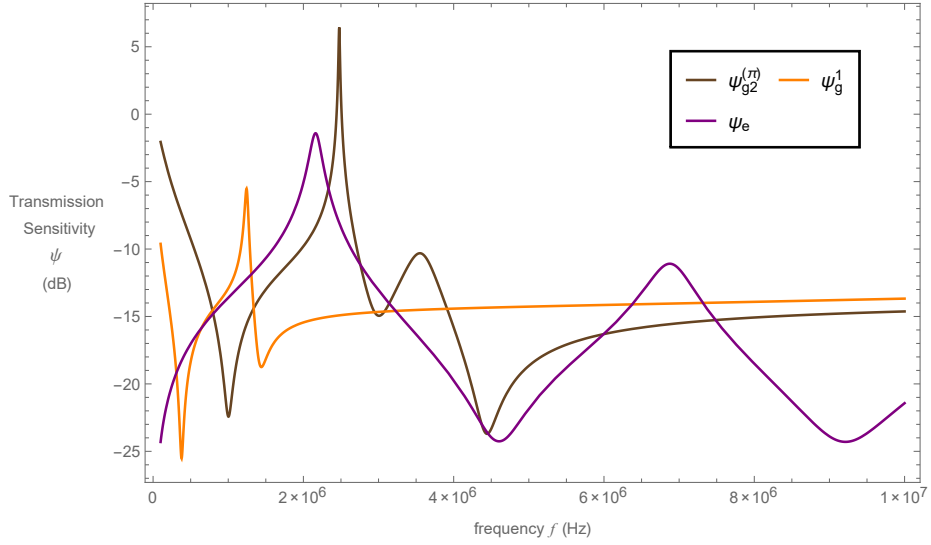
Figure 5.8: Non-dimensionalised transmission sensitivity ψ (dB) versus frequency f (Hz) for the model 2 Sierpinski gasket product lattice inspired transducer (model two, $\psi_{g2}^{(\pi)}$ brown full line, equation (2.169), with the appropriate substitutions), the Sierpinski gasket fractal inspired transducer at generation level $n = 1$ (ψ_g^1 orange full line, equation (2.169)) and the traditional Euclidean transducer (ψ_e purple full line, equation (2.54)).

ure shows that amplitude for the transmission sensitivity exceeds the Sierpinski gasket inspired and Euclidean devices. Furthermore, the gain bandwidth product surpasses the fractal-inspired device. However, there is still no improvement in the bandwidth of the device compared to the Sierpinski gasket inspired and standard designed transducers. The figures of merit for the transmission and reception sensitivities for model 2 are presented in Table 5.4.

The reception sensitivities profiles for model 2 and the Sierpinski gasket in-

179

	Maximum Amplitude (Gain) (dB)	3-dB Bandwidth (MHz)	Gain Bandwidth Product
Transmission	6.457	0.027	0.119
Reception	1.686	0.347	0.512

Table 5.4: Figures of merit for the model 2 Sierpinski gasket product lattice inspired transducer.

spired and Euclidean transducers are shown in Figure 5.9. Unlike the previous model there is some considerable improvement in the reception sensitivity of the device. In particular, there is a significant increase in device bandwidth. There is an increase in the operational bandwidth of 32% against the traditional design and a 5% increase compared to that of the Sierpinski gasket inspired transducer. Furthermore, all figures of merit have improved compared to that of the Sierpinski
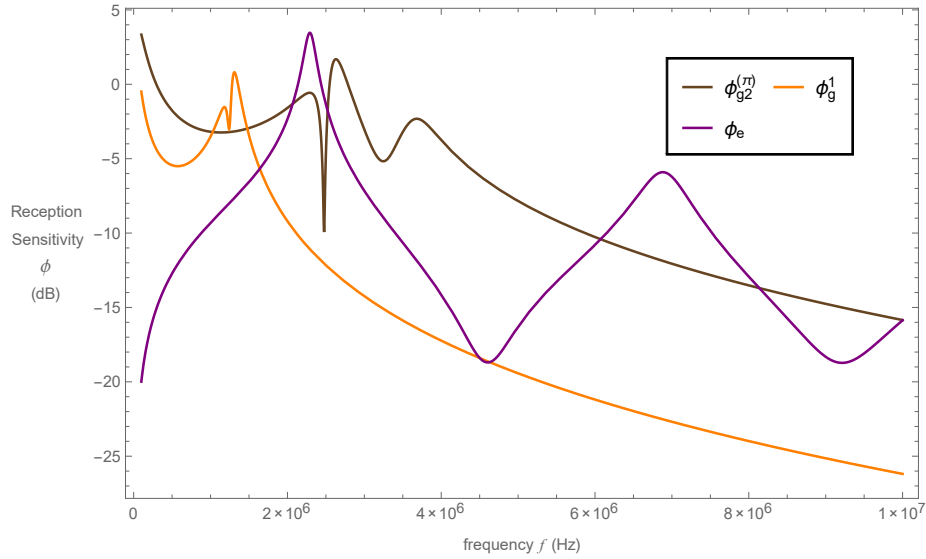
Figure 5.9: Non-dimensionalised reception sensitivity ϕ (dB) versus frequency f (Hz) for the model 2 Sierpinski gasket product lattice inspired transducer (model two, $\phi_{g2}^{(\pi)}$ brown full line, equation (2.173), with the appropriate substitutions), the Sierpinski gasket fractal inspired transducer at generation level $n = 1$ (ϕ_g^1 orange full line, equation (2.173)) and the traditional Euclidean transducer (ϕ_e purple full line, equation (2.58)).

gasket inspired device.

The second model of the Cartesian product design presents a substantial improvement in transducer performance, when comparing against the Sierpinski gasket inspired design. Though there is also some improvement against the traditional design. While additional resonances are absent in the device, the bandwidth at the resonate frequency is larger than the Sierpinski gasket inspired device and the traditional designed transducer in reception mode. Moreover, the results obtained for the two models are only illustrative of the product graph of two Sierpinski gaskets at the first fractal generation level. Consequently, it is assumed that the product graph at higher fractal generation levels would result in a richer range of resonating frequencies and increased device performance.

5.3.2 The Sierpinski Carpet Product Lattice Transducer
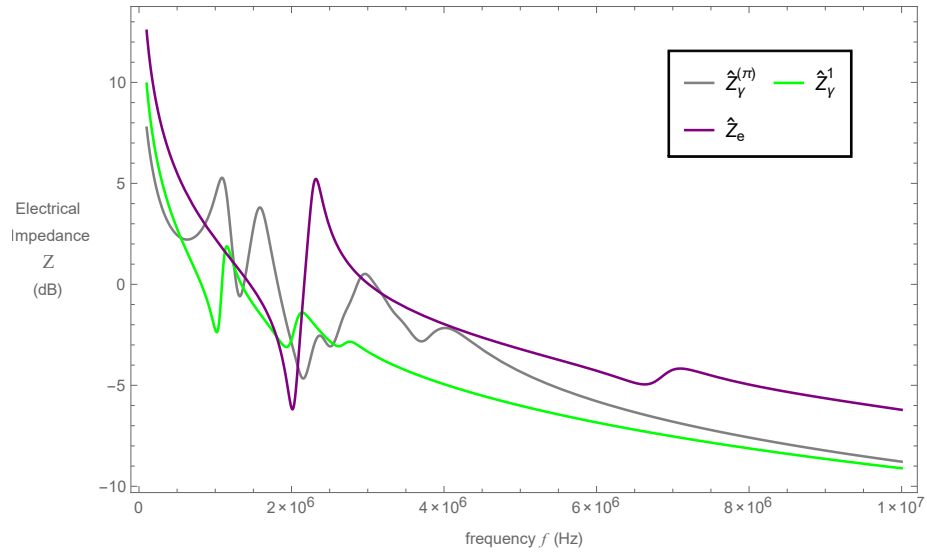
Figure 5.10: Non-dimensionalised electrical impedances $\hat{Z}$ (dB) versus frequency f (Hz) for the Sierpinski carpet product lattice inspired transducer ($\hat{Z}_\gamma^{(\pi)}$ grey full line, equation (3.70), with the appropriate substitutions), the Sierpinski carpet fractal inspired transducer at generation level $n = 1$ ($\hat{Z}_\gamma^1$ green full line, equation (3.80)) and the traditional Euclidean transducer ($\hat{Z}_e$ purple full line, equation (2.45)).

181

The electrical impedance profile for the proposed Sierpinski carpet product lattice inspired transducer (Figure 5.3) is plotted in Figure 5.10. This figure also illustrates the electrical impedance profiles for the Sierpinski carpet model γ device, at generation level $n = 1$, and the traditional Euclidean design transducer. The Cartesian product model displays a more resonant behaviour as a result of the increased range of length scales. Furthermore, the electrical and mechanical resonant frequencies occur at lower frequencies; see Table 5.5.

	Electrical Resonant Frequency		Mechanical Resonant Frequency	
	f_e (MHz)	Z (dB)	f_m (MHz)	Z (dB)
Sierpinski Carpet Product Lattice	0.532	2.218	0.990	5.278
Sierpinski Carpet model γ	0.906	-2.517	1.033	1.132
Euclidean	2.063	-6.191	2.220	5.218

Table 5.5: Electrical and mechanical resonant frequencies for the Euclidean, Sierpinski carpet inspired (model γ at generation level one) and Sierpinski carpet product lattice inspired transducers.

In Figure 5.11 it is clear that the transmission sensitivity of the Cartesian product design outperforms the standard and Sierpinski carpet model devices at all frequency ranges in terms of peak amplitude. Although from a frequency range of around 4 MHz and over, a flat response develops with a declining sensitivity value. Also, these peak amplitudes have resulted in reduced operating bandwidths, at the respective resonant frequencies, of 34% against the traditional design and 60% against the Sierpinski carpet model. Even though the increased amplitudes have caused restricted bandwidths, they have also lead to superior values for the gain bandwidth product. The figures of merit in transmission and reception mode for the Cartesian product device are tabulated in Table 5.6.
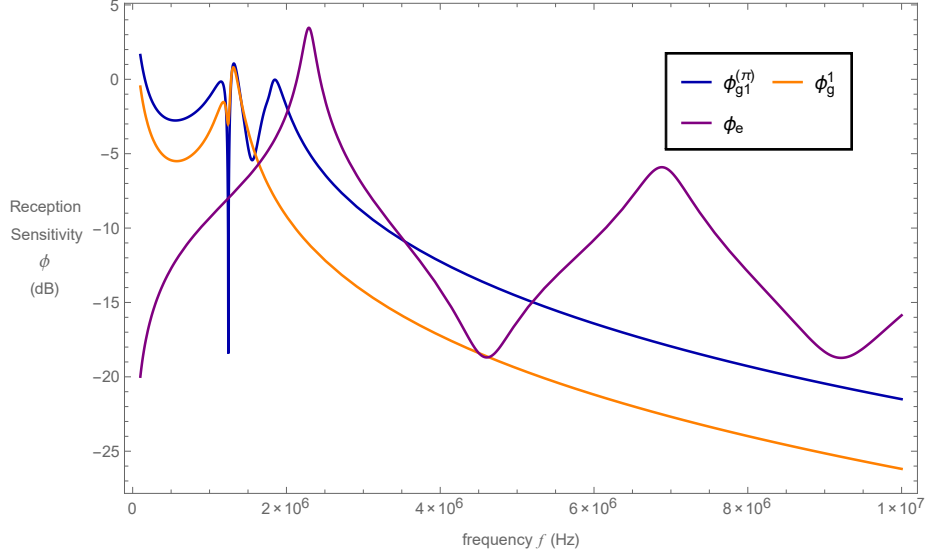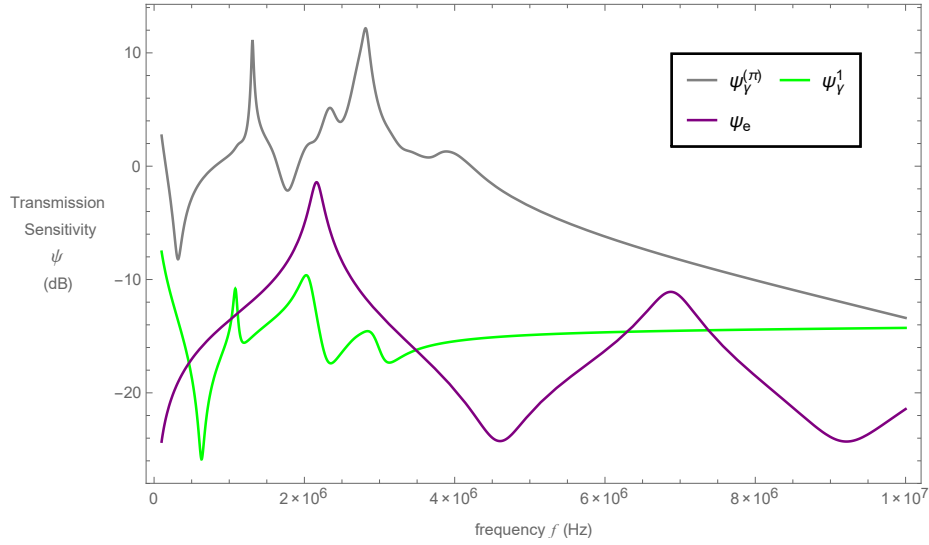
Figure 5.11: Non-dimensionalised transmission sensitivity ψ (dB) versus frequency f (Hz) for the Sierpinski carpet product lattice inspired transducer ($\psi_\gamma^{(\pi)}$ grey full line, equation (3.101), with the appropriate substitutions), the Sierpinski carpet fractal inspired transducer at generation level $n = 1$ (ψ_γ^1 green full line, equation (3.101)) and the traditional Euclidean transducer (ψ_e purple full line, equation (2.54)).

	Maximum Amplitude (Gain) (dB)	3-dB Bandwidth (MHz)	Gain Bandwidth Product
Transmission	12.171	0.171	2.822
Reception	15.022	0.236	7.516

Table 5.6: Figures of merit in for the Sierpinski carpet product lattice inspired transducer.

In reception mode the Cartesian product device contains more resonances than the comparative transducers; see Figure 5.12. As previously mentioned, this is as a result of the complexity of the structure. That is to say, the device has a wider range of length scales. Analogous to transmission mode, the reception sensitivity of the device displays higher peak amplitudes than the Sierpinski carpet inspired device and the traditional design transducer. In particular the Cartesian product device has a maximum amplitude that is 11.559 dB greater than the Euclidean de-
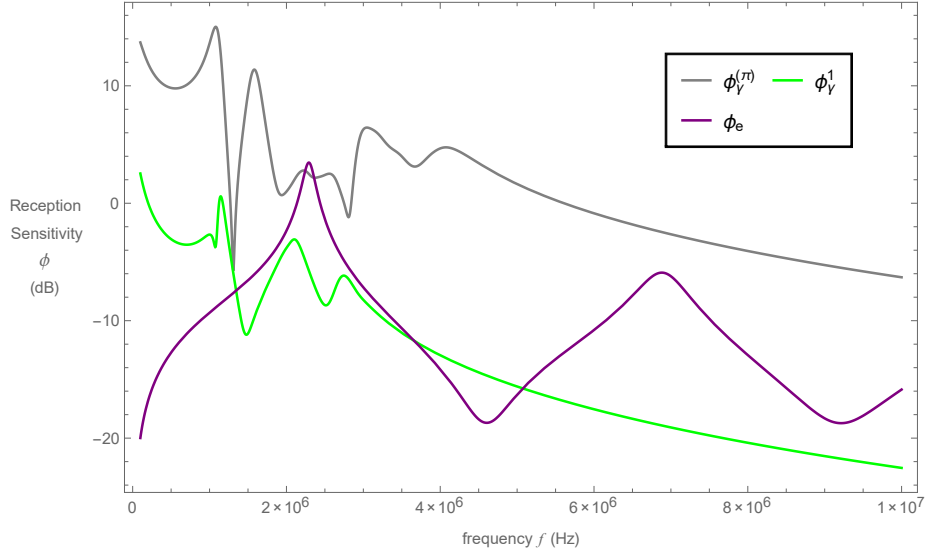
Figure 5.12: Non-dimensionalised reception sensitivity $\phi\,(\text{dB})$ versus frequency $f\,(\text{Hz})$ for Sierpinski carpet product lattice inspired transducer ($\phi_\gamma^{(\pi)}$ grey full line, equation (3.109), with the appropriate substitutions), the Sierpinski carpet fractal inspired transducer at generation level $n = 1$ (ϕ_γ^1 green full line, equation (3.109)) and the traditional Euclidean transducer (ϕ_e purple full line, equation (2.58)).

sign and $14.439\,\text{dB}$ higher than the Sierpinski carpet inspired device. Moreover the operational bandwidth of the Cartesian design improves on the Sierpinski carpet inspired design by 82%. However, it fails to surpass the traditional design bandwidth, where there is a 10% drop in efficiency. Nevertheless there is a significant improvement in regards to the gain bandwidth product over both the Euclidean and Sierpinski carpet inspired devices.

The results for the Cartesian product of the Sierpinski carpet demonstrated that the inclusion of a greater range of length scales does result in a more resonant device, with much higher peak amplitudes compared to the simpler fractal and Euclidean designs. However, in transmission mode the bandwidth of the new design was outperformed by the other two devices. Furthermore, the reception bandwidth was smaller than for the traditional design. Yet the gain bandwidth product exceeded both designs, which is attributed to the significant increase in the amplitude.

5.4 Conclusions

This chapter investigated the operating characteristics of two fractal-inspired devices obtained from the Cartesian product of two fractal lattices. The input/output renormalization method used in earlier chapters was extended to obtain the individual entries of the Green function matrix. This extension to Green function analysis has previously been described [39, 40, 111]. However, it has only been applied to transport properties on fractal structures, whereas this chapter has utilised this method to predict the theoretical performances of ultrasonic transducers with novel designs. To keep the results consistent with former chapters, the hypothetical designs discussed within this chapter have once again been modelled on a PZT-5H ceramic.

The first structure considered in this chapter was the Cartesian product of two Sierpinski gasket pre-fractal lattices, at generation level one. Only lattice structures of the first generation level have been considered. For structures of generation level two and higher, the complexity of the product lattice increase considerably and thus present computer difficulties in generating analytical results. The analysis is then continued to investigate a structure that is obtained as the Cartesian product of two Sierpinski carpet pre-fractal lattices at generation level one. In the case of the Cartesian product of the Sierpinski carpet, the results presented here are purely analytical since the structure of such a device is too complex.

As with earlier chapters, a computer model was used to produce the operating characteristics for the Cartesian product inspired devices. That, is the electrical impedance, transmission and reception sensitivities were evaluated at a given frequency range. Comparisons in performance between these novel designs with that of the previously investigated Sierpinski gasket and Sierpinski carpet pre-fractal transducers have been made. These designs were appropriate as the Cartesian product devices are an extension on the pre-fractal designs. Furthermore, the potential suitability of the devices for ultrasonic design purposes was compared to

185

that of the traditional Euclidean transducer.

It was anticipated that the Cartesian product of two Sierpinski gasket lattices would be more resonant than the single Sierpinski gasket lattice. However, it was not as resonant as expected since there was merely the addition of a single extra resonance. This may be due to the arrangement of the transducer in the circuit being very similar to the arrangement of the Sierpinski gasket inspired device. Specifically, the input vertex interacts with electrical loads at vertex $(a, 1)$ and mechanical loads interact with output vertices, $(a, 2)$ and $(a, 3)$. Accordingly, this seems to have resulted in comparatively similar profiles. Furthermore, there are no higher frequency resonances in the Cartesian product device (in fact these are absent in both the Cartesian product and fractal-inspired devices), which most likely relates to generation level. In previous chapters and published papers [19, 20], it was apparent that increasing the fractal generation level, the transducer resonated at many more frequencies. Hence, if the Cartesian product was taken as the product of two higher generation level fractal lattices, the presence of additional and higher frequency resonances should occur. Even with the absence of higher frequency resonances, there is a substantial improvement in the transmission sensitivity amplitudes compared with the fractal-inspired and Euclidean transducers. However, the increase in amplitude resulted in a reduced bandwidth and gain bandwidth product at its resonant frequency compared to the traditional design and previously investigated fractal-inspired device at their relative resonant frequencies. Moreover, the Cartesian product design is outperformed by the Euclidean transducer in all figures of merit in reception mode. An alternative arrangement of the transducer in the circuit was also considered. In this case, the location of the output vertices changed. For the second model of the Cartesian product of two Sierpinski gasket lattices, the outputs vertices were $(b, 2)$ and $(c, 3)$. By varying these output vertices, there was a substantial improvement in all figures of merit, with the exception of the transmission sensitivity amplitude, compared to the previous layout. Furthermore, the Cartesian product design outperformed the

fractal-inspired design in all figures of merit in reception mode, and attains higher maximum amplitude and gain bandwidth product values in transmission mode.

The extension to the Green function renormalization method was also applied to the Cartesian product of two Sierpinski carpet lattices at generation level one, to determine the likely behaviour of a transducer with this design. Of course, current manufacturing constraints make construction of such designs challenging, and therefore the results presented are only to determine the possible benefits of implementing transducers with finer details. The results show that the Cartesian product design contains more resonances, but resonances at higher frequencies were absent. This is most likely as a result of the generation level. In transmission mode, it was found that the Cartesian product design outperformed the fractal-inspired and Euclidean design in terms of peak amplitudes. However, the operational bandwidth of the device at its resonant frequency is smaller than those of the other two devices at each of their resonant frequencies. Yet, due to the rise in peak amplitudes, the gain bandwidth product of the design has significantly increased. Furthermore, the Cartesian product design outperforms the Sierpinski carpet inspired design for each figure of merit in reception mode. On the other hand, in reception mode, the devices bandwidth still fails to supersede the operational bandwidth of the Euclidean transducer. However, the peak amplitude and gain bandwidth product have considerably increased in comparison to the Euclidean design.

Within this chapter the performance of two novel theoretical designed transducers has been studied. In each case, the two fractal structures used to create the Cartesian product graph only considered the product graph of two matching fractal lattices. This is not a requirement in obtaining the product graphs. Therefore, it would be interesting to consider new designs, where the lattices used to create the product graph differ to one another. For example, the Cartesian product of the Sierpinski gasket at its second generation level with the one-dimensional line is one such design that could be considered. Furthermore, it would be beneficial to

be able to obtain higher generation level results for the Sierpinski gasket Cartesian product lattice for analytical purposes.

Chapter 6

Conclusions

Ultrasonic transducers are crucial devices in numerous fields with important operating characterises that determine the efficiency of these devices. Currently, manufactured transducers operate effectively over narrow bandwidths as a result of their regular structures which incorporate a single length scale. With a growing demand for improved proficiency in the transmission and reception of ultrasonic waves, there is motive to explore new designs. To increase the operational bandwidth of ultrasonic transducers, consideration has been given to the implementation of designs that contain a range of length scales. Possible structures whose geometric pattern comprises a wide range of length scales are fractals. One-dimensional models have been executed on several new piezoelectric transducer designs to predict their performance. In each case the electrical impedance, transmission and reception sensitivities were the key parameters of interest.

For all the pre-fractal designs considered, the Green function renormalization method (or an extension on this model) was used to derive the transducers' output parameters. Furthermore, the properties of the ceramic phase were modelled on a PZT-5H ceramic. Although the pre-fractal transducers are to be composed of two phases, an active piezoelectric element and passive polymer filler, the performance of these hypothetical designs have been modelled solely on the piezoelectric material. This is typical of research in this field [7, 12, 19, 20, 86]. The transmission and reception sensitivities of these devices generally improve when the transducer is

composed from the two phases. Thus, the operational characteristics of composite pre-fractal transducers ought to exceed the single phase devices.

In Chapter 2 the performance of a standard piezoelectric plate transducer is reviewed using the linear systems model [46]. This is then extended to determine behaviour of the presently used 1-3 composite device, where the polymer phase is characterised by the hardset material HY1300/CY1301 [96]. For the two devices, their respective electrical impedance, transmission and reception sensitivities were plotted. The performances of the transducers were then assessed by obtaining the devices maximum amplitude (gain), bandwidth and gain bandwidth product. Comparison between these figures of merit found that the composite device outperformed the piezoelectric plate transducer in amplitude in reception mode, and there was a significant increase in all figures of merit in transmission mode. The composite transducer was modelled with an initial ceramic volume fraction of $v_f = 0.5$. The operating characteristics were further evaluated by varying this volume fraction, where $v_f = 1$ is the pure ceramic instance.

The analysis of employing a pre-fractal structure into the design of ultrasonic transducers is also presented within this chapter. The structure considered was the previously investigated Sierpinski gasket [86]. Green function renormalization was a method used to determine likely performance of the pre-fractal device and expressions for the transducers operating features were derived. These were then plotted against the operating frequency, along with the two homogeneous devices. On the whole, it was found that the pre-fractal transducer provided better figures of merit in reception mode, and some improvement in bandwidth at higher generation levels in transmission mode. The original contributions to this chapter was the model analysis performed on each of the three devices to obtain the significant figures of merit; maximum amplitude, operational bandwidth and gain bandwidth product. Moreover, corrections to the analysis of the Sierpinski gasket inspired transducer model have been highlighted and addressed.

In Chapter 3 the Green function renormalization method was adapted to establish the potential performance of an infinitely ramified transducer. Previously, this renormalization approach was applied to finitely ramified structures, where the connection process only involves the input/output vertices. The transmission and reception responses were investigated for the first three fractal generation levels of a transducer with Sierpinski carpet geometry. The effects of a propagating ultrasonic wave within the pre-fractal lattice were investigated using three transducer models, whereby the difference in models corresponded to the number of output vertices. The non-constant vertex degrees for the Sierpinski carpet pre-fractals necessitated a more computationally demanding approach to produce the Green function recurrent relations than was employed for the Sierpinski gasket inspired transducer. In transmission mode, when increasing the generation level, it was found that the bandwidth at the resonant frequency also increased. This increase, however, led to the reduction in amplitude. Importantly, the results indicated that each of the Sierpinski carpet models outperformed the Sierpinski gasket inspired transducer and standard design. The results demonstrated that increasing the generation level in reception mode, increased the devices' amplitude and bandwidth. To determine the most effective device, the gain bandwidth product was used as the principal figure of merit.

The Green function renormalization method was again utilised to predict the performance of a three-dimensional pre-fractal transducer in Chapter 4. The fractal used in the design of this novel device was the Sierpinski tetrix, which is the three-dimensional equivalent of the Sierpinski gasket [60, 63, 100]. By allowing for a number of assumptions of the propagating wave in the fractal lattice, the three-dimensional model was reduced to an effective one-dimensional model. This was relevant in simplifying the model considerably, which led to the rapid analysis on the performance of the pre-fractal transducer. The behaviour of the device was determined for the first five generation levels as well as for generation level fifteen. Generation level fifteen was analysed simply to determine the effects higher

generation levels have on the performance of the device. In practical situations such a design would be too complex to manufacture. Furthermore, analysis of the convergence for the transducers' operating characteristics was obtained. The results suggested that only low generation level (those within manufacturing tolerances) pre-fractal designs are required to obtain maximum potential output. It was found that increasing the generation level resulted in an abundance of resonances over a greater operating frequency range. Low generation level devices demonstrated a flat response after a given frequency. Consequently, to achieve operation at a high frequency, a specific generation level could be chosen for the given purpose. However, the generation level would still need to be relativity low to conform to manufacturing constraints. The transmission sensitives of the device resulted in greater bandwidths as the generation level was increased, yet the corresponding amplitudes and the value of the gain bandwidth product decreased. Unfortunately, both the Sierpinski gasket design and traditional transducers outperformed the Sierpinski tetrix device in transmission mode. For the reception sensitives of the device, an increase in generation level resulted in increased amplitudes and gain bandwidth product. However, in this function, the bandwidths at the resonant frequencies were smaller than the previous fractal generation level. While the Sierpinski gasket device still outperforms the Sierpinski tetrix design in reception mode, this model does show an improvement in comparison to standard design transducers.

An extension to the Green function renormalization method was derived in Chapter 5, to estimate the performance of a transducer whose design is obtained as the Cartesian product of two identical graphs. The performance of a device inspired by the Cartesian product of two Sierpinski gasket lattices at their first generation level was considered. While this is much more detailed than the Sierpinski gasket pre-fractal, construction may be possible but only at the first generation level. The main differences between this model and previous fractal-inspired transducers, is the process of obtaining the Green function elements. In this chapter,

specific Green function entries were obtained by making use of spectral decomposition of the product Green function matrix. From the results, the profiles between the Sierpinski gasket pre-fractal and Cartesian product of the Sierpinski gasket were shown to be qualitatively similar, but importantly the Cartesian product device presented higher amplitudes. However, similar to the pre-fractal transducer, higher frequency resonances were absent. This is most probably a result of the generation level. While the Cartesian product device displays higher transmission amplitudes than the Sierpinski gasket inspired and Euclidean transducers, the operational bandwidth at the resonant frequency was significantly reduced. Furthermore, in reception mode, this new device is outperformed in each figure of merit by the Euclidean transducer. To increase the values of the figures of merit in this new design, an alternative circuit layout was considered. This new arrangement resulted in exceptional figures of merit against the Sierpinski gasket inspired device in reception mode, as well as increased bandwidth and gain bandwidth product compared to that of the Euclidean design, in reception mode. Furthermore, there was an increase in amplitude at the resonant frequency and gain bandwidth product in transmission mode, when compared to the fractal-inspired transducer.

The extension to the Green function renormalization model was also used to investigate the Cartesian product of two Sierpinski carpet lattices. This was once again taken at the first generation level. The resulting graph is a very complex structure with a significant increase in the number of edges in the product lattice. As such, construction of such a device would likely be too challenging. It was found that the Cartesian product design contained more resonances than the Sierpinski carpet pre-fractal and Euclidean designs. Again higher frequency resonances were not present. At each of the devices' resonant frequencies, it was found that the Cartesian product device had the smallest bandwidth in the transmission model. In reception mode, the bandwidth of the device was also smaller than the Euclidean transducer, yet there was an improvement against the Sierpinski carpet pre-fractal design. Furthermore, the Cartesian product design surpassed the Sierpinski carpet

193

pre-fractal and Euclidean transducers in terms of amplitude and gain bandwidth product in both operation modes.

This thesis has highlighted the benefits of increasing the range of length scales in ultrasonic transducers. This has been demonstrated by modelling novel devices whose designs incorporated a fractal-like geometry. For each of the new models it was assumed that the transducer is composed entirely of a piezoelectric ceramic material. Currently, ultrasonic transducers are typically manufactured from an active piezoelectric material and passive polymer filler to improve the transmission and reception sensitivities of the device. Therefore, the analysis presented in this thesis can be extended to study the performance of fractal-inspired devices that encompass the two materials. A further benefit for including the polymer material is that the ceramic volume fraction can be varied and chosen for optimal performance. Moreover, each device has been modelled on a PZT-5H ceramic. Thus, there is further scope to investigate the performance of these novel designs when the active material properties are changed. Particular material parameters can be varied to determine the most suitable material to enhance transducer performance [12].

As a result of the one-dimensional model used to predict the potential performance of new ultrasonic transducers, only the propagation of longitudinal waves has been considered. Consequently, the behaviour of shear propagating waves in the fractal lattices is assumed to have no effect on the performance of the devices. To study the full behaviour of the transducer, employing finite element analysis (for example) can account for all directions of the propagating ultrasonic wave [83].

For the Sierpinski carpet transducer models, it may be possible to construct a system capable of determining the vertex degree for each vertex in the sequence of lattices. This may enable the application of the Green function renormalization in a similar manner as used for finitely ramified fractals, employing the recurrent relation equation to extract the next generation level pivotal Green functions. Hence, the need to obtain the inverse matrices at each fractal generation level would be

removed, reducing considerable computational cost. Furthermore, investigating the inverse problem of finding material and design parameters which produce a desired output would also be beneficial. Such inverse problems would require the consideration of the well-posedness of the model [21, 62, 65, 85].

This research is concerned with increasing the operational bandwidth of piezo-electric ultrasonic transducers by incorporating pre-fractal geometries into their design. These geometries were of interest as they span a range of length scales. More fractal-inspired transducers may be designed by implementing other fractal structures or through the modification of these structures. Specifically modified Sierpinski carpets could realise improved operating characteristics over conventional designs.

The study of work presented in this thesis contributes to a growing body of research in the field of fractal-inspired ultrasonic transducers. Furthermore, some of the results obtained suggest significant improvements over regular designs, as well as improved performance over a previously investigated fractal-inspired device. Thus, experimental work on certain designs presented in this thesis would be highly beneficial.

Appendix A

Material Properties

The constitutive relations for the ceramic phase in tensor notation are given by

$$
\begin{bmatrix} T_1^c \\ T_2^c \\ T_3^c \\ T_4^c \\ T_5^c \\ T_6^c \end{bmatrix} = \begin{bmatrix} c_{11}^c & c_{12}^c & c_{13}^c & 0 & 0 & 0 \\ c_{12}^c & c_{11}^c & c_{13}^c & 0 & 0 & 0 \\ c_{13}^c & c_{13}^c & c_{33}^c & 0 & 0 & 0 \\ 0 & 0 & 0 & c_{44}^c & 0 & 0 \\ 0 & 0 & 0 & 0 & c_{44}^c & 0 \\ 0 & 0 & 0 & 0 & 0 & c_{66}^c \end{bmatrix} \begin{bmatrix} S_1^c \\ S_2^c \\ S_3^c \\ S_4^c \\ S_5^c \\ S_6^c \end{bmatrix} - \begin{bmatrix} 0 & 0 & e_{31} \\ 0 & 0 & e_{31} \\ 0 & 0 & e_{33} \\ 0 & e_{51} & 0 \\ e_{51} & 0 & 0 \\ 0 & 0 & 0 \end{bmatrix} \begin{bmatrix} E_1^c \\ E_2^c \\ E_3^c \end{bmatrix} , \qquad \text{(A.1)}
$$

$$
\begin{bmatrix} D_1^c \\ D_2^c \\ D_3^c \end{bmatrix} = \begin{bmatrix} 0 & 0 & 0 & 0 & e_{15} & 0 \\ 0 & 0 & 0 & e_{15} & 0 & 0 \\ e_{31} & e_{31} & e_{33} & 0 & 0 & 0 \end{bmatrix} \begin{bmatrix} S_1^c \\ S_2^c \\ S_3^c \\ S_4^c \\ S_5^c \\ S_6^c \end{bmatrix} + \begin{bmatrix} \epsilon_{11}^c & 0 & 0 \\ 0 & \epsilon_{11}^c & 0 \\ 0 & 0 & \epsilon_{33}^c \end{bmatrix} \begin{bmatrix} E_1^c \\ E_2^c \\ E_3^c \end{bmatrix} , \qquad \text{(A.2)}
$$

and for the polymer phase,

$$
\begin{bmatrix} T_1^p \\ T_2^p \\ T_3^p \\ T_4^p \\ T_5^p \\ T_6^p \end{bmatrix} = \begin{bmatrix} c_{11} & c_{12} & c_{12} & 0 & 0 & 0 \\ c_{12} & c_{11} & c_{12} & 0 & 0 & 0 \\ c_{12} & c_{12} & c_{11} & 0 & 0 & 0 \\ 0 & 0 & 0 & c_{44} & 0 & 0 \\ 0 & 0 & 0 & 0 & c_{44} & 0 \\ 0 & 0 & 0 & 0 & 0 & c_{44}^c \end{bmatrix} \begin{bmatrix} S_1 \\ S_2 \\ S_3 \\ S_4 \\ S_5 \\ S_6 \end{bmatrix} , \qquad \text{(A.3)}
$$

$$
\begin{bmatrix} D_1^p \\ D_2^p \\ D_3^p \end{bmatrix} = \begin{bmatrix} \epsilon_{11} & 0 & 0 \\ 0 & \epsilon_{11} & 0 \\ 0 & 0 & \epsilon_{11} \end{bmatrix} \begin{bmatrix} E_1 \\ E_2 \\ E_3 \end{bmatrix} . \qquad \text{(A.4)}
$$

These forms were given previously in equations (2.81)-(2.84).

Description	Constant	Value	Units
Transducer thickness	l	10^{-3}	m
Transit time	τ	3.25×10^{-7}	s
Mechanical impedance of the load	Z_L	1.50×10^6	kg/m^{2}s
Mechanical impedance of the backing layer	Z_B	2.20×10^6	kg/m^{2}s
Cross-sectional area for the Euclidean transducer	A_r	10^{-4}	m^2
Front reflection coefficient	R_F	0.65	-
Back reflection coefficient	R_B	0.52	-
Front-face transmission coefficient	T_F	1.65	-
Back-face transmission coefficient	T_B	1.52	-

Table A.1: Properties for the PZT-5H ceramic material and the physical transducer [96].

Appendix B

Development of Green Function Equations

Model δ is concerned with the inclusion of three boundary conditions: one input vertex and two output vertices. For this model the application of equation (2.133) resulted in the following four equations

$$x_\delta = \hat{x}_\delta + \hat{x}_\delta b_{1,\delta} x_\delta + 2\hat{y}_\delta b_{2,\delta} y_\delta, \tag{B.1}$$

$$y_\delta = \hat{y}_\delta + \hat{y}_\delta b_{1,\delta} x_\delta + \hat{w}_\delta b_{2,\delta} y_\delta + \hat{t}_\delta b_{2,\delta} y_\delta, \tag{B.2}$$

$$t_\delta = \hat{t}_\delta + \hat{y}_\delta b_{1,\delta} y_\delta + \hat{w}_\delta b_{2,\delta} t_\delta + \hat{t}_\delta b_{2,\delta} w_\delta, \tag{B.3}$$

$$w_\delta = \hat{w}_\delta + \hat{y}_\delta b_{1,\delta} y_\delta + \hat{w}_\delta b_{2,\delta} w_\delta + \hat{t}_\delta b_{2,\delta} t_\delta. \tag{B.4}$$

Solving these simultaneously resulted in equations (3.8) - (3.11).

For model γ the use of equation (2.133) results in seven equations,

$$x_\gamma = \hat{x}_\gamma + \hat{x}_\gamma b_{1,\gamma} x_\gamma + 2\hat{y}_\gamma b_{2,\gamma} y_\gamma + \hat{z}_\gamma b_{2,\gamma} z_\gamma, \tag{B.5}$$

$$y_\gamma = \hat{y}_\gamma + \hat{y}_\gamma b_{1,\gamma} x_\gamma + \hat{x}_\gamma b_{2,\gamma} y_\gamma + \hat{y}_\gamma b_{2,\gamma} z_\gamma + \hat{z}_\gamma b_{2,\gamma} y_\gamma, \tag{B.6}$$

$$z_\gamma = \hat{z}_\gamma + \hat{z}_\gamma b_{1,\gamma} x_\gamma + 2\hat{y}_\gamma b_{2,\gamma} y_\gamma + \hat{x}_\gamma b_{2,\gamma} z_\gamma, \tag{B.7}$$

$$u_\gamma = \hat{y}_\gamma + \hat{z}_\gamma b_{1,\gamma} y_\gamma + \hat{y}_\gamma b_{2,\gamma} w_\gamma + \hat{x}_\gamma b_{2,\gamma} u_\gamma + \hat{y}_\gamma b_{2,\gamma} t_\gamma, \tag{B.8}$$

$$t_\gamma = \hat{z}_\gamma + \hat{y}_\gamma b_{1,\gamma} y_\gamma + \hat{x}_\gamma b_{2,\gamma} t_\gamma + \hat{y}_\gamma b_{2,\gamma} u_\gamma + \hat{z}_\gamma b_{2,\gamma} w_\gamma, \tag{B.9}$$

$$w_\gamma = \hat{x}_\gamma + \hat{y}_\gamma b_{1,\gamma} y_\gamma + \hat{x}_\gamma b_{2,\gamma} w_\gamma + \hat{y}_\gamma b_{2,\gamma} u_\gamma + \hat{z}_\gamma b_{2,\gamma} t_\gamma, \qquad (\text{B.10})$$

$$v_\gamma = \hat{x}_\gamma + \hat{z}_\gamma b_{1,\gamma} z_\gamma + 2\hat{y}_\gamma b_{2,\gamma} u_\gamma + \hat{x}_\gamma b_{2,\gamma} v_\gamma \qquad (\text{B.11})$$

which again are solved simultaneously to produce equations (3.21) - (3.27).

Appendix C

Figures of Merit

In order to determine the potential performance of a fractal inspired transducer, it is important to obtain numerical expressions of specific parameters. The figures of merit of interest for the transmission and reception sensitivities are tabulated for each Sierpinski carpet transducer model for generation's level one to three. The electrical and mechanical resonant frequencies for the devices are tabulated also.

Generation (n)	Electrical Resonant Frequency		Mechanical Resonant Frequency	
	f_e (MHz)	Z_η (dB)	f_m (MHz)	Z_η (dB)
1	0.945	-3.534	1.039	3.687
2	1.332	3.112	1.418	6.393
3	1.416	9.261	1.456	10.380

Table C.1: Electrical and mechanical resonant frequencies of the first three fractal generation levels for the Sierpinski carpet model η.

Generation (n)	Maximum Amplitude (Gain) (dB)	3-dB Bandwidth (MHz)	Gain Bandwidth Product
1	1.218	0.041	0.055
2	−6.717	0.203	0.043
3	−11.441	0.752	0.054

Table C.2: Figures of merit in transmitting mode for Sierpinski carpet model η.

Generation (n)	Maximum Amplitude (Gain) (dB)	3-dB Bandwidth (MHz)	Gain Bandwidth Product
1	5.751	0.126	0.473
2	5.286	0.162	0.547
3	5.723	0.246	0.917

Table C.3: Figures of merit in receiving mode for Sierpinski carpet model η.

Generation (n)	Electrical Resonant Frequency		Mechanical Resonant Frequency	
	f_e (MHz)	Z_δ (dB)	f_m (MHz)	Z_δ (dB)
1	0.995	−1.431	1.153	0.835
2	2.301	4.200	2.401	4.853
3	2.381	9.718	2.433	9.758

Table C.4: Electrical and mechanical resonant frequencies of the first three fractal generation levels for the Sierpinski carpet model δ.

Generation (n)	Maximum Amplitude (Gain) (dB)	3-dB Bandwidth (MHz)	Gain Bandwidth Product
1	−6.986	0.273	0.055
2	−7.525	0.381	0.067
3	−11.558	0.467	0.033

Table C.5: Figures of merit in transmitting mode for Sierpinski carpet model δ.

Generation (n)	Maximum Amplitude (Gain) (dB)	3-dB Bandwidth (MHz)	Gain Bandwidth Product
1	−0.182	0.553	0.530
2	1.226	0.468	0.620
3	2.660	0.520	0.959

Table C.6: Figures of merit in receiving mode for Sierpinski carpet model δ.

Generation (n)	Electrical Resonant Frequency		Mechanical Resonant Frequency	
	f_e (MHz)	Z_γ (dB)	f_m (MHz)	Z_γ (dB)
1	0.906	−2.517	1.033	1.132
2	1.347	3.828	1.408	5.350
3	1.416	9.609	1.438	10.030

Table C.7: Electrical and mechanical resonant frequencies of the first three fractal generation levels for the Sierpinski carpet model γ.

Generation (n)	Maximum Amplitude (Gain) (dB)	3-dB Bandwidth (MHz)	Gain Bandwidth Product
1	−9.621	0.424	0.046
2	−9.597	0.465	0.051
3	−13.030	0.850	0.042

Table C.8: Figures of merit in transmitting mode for Sierpinski carpet model γ.

Generation (n)	Maximum Amplitude (Gain) (dB)	3-dB Bandwidth (MHz)	Gain Bandwidth Product
1	0.583	0.130	0.149
2	1.288	0.511	0.688
3	2.648	1.528	2.812

Table C.9: Figures of merit in receiving mode for Sierpinski carpet model γ.

Appendix D

Green Function Equations for the Sierpinski Gasket Product Lattice

In this appendix, the Green functions for the Cartesian product of two Sierpinski gasket lattices are presented. The Green function elements displayed in this section correspond to model one, where the input vertex is positioned at $(a, 1)$ and the output vertices are $(a, 2)$ and $(a, 3)$.

$$
\begin{aligned}
G^{(\pi)}_{(a,1)(a,1)} &= \frac{2\left(p^2 - b_1 - b_2 + 5\right)}{p^4 - 2p^2\left(b_1 + b_2 - 5\right) + 4\left(b_1\left(b_2 - 2\right) - 3b_2 + 4\right)}, \qquad \text{(D.1)} \\
&\quad - \frac{2}{p^2 + b_1 + b_2 - 5}
\end{aligned}
$$

$$
\begin{aligned}
G^{(\pi)}_{(a,1)(a,2)} &= \frac{1}{2}\left(\frac{b_1 - b_2 - 1}{b_1 + b_2 - 5 - p^2}\right. \qquad\qquad \text{(D.2)} \\
&\quad \left. + \frac{2(7 + b_1^2 + 3b_2 - b_1(4 + b_2)) + (1 - b_1 + b_2)p^2}{4(4 + b_1(b_2 - 2) - 3b_2) - 2(b_1 + b_2 - 5)p^2 + p^4}\right),
\end{aligned}
$$

$$
\begin{aligned}
G^{(\pi)}_{(a,2)(a,2)} \;=\;& \frac{2}{13 - b_1 - 3b_2 + 2p^2 + \sqrt{9 + b_1^2 - 2b_1(1 + b_2) + b_2(2 + b_2)}} \qquad \text{(D.3)} \\[2ex]
&+ \frac{\left(3 - b_1 + b_2 - \sqrt{9 + b_1^2 - 2b_1(1 + b_2) + b_2(2 + b_2)}\right)^2}{\left(b_2 - b_1 - 3 + \sqrt{9 + b_1^2 - 2b_1(1 + b_2) + b_2(2 + b_2)}\right)^2} \\
&\hspace{6em} \times (b_1 + b_2 - 5 - p^2) \\[2ex]
&- \frac{\left(3 - b_1 + b_2 + \sqrt{9 + b_1^2 - 2b_1(1 + b_2) + b_2(2 + b_2)}\right)^2}{\left(3 + b_1 - b_2 + \sqrt{9 + b_1^2 - 2b_1(1 + b_2) + b_2(2 + b_2)}\right)^2} \\
&\hspace{6em} \times (b_1 + b_2 - 5 - p^2) \\[2ex]
&- \frac{\left(3 - b_1 + b_2 + \sqrt{9 + b_1^2 - 2b_1(1 + b_2) + b_2(2 + b_2)}\right)^2}{\left(3 + b_1 - b_2 + \sqrt{9 + b_1^2 - 2b_1(1 + b_2) + b_2(2 + b_2)}\right)^2} \\
&\hspace{4em} \times (b_1 + b_2 - 5 - p^2 + \sqrt{9 + b_1^2 - 2b_1(1 + b_2) + b_2(2 + b_2)}) \\[2ex]
&+ \frac{\left(-3 + b_1 - b_2 + \sqrt{9 + b_1^2 - 2b_1(1 + b_2) + b_2(2 + b_2)}\right)^2}{\left(-3 - b_1 + b_2 + \sqrt{9 + b_1^2 - 2b_1(1 + b_2) + b_2(2 + b_2)}\right)^2} \\
&\hspace{4em} \times (5 - b_1 - b_2 + \sqrt{9 + b_1^2 - 2b_1(1 + b_2) + b_2(2 + b_2)} + p^2) \\[2ex]
&- \frac{2}{-13 + b_1 + 3b_2 + \sqrt{9 + b_1^2 - 2b_1(1 + b_2) + b_2(2 + b_2)} - 2p^2} \quad ,
\end{aligned}
$$

204

$$G^{(\pi)}_{(a,2)(a,3)} = \frac{2}{2p^2 + b_1 + 3b_2 - 13 + \sqrt{9 + b_1^2 - 2b_1(1 + b_2) + b_2(2 + b_2)}} \quad \text{(D.4)}$$

$$-\frac{\left(b_1 - b_2 - 3 + \sqrt{9 + b_1^2 - 2b_1(1 + b_2) + b_2(2 + b_2)}\right)^2}{\left(b_2 - b_1 - 3 + \sqrt{9 + b_1^2 - 2b_1(1 + b_2) + b_2(2 + b_2)}\right)^2} \\ \times (b_1 + b_2 - 5 - p^2)$$

$$-\frac{\left(3 - b_1 + b_2 + \sqrt{9 + b_1^2 - 2b_1(1 + b_2) + b_2(2 + b_2)}\right)^2}{\left(3 + b_1 - b_2 + \sqrt{9 + b_1^2 - 2b_1(1 + b_2) + b_2(2 + b_2)}\right)^2} \\ \times (b_1 + b_2 - 5 - p^2)$$

$$-\frac{\left(3 - b_1 + b_2 + \sqrt{9 + b_1^2 - 2b_1(1 + b_2) + b_2(2 + b_2)}\right)^2}{\left(3 + b_1 - b_2 + \sqrt{9 + b_1^2 - 2b_1(1 + b_2) + b_2(2 + b_2)}\right)^2} \\ \times (b_1 + b_2 - 5 - p^2 + \sqrt{9 + b_1^2 - 2b_1(1 + b_2) + b_2(2 + b_2)})$$

$$+\frac{\left(-3 + b_1 - b_2 + \sqrt{9 + b_1^2 - 2b_1(1 + b_2) + b_2(2 + b_2)}\right)^2}{\left(-3 - b_1 + b_2 + \sqrt{9 + b_1^2 - 2b_1(1 + b_2) + b_2(2 + b_2)}\right)^2} \\ \times (5 - b_1 - b_2 + \sqrt{9 + b_1^2 - 2b_1(1 + b_2) + b_2(2 + b_2)} + p^2)$$

$$-\frac{2}{13 - b_1 - 3b_2 + \sqrt{9 + b_1^2 - 2b_1(1 + b_2) + b_2(2 + b_2)} - 2p^2} \quad .$$

References

[1] Echolocation. - The Bat Conservation Trust (BCT). http://www.bats.org. uk/pages/echolocation.html, 1991. [Accessed 14 February 2015].

[2] Characteristics of piezoelectric transducers. - NDT Resource Center. http://www.ndt-ed.org/index_flash.htm, 2001-2012. [Accessed 10 July 2013].

[3] 1-3 piezo ceramic composites. - Smart Material. http://www.smart-material. com/13CompOverview.html, 2003-2013. [Accessed 22 April 2013].

[4] M. F. Abd Kadir, A. S. Jaafar, and M. Z. A. Abd Aziz. Sierpinski carpet fractal antenna. In *Asia-Pacific Conference on Applied Electromagnetics (APACE)*, pages 1–4, Melaka, Malaysia, 2007.

[5] P. S. Addison. *Fractals and Chaos: An Illustrated Course*. CRC Press, Bristol England, 1997.

[6] S. Ahmad, N. S. Saidin, and C. M. C. Isa. Development of embroidered Sierpinski carpet antenna. In *Asia-Pacific Conference on Applied Electromagnetics (APACE)*, pages 123–127, Melaka, Malaysia, 2012.

[7] E. A. Algehyne and A. J. Mulholland. A finite element approach to modelling fractal ultrasonic transducers. *IMA J Appl Math*, 80:1684–1702, 2015.

[8] E. A. Algehyne and A. J. Mulholland. Renormalization analysis of a composite ultrasonic transducer with a fractal architecture. *Fractals*, 25(2):1750015 (14 pages), 2017.

[9] V. at English Wikipedia. https://commons.wikimedia.org/wiki/File:
Square-townsend-fledermaus.jpg, 2007. Permission to reproduce image
granted under the GNU Free Documentation License, Version 1.2. [Accessed
31 May 2016].

[10] H. Azhari. *Basics of Biomedical Ultrasound for Engineers*. John Wiley and
Sons Ltd, Hoboken, New Jersey, United States, 2010.

[11] R. Banks, R. L. O'Leary, and G. Hayward. Enhancing the bandwidth of
piezoelectric composite transducers for air-coupled non-destructive evalua-
tion. *Ultrasonics*, 75:132–144, 2017.

[12] E. Barlow, E. A. Algehyne, and A. J. Mulholland. Investigating the perfor-
mance of a fractal ultrasonic transducer under varying system conditions.
Symmetry, 8:43 (30 pages), 2016.

[13] M. T. Barlow and R. F. Bass. Random walks on graphical Sierpinski carpets.
In *Random walks and discrete potential theory*. Cambridge University Press,
1st edition, 1999.

[14] M. T. Barlow, R. F. Bass, T. Kumagai, and A. Teplyaev. Uniqueness of
Brownian motion on Sierpinski carpets. *JEMS*, 12:655–701, 2010.

[15] S. K. Bhattacharya. *Basic Electrical and Electronics Engineering*. Pearson
Education, India, 2011.

[16] V. Bucur. *Acoustics of Wood*. Springer Science & Business Media, Berlin
Heidelberg, 2006.

[17] A. Bunde and S. Havlin. *Fractals in Science*. Springer, Berlin Heidelberg,
2013.

[18] T. M. Cabral and R. Rangayyan. *Fractal Analysis of Breast Masses in
Mammograms*. Morgan & Claypool Publishers, Connecticut, United States,
2012.

[19] S. Canning, A. J. Walker, and P. A. Roach. The effectiveness of a Sierpinski carpet inspired transducer. *Submitted to Fractals*, 2016.

[20] S. Canning, A. J. Walker, and P. A. Roach. A mathematical model of a novel 3D fractal-inspired piezoelectric ultrasonic transducer. *Sensors*, 16:2170 (16 pages), 2016.

[21] S. N. Chandler-Wilde and D. P. Hewett. Well-posed PDE and integral equation formulations for scattering by fractal screens. Submitted for publication (Preprint at arXiv:1611.0953), 2016.

[22] A. R. Chandran, T. Mathew, C. K. Aanandan, P. Mohanan, and K. Vasudevan. Low backscattered dual-polarised metallo-dielectric structure based on Sierpinski carpet. *Microw Opt Technol Lett*, 40:246–248, 2004.

[23] T. L. Chen, D. J. Dikken, J. C. Prangsma, F. Segerink, and J. L. Herek. Characterization of Sierpinski carpet optical antenna at visible and near-infrared wavelengths. *New J Phys*, 16:093024, 2014.

[24] C. W. de Silva. *Sensors and Actuators: Engineering System Instrumentation.* CRC Press, Boca Raton, Florida, United States, 2015.

[25] T. G. Dewey. *Fractals in Molecular Biophysics.* Oxford University Press, New York, United States, 1998.

[26] D. Ensminger and L. J. Bond. *Ultrasonics Fundamentals, Technologies, and Applications.* CRC Press, Boca Raton, Florida, United States, third edition, 2011.

[27] K. J. Falconer. *Techniques in Fractal Geometry.* Wiley, Chichester, England, 1997.

[28] K. J. Falconer. *Fractal Geometry: Mathematical Foundations and Applications.* John Wiley and Sons Ltd, Chichester, England, 2003.

[29] K. J. Falconer. *Fractals: A Very Short Introduction.* Oxford University Press, New York, United States, 2013.

[30] G. S. A. Fam, Y. F. Rashed, and J. T. Katsikadelis. The analog equation integral formulation for plane piezoelectric media. *Eng Anal Bound Elem*, 51:199–212, 2015.

[31] Q. Fan, D.-G. Xiao, and X.-H. Zhang. Research on the ultrasonic transducer sensitivity. In *Proceedings of the Symposium on Piezoelectricity, Acoustic Waves, and Device Applications*, pages 433–436, Beijing, China, 2014.

[32] H. Fang, Z. Qiu, R. L. O'Leary, A. Gachagan, and A. J. Mulholland. Improving the operational bandwidth of a 1-3 piezoelectric composite transducer using Sierpinski gasket fractal geometry. In *IEEE International Ultrasonics Symposium*, 2016.

[33] A. Fenster and J. C. Lacefield. *Ultrasound Imaging and Therapy.* Taylor & Francis, Boca Raton, Florida, United States, 2015.

[34] Fiedorowicz. Wikimedia commons. https://commons.wikimedia.org/wiki/File:Hilbert_curve.png, 2005. Permission to reproduce image granted under the Creative Commons Attribution-Share Alike 3.0 Unported license. [Accessed 20 March 2017].

[35] J. A. Flint. A biomimetic antenna in the shape of a bats ear. *IEEE Antennas Wireless Propag Lett*, 5:145–147, 2006.

[36] R. Gazzinelli, R. L. Moreira, and W. N. Rodrigues. *Physics and Industrial Development: Proceedings of the 2nd International Conference on Physics and Industrial Development: Bridging the Gap.* World Scientific, Belo Horizonte, Brazil, 1997.

[37] V. Gibbs, D. Cole, and A. Sassano. *Ultrasound Physics and Technology: How, Why, and When.* Churchill Livingstone, London, England, 2009.

209

[38] M. Giona. Transport phenomena in fractal and heterogeneous media - Input/ Output renormalisation and exact results. *Chaos Soliton Fract*, 7:1371–1396, 1996.

[39] M. Giona and A. Adrover. Solution of transport schemes on fractals by means of Green function renormalization - Application to integral quantities. *Fractals*, 5:473–491, 1997.

[40] M. Giona, W. A. Schwalm, A. Adrover, and M. K. Schwalm. Analysis of linear transport phenomena on fractals. *Chem Eng J*, 64:45–61, 1996.

[41] M. Giona, W. A. Schwalm, M. K. Schwalm, and A. Adrover. Exact solution of linear transport equations in fractal media - I. Renormalization analysis and general theory. *Chem Eng Sci*, 51:4717–4729, 1996.

[42] R. F. Graf. *Modern Dictionary of Electronics*. Newnes, Woburn, England, seventh edition, 1999.

[43] T. R. Gururaja, W. A. Schulze, L. E. Cross, and R. E. Newnham. Piezoelectric composite materials for ultrasonic transducer application. Part II: Evaluation of ultrasonic medical applications. *IEEE T Son Ultrason*, 32:499–513, 1985.

[44] Hatch. Wikimedia commons. https://commons.wikimedia.org/wiki/File: Tree_Fractal.jpeg?uselang=en-gb, 2015. Permission to reproduce image granted under the Creative Commons Attribution-Share Alike 4.0 International licence. [Accessed 22 May 2016].

[45] S. Havlin, D. Ben-Avraham, and D. Movshovitz. Percolation on infinitely ramified fractals. *J Stat Phys*, 36:831–841, 1984.

[46] G. Hayward. A systems feedback representation of piezoelectric transducer operational impedance. *Ultrasonics*, 22:153–162, 1984.

[47] G. Hayward, D. Gillies, and T. S. Durrani. A multidimensional linear systems model of the piezoelectric transducer. In *IEEE Ultrasonics Symposium*, pages 790–793, Dallas, Texas, United States, 1984.

[48] G. Hayward and M. N. Jackson. A lattice model of the thickness-mode piezo-electric transducer. *IEEE Trans Ultrason Ferroelect Freq Control*, 33:41–50, 1986.

[49] W. R. Hedrick. *Technology for Diagnostic Sonography*. Elsevier Health Sciences, United States, 2013.

[50] W. Heywang, K. Lubitz, and W. Wersing. *Piezoelectricity: Evolution and Future of a Technology*. Springer Science & Business Media, Berlin Heidelberg, 2008.

[51] P. R. Hoskins, K. Martin, and A. Thrush. *Diagnostic Ultrasound: Physics and Equipment*. Cambridge University Press, Cambridge, England, 2010.

[52] J. A. Hossack and G. Hayward. Finite-element analysis of 1-3 composite transducers. *IIEEE Trans Ultrason Ferroelect Freq Control*, 38:618–629, 1991.

[53] R. Y.-M. Huang, editor. *Sensors: Advancements in Modeling, Design Issues, Fabrication and Practical Applications*. Springer, Berlin Heidelberg, 2008.

[54] J. W. Hunt, M. Arditi, and F. S. Foster. Ultrasound transducers for pulse-echo medical imaging. *IEEE Trans Biomed Eng*, BME-30:453–481, 1983.

[55] P. Iannaccone and M. Khokha. *Fractal Geometry in Biological Systems: An Analytical Approach*. CRC Press, Boca Raton, Florida, United States, 1996.

[56] M. N. Jackson and G. Hayward. A new three-port model of the thickness mode piezoelectric transducer. In *IEEE Ultrasonics Symposium*, pages 878–882, Atlanta, Georgia, United States, 1983.

[57] B. Jaffe, W. R. Cook Jr, and H. Jaffe. *Piezoelectric Ceramics.* Academic Press Inc. Ltd, London, England, 1971.

[58] M. N. Jahromi, A. Falahati, and R. M. Edwards. Bandwidth and impedance-matching enhancement of fractal monopole antennas using compact grounded coplanar waveguide. *IEEE Trans. Antennas. Propag.*, 59:2480–2487, 2011.

[59] G. Jones. Echolocation. *Curr Biol*, 15(13):484–488, 2005.

[60] H. Jones. *Computer Graphics through Key Mathematics.* Springer Science & Business Media, London, England, 2001.

[61] J. P. Jones. *Acoustical Imaging, Volume 21.* Springer Science & Business Media, California, United States, 1995.

[62] B. Kaltenbacher, T. Lahmer, M. Mohr, and M. Kaltenbacher. PDE based determination of piezoelectric material tensors. *Eur. J. Appl. Math.*, 2006:383–416., 17.

[63] A. Kent and J. G. Williams. *Encyclopedia of Computer Science and Technology.* CRC Press, New York, United States, 1997.

[64] R. Krimholtz, D. A. Leedom, and G. L. Matthaei. New equivalent circuits for elementary piezoelectric transducers. *Electron. Lett.*, 6(13):398–399, 1970.

[65] T. Lahmer and B. Kaltenbacher. Optimal measurement selection for piezoelectric material tensor identification. *Inverse Probl. Sci. Eng.*, 16:369–387, 2008.

[66] H. J. Lee, S. Zhang, Y. Bar-Cohen, and S. Sherrit. High temperature, high power piezoelectric composite transducers. *Sensors*, 14:14526–14552, 2014.

[67] D. A. Leedom, R. Krimholtz, and G. L. Matthaei. Equivalent circuits for transducers having arbitrary even- or odd-symmetry piezoelectric excitation. *IEEE T Son Ultrason*, SU-18(3):128–141, 1971.

[68] S. J. Leigh, R. J. Bradley, C. P. Purssell, D. R. Billson, and D. A. Hutchins. A simple, low-cost conductive composite material for 3D printing of electronic sensors. *PLoS ONE*, 7:e49365, 2012.

[69] S. J. Leigh, C. P. Purssell, D. R. Billson, and D. A. Hutchins. Using a magnetite/thermoplastic composite in 3D printing of direct replacements for commercially available flow sensors. *Smart Mater. Struct.*, 23(9):5039, 2014.

[70] C. Loughlin. *Sensors for Industrial Inspection*. Springer Science & Business Media, Dordrecht, 2012.

[71] C. J. Macleod, T. S. Durrani, and G. Hayward. A new model of the piezo-electric ultrasonic transducer. *IEEE T Acoust Speech*, 6:1046–1049, 1981.

[72] C. V. Madhusudhana Rao and G. Prasad. Characterization of 1-3 piezoelectric polymer composites - A numerical and analytical evaluation procedure for thickness mode vibrations. *Condens Matter Phys*, 13:13703: 1–10, 2010.

[73] V. M. Malhotra and N. J. Carino. *Handbook on Nondestructive Testing of Concrete*. CRC Press, Boca Raton, Florida, United States, 2004.

[74] B. B. Mandelbrot. *The Fractal Geometry of Nature*. W. H. Freeman and Co., San Francisco, United States, 1982.

[75] T. Manh, G. Uri Jensen, T. F. Johansen, and L. Hoff. Microfabricated 1-3 composite acoustic matching layers for 15 MHz transducers. *Ultrasonics*, 53:1141–1149, 2013.

[76] W. P. Mason. *Electromechanical transducers and wave filters*. D. Van Nostrand Company, New York, United States, 1948.

[77] S. G. McSweeney and W. M. D. Wright. Improving the bandwidth of air coupled capacitive ultrasonic transducers using selective networks. In *IEEE Ultrasonics Symposium*, pages 1191–1194, Beijing, China, 2008.

[78] P. Meakin. *Fractals, Scaling and Growth Far from Equilibrium.* Cambridge University Press, Cambridge, England, 1998.

[79] T.-H. Meen, S. Prior, and A. D. K.-T. Lam, editors. *Innovation, Communication and Engineering.* CRC Press, London, England, 2013.

[80] R. A. Meyers, editor. *Mathematics of Complexity and Dynamical Systems.* Springer Science & Business Media, New York, United States, 2011.

[81] M. Molitch-Hou. 3D printed piezoceramics give new shape to electronics. https://3dprintingindustry.com/news/3d-printed-piezoceramics-give-new-shape-to-electronic-devices-66313/, February 2016. [Accessed 6 September 2016].

[82] A. J. Mulholland. Bounds on the Hausdorff dimension of a renormalisation map arising from an excitable reaction-diffusion system on a fractal lattice. *Chaos Soliton Fract*, 35(2):274–284, 2008.

[83] A. J. Mulholland, J. W. Mackersie, R. L. O'Leary, A. Gachagan, A. J. Walker, and N. Ramadas. The use of fractal geometry in the design of piezoelectric ultrasonic transducers. In *IEEE International Ultrasonics Symposium Proceedings*, pages 1559–1562, Orlando, Florida, United States, 2011.

[84] A. J. Mulholland, R. L. O'Leary, S. N. Ramadas, A. Parr, A. Troge, R. A. Pethrick, and G. Hayward. A theoretical analysis of a piezoelectric ultrasound device with an active matching layer. *Ultrasonics*, 47:102–110, 2007.

[85] A. J. Mulholland, R. Picard, S. Trostorff, and M. Waurick. On well-posedness for some thermo-piezoelectric coupling models. *Math. Meth. Appl. Sci.*, 39:4375–4384, 2016.

214

[86] A. J. Mulholland and A. J. Walker. Piezoelectric ultrasonic transducers with fractal geometry. *Fractals*, 19:469–479, 2011.

[87] Y. Na and S. Xiao-Wei. Analysis of the multiband behavior on Sierpinski carpet fractal antennas. In *Microwave Conference Proceedings (APMC) Asia-Pacific Conference Proceedings*, 2005.

[88] K. Nakamura. *Ultrasonic Transducers: Materials and Design for Sensors, Actuators and Medical Applications.* Woodhead Publishing Ltd, Cambridge, England, 2012.

[89] T. Nakayama and K. Yakubo. *Fractal Concepts in Condensed Matter Physics.* Springer Science & Business Media, Berlin Heidelberg, 2013.

[90] N. T. Nguyen, M. Lethiecq, B. Karlsson, and F. Patat. Highly attenuative rubber modified epoxy for ultrasonic transducer backing applications. *Ultrasonics*, 34:669–675, 1996.

[91] R. A. Nobel, A. D. R. Jones, T. J. Robertson, D. A. Hitchins, and D. R. Billson. Novel wide bandwidth, micromachined ultrasonic transducers. *IEEE Trans Ultrason Ferroelectr Freq Control*, 48:1495–1507, 2001.

[92] A. Nowicki, K. Kycia, T. D. Hien, O. Gajl, and M. Kleiber. Numerical calculations of the acoustic properties of the 1-3 composite transducers for medical applications. *IEEE Ultrasonics Symposium*, 2:1041–1044, Seattle, Washington, USA, November 1995.

[93] M. W. Nygren. Finite element modeling of piezoelectric ultrasonic transducers. Master's thesis, Norwegian University of Science and Technology, 2011.

[94] S. Olcum, M. N. Senlik, and A. Atalar. Optimization of the gain-bandwidth product of capacitive micromachined ultrasonic transducers. *IEEE Trans Ultrason Ferroelect Freq Control*, 52:2211–2219, 2005.

[95] S. Olcum, M. N. Senlik, C. Bayram, and A. Atalar. Design charts to maximize the gain-bandwidth product of capacitive micromachined ultrasonic transducers. *IEEE Ultrasonics Symposium*, 4:1941–1944, 2005.

[96] L.-A. Orr. *Plane Wave Expansion Analysis of Lossy Composite Transducers Incorporating Anisotropic Polymers*. PhD thesis, University of Strathclyde, 2007.

[97] L.-A. Orr, A. J. Mulholland, R. L. O'Leary, and G. Hayward. Analysis of ultrasonic transducers with fractal architecture. *Fractals*, 16:333–349, 2008.

[98] L.-A. Orr, A. J. Mulholland, R. L. O'Leary, A. Parr, R. A. Pethrick, and G. Hayward. Theoretical modelling of frequency dependent elastic loss in composite ultrasonic transducer. *Ultrasonics*, 47:130–137, 2007.

[99] E. P. Papadakis, R. N. Thurston, and A. D. Pierce. *Reference for Modern Instrumentation, Techniques, and Technology: Ultrasonic Instruments and Devices II*. Elsevier, San Diego, United States, 1998.

[100] H.-O. Peitgen, H. Jürgens, D. Saupe, E. Maletsky, T. Perciante, and L. Yunker. *Fractals for the Classroom: Strategic Activities Volume One*. Springer Science & Business Media, New York, United States, 2012.

[101] S. N. Ramadas and G. Hayward. A knowledge based approach for design optimization of ultrasonic transducers and arrays. In *IEEE Ultrasonics Symposium*, pages 2247–2250, Rotterdam, The Netherlands, 2005.

[102] S. N. Ramadas, G. Hayward, R. L. O'Leary, T. F. McCunnie, A. J. Mulholland, A. Troge, R. A. Pethrick, D. Robert, and V. Murray. A three-port acoustic lattice model for piezoelectric transducers containing opposing zones of polarization. In *IEEE International Ultrasonics Symposium*, pages 10–31, New, York, United States, 2007.

[103] R. Rammal. Spectrum of harmonic excitations on fractals. *J Phys-Paris*, 45(2):191–206, 1984.

[104] R. Rammal and G. Toulouse. Random walks on fractal structures and percolation clusters. *J Phys Lett-Paris*, 44(1):13–22, 1983.

[105] D. Robert and M. C. Göpfert. Novel schemes for hearing and orientation in insects. *Curr Opin Neurobiol*, 12:715–720, 2002.

[106] J. L. Rose. *Ultrasonic Waves in Solid Media*. Cambridge University Press, Cambridge, England, 2004.

[107] M. Sakthivel and A. Arockiarajan. An effective matrix poling characteristics of 1-3-2 piezoelectric composites. *Sensor Actuat A-Phys*, 167:34–43, 2011.

[108] D. W. Schindel, D. A. Hutchins, L. Zou, and M. Sayer. The design and characterization of micro-machined air-coupled capacitance transducers. *IEEE Trans Ultrason Ferroelectr Freq Control*, 42:42–50, 1995.

[109] Schnobby. https://en.wikipedia.org/wiki/File:Frost_patterns_2.jpg, 2010. Permission to reproduce image granted under the Creative Commons Attribution-Share Alike 3.0 Unported license. [Accessed 22 May 2016].

[110] M. K. Schwalm, M. Giona, W. A. Schwalm, A. Adrover, and M. Giustiniani. Renormalization analysis and adsorption on fractal and disordered lattices in the presence of energetic disorder. *Langmuir*, 13(5):1128–1137, 1997.

[111] W. A. Schwalm and M. K. Schwalm. Extension theory for lattice Green functions. *Phys Rev B*, 37:9524–9542, 1988.

[112] W. A. Schwalm and M. K. Schwalm. Closed formulae for Green functions on fractal lattices. *Physica A*, 185:195–201, 1992.

[113] W. A. Schwalm and M. K. Schwalm. Explicit orbits for renormalisation maps for Green functions on fractal lattices. *Phys Rev B*, 47:7847–7858, 1993.

[114] M. Schwartz. *Smart Materials.* CRC Press, Boca Raton, Florida, United States, 2008.

[115] L. Seuront. *Fractals and Multifractals in Ecology and Aquatic Science.* CRC Press, Boca Raton, Florida, United States, 2009.

[116] Shung. https://commons.wikimedia.org/wiki/File:Bat_echolocation.jpg, 2010. Permission to reproduce image granted under the public domain. [Accessed 31 May 2016].

[117] K. K. Shung. *Diagnostic Ultrasound: Imaging and Blood Flow Measurements.* CRC Press, Boca Raton, Florida, United States, 2005.

[118] B. Siciliano and O. Khatib. *Handbook of Robotics.* Springer Science & Business Media, Berlin Heidelberg, 2008.

[119] K. T. Sillar, L. D. Picton, and W. J. Heitler. *The Neuroethology of Predation and Escape.* John Wiley and Sons Ltd, Chichester, West Sussex, 2016.

[120] W. A. Smith. Modeling 1-3 composite piezoelectrics: Hydrostatic response. *IEEE Trans Ultrason Ferroelect Freq Control*, 40:41–49, 1993.

[121] W. A. Smith and B. A. Auld. Modeling 1-3 composite piezoelectrics : Thickness-mode oscillations. *IEEE Trans Ultrason Ferroelect Freq Control*, 38:40–47, 1991.

[122] W. A. Smith, A. Shaulov, and B. A. Auld. Tailoring the properties of composite piezoelectric materials for medical ultrasonic transducers. In *IEEE Ultrasonics Symposium*, pages 642–647, San Francisco, California, United States, 1985.

[123] D. Sparks. *Advances in Agronomy*, volume 63. Academic Press Inc. Ltd, San Diego, United States, 1997.

[124] P. Spies, M. Pollak, and L. Mateu. *Handbook of Energy Harvesting Power Supplies and Applications.* CRC Press, Boca Raton, Florida, United States, 2015.

[125] M. State, P. J. Brands, and F. N. van de Vosse. Improving the thermal dimensional stability of flexible polymer composite backing materials for ultrasound transducers. *Ultrasonics*, 50:458–466, 2010.

[126] T. L. Szabo and P. A. Lewin. Ultrasound transducer selection in clinical imaging practice. *J Ultrasound Med*, 32(4):573–582, 2013.

[127] M. Toda. Narrowband impedance matching layer for high efficiency thickness mode ultrasonic transducers. *IEEE Trans Ultrason Ferroelect Freq Control*, 49:299–306, 2002.

[128] K. Uchino. *Ferroelectric Devices.* CRC Press, Boca Raton, Florida, United States, second edition, 2009.

[129] M. S. Vijaya. *Piezoelectric Materials and Devices: Applications in Engineering and Medical Sciences.* CRC Press, Boca Raton, Florida, United States, 2012.

[130] A. A. Vives. *Piezoelectric Transducers and Applications.* Springer, Berlin Heidelberg, second edition, 2008.

[131] A. J. Walker and A. J. Mulholland. A theoretical model of an electrostatic ultrasonic transducer incoporating resonating conduits. *IMA J Appl Math*, 75:769810, 2010.

[132] A. J. Walker and A. J. Mulholland. A theoretical model of an ultrasonic transducer incorporating spherical resonators. *IMA J Appl Math*, 81:1–25, 2015.

[133] A. J. Walker and A. J. Mulholland. A pipe organ-inspired ultrasonic transducer. *Submitted to IMA J Appl Math*, 2016.

[134] A. J. Walker, A. J. Mulholland, E. Campbell, and G. Hayward. A theoretical model of a new electrostatic transducer incorporating fluidic amplification. In *IEEE Ultrasonics Symposium*, pages 1409–1412, Beijing, China, 2008.

[135] R. H. Warring and S. Gibilisco. *Fundamentals of Transducers*. Tab Books Inc., Blue Ridge Summit, Pennsylvania, United States, 1985.

[136] S. Wong and B. L. Ooi. Analysis and bandwidth enhancement of Sierpinski carpet antenna. *Microw Opt Techn Let*, 31:13–18, 2001.

[137] D. I. Woodward, C. P. Purssell, D. R. N. Billson, D. A. Hutchins, and S. J. Leigh. Additively-manufactured piezoelectric devices. *Phys. Status Solidi A*, 212 (10):2107–2113, 2015.

[138] J. Yang. *Analysis of Piezoelectric Devices*. World Scientific, Singapore, 2006.

[139] M. Zhu and G. Leighton. Dimensional reduction study of piezoelectric ceramics constitutive equations from 3-D to 2-D and 1-D. *IEEE Trans Ultrason Ferroelect Freq Control*, 55:2377–2383, 2008.